VNiVERSiDAD DE SALAMANCA

FACVLTAD DE CiENCiAS QVíMiCAS

DEPARTAMENTO DE iNGENiERíA QVíMiCA Y TEXTiL

Tesis Doctoral del programa de Doctorado en Ciencia y Tecnología Químicas:

SíNTESiS Y DiSEÑO DE EQViPOS DE TRANSFERENCiA DE ENERGíA PARA PLANTAS DE ENERGíA TERMOSOLAR

Memoria para optar al grado de Doctor presentada por:

JOSÉ ANTONIO LUCEÑO SÁNCHEZ

SALAMANCA, 2021

"*Frustra fit per plura, quod potest fieri per pauciora*"

(No tiene sentido hacer con más lo que se puede hacer con menos)

Guillermo de Ockham: Summa Totius Logicae, i. 12 - 1327

APOYO FINANCIERO

La presente Tesis Doctoral no habría sido posible sin las licencias de software suministradas por la Universidad de Salamanca, así como su acceso a publicaciones científicas y herramientas de teletrabajo.

Se agradece el apoyo económico recibido por la Fundación General de la Universidad de Salamanca en el año 2015 a través del programa de Prototipos Orientados al Mercado en TCUE Universidad-Empresa, ya que supuso el germen original desde el que se concibió el inicio de la presente Tesis Doctoral.

Se debe hacer especial mención al grupo de investigación Process System Engineering M3 (PSEM3) del Departamento de Ingeniería Química y Textil, de la Facultad de Ciencias Químicas de la Universidad de Salamanca, ya que dicho grupo facilitó el acceso a equipamiento informático y licencias específicas de programas de optimización que fueron cruciales para el desarrollo de la presente Tesis Doctoral.

AGRADECIMIENTOS

Quiero reconocerle al profesor Mariano Martín Martín todo lo que ha hecho por mi desde que me impartió clase por primera vez. Desde hace más de siete años, no has parado en intentar fomentar la curiosidad y el desarrollo profesional de tus estudiantes y, en casos como el mío, apoyarnos en la idea de iniciar una carrera investigadora mediante un doctorado y darnos consejos para poder alcanzar las sucesivas metas que iban surgiendo.

Asimismo, agradecer al profesor Sandro Macchietto, del Imperial College London, la posibilidad de poder trabajar con su estudiante. Aún con las circunstancias que hemos vivido, la colaboración con Federico ha sido muy fructífera para expandir mi conocimiento en el campo de la optimización en Ingeniería Química.

DOCVMENTACIÓN

La presente sección contiene las aclaraciones y documentación requeridas por la normativa de la Universidad de Salamanca "*Procedimiento para la presentación de la Tesis Doctoral en la Universidad de Salamanca en el formato de compendio de artículos/publicaciones, aprobado por la Comisión de Doctorado y Postgrado, 15 de febrero de 2013*".

La presente Tesis Doctoral ha sido presentada en el formato de compendio de artículos, utilizándose para cumplir el punto 2.2 de la normativa anteriormente mencionada los siguientes tres artículos:

Autor/es	Luceño, J.A.[a]; Martín, M.[a]
Afiliación	[a]Department of Chemical Engineering, University of Salamanca, 37008 Salamanca, Spain
Título	Two-step optimization procedure for the conceptual design of A-frame systems for solar power plants
Revista	Energy
Año	2018
Volumen, pp.	165, 483-500
DOI	10.1016/j.energy.2018.09.177
Indicadores	Q1 2018 JCR, 15/103 (Energy and fuels)

Autor/es	Luceño, J.A.[a]; Martín, M.[a]
Afiliación	[a]Department of Chemical Engineering, University of Salamanca, 37008 Salamanca, Spain
Título	Optimal design of aging systems: A-frame coolers design under fouling
Revista	*Computers & Chemical Engineering*
Año	2019
Volumen, pp.	122, 47-58
DOI	10.1016/j.compchemeng.2018.05.015
Indicadores	Q1 2019 JCR, 33/143(Engineering, Chemical)

Autor/es	Luceño, J.A.[a]; de la Fuente, E.[a]; Martín, M.[a]
Afiliación	[a]Department of Chemical Engineering, University of Salamanca, 37008 Salamanca, Spain
Título	Optimal Design of Solar Receivers in CSP Plants: Effects of Facility Location
Revista	*Industrial & Engineering Chemistry Research*
Año	2021
Volumen, pp.	Article ASAP
DOI	10.1021/acs.iecr.0c05383
Indicadores	Q2 2019 JCR, 43/143 (Engineering, Chemical), (no disponibles índices de 2020-2021)

La Tesis ha sido estructurada en un conjunto de 6 capítulos precedidos de un resumen, en el cual se presentan brevemente los objetivos de los diferentes trabajos, sus metodologías, y los resultados y conclusiones obtenidos.

En el Capítulo I "*Introducción*" se realiza una exposición de los antecedentes del tema objeto de estudio, como es la presentación de las plantas de concentración solar y de los métodos de programación matemática utilizados para formular problemas relacionados con la Ingeniería Química.

En el Capítulo II "*Objetivos*" se enumeran los objetivos fijados, y brevemente cómo se piensan alcanzar.

En los Capítulos III "*Enfriamiento seco: A-frame*" y IV "*Calentamiento de sales fundidas: Colector solar*" se presentan los artículos científicos originales publicados, que recogen la investigación realizada durante la Tesis.

En el Capítulo V "*Conclusiones y Trabajos Futuros*" se exponen las conclusiones principales obtenidas después de evaluar críticamente los resultados, y las posibles vías de futuros trabajos.

Por último, el Capítulo VI "*Listado de contribuciones*" recoge toda la producción científica derivada de los estudios, colaboraciones y divulgación de los resultados de investigación.

Dr. D. **Mariano Martín Martín**, Profesor titular de Ingeniería Química de la Universidad de Salamanca

Informa:

Que la memoria titulada "Síntesis y diseño de equipos de transferencia de energía para plantas de energía termosolar" que para optar al Grado de Doctor en Ingeniería Química, Programa de Doctorado de "Ciencia y Tecnología Químicas " presenta D José Antonio Luceño Sánchez, ha sido realizada bajo mi dirección en el Departamento de Ingeniería Química y Textil de la Universidad de Salamanca.

Considerando que constituye trabajo de tesis, se autoriza su presentación ante la Escuela de Doctorado de la Universidad de Salamanca.

Y para que así conste se firma el presente informe,

VNiVERSiDAD D SALAMANCA
CAMPUS DE EXCELENCIA INTERNACIONAL

EJECUCIÓN DE ACUERDOS

La Comisión Académica del Programa de Doctorado en Ciencia y Tecnología Químicas reunida en sesión ordinaria virtual el día 14 de mayo de 2021,

ACORDÓ

AUTORIZAR a D. José Antonio Luceño Sánchez a presentar la Tesis Doctoral titulada "*Síntesis y diseño de equipos de transferencia de energía para plantas de energía termosolar*" en el **formato de compendio de artículos/publicaciones** por cumplir la normativa de la Universidad de Salamanca "*Procedimiento para la presentación de la Tesis Doctoral en la Universidad de Salamanca en el formato de compendio de artículos/publicaciones*, aprobado por la Comisión de Doctorado y Postgrado, 15 de febrero de 2013".

Salamanca, 14 de mayo de 2021.

Dña. Ester De la Fuente Gómez, con DNI 70940030A, coautora del trabajo científico titulado "*Optimal Design of Solar Receivers in CSP Plants: Effects of Facility Location*", publicado en la revista *Industrial & Engineering Chemistry Research* de la editorial *ACS Publications* [doi: 10.1021/acs.iecr.0c05383]:

INFORMA que, de acuerdo con la normativa vigente de la Universidad de Salamanca en materia de presentación de Tesis doctorales por compendio de artículos y autoría de trabajos científicos:

1. Acepta que D. José Antonio Luceño Sánchez presente el citado trabajo científico en su Tesis doctoral en la Universidad de Salamanca titulada "*Síntesis y diseño de equipos de transferencia de energía para plantas de energía termosolar*".

2. Reconoce que D. José Antonio Luceño Sánchez es el autor principal de la investigación recogida en el citado trabajo científico.

3. Certifica su renuncia expresa y formal a utilizar el citado trabajo científico como parte de otra Tesis doctoral.

Para que así conste y surta los efectos oportunos, se firma el presente documento en BÉJAR a día 03 de mayo de 2021.

RESVMEN

RESUMEN

La producción de energía es uno de los temas más importantes para la sociedad actual. Cada día que pasa crece la necesidad de sustituir las antiguas fuentes de energía fósiles por otras más sostenibles o renovables, debido al aumento de la población mundial y al consumo asociado al desarrollo tecnológico. Dentro de las energías renovables se enmarca la energía solar, una fuente renovable de energía disponible en toda la Tierra ya que la radiación solar alcanza toda la superficie. Esta radiación solar puede ser aprovechada mediante dos enfoques diferentes: las tecnologías fotovoltaicas, con células fotovoltaicas; o las tecnologías de concentración termosolar, con centrales de potencia de concentración solar.

Las centrales de potencia de concentración solar son plantas industriales que aplican todo el conocimiento disponible de las plantas de potencia térmica típicas (ej. quema de biomasa o carbón), creando unas instalaciones de producción de energía verde y sostenible mediante el aprovechamiento de la radiación solar para calentar un fluido que permitirá producir vapor de agua o gas sobrecalentado y, mediante un sistema de turbinas, electricidad. Estas plantas tienen diferentes secciones como pueden ser el sistema de refrigeración o el campo solar, pero todas ellas tienen en común que la transferencia de energía está fuertemente presente en su funcionamiento.

La primera parte de la presente Tesis trata de los sistemas de refrigeración seca que utilizan aire como fluido refrigerante, centrándose en la arquitectura de enfriador de aire A-frame. Este tipo de equipos reduce el consumo de agua de la instalación, debido a que no se utiliza agua para refrigerar las corrientes, pero genera un consumo de energía adicional por el empleo de ventiladores para mover el aire circundante.

Como punto de partida, se procedió a establecer un proceso de optimización en dos etapas para el diseño conceptual y la operación de este tipo de equipos: la primera etapa consistió en el modelado del equipo considerando las particularidades geométricas de los A-frames, incluyendo variables como la longitud de los tubos, su configuración, y el

cálculo de los ventiladores necesarios; la segunda etapa se basó en la evaluación de la operación del equipo durante un año, buscando el mínimo consumo de energía. La primera etapa se formuló como un problema de programación mixta entera no lineal (MINLP), resulto mediante un algoritmo de ramificación y acotamiento diseñado a medida. La segunda etapa se resolvió aplicando una formulación de problemas MINLP multi-periodo, en los cuales se fijó la geometría atendiendo a los resultados de la primera etapa. Los resultados obtenidos sugirieron un diseño con un ángulo de apertura de 63°, 4 módulos de 75 tubos de 13.5m de largo y 3.3 cm de diámetro distribuidos en una única fila de tubos, y 4 ventiladores. Los módulos presentaban una operación variable durante el año, funcionando a plena capacidad durante verano, y permitiendo reducir en un 20% el consumo de energía del equipo. Además, la energía requerida solamente representaba alrededor del 4% de la producción de la instalación. Por último, se determinó que el diseño del equipo podía verse afectado por la disponibilidad de terreno y/o el diseño de la instalación.

Posteriormente, se procedió a estudiar el efecto de la pérdida de eficiencia por ensuciamiento en el diseño de los sistemas A-frame, y las posibles consecuencias durante su operación, ya que el ensuciamiento afecta a la pérdida de carga y al coeficiente global de transferencia de calor. Se presentó un procedimiento de dos etapas: la primera etapa se centró en el diseño del equipo, considerando las condiciones de operación más exigentes antes del mantenimiento del equipo; y la segunda etapa se enfocó en la evaluación de la operación, buscando reducir los costes de operación y limpieza del equipo. El ciclo de operación y el diseño del equipo se determinaron a partir del coste mínimo de operación en función de la duración del ciclo de operación. Al considerarse un perfil sigmoidal de ensuciamiento, se obtuvo como resultado un ciclo óptimo de 8 años de operación y un diseño que permitía reducir la energía requerida por debajo del 4% de la producción de la instalación.

La segunda parte de la Tesis se dedicó al estudio de la transferencia de energía en los colectores solares centrales. Se desarrolló un procedimiento de dos etapas para el diseño y operación de los colectores centrales tubulares: la primera etapa se centraba en el diseño del equipo formulando un problema de optimización MINLP, considerando las condiciones climáticas y de radiación de la localización; la segunda etapa consistía en la

evaluación de la operación del equipo durante un año aplicando una formulación NLP, y utilizando como diseño del equipo el obtenido en la etapa anterior. Se estudiaron 3 localizaciones diferentes (Almería, Arizona, y Escocia) para evaluar el efecto del clima y el perfil de radiación en los resultados. Los diseños obtenidos mostraron el efecto de la elección de la localización en el dimensionamiento del equipo. El estudio de la operación durante un año mostró las características de la transferencia de calor del equipo, así como el efecto del perfil de velocidad del viento de la localización en la transferencia de calor por convección. Además, se identificó que un análisis más exhaustivo de este tipo de equipos permitiría determinar con mayor precisión la reducción de la caída de presión en el interior de los tubos, y el posiblemente aumento de la tensión térmica.

TABLA DE CONTENIDOS

CAPíTVLO i

iNTRODVCCiÓN

I. INTRODUCCIÓN

I.1. Energía Solar

I.1.1. Importancia de la producción de energía

La energía es el motor que mueve toda la sociedad en la actualidad, y el aumento de consumo se encuentra estrechamente ligado a varios factores de desarrollo de un país [1,2], como son el aumento de población y producción de empresas, el aumento del uso de nuevas tecnologías (ej. centros de datos), o la mejora de la calidad de vida.

Las Revoluciones Industriales que ha experimentado la civilización humana desde el siglo XVIII han supuesto un cambio radical en la forma en que los humanos viven en el planeta. Durante la Primera Revolución Industrial se puso de manifiesto la nueva importancia que tendría la producción de energía en el desarrollo y progreso futuro de la humanidad, ya que la implementación de las máquinas de vapor en la industria supuso un cambio drástico en la producción. Durante la Segunda Revolución Industrial (s. XIX), se investigaron y mejoraron tecnologías para la producción de electricidad a partir de combustibles fósiles, como el carbón, petróleo o gas, y se extendió el uso de la energía eléctrica a nivel tanto industrial como urbano.

Sin embargo, a lo largo de las últimas décadas, la sociedad ha sido más consciente del impacto medioambiental que los combustibles fósiles suponen [3,4], y por ello se han investigado nuevas fuentes de energía limpia o renovable. Este cambio del modelo de producción de energía ha llevado a la estabilización o reducción de la producción utilizando combustibles fósiles, como es el caso del carbón (Figura 1 [5]), y a una mayor presencia de fuentes de energía menos contaminantes, como son el gas natural o las energías renovables, en el mix energético global.

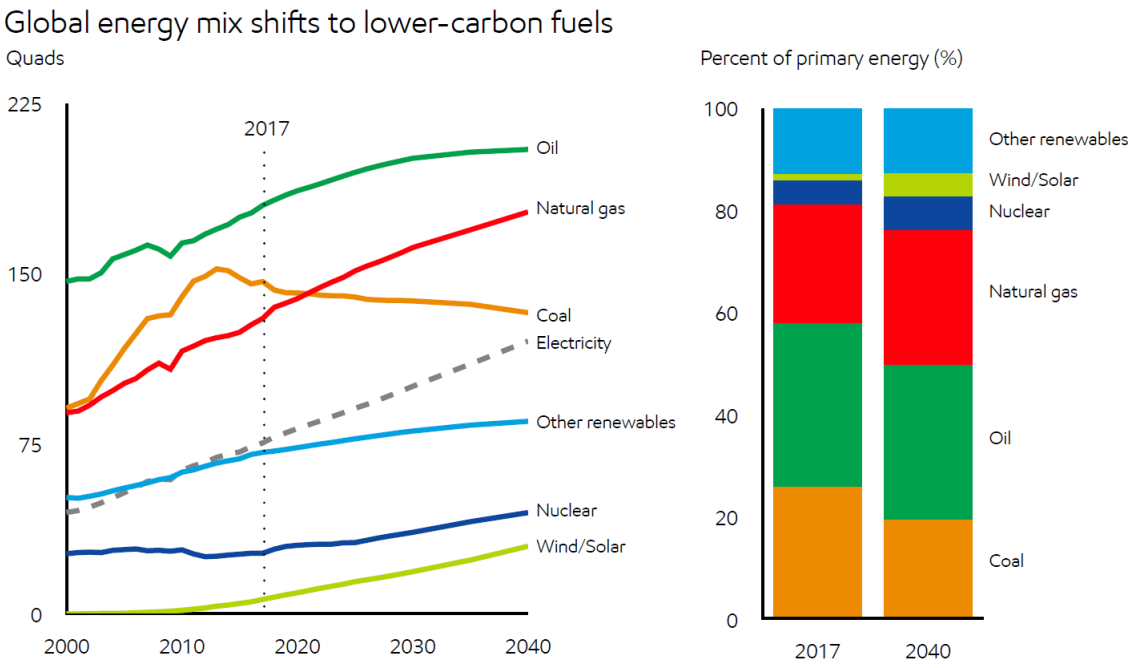

Figura 1. Estimación del mix energético global. Reproducida de [5].

Las energías renovables se caracterizan porque la materia prima consumida para obtener energía eléctrica puede ser repuesta, o renovada su disponibilidad, en un intervalo de tiempo aceptable, o incluso que se trate de un recurso que se genere de manera natural de manera que para el ser humano sea inacabable, como es el caso de la radiación solar. Dentro de este conjunto de nuevas energías renovables se encuentra la energía obtenida del aprovechamiento de la radiación solar, o comúnmente denominada Energía Solar.

I.1.2. Conceptos básicos de Energía Solar

El Sol es una gigantesca esfera de principalmente de átomos de hidrógeno y helio (~91%, ~8.9% He, ~0.1% resto) que se encuentra ubicada en el centro del Sistema Solar [6]. En su interior tienen lugar reacciones de fusión nuclear de H para dar He, que generan enormes cantidades de energía que se desprende al exterior; parte de esa energía abandona el Sol en forma de calor y radiación, que es la radiación solar que alcanza la Tierra. La radiación solar representa una fuente casi inagotable de energía para la humanidad, dado que la estimación de la vida restante del Sol supera con creces la historia no solo humana, sino del planeta [6]. En términos de consumo energético, la radiación

solar incidente de la Tierra equivaldría a varias veces la demanda acumulada de energía actual de todo el planeta [7]. La disponibilidad de radiación solar no es igual a lo largo de la superficie terrestre debido a distintos factores, que cubren desde condiciones atmosféricas, el clima, e incluso la topografía (Figura 2 [8]).

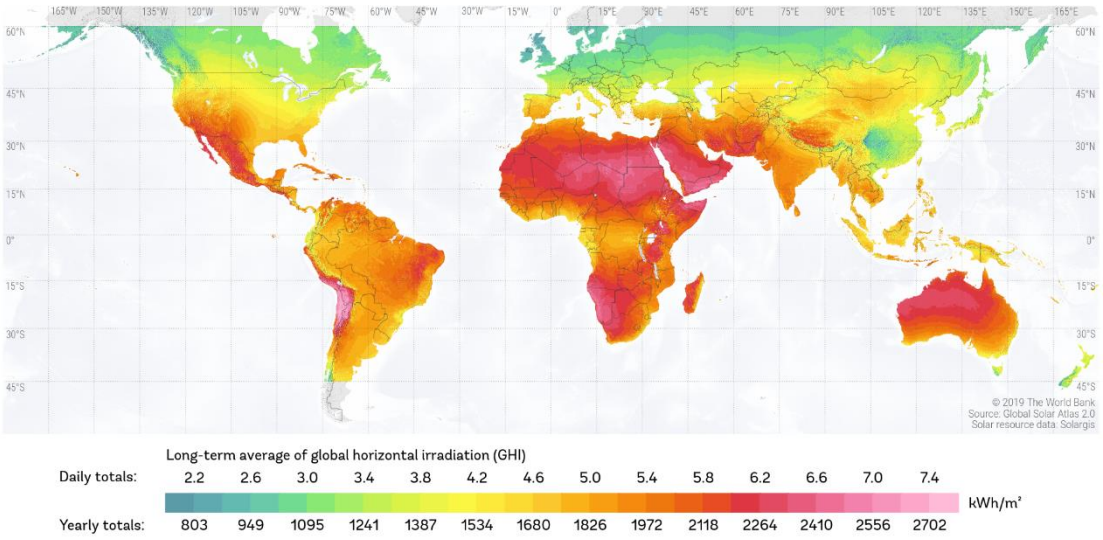

Figura 2. Valores medios de radiación horizontal global en la Tierra. Adaptada de [8].

El aprovechamiento de la radiación solar ha sido estudiado desde diversos enfoques, como pueden ser: trabajos centrados en la predicción de los valores para mejorar los diseños de las instalaciones [9,10]; integración de dispositivos fotovoltaicos en instalaciones y edificios para el aprovechamiento directo [11]; generación de energía eléctrica para consumo mediante ciclos de potencia [12]; y conversión de electricidad en sustancias de almacenamiento de energía para su futuro uso [13]. Aunque existen trabajos previos para comparar diferentes sistemas de aprovechamiento, véase la tradicional comparación de las tecnologías fotovoltaicas con las de energía solar térmica [14,15], en la presente Tesis se considerará únicamente el caso de la energía solar térmica.

La energía solar térmica, o energía termosolar, es la energía obtenida a partir del aprovechamiento indirecto de la radiación solar mediante la absorción de la radiación por un fluido de trabajo que aumentará su contenido energético, y que posteriormente será empleado para producir electricidad mediante un ciclo de potencia [16]. Las instalaciones termosolares son una interesante opción para la producción de energía eléctrica de manera renovable, ya que no se genera CO_2 durante su operación y pueden localizarse en un amplio abanico de lugares. Este tipo de instalaciones tienen una serie de equipos que

dependen de manera decisiva del correcto diseño de los mecanismos de transferencia de energía involucrados.

I.2. Plantas de Potencia de Concentración Solar

Las plantas de potencia de concentración solar, o plantas CSP (Concentrated Solar Power), son las instalaciones industriales destinadas a la conversión de la radiación procedente del Sol en energía eléctrica mediante un ciclo de potencia. La concepción de las plantas CSP se fundamenta en las plantas térmicas clásicas para la producción de electricidad, como pueden ser las centrales de carbón o biomasa [17-20].

El funcionamiento de este tipo de plantas se rige a través de los ciclos térmicos a nivel industrial, como son el ciclo Rankine o el ciclo Brayton. La diferencia más significativa entre el uso de un ciclo u otro reside en si se realiza una expansión de una corriente de gas o una expansión de una corriente de vapor de agua, para generar electricidad mediante el uso de un sistema de turbinas, ya que eso conlleva una arquitectura diferente de la instalación:

a) Ciclo Rankine:

   El ciclo Rankine involucra cambios de fase de la corriente que se utiliza para obtener la energía eléctrica. En este caso, normalmente se emplea una corriente de vapor de agua como fluido de trabajo. El vapor de agua se genera mediante la transferencia del calor procedente de la radiación a una corriente de agua en una serie de intercambiadores de calor, para posteriormente ser alimentado al sistema de turbinas. Al ser expandida la corriente de vapor de agua, que posee una alta temperatura y alta presión, se genera electricidad a partir del trabajo mecánico realizado en la turbina, y se obtiene una corriente de vapor con menor temperatura y menor presión. En la Figura 3 se presentan diferentes variaciones del ciclo Rankine, dependiendo de las etapas que siga el fluido de trabajo.

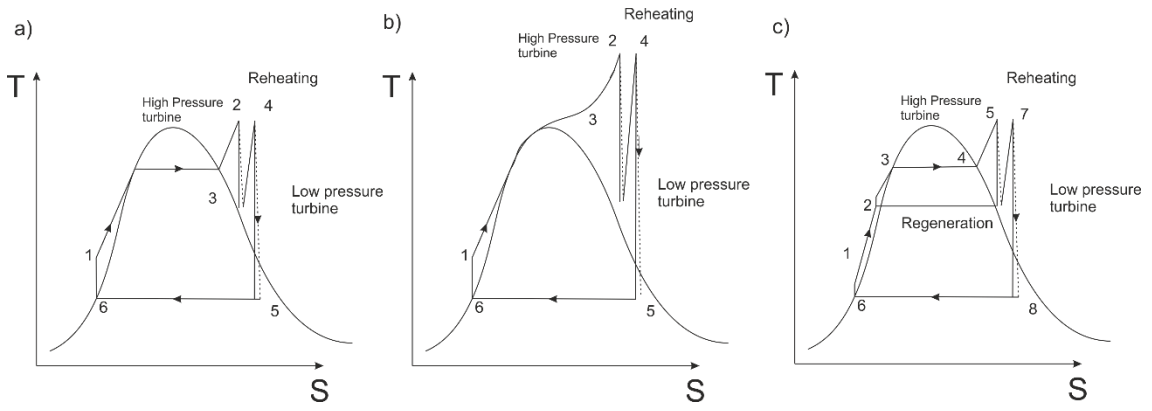

Figura 3. Tipos de ciclos Rankine para una turbina de vapor: a) ciclo con sobrecalentamiento y recalientamiento; b) ciclo supercrítico con recalientamiento; c) ciclo con sobrecalentamiento, recalientamiento y regenación.

b) Ciclo Brayton:

A diferencia del ciclo Rankine, la energía eléctrica se consigue mediante un ciclo térmico que no conlleva cambio de fase ya que se emplea una corriente de aire o gas. Inicialmente, la corriente de aire o gas es introducida en el sistema colector de radiación solar para ser sobrecalentada, hasta alcanzar las condiciones de operación deseadas. A continuación, la corriente sobrecalentada se alimenta al sistema de turbinas, y se procede a su expansión para generar electricidad. En la Figura 4 se presentan dos variaciones del ciclo Brayton, dependiendo de las etapas que siga el fluido de trabajo.

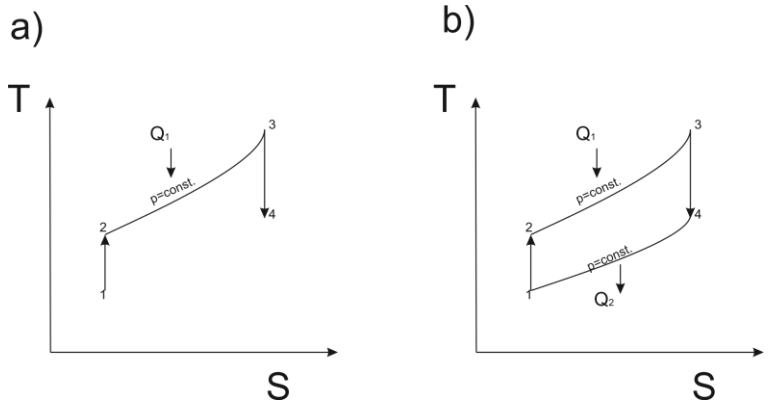

Figura 4. Tipos de ciclo Brayton para una turbina de gas: a) ciclo abierto; b) ciclo cerrado con refrigeración.

Independientemente del ciclo térmico empleado, todas las instalaciones CSP presentan una arquitectura similar dividida en 5 secciones, que puede variar ligeramente de una a otra planta:

1. Un campo de heliostatos con un colector solar; o un campo de heliostatos con un sistema de tuberías por donde se calienta el fluido.
2. Un sistema de almacenamiento térmico.
3. Una red o tren de intercambiadores de calor
4. El sistema de turbinas.
5. Un sistema de refrigeración.

Las centrales CSP pueden presentar diferentes sistemas de captación de la radiación solar, y en función de dicho sistema serán necesarias unas consideraciones distintas. En la actualidad existe un abanico de posibles tecnologías de captación, aunque pueden ser englobadas en 4 categorías [21,22], las cuales se muestran en la Figura 5 [23]: 1) discos parabólicos; 2) colector central; 3) reflectores lineales Fresnel; y 4) cilindro parabólico.

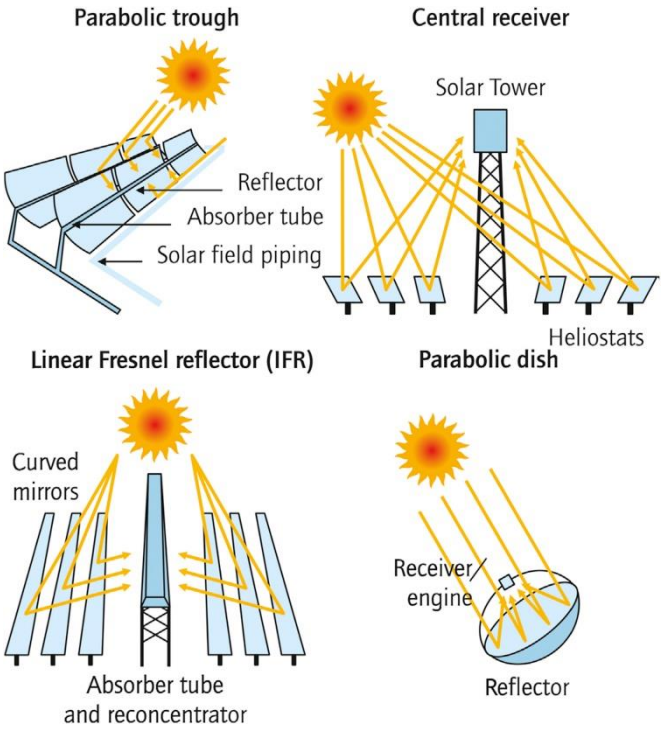

Figura 5. Tecnologías de captación térmica de radiación solar. Reproducido con permisos de DLR [23]

Cada tecnología en sí presenta un campo de estudio y desarrollo propio, ya que los parámetros de diseño de cada tecnología no son comunes entre sí [24,25], por lo que cada estudio suele centrarse en una de ellas. En la presente Tesis, se tratarán las centrales CSP que incluyen un colector central, como se muestra en la Figura 6.

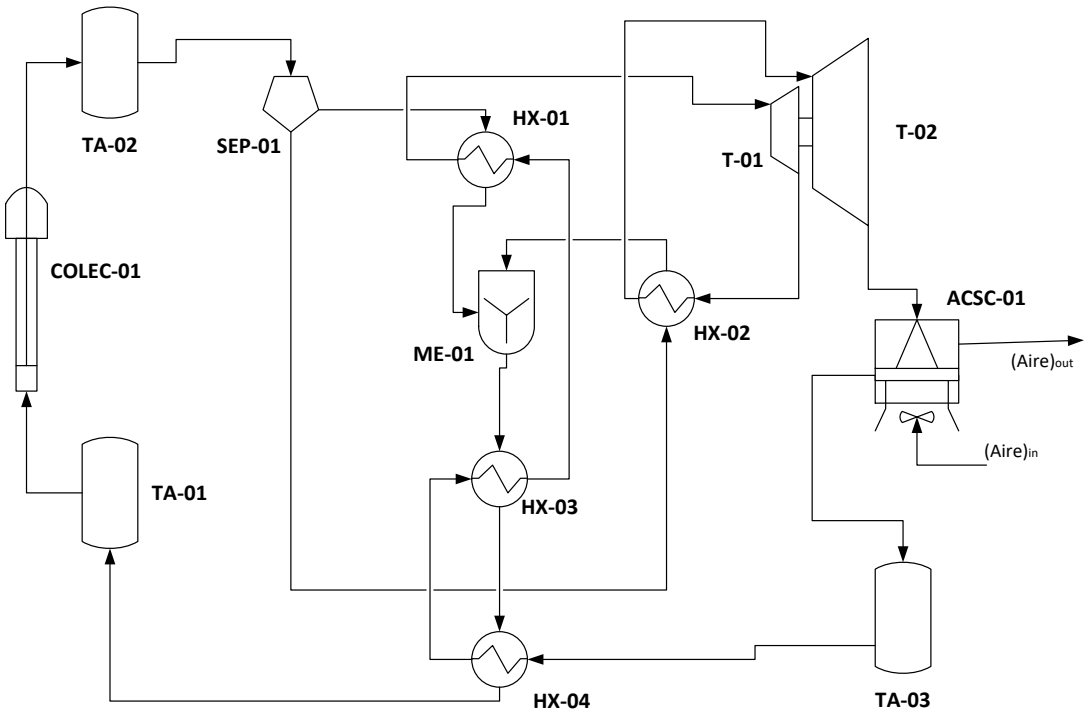

Figura 6. Ejemplo de diagrama de proceso de una planta CSP. Leyenda: COLEC – colector solar; TA – tanque de almacenamiento; SEP – separador de corrientes; ME – mezclador de corrientes; HX – intercambiador de calor; T – turbina; ACSC – sistema de refrigeración con aire.

I.2.1. Campo de heliostatos y Colector solar

El conjunto del campo de heliostatos y el colector térmico o solar conforman el foco caliente del ciclo térmico. Los heliostatos son unos espejos situados en un área alrededor de una torre central [26], en cuya parte superior se encuentra localizado un intercambiador de calor, el colector solar. Existen múltiples diseños de colectores solares que involucran diferentes tecnologías, como pueden ser los colectores tubulares centrales [27], los colectores de partículas [28], los colectores de cavidad porosa [29], o los colectores volumétricos de aire [30]. Frecuentemente, el colector es dispuesto en la parte superior de una torre alrededor de la cual se disponen los heliostatos, como se observa en la Figura 7 [31]. La función de los heliostatos es redirigir la radiación incidente hacia el colector solar, de tal manera que se obtenga la suficiente energía térmica para poder ser empleada en un ciclo de potencia posteriormente. El correcto diseño del campo de heliostatos conlleva un estudio de optimización particular de cada instalación y localización [32,33].

Figura 7. Plantas CSP PS20 y PS10 en Andalucía, España. (Reproducida con CC BY 3.0) [31]

A través del colector solar fluye el fluido de transferencia de calor (Heat Transfer Fluid, HTF) que, gracias al calor proporcionado por la radiación, experimentará un aumento de su contenido energético a medida que fluye con el interior. El HTF suele ser un compuesto que permita retener el calor durante más tiempo, como pueden ser las sales fundidas [34,35].

I.2.2. Almacenamiento térmico

El sistema de almacenamiento térmico o de energía (Thermal Energy Storage, TES) es una sección presente en la mayoría de instalación CSP, ya que permite la operación de la planta durante las horas donde no se alcanza los valores de radiación solar necesarios para generar electricidad [36]. Existen diferentes tipos de TES dependiendo del HTF utilizado [37-39], a la vez de si existe o no cambio de fase durante el proceso [40], o de los materiales de diseño para evitar la corrosión [41]. Como HTF se pueden emplear un amplio abanico de compuestos, que cubre desde aceites, siliconas, y mezclas de sales fundidas de $NaNO_3$/KNO_3. Las ventajas e inconvenientes de cada compuesto deben ser evaluadas para cada instalación en particular, aunque puede indicarse que la producción de la instalación alcanza valores mayores si se utilizan sales fundidas [42].

En el caso de utilizar sales fundidas, siliconas o aceites sintéticos [43], el TES consiste generalmente en dos tanques de almacenamiento: uno situado antes de la entrada del HTF al colector solar, y otro localizado después del colector solar. En el primer tanque se almacena el HTF a baja-media temperatura, y a partir de él se bombea el flujo requerido en el colector solar para absorber la radiación. El HTF a alta temperatura obtenido se almacena en el segundo tanque, en el cual se mantendrá sin perder demasiada energía en forma de calor, hasta que se extrae para utilizarlo como fluido calefactor en la red de intercambiadores de calor.

I.2.3. Red de intercambiadores de calor

La red de intercambiadores de calor (HEN) es un conjunto de intercambiadores de calor en los cuales el HTF transfiere su energía al fluido de trabajo de la planta CSP (ya sea agua, líquido orgánico o gas (ej. CO_2/aire)). La síntesis de la HEN viene condicionada en función de diferentes factores como pueden ser la evaluación de riesgos de los equipos [44], los fluidos de trabajo escogidos [45], el diseño y optimización de los equipos y cruces de corrientes para maximizar la transferencia de energía [46-49], o los costes de operación de los equipos y de fenómenos como el ensuciamiento [50,51]. De manera general, se puede esquematizar la HEN en los siguientes puntos:

- Un conjunto de intercambiador de calor destinado a calentar el fluido de trabajo desde la temperatura de almacenamiento a la temperatura de alimentación de la primera turbina.
- Si hay más de una turbina, es posible recalentar entre turbina y turbina el fluido de trabajo utilizando un nuevo paso por un intercambiador.
- En las turbinas de plantas térmicas suele haber hasta 7 extracciones que son empleadas para precalentar la corriente original al inicio de la HEN. Esto permitiría un ahorro energético de calentamiento.
- Si el fluido de trabajo experimenta cambio de fase antes de la entrada a la turbina, es recomendable que los intercambiadores de calor se agrupen con tres propósitos diferentes: 1) un primer conjunto de intercambiadores para calentar hasta las condiciones de equilibrio del cambio de fase; 2) un set de

intercambiadores donde tendrá lugar el cambio de fase; y 3) un grupo de intercambiadores destinado a aumentar la temperatura de la nueva corriente gaseosa obtenida.

I.2.4. Sistema de turbinas

El sistema de turbinas está compuesto por una o varias turbinas de vapor (ciclo Rankine) o de gas (ciclo Brayton) para obtener electricidad a partir del movimiento de los álabes de las turbinas. Al atravesar la corriente de vapor o gas por el interior de la turbina, se produce un trabajo mecánico que reduce la presión de la corriente y su temperatura (si es un proceso no ideal), obteniéndose electricidad con el generador acoplado y una corriente de vapor o gas con menor contenido energético.

El sistema de turbinas de vapor puede poseer varios cuerpos que trabajen a distinta presión (alta presión, media presión, y baja presión) para aumentar la eficiencia del proceso [52]; estos cuerpos de turbinas pueden disponerse como un único equipo, con extracciones entre cada cuerpo, o como equipos separados. En el escenario de disponer de múltiples cuerpos de turbinas, es posible realizar una desviación de la corriente de salida de un cuerpo para recalentarla y obtener más trabajo en la siguiente turbina, o llevar a cabo una extracción de parte de la corriente para precalentar la corriente de entrada a la HEN.

I.2.5. Sistema de refrigeración

El sistema de refrigeración representa el foco frío de la instalación, y se utiliza para extraer el calor sobrante de las corrientes que abandonan el sistema de turbinas y adecuarlas a las condiciones de entrada en los siguientes equipos. Los sistemas de refrigeración de las plantas CSP se clasifican utilizando la misma tipología que en el resto de instalaciones industriales [53]: refrigeración húmeda; refrigeración seca; y refrigeración híbrida.

La refrigeración húmeda consiste en sistemas que involucran el uso de corrientes de agua para absorber el calor residual de las corrientes calientes. Una vez la corriente de agua absorbe el calor, esta se pone en contacto con una corriente de aire ambiente para que tenga lugar un proceso de enfriamiento evaporativo, mediante el cual se retira el calor de la corriente de agua y se reduce su temperatura [54]; se debe tener en cuenta que parte del agua es evaporada en el proceso, por lo que el uso de este tipo de sistema conlleva un consumo adicional de agua que debe ser estudiado para cada caso particular [55]. El ejemplo clásico de este tipo de sistemas son las torres de enfriamiento o humidificación, las cuales son esquematizadas en la Figura 8.A [56].

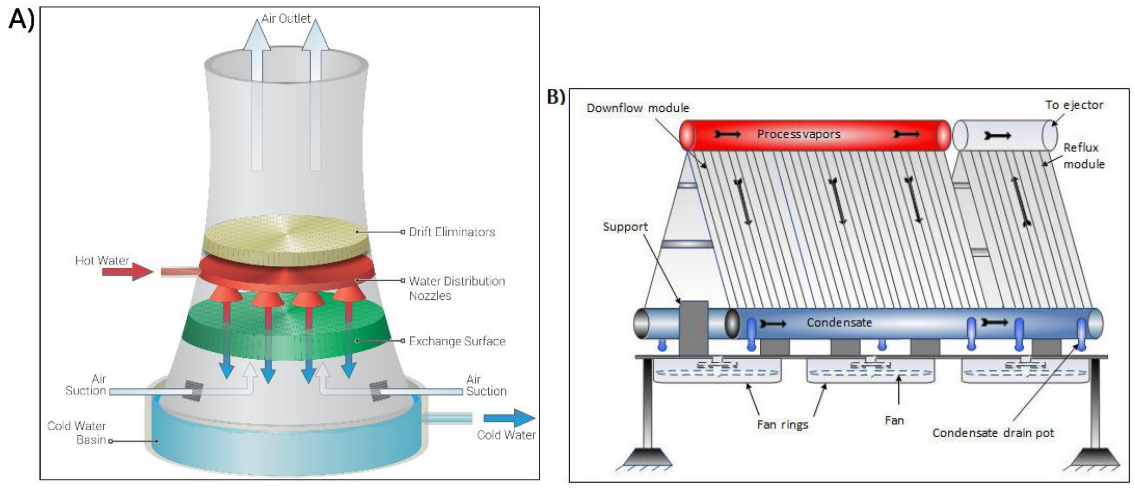

Figura 8. Sistemas de refrigeración convencionales: A) Refrigeración húmeda – torre de enfriamiento [56]; B) Refrigeración seca – refrigerador de aire [58].

Los sistemas de refrigeración seca evitan el uso de corrientes de agua, y en su lugar suelen emplear el aire ambiente para refrigerar directamente las corrientes [57]. Un esquema de este tipo de refrigeración se muestra en la Figura 8.B [58]. Estos sistemas de refrigeración tienen la ventaja de que, al no emplear agua, permite que las plantas CSP localizadas en zonas desérticas o semidesérticas no necesiten un suministro de agua que podría ser costoso o técnicamente inviable, aunque como contraparte conllevan un mayor consumo energético debido al uso de ventiladores para desplazar el aire [59].

Existe un tipo de sistema intermedio entre la refrigeración seca y la refrigeración húmeda. En los sistemas de refrigeración híbrida una sección trabaja como un sistema húmedo, mientras que en la otra parte se opera en condiciones secas [60]; este tipo de

diseño permite reducir el consumo de agua respecto a un sistema húmedo, y el reducir el consumo de energía frente a un sistema seco.

I.3. Diseño sistemático de unidades y procesos

I.3.1. Casos de programación matemática aplicada en Ingeniería Química

La Ingeniería Química es un campo de la ciencia que involucra frecuentemente en sus cálculos ecuaciones y expresiones matemáticas de muy diferente naturaleza [61]: relaciones lineales (ej. balances de materia, de coste-beneficio), ecuaciones de segundo grado o potenciales (ej. ecuaciones cinéticas), ecuaciones empíricas para ajustar datos experimentales (ej. ecuaciones paramétricas), conjuntos discretos de datos (ej. números enteros), etc. Esta gran diversidad de términos generalmente da lugar a problemas matemáticos que no pueden ser resueltos de manera sencilla, y requieren la aplicación de técnicas de programación matemática. La resolución de este tipo de problemas es de vital importancia para optimizar los beneficios de las instalaciones industriales y desarrollar soluciones tecnológicas más eficientes en el futuro. De manera ilustrativa, la Tabla 1 presenta un listado de casos de interés junto con las metodologías matemáticas recomendables para cada uno [62]. Dado que la presente Tesis se enmarca en el diseño de equipos e instalaciones, se tratarán a continuación los métodos no lineales.

Tabla 1. Propuestas de aplicación de los diferentes métodos de programación matemática (Reproducida con permiso [62]).

	LP	**MILP**	**QP, LCP**	**NLP**	**MINLP**	**Global**	**SA/GA**
Diseño y síntesis							
HENS	x	x		x	x	x	x
MENS	x	x		x	x	x	x
Separaciones		x			x		
Reactores	x			x	x	x	
Diseño de equipos				x	x		x
Diagramas de flujo				x	x		

Tabla 1 (Continuación). Propuestas de aplicación de los diferentes métodos de programación matemática (Reproducida con permiso [62]).

	LP	MILP	QP, LCP	NLP	MINLP	Global	SA/GA
Operación							
Scheduling	x	x			x		x
Supply chain	x	x			x		
Optimización en tiempo real	x		x	x			
Control							
MPC lineal	x		x				
MPC no lineal				x		x	
Híbrido		x		x	x		

Abreviaturas utilizadas: LP – programación lineal; MILP – programación mixta entera lineal; QP – programación cuadrática; LCP – programación complementaria lineal; NLP – programación no lineal; MINLP – programación mixta entera no lineal; SA – alineación de secuencias; GA – algoritmos genéticos; HENS – redes de intercambiadores de calor; MENS – redes de intercambiadores de masa; MPC – Control predictivo por modelo.

El método de programación matemática más riguroso es la programación mixta entera no lineal (mixed-integer non-linear programming, MINLP), que a su vez es la forma más compleja que puede ser presentada para un problema o modelo matemático dado [63]. La expresión general de los problemas MINLP se muestra en el problema P1:

$$\begin{aligned} \min_{x,y} \quad & f(x,y) \\ \text{s.t.} \quad & h(x,y)=0 \\ & g(x,y)\le 0 \\ & x\in X\subseteq\mathbb{R},\ y\in Y\subseteq\mathbb{Z} \end{aligned} \qquad \text{(P1)}$$

Los problemas MINLP presentan un conjunto de ecuaciones que pueden tener tanto carácter lineal como no lineal, así como condiciones de igualdad $h(x,y)$ o de desigualdad $g(x,y)$ del modelo. Además, las variables implicadas pueden ser clasificadas como variables continuas $x\in X\subseteq\mathbb{R}$, y otro conjunto de las variables como variables enteras $y\in Y\subseteq\mathbb{Z}$. Este abordaje riguroso de los problemas matemáticos permite considerar situaciones reales al introducir variables enteras, como puede ser el modelado de un fenómeno concreto considerando conjuntos binarios $y\in\{0,1\}$ (ej. seleccionar entre tipos de días: siendo 0 el caso de un día nublado, y 1 el escenario con un cielo despejado), o la selección de un conjunto determinado de unidades de procesos con variables enteras naturales $y\in\mathbb{N}$ (ej. número de tubos en un intercambiador de carcasa y tubos).

Sin embargo, el abordaje de problemas MINLP puede requerir un gran trabajo de computación, e incluso llegar a límites en los cuales no es posible o razonable su resolución rigurosa. Para ese tipo de escenarios, los problemas MINLP se relajan convirtiendo las variables enteras en variables continuas, de tal manera que se obtiene un problema de programación no lineal (non-linear programming, NLP). Este tipo de problemas se presenta en el problema P2:

$$\begin{aligned} \min_{x} \quad & f(x) \\ \text{s.t.} \quad & h(x) = 0 \\ & g(x) \le 0 \\ & x \in X \subseteq \mathbb{R} \end{aligned} \qquad \text{(P2)}$$

Como se observa en el problema P2, las variables enteras y ya no están presentes en el modelo porque han pasado a ser parte de las variables continuas x, pero la función objetivo $f(x)$, las restricciones de desigualdad $g(x)$ o de igualdad $h(x)$, y/o ambas expresiones matemáticas siguen presentando un carácter no lineal, al igual que en los problemas MINLP. Los problemas NLP son generalmente más sencillos de resolver que los problemas MINLP, y frecuentemente son utilizados en metodologías de descomposición junto con problemas de programación mixta entera lineal (MILP) para obtener soluciones de problemas MINLP más complejos.

I.3.2. Metodologías de resolución y Paquetes comerciales

I.3.2.1. Método de Ramificación y Acotamiento

El método de ramificación y acotamiento, o Branch and Bound (BB), es un método de resolución de problemas MILP o MINLP que se basa en la resolución consecutiva de problemas menos complejos que el problema original [63].

En el caso de un MINLP, el método BB se inicia mediante la relajación del problema MINLP para convertirlo en un NLP, es decir, un problema NLP donde las variables enteras pasan a ser variables continuas y pueden tomar valores continuos o se han fijado; estas variables enteras también son conocidas como “variables de decisión” dentro del método

BB, por motivos que se exponen a continuación. En la Figura 9 se esquematiza la resolución de un problema MINLP que cuenta con dos variables de decisión:

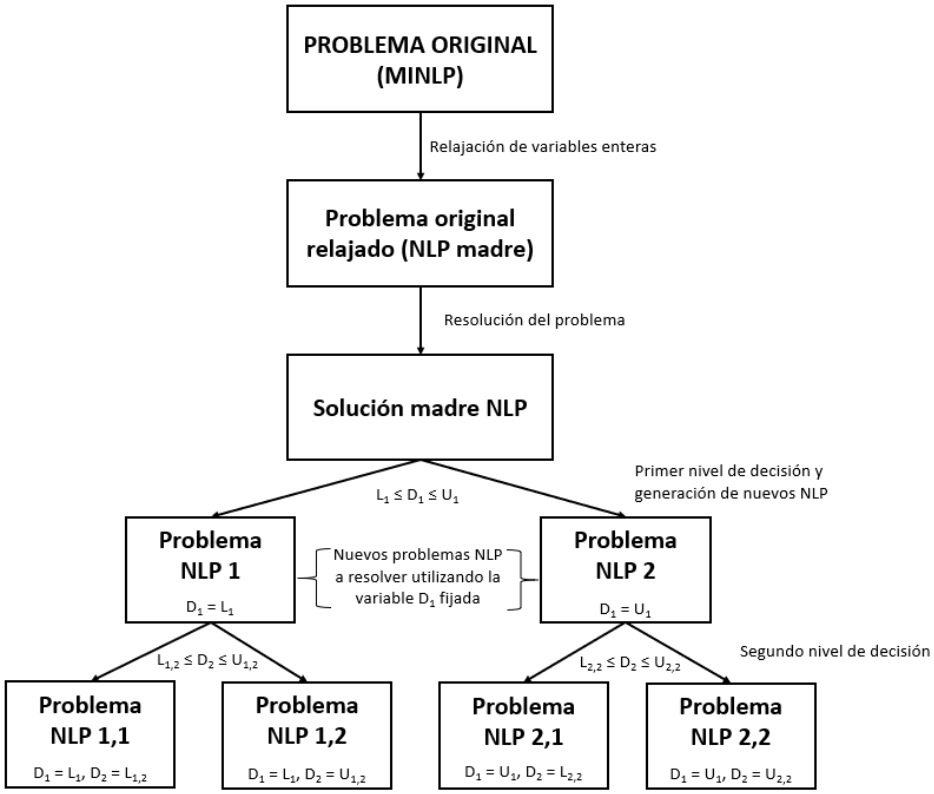

Figura 9. Esquema del método BB para un MINLP con dos variables de decisión.

Una vez se formula el NLP madre, se resuelve el problema y se obtiene una solución madre del problema original relajada, en la cual cada variable de decisión presentará un valor continuo que se encuentra entre un valor inferior entero posible (L_i) y un valor superior entero posible (U_i). En este punto, se debe seleccionar una variable de decisión D_1 que será fijada en el primer nivel del árbol; el orden de las variables D_i se determina considerando la importancia de las variables respecto al problema original (ej., fijar primero el número de equipos necesarios, después su número de componentes, etc.). Una vez seleccionada la variable D_1, se abre el primer nivel del árbol reformulando el problema NLP fijando el valor de la variable D_1 en su valor inferior L_1 para un caso, y en su valor superior U_1 para el otro. A continuación, se resuelven los nuevos problemas NLP1 y NLP2 para obtener una nueva solución del problema.

Estos pasos se deben seguir hasta haber fijado valores enteros para todas las variables enteras que fueron relajadas en la reformulación del problema original. Cabe

decir que es posible que, en algún nivel del árbol, puedan ser fijadas dos o más variables simultáneamente porque presenten ya valores enteros que no se verían afectados al fijar una variable D_{i-1} anterior.

Para problemas MINLP con un gran número de variables enteras la formulación de todas las combinaciones de NLP puede suponer un gran tiempo de procesamiento, por lo que existe la posibilidad de ignorar o trucar ramales del árbol a medida que se evalúan los nuevos niveles.

Los paquetes comerciales que aplican el método BB más utilizados son los solvers Branch And Reduced Optimization Navigator (BARON) [64], Convex Over and Under Envelopes for Nonlinear Estimation (COUENNE) [65], Basic Open-source Nonlinear Mixed Integer programing (BONMIN) [66], y Simple Branch and Bound (SBB) [67]. Estos paquetes emplean a su vez solucionadores de problemas no lineales, como pueden ser CONOPT, SNOPT y KNITRO.

I.3.2.2. Método de la Aproximación Exterior

El método de la Aproximación Exterior (Outer Approximation, OA) es un método de resolución de problemas MINLP que se basa en la descomposición del problema y relajaciones del problema, de manera que se resuelven múltiples subproblemas NLP y un problema maestro MILP relajado [68]. La formulación del método OA se expone en el problema P3:

$$\begin{aligned} \min_{x,y} \quad & f(x,y) \\ \text{s.t.} \quad & g(x,y) \le 0 \\ & x \in X \subseteq \mathbb{R}; \quad y \in Y \subseteq \mathbb{Z} \end{aligned} \qquad \text{(P3)}$$

Donde las funciones $f(x,y)$ y $g(x,y)$ deben ser convexas para garantizar un óptimo global del problema MINLP original. El método OA puede ser aplicado si no se da convexidad, pero no se podrá garantizar que la solución obtenida no sea más que un óptimo local [68]. Además, dado que el método OA sólo funciona con desigualdades, en el caso de existir restricciones de igualdad se deben relajar para lo cual se utilizarán los multiplicadores de Lagrange para relajar el problema y poder incluirlas [69].

La aplicación del método OA se inicia fijando unos valores iniciales y^k, de tal manera que se obtiene el NLP presentado a continuación (problema P4), en el cual se evalúa una condición de factibilidad (problema P5): si $u \leq 0$ es factible el NLP; si $u > 0$, el problema es no factible.

$$\begin{aligned} \min_{x,y} \quad & C^T y^k + f(x) \\ \text{s.t.} \quad & g(x) + By^k \leq 0 \\ & x \in X \subseteq \mathbb{R} \end{aligned} \qquad \text{(P4)}$$

$$\begin{aligned} \min_{u} \quad & u \\ \text{s.t.} \quad & g(x) + By^k \leq u \\ & x \in X \subseteq \mathbb{R};\quad u \in \mathbb{R} \end{aligned} \qquad \text{(P5)}$$

Una vez resuelto este primer NLP, se obtiene una solución x^k, que es mayor que el valor de la solución óptima para un problema de minimización, por lo que puede ser utilizada como límite superior (upper bound, UB) en el problema MILP. Con el valor de x^k se reformula el problema MINLP original introduciendo una nueva variable de relajación α, tal y como se muestra en los problemas P6-7:

$$\begin{aligned} \min_{x,y} \quad & \alpha \geq C^T y + f(x) \\ \text{s.t.} \quad & g(x) + By \leq 0 \\ & Ay \leq a \\ & x \in X \subseteq \mathbb{R}; \\ & y \in Y = \{0,1\}^m; \\ & \alpha \in \mathbb{R} \end{aligned} \qquad \text{(P6)}$$

$$\begin{aligned} \min_{\alpha} \quad & \alpha^T \\ \text{s.t.} \quad & \alpha \geq C^T y + f\left(x^k\right) + \nabla f\left(x^k\right)^T \left(x - x^k\right) \\ & g\left(x^k\right) + \nabla g\left(x^k\right)^T \left(x - x^k\right) + By \leq 0 \\ & Ay \leq a \\ & x \in X \subseteq \mathbb{R};\quad y \in Y = \{0,1\}^m;\quad \alpha \in \mathbb{R} \end{aligned} \qquad \text{(P7)}$$

Al resolver el nuevo problema relajado MILP se obtiene una solución y que es un límite inferior (lower bound, LB) del problema. Comparando el valor del UB y el LB se puede determinar el siguiente paso a seguir dependiendo de la tolerancia ε fijada:

a) $UB - LB \leq \varepsilon$: se ha encontrado una solución que satisface la optimalidad del problema.
b) $UB - LB > \varepsilon$: no es una solución óptima del problema. Se debe resolver un nuevo problema NLP fijando el nuevo valor de y, obtener el nuevo UB, resolver el problema relajado MINLP, y comparar de nuevo los UB y LB.

I.3.2.3. Método de descomposición de Benders generalizada

El método de descomposición de Benders generalizada (Generalized Benders Descomposition, GBD) es un algoritmo de resolución de problemas similar al método OA [70]. Al igual que el método OA, se parte de un problema MINLP general formulado como el problema P8:

$$\begin{aligned} \min_{x,y} \quad & f(x,y) \\ \text{s.t.} \quad & h(x,y) = 0 \\ & g(x,y) \le 0 \\ & x \in X \subseteq \mathbb{R}; \quad y \in Y = \{0,1\}^q \end{aligned} \tag{P8}$$

La diferencia con el OA se observa en la construcción de la relajación MILP. Se formula un problema maestro M-MILP utilizando las variables enteras, y se resuelve para obtener un valor de y y un límite UB del problema original. Con dicho valor de y, se formula un problema NLP con las variables continuas e introduciendo como parámetro fijo el valor de y; al resolver el subproblema NLP, se obtiene un LB del problema original que, en caso de no coincidir con el UB anterior o no cumplirse un error dado, se introduce como un nuevo plano de corte en el problema maestro (es decir, se añade una expresión de restricción adicional) y se continúa iterando añadiendo planos hasta cumplir con la tolerancia especificada.

I.4. Bibliografía

1. Scheffran, J.; Felkers, M.; Froese, R. Economic Growth and the Global Energy Demand. In *Green Energy to Sustainability.* John Wiley & Sons, Ltd: Chichester, UK, 2020; pp. 1-44.

2. van Ruijven, B.J.; De Cian, E.; Sue Wing, I. Amplification of future energy demand growth due to climate change. *Nature communications* **2019***, 10*, 2762-12, DOI 10.1038/s41467-019-10399-3.

3. Lastra Lastra, J.M. Rifkin, J. La Tercera Revolución Industrial. *Boletín mexicano de derecho comparado* **2017***, 50*, 1457-1462, DOI 10.22201/iij.24484873e.2017.150.11847.

4. Zita Gurmai, Anders Wijkman, Vittorio Prodi, Umberto Guidoni y Claude Turmes Declaración por escrito sobre el establecimiento de una economía verde basada en el hidrógeno y una tercera revolución industrial en Europa, mediante una asociación con las regiones, las ciudades, las PYME y las organizaciones de la sociedad civil interesadas. **2008**. *Diario Oficial n° 102 E de 24/04/2008*; p. 0139-0140. Available online: https://eur-lex.europa.eu/legal-content/ES/TXT/?uri=CELEX:52007IP0197.

5. ExxonMobile. Outlook for Energy. **2019** (Accessed on March 2021). Available online: https://corporate.exxonmobil.com/Energy-and-innovation/outlook-for-energy.

6. NASA Solar System exploration. In Depth, Sun. **2019** (Accessed on March 2021). Available online: https://solarsystem.nasa.gov/solar-system/sun/in-depth/.

7. World energy council. World Energy Resources: Solar. **2013.** Available online: https://www.worldenergy.org/assets/images/imported/2013/10/WER_2013_8_Solar_revised.pdf.

8. SOLARGIS. Solar resource maps of World. **2021.** Available online: https://solargis.com/en/maps-and-gis-data/download/world.

9. Katiyar, A.K.; Pandey, C.K. A Review of Solar Radiation Models—Part I. *Journal of Renewable Energy (Hindawi)* **2012***, 2013*, 1-11, DOI 10.1155/2013/168048.

10. Pang, Z.; Niu, F.; O'Neill, Z. Solar radiation prediction using recurrent neural network and artificial neural network: A case study with comparisons. *Renewable energy* **2020***, 156*, 279-289, DOI 10.1016/j.renene.2020.04.042.

11. Jayathissa, P.; Luzzatto, M.; Schmidli, J.; Hofer, J.; Nagy, Z.; Schlueter, A. Optimising building net energy demand with dynamic BIPV shading. *Applied energy* **2017***, 202*, 726-735, DOI 10.1016/j.apenergy.2017.05.083.

12. Belgasim, B.; Aldali, Y.; Abdunnabi, M.J.R.; Hashem, G.; Hossin, K. The potential of concentrating solar power (CSP) for electricity generation in Libya. *Renewable & sustainable energy reviews* **2018***, 90*, 1-15, DOI 10.1016/j.rser.2018.03.045.

13. Kabir, E.; Kumar, P.; Kumar, S.; Adelodun, A.A.; Kim, K. Solar energy: Potential and future prospects. *Renewable & sustainable energy reviews* **2018***, 82*, 894-900, DOI 10.1016/j.rser.2017.09.094.

14. Valenzuela, C.; Mata-Torres, C.; Cardemil, J.M.; Escobar, R.A. CSP+PV hybrid solar plants for power and water cogeneration in northern Chile. *Solar energy* **2017***, 157*, 713-726, DOI 10.1016/j.solener.2017.08.081.

15. Awan, A.B.; Zubair, M.; Praveen, R.P.; Bhatti, A.R. Design and comparative analysis of photovoltaic and parabolic trough based CSP plants. *Solar energy* **2019***, 183*, 551-565, DOI 10.1016/j.solener.2019.03.037.

16. U.S. Energy Information Administration. Solar thermal power plants. **2021**. Available online: https://www.eia.gov/energyexplained/solar/solar-thermal-power-plants.php.

17. Suresh, M.V.J.J.; Reddy, K.S.; Kolar, A.K. Thermodynamic analysis of a coal-fired power plant repowered with pressurized pulverized coal combustion. *Proceedings of the Institution of Mechanical Engineers. Part A, Journal of power and energy* **2012***, 226*, 5-16, DOI 10.1177/0957650911418421.

18. Samir Ansari; Vikash Kumar; Arindam Ghosal A Review on Power Generation in Thermal Power Plant for Maximum Efficiency. *International Journal of Advanced Mechanical Engineering* **2014***, 4*, 1-8.

19. International Renewable Energy Agency. Biomass for Heat and Power. **2015** Available online: https://www.irena.org/-/media/Files/IRENA/Agency/Publication/2015/IRENA-ETSAP_Tech_Brief_E05_Biomass-for-Heat-and-Power.pdf.

20. Nunes, L.J.R.; Matias, J.C.O.; Catalão, J.P.S. Biomass in the generation of electricity in Portugal: A review. *Renewable & sustainable energy reviews* **2017***, 71*, 373-378, DOI 10.1016/j.rser.2016.12.067.

21. Fernández, A.G.; Gomez-Vidal, J.; Oró, E.; Kruizenga, A.; Solé, A.; Cabeza, L.F. Mainstreaming commercial CSP systems: A technology review. *Renewable Energy* **2019**, *140*, 152-176, DOI 10.1016/j.renene.2019.03.049.

22. Zhang, H.L.; Baeyens, J.; Degrève, J.; Cacères, G. Concentrated solar power plants: Review and design methodology. *Renewable Sustainable Energy Reviews* **2013**, *22*, 466-481, DOI 10.1016/j.rser.2013.01.032.

23. Fuqiang, W.; Ziming, C.; Jianyu, T.; Yuan, Y.; Yong, S.; Linhua, L. Progress in concentrated solar power technology with parabolic trough collector system: A comprehensive review. *Renewable & sustainable energy reviews* **2017***, 79*, 1314-1328, DOI 10.1016/j.rser.2017.05.174.

24. Islam, M.K.; Hasanuzzaman, M.; Rahim, N.A. Modelling and analysis of the effect of different parameters on a parabolic-trough concentrating solar system. *RSC Adv.* **2015***, 5*, 36540-36546, DOI 10.1039/C4RA12919A.

25. Hafez, A.Z.; Soliman, A.; El-Metwally, K.A.; Ismail, I.M. Solar parabolic dish Stirling engine system design, simulation, and thermal analysis. *Energy conversion and management* **2016***, 126*, 60-75, DOI 10.1016/j.enconman.2016.07.067.

26. Barberena, J.G.; Larrayoz, A.M.; Sánchez, M.; Bernardos, A. State-of-the-art of Heliostat Field Layout Algorithms and their Comparison. *Energy procedia* **2016***, 93*, 31-38, DOI 10.1016/j.egypro.2016.07.146.

27. Potter, D.F.; Kim, J.; Khassapov, A.; Pascual, R.; Hetherton, L.; Zhang, Z. Heliosim: An integrated model for the optimisation and simulation of central receiver CSP facilities. *AIP conference proceedings* **2018***, 2033*, DOI 10.1063/1.5067213.

28. Tan, T.; Chen, Y. Review of study on solid particle solar receivers. *Renewable & sustainable energy reviews* **2010***, 14*, 265-276, DOI 10.1016/j.rser.2009.05.012.

29. Milani Shirvan, K.; Mamourian, M.; Mirzakhanlari, S.; Ellahi, R.; Vafai, K. Numerical investigation and sensitivity analysis of effective parameters on combined heat transfer performance in a porous solar cavity receiver by response surface methodology. *International journal of heat and mass transfer* **2017***, 105*, 811-825, DOI 10.1016/j.ijheatmasstransfer.2016.10.008.

30. Patidar, D.; Tiwari, S.; Sharma, P.K.; Chandra, L.; Shekhar, R. Open Volumetric Air Receiver Based Solar Convective Aluminum Heat Treatment Furnace System. *Energy procedia* **2015***, 69*, 506-517, DOI 10.1016/j.egypro.2015.03.059.

31. Koza1983. PS20 and PS10 plants. Available online: https://commons.wikimedia.org/wiki/File:PS20andPS10.jpg.

32. Agarwal, N.; Raj, M.; Bhattacharya, J. Solar tower on an uneven terrain: methodology and case study. *Renewable energy* **2020***, 161*, 543-558, DOI 10.1016/j.renene.2020.07.113.

33. Wagner, M.J.; Watkins, M.F.; Sullivan, S.D. Optimal heliostat assignment strategy for multiple-receiver systems. *AIP conference proceedings* **2020***, 2303*, DOI 10.1063/5.0031188.

34. Sau, S.; Corsaro, N.; Crescenzi, T.; D'Ottavi, C.; Liberatore, R.; Licoccia, S.; Russo, V.; Tarquini, P.; Tizzoni, A.C. Techno-economic comparison between CSP plants presenting two different heat transfer fluids. *Applied energy* **2016***, 168*, 96-109, DOI 10.1016/j.apenergy.2016.01.066.

35. Xu, X.; Guo, P.; Liu, W.; Yang, W. Entropy generation and Carnot efficiency comparisons of high temperature heat transfer fluid candidates for CSP plants. *International journal of hydrogen energy* **2017***, 42*, 20316-20323, DOI 10.1016/j.ijhydene.2017.05.237.

36. Mahmood, M.; Traverso, A.; Traverso, A.N.; Massardo, A.F.; Marsano, D.; Cravero, C. Thermal energy storage for CSP hybrid gas turbine systems: Dynamic modelling and experimental validation. *Applied energy* **2018***, 212*, 1240-1251, DOI 10.1016/j.apenergy.2017.12.130.

37. Zavattoni, S.A.; Zanganeh, G.; Pedretti, A.; Barbato, M.C. Numerical analysis of the packed bed TES system integrated into the first parabolic trough CSP pilot-plant using air as heat transfer fluid. *AIP conference proceedings* **2018***, 2033*, DOI 10.1063/1.5067121.

38. Bonk, A.; Sau, S.; Uranga, N.; Hernaiz, M.; Bauer, T. Advanced heat transfer fluids for direct molten salt line-focusing CSP plants. *Progress in energy and combustion science* **2018***, 67*, 69-87, DOI 10.1016/j.pecs.2018.02.002.

39. Prieto, C., Advanced thermal energy storage research in demo plants for commercial systems. PhD Thesis, Universitat de Lleida, 2016.

40. Prieto, C.; Cabeza, L.F. Thermal energy storage (TES) with phase change materials (PCM) in solar power plants (CSP). Concept and plant performance. *Applied energy* **2019***, 254*, 113646, DOI 10.1016/j.apenergy.2019.113646.

41. Fernández, A.G.; Cabeza, L.F. Corrosion monitoring and mitigation techniques on advanced thermal energy storage materials for CSP plants. *Solar energy materials and solar cells* **2019***, 192*, 179-187, DOI 10.1016/j.solmat.2018.12.028.

42. García, S.; Martín, M. Analysis of the performance of concentrated solar power facilities using different thermal fluids. *Chemical engineering research & design* **2021***, 168*, 46-58, DOI 10.1016/j.cherd.2021.01.030.

43. Martín, L.; Martín, M. Optimal year-round operation of a concentrated solar energy plant in the south of Europe. *Applied thermal engineering* **2013***, 59*, 627-633, DOI 10.1016/j.applthermaleng.2013.06.031.

44. Nemet, A.; Klemeš, J.J.; Moon, I.; Kravanja, Z. Synthesis of Safer Heat Exchanger Networks. *Chemical engineering transactions* **2017***, 56*, DOI 10.3303/CET1756315.

45. Towler, G.; Sinnot, R. Chapter 12. Heat transfer equipment. In C*hemical Engineering Design. Principles, Practice and Economics of Plant and Process Design*. Elsevier: USA, 2008: pp. 793-957; ISBN 978-0-7506-8423-1.

46. Yee, T.F.; Grossmann, I.E. Simultaneous optimization models for heat integration—II. Heat exchanger network synthesis. *Computers & chemical engineering* **1990***, 14*, 1165-1184, DOI 10.1016/0098-1354(90)85010-8.

47. Ravagnani, M.A.S.S.; Caballero, J.A. A MINLP Model for the Rigorous Design of Shell and Tube Heat Exchangers Using the Tema Standards. *Chemical engineering research & design* **2007***, 85*, 1423-1435, DOI 10.1016/S0263-8762(07)73182-9.

48. Angsutorn, N.; Siemanond, K.; Chuvaree, R. A robust design method for retrofit of industrial heat exchanger networks using modified stage-wise model. *Chemical engineering science* **2021***, 229*, 116005, DOI 10.1016/j.ces.2020.116005.

49. Pavão, L.V.; Miranda, C.B.; Caballero, J.A.; Ravagnani, M.A.S.S.; Costa, C.B.B. Multiperiod work and heat integration. *Energy conversion and management* **2021***, 227*, DOI 10.1016/j.enconman.2020.113587.

50. Rao, R.V.; Saroj, A. Economic optimization of shell-and-tube heat exchanger using Jaya algorithm with maintenance consideration. *Applied thermal engineering* **2017***, 116*, 473-487, DOI 10.1016/j.applthermaleng.2017.01.071.

51. Wang, Y.; Feng, X. Fouling Mitigation in Heat Exchanger Network Through Process Optimization. *Process Intensification and Integration for Sustainable Design* **2021**, 167-200, DOI 10.1002/9783527818730.ch9.

52. Tanuma, T. Advances in Steam Turbines for Modern Power Plants. Elsevier: 2017; ISBN 978-0-08-100314-5.

53. Palenzuela, P.; Zaragoza, G.; Alarcón-Padilla, D.C.; Blanco, J. Evaluation of cooling technologies of concentrated solar power plants and their combination with desalination in the mediterranean area. *Applied thermal engineering* **2013***, 50*, 1514-1521, DOI 10.1016/j.applthermaleng.2011.11.005.

54. Geankoplis, C.J. 10.5 Procesos continuos de humidificación. In *Procesos de transporte y operaciones unitarias*, 3rd ed. Compañía editorial Continental, S.A.: México, 1998; pp. 670-679; ISBN 978-968-26-13166.

55. Guerras, L.S.; Martín, M. On the water footprint in power production: Sustainable design of wet cooling towers. *Applied energy* **2020***, 263*, 114620, DOI 10.1016/j.apenergy.2020.114620.

56. Engineeringclicks. Cooling tower. **2021**. Available online: https://www.engineeringclicks.com/cooling-tower/.

57. Kröger, D.G. AirCooled Heat Exchangers and Cooling Towers. In *Air-cooled heat exchangers and cooling towers: thermal-flow performance evaluation and design*, vol. II. Pennwell: Tulsa (Oklahoma); 2004: pp. 1-55; ISBN 9780878148967.

58. Wateronline. Developments in heat transfer technology can improve exchanger efficiency and reduce water demand. (Accessed on March 2021). Available online: https://www.wateronline.com/doc/developments-in-heat-transfer-technology-can-improve-exchanger-efficiency-and-reduce-water-demand-0001.

59. Martín, M. Optimal annual operation of the dry cooling system of a concentrated solar energy plant in the south of Spain. *Energy (Oxford)* **2015***, 84*, 774-782, DOI 10.1016/j.energy.2015.03.041.

60. Heyns, J.A., Performance characteristics of an air-cooled steam condenser incorporating a hybrid (dry/wet) dephlegmator. Stellenbosch University.

61. Perry, R.H.; Green, D.W. *Perry's chemical engineers' handbook,* 8th ed.; McGraw-Hill: New York, USA, 2008.

62. Biegler, L.T.; Grossmann, I.E. Retrospective on optimization. *Computers & chemical engineering* **2004***, 28*, 1169-1192, DOI 10.1016/j.compchemeng.2003.11.003.

63. B. Borchers, B.; J. E. Mitchell, J.E. An improved branch and bound algorithm for mixed integer nonlinear programs. **1991**. *Technical Report RPI Math Report No. 200*, Renssellaer Polytechnic Institute.

64. The Optimization Firm, L. BARON. Available online: https://minlp.com/baron.

65. COIN|OR. COUENNE, an exact solver for nonconvex MINLPs. Available online: https://projects.coin-or.org/Couenne.

66. COIN|OR. Basic Open-source Nonlinear Mixed INteger programming. Available online: https://www.coin-or.org/Bonmin/.

67. GAMS Development Corp. SBB. Available online: https://www.gams.com/latest/docs/S_SBB.html.

68. Northwestern University. Outer-approximation (OA). **2014** Available online: https://optimization.mccormick.northwestern.edu/index.php/Outer-approximation_(OA).

69. Kocis, G.R.; Grossmann, I.E. Relaxation strategy for the structural optimization of process flow sheets. *Industrial & engineering chemistry research* **1987***, 26*, 1869-1880, DOI 10.1021/ie00069a026.

70. Zhu, Y.; Kuno, T. Global Optimization of Nonconvex MINLP by a Hybrid Branch-and-Bound and Revised General Benders Decomposition Approach. *Industrial & engineering chemistry research* **2003**, *42*, 528-539, DOI 10.1021/ie0200813.

CAPíTVLO ii

OBJETiVOS

II. OBJETIVOS

La importancia del estudio de la energía termosolar y su implantación a medio y largo plazo en zonas con una limitada disponibilidad de agua hacen que el estudio de la eficacia de captura de energía solar y el nexo agua-energía sean de vital importancia para la competitividad de estas plantas. Para reducir el consumo de agua, la refrigeración por aire es la tecnología más prometedora, pero requiere del diseño adecuado de los equipos. La operación y las características físicas de los equipos de transferencia de calor plantean el reto que soporta esta Tesis.

El objetivo fundamental de la Tesis es el diseño óptimo conceptual de los equipos de transferencia de energía de las centrales de potencia por concentración solar (CSP). Los casos de estudio para evaluar las diferentes ecuaciones serán las instalaciones y los equipos que típicamente se pueden encontrar en una central termosolar, como pueden ser el colector solar y el sistema de refrigeración. Para ello se plantean una serie de objetivos particulares:

1. Modelado de los equipos de transferencia de calor en base a principios fundamentales y características de operación de equipos industriales.
2. Evaluación de las características matemáticas de los modelos, tipo de términos y ecuaciones involucradas.
3. Evaluación del efecto del ensuciamiento en el diseño de los equipos.
4. El desarrollo de metodologías y estrategias de solución basadas en la optimización matemática.

Estos objetivos serán alcanzados de manera individual para cada caso de estudio ya que, de manera indirecta, al estudiar un equipo se están definiendo las ecuaciones y las variables involucradas en la transferencia de energía, y se realiza una discusión sobre la problemática presente en cada caso. Para cada caso de estudio se realizará una evaluación de la situación actual de las investigaciones sobre el mismo, y posteriormente se procederá a su optimización de acuerdo con un escenario dado.

CAPÍTVLO iii

ENFRIAMIENTO SECO: A-FRAME

ELSEVIER

Two-step optimization procedure for the conceptual design of A-frame systems for solar power plants

Luceño, J.A. and Martín, M.

Energy, **2018**, *165*, 483-500

DOI: 10.1016/j.energy.2018.09.177

III.1.1. Introduction

Solar energy is a plentiful source that can provide several times the mankind needs [1]. However, the use of solar energy to produce power is still not competitive compared to fossil based thermal plants [2]. The disadvantage of concentrated solar power facilities (CSP) is that, unlike fossil based ones, they need to be allocated in specific regions with high solar incidence. This particular feature is a handicap in terms of cooling. There are two main cooling technologies for thermal plants: wet or dry cooling. Wet cooling is the most used technology for power plants, but it requires around 1.8 L of water per kWh produced [2]. On the other hand, dry cooling technologies require the use of a fraction of the power generated to operate the fans that move the air used to condensate the exhaust steam. As a result, the global efficiency of the facility is reduced.

In the literature, a number of studies compare wet and dry cooling systems for solar and fossil based thermal plants. Most of them use a simulation based approach to compare power plants that use both cooling technologies. Kelly and Prince [3] evaluated the performance of air cooled condensers using the Excelergy package and compared the cost of power production using both cooling systems showing that dry is still more expensive. Turchi et al. [4] studied 13 different real cases using SAM software, where the use of dry cooling increased the cost of electricity by 8%, but with reduction of water consumption of 90% in CSP plants. No details on the air cooler geometry are presented. Zhai and Rubin [5] focused on comparing the cost and performance of both cooling technologies on coal based facilities. A-frame coolers are used but no details of the unit are described. Barigozzi et al. [6] optimized wet and dry cooling systems for waste-to-energy plants evaluating the effect of air conditions on the cycle performance using Thermoflex software, but no unit design characteristics are commented. Blanco-Marigorta et al. [7] used exergy as metric to compare both technologies in terms of thermodynamic yield of the process. Habl et al. [8] extended previous work by including cost estimation. Liqreina [9] only focused on dry systems for a CSP plant located in a desert area, Jordan, from the thermodynamic poinf of view. Palenzuela et al. [10] evaluated various cooling technologies in the context of desalination. Lately, a programming optimization approach has been used to evaluate wet, Martín and Martín [2], and dry

cooling systems Martín [11] towards the trade-off between water consumption and power generation. A monthly basis analysis is performed. Dry cooling technologies reported higher power production and investment costs. Around 5–10% of the produced energy is consumed to power the fans using dry cooling technologies [11], while the use of wet cooling towers resulted in an average consumption of 2.1 L/kWh of water [2]. Cooling technologies have been developed lately not only for renewable based power plants but also to address residential needs evaluating system [12], comparing previous work with air cooling [13] and finally evaluating various renewable resources [14]. However, these studies used simplified models to represent the cooling technologies in order to be able to address the analysis or the optimization of the entire power facilities. The increase in power demand together with the future water scarcity [15] requires better dry cooling systems [16].

Literature on the design of dry cooling systems focuses on different aspects. Some studies evaluate the layout of the units for their allocation in the facility using Computational Fluid dynamics (CFD), suggesting novel layouts [17] and evaluating the effect of wind speed direction [18]. In terms of the actual unit design, two approaches can be found in the literature, iterative design and mathematical optimization formulations. The most common approach uses guidelines, figures and design equations in an interative procedure. The general rules can be found in technical reports [19], or reference books where the design procedure is described in detail in Ref. [20]. Industry also provides their guidelines based on the experience on the operation of such units [21]. Apart from the basic design, the effect of the wind can also be accounted for in the design [22]. Finally, specific problems such as freezing [23], or the evaluation of the fan performance with no further reference to the entire design and the heat transfer section [24] have also been considered. Alternatively, mathematical optimization approaches have been developed. However, most of these studies have been performed for regular units either evaluating their performance [25] or developing a mathematical model for their optimization [26]. The optimization of the particular geometry of the A-frames has only been addressed in Ref. [27] for a reduced number of variables. Conradie's et al. work [27] used a mathematical optimization approach for the geometric design of A-frame systems.

However, it does not evaluate the effect on the flow on the heat transfer coefficients, the effects of the geometry on the pressure drop nor its operation over a year time.

Apart from the geometrical design of the unit, the variability in the solar incidence represents the second challenge in the operation of CSP plants. In particular, cooling units are affected in two ways, the variable heat load to be rejected and the variable conditions of the cooling agent. Typically, the design is based on a certain month of operation [20], but in the case of solar facilities this approach leads to inefficiencies over a year. Even though flexible design of chemical plants has been addressed in the literature using mathematical optimization approaches [28], its application to the detailed design of industrial units considering the monthly variability is challenging due to the mathematical complexity. Reference to multi-period operation can be found in some studies that evaluate the performance for regular air coolers [26] or that focuses on the evolution of fouling and its effect on the energy transfer [29], but work on the detail optimal design of A-frames considering seasonality operation is not available.

In this work a two-stage methodology has been proposed for the conceptual optimal geometric design and monthly operation of A-frames aiming at minimum power consumption to meet the cooling needs of a CSP plant. The methodology is based on the detailed geometric design for a month considering the piping system and its layout, the fan blade geometry, pressure drop across the system and heat transfer resistances. Next, as a recourse, the second step a multiperiod optimization allows considering the operation of such design over time to minimize energy consumption The aim is to improve current designs reducing the energy required to operate such units. For reference, the case study is based on a CSP facility located in Almería (Spain), a region with one of the highest solar radiations in Europe, and uses operating data from previous work [2]. The paper is organized as follows: In Section 2, the design method is depicted. In Section 3, the features of the model are described. In Section 4 the optimization procedure developed to solve the MINLP problem is presented. Next, in Section 5 the case study and the main results are discussed such as the major operating conditions, the power consumed by the cooling system and the units of the A-frame needed followed by an economic evaluation and a comparison between dry and wet cooling facilities based on CO_2 savings. Finally, Section 6 draws some conclusions.

III.1.2. Design method

A two-step optimization procedure is proposed for the conceptual design of A-frame units considering seasonality over a year of operation. The first problem is the optimal design of the geometry for the month with the highest energy production and heat rejection. A detailed model for the A-frame described in Section 3 is used to determine the geometric features of the unit. This model is formulated as an MINLP optimization problem. Section 4.1 shows the tailor-made branch and bound algorithm to determine the number of tubes, number of bundles and rows as well as a standard pipe diameter, tube length and fan blade angle. This problem is solved for the optimal design capable of providing the cooling required.

The seasonal operation of the A-frame over time is addressed for the geometry computed in the design problem. This problem is formulated as a multi-period MINLP to determine the usage of fans, bundles and flow per fan operating on a monthly basis for minimum energy consumption making the most of the unit geometry defined in the first stage. To solve the multiperiod problem the model of the unit is simplified by fixing the geometry. Section 4.2 shows the formulation of the second stage problem. Section 5 reports the main operating data of the case study, heat rejection and weather conditions.

III.1.3. Modeling

III.1.3.1. CSP facility description

The plant consists of three sections: the heliostat field, including the collector and the molten salts storage tanks, the steam turbine and the air cooler steam condenser. Fig. 1 presents the flowsheet for the process. This process uses a tower to collect the solar energy and a regenerative Rankine cycle. The steam is generated in a system of three heat exchangers where water is heated up to saturation and then evaporated using the total flow of molten salts. However, only a fraction of the flow of salts is used to superheat the steam before it is fed to the first section of the turbine. The rest is used to reheat up the steam before it is fed to the medium pressure turbine. In the medium pressure turbine,

part of the steam is extracted and it is used to heat up the condensate. The rest of the steam is finally expanded to an exhaust pressure, condensed and recycled. For the condensation of the steam we propose the use of a direct air cooled system, an A-frame. For the detailed information on the modeling features of the heliostat field and the steam turbine, we refer to previous work [2].

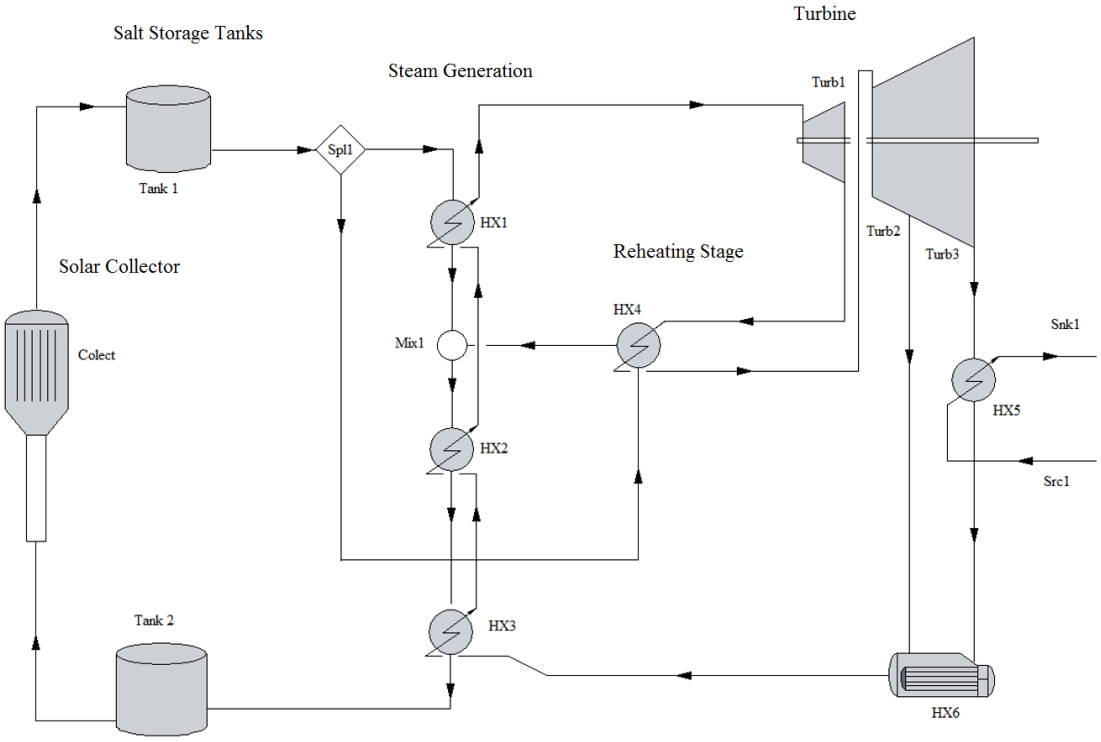

Fig. 1. Flowsheet of the concentrated power plant facility (With permission [11]).

III.1.3.2. Air cooling system

A scheme of A-frame type of air condenser can be found in Fig. 2. The exhaust steam from the turbine circulates in a large pipe and it is distributed into the pipes that form a roof over a system of fans in the form of an A. The steam condensers inside the tubes as it descends.

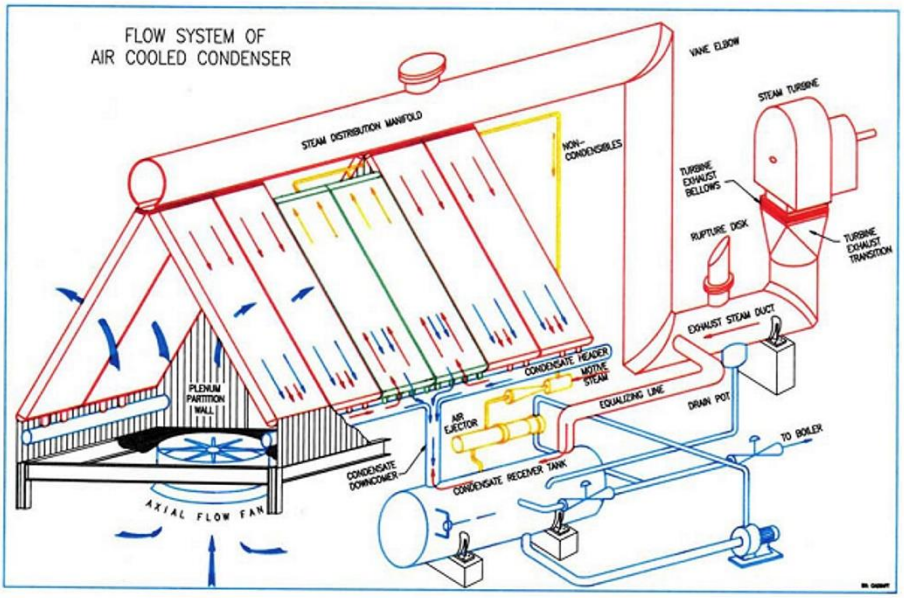

Fig. 2. Scheme of an A-frame type of unit (with permission [19]).

III.1.3.3. Model structure

The model is divided in 3 sections: mass and energy balances, A-frame design, and fans design. The mass and energy balances compute the need for air to condense the exhaust steam. Within the A-frame design three main items are evaluated, the heat transfer coefficient, the temperature gradient and the contact area. This area is given by a number of pipes allocated in an inverted V layout, the A-frame. The number of rows of tubes, their length and diameter as well as the number of fins per tube are also calculated. The heat transfer coefficient is highly dependent on the geometry. Internal, external and material resistances are considered to compute the global heat transfer coefficient. Finally, to allow for the air to cross the A-frame structure a certain amount of power is required. It depends on the air flow and the pressure drop generated by the structure. The model is formulated based on first principles, design correlations to estimate heat transfer coefficient, standard characteristics of pipes and fins [20] and literature data of the operation of the fans. Surrogate models are developed to capture the performance of the fans provided in the form of figures. The heat transfer performance is modelled using widely accepted design equations from the literature. However, if additional fan

performance data is available and/or other correlations are developed, the model can be easily updated. The model is optimized for minimum energy consumption.

III.1.3.3.1. Mass and energy balances

The two energy balances considered are that to the air flow and the one to the steam. The first of the two determines the air flow required for the operation and is given by Eq. (1):

$$Q = m_{air} \cdot \left[C_{p_{air}} \cdot \left(T_{out,air} - T_{in,air} \right) + H \cdot C_{p_{w,vap}} \cdot \left(T_{out,air} - T_{in,air} \right) \right] \quad (1)$$

The energy that has to be removed, Q, comes from the energy balance to the steam, as given by Eq. (2) and the data of the operation of the CSP plant [2].

$$Q = m_w \cdot \lambda_w \quad (2)$$

III.1.3.3.2. A-frame design

III.1.3.3.2.1. Heat exchanger design

The general design equation of any heat exchanger is Eq. (3):

$$Q = U \cdot A_{out} \cdot LMTD \quad (3)$$

This equation has three terms that must be analyzed separately: the logarithmic mean temperature difference, *LMTD*, the outside contact area, A_{out}, and the global heat transfer coefficient, *U*.

-The logarithmic mean temperature difference LMTD is calculated using Eq. (4):

$$LMTD = \frac{\left(\Delta T_a - \Delta T_b \right)}{ln\left(\Delta T_a / \Delta T_b \right)} \quad (4)$$

However, Eq. (4) is a complex mathematical expression that is typically approximated using Chen approximation within optimization formulations to avoid numerical issues [30], Eq. (5):

$$LMTD \approx \left[\Delta T_a \cdot \Delta T_b \cdot \frac{\left(\Delta T_a + \Delta T_b\right)}{2} \right]^{1/3} \tag{5}$$

The temperature's increments ΔT_a and ΔT_b are calculated using Eqs. (6), (7) where T_v is the steam temperature and $T_{in,air}$ and $T_{out,air}$ the air inlet and outlet temperature:

$$\Delta T_a = T_v - T_{in,air} \tag{6}$$

$$\Delta T_b = T_v - T_{out,air} \tag{7}$$

-The external contact area of the heat exchanger A_{out} is the area exposed to the heat flow and it is given by the number of pipes per row and bundle, N_t and N_r, and the number of bundles, N_b, Eq. (8).

$$A_{out} = N_b \cdot N_t \cdot N_r \cdot A_{out,pipe} \tag{8}$$

-The global heat transfer coefficient referred to A_{out}, U, can be computed using the equation presented by Pieve and Salvadori [25]. This equation considers the resistances to heat transfer related to steam condensation and the convective heat transfer on the air side; we include also a term that considers the heat transfer resistance due to the conduction of heat across the pipes wall. Thus, U is computed as Eq. (9):

$$\frac{1}{U} = \frac{A_{out}}{\eta_0 \cdot h_{air} \cdot A_{out}} + \frac{e \cdot A_{out}}{k_{mat} \cdot A_k} + \frac{A_{out}}{h_c \cdot A_{in}} \tag{9}$$

We need to compute a large number of variables with remarkable mathematical complexity. The external area efficiency, η_0, is given by Eq. (10) [25]:

$$\eta_0 = 1 - \frac{A_{tf}}{A_{out}}\left(1 - \eta_f\right) \tag{10}$$

where is defined with Eq. (11):

$$A_{tf} = A_f \cdot N_t \cdot N_r \cdot N_b \tag{11}$$

where N_t, N_r and N_b are the number of pipes, the number of rows and the number of bundles respectively. The total fins area, A_f , is computed using the outer fin area $A_{out,fin}$ and Eqs. (12), (13):

$$A_{out,fin} = \pi \cdot D_f \cdot t_f + \frac{\pi}{2} \cdot \left(D_f^2 - D_{out}^2 \right) \tag{12}$$

$$A_f = n_f \cdot A_{out,fin} \tag{13}$$

The fins efficiency is given by Eq. (14) [25]:

$$\eta_f = \frac{tanh(m\varphi)}{m\varphi} \tag{14}$$

where m and φ are calculated using Eqs. (15), (16) respectively [25] as a function of the pipe geometry, lay out (D_f, D_{out} and t_f) and material (k_f) and the heat transfer coefficient, h_{air}:

$$m = \left(\frac{2 \cdot h_{air}}{k_f \cdot t_f} \right)^{1/2} \tag{15}$$

$$\varphi = 0.5 \cdot \left[D_f - D_{out} + t_f \right] \cdot \left(\frac{D_f}{D_{out}} \right)^{\exp\left[0.065 \cdot m \cdot \left(D_f - D_{out} + t_f\right) - 1.3863\right]} \tag{16}$$

The air side coefficient, hair, is calculated using the air Nusselt number. The Nusselt number is defined as presented by Heyns [20] by Eq. (17):

$$Nu = \frac{h_{air} \cdot D_{eq}}{k_{air}} \tag{17}$$

Pieve and Salvadori's equation is used to include the effect of the geometry of the pipes and its lay out (D_f, D_{out}, p_f and t_f) on Nu , Eq. (18) [25]:

$$Nu = 0.134 \cdot \mathrm{Re}^{0.681} \cdot \mathrm{Pr}^{1/3} \cdot \left(\frac{p_f - t_f}{0.5 \cdot \left(D_f - D_{out} \right)} \right)^{0.2} \cdot \left(\frac{p_f - t_f}{t_f} \right)^{0.11} \tag{18}$$

where Reynolds and Prandtl numbers are computed as per Eqs. (19), (20) [25]:

$$\mathrm{Re} = \frac{\Gamma \cdot D_{eq}}{\mu_{air}} \tag{19}$$

$$\mathrm{Pr} = \frac{\mu_{air} \cdot C_{p_{air}}}{k_{air}} \tag{20}$$

Variable Γ is the airflow across the minimum flow area and the rest are air properties and the equivalent diameter, D_{eq}, for flow purposes. The minimum flow area is computed using Eq. (21) [25]:

$$S_{\min-t} = \left[X_t - D_{out} - \frac{t_f}{p_f} \cdot \left(D_f - D_{out} \right) \right] \cdot L_t \cdot N_t \tag{21}$$

Equation (21) can be used only if equation (22) is satisfied:

$$\frac{X_l}{D_{out}} > 0.5 \sqrt{1 + \frac{2X_t}{D_{out}}} \tag{22}$$

However, in this particular case, Eq. (22) is always satisfied because a pipe isosceles triangle layout is selected, see Fig. 3, $X_t = X_l \geq D_{out}$. Thus, Eq. (18) can be used without formulating a disjunction.

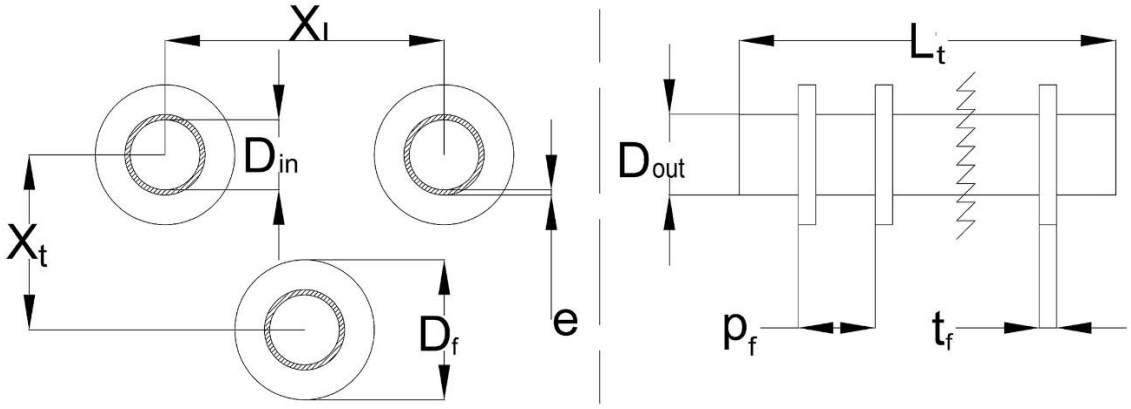

Fig. 3. Geometry of pipes.

The steam side film coefficient, h_c, is computed using Eq. (23), as suggested by Heyns [20]:

$$h_c = 0.9245 \cdot \left\{ \frac{L_t \cdot \rho_c^2 \cdot k_c^3 \cdot g \cdot \cos(90 - \theta) \cdot \lambda_w}{\mu_c \cdot m_{at} \cdot C_{p_{air}} \cdot \left(T_v - T_{in,air} \right) \cdot \left(1 - \exp\left[-U_c H_t L_t / \left(m_{at} \cdot C_{p_{air}} \right) \right] \right)} \right\}^{0.25} \tag{23}$$

where and can be computed as per Eqs. (24), (25) respectively [17]:

$$m_{at} = \frac{m_{air}}{2 \cdot N_t \cdot N_b} \tag{24}$$

$$U_c H_t L_t = \frac{h_{ae} A_a}{2 \cdot N_t \cdot N_b} \tag{25}$$

The $h_{ae}A_a$ term can be computed as follows, Eq. (26) [20]:

$$h_{ae} A_a = k_{air} \cdot \mathrm{Pr}^{0.33} \cdot N_b \cdot A_{fr} \cdot Ny \tag{26}$$

where Ny is computed using Eq. (27) [20]:

$$Ny = 366.007945 \cdot Ry^{0.433256} \tag{27}$$

and Ry by Eq. (28) [17]:

$$Ry = \frac{m_{air}}{\mu_{air} \cdot N_b \cdot A_{fr}} \tag{28}$$

Finally, the material resistance to the heat transfer depends on the thermal conductivity of the pipe, k_{mat}. It is estimated as an average for the range of working temperature ranges [31] so that a value of k_{mat} equal to $45 \cdot 10^{-3}$ kJ/(K m^2/m s) is used.

The mean area A_k is computed using Eq. (29):

$$A_k = \frac{\left(A_{out} - A_{in}\right)}{\ln\left(\frac{A_{out}}{A_{in}}\right)} \tag{29}$$

where A_{in} and A_{out} are calculated as in Eqs. (8), (30):

$$A_{in} = N_b \cdot N_t \cdot N_r \cdot A_{in,pipe} \tag{30}$$

III.1.3.3.2.2. Pipes design for area availability

The pipes are the units that provide the contact area for heat transfer. For an enhanced area, these pipes present fins. The design variables and geometry of pipes are plotted in Fig. 3.

The internal area of a pipe $A_{in,pipe}$ is the area of a cylinder of diameter D_{in} and length L_t. Thus, the area is given as presented in Eq. (31):

$$A_{in,pipe} = \pi \cdot L_t \cdot D_{in} \tag{31}$$

The outside area of a pipe is the sum of fins area A_f and the smooth tube area A_{smooth}, and can be calculated as Eq. (32):

$$A_{out,pipe} = A_f + A_{smooth} \tag{32}$$

Where the smooth area is computed by Eq. (33) with is the number of fins per tube length n_{fins} and the mean fin thickness t_f:

$$A_{smooth} = 2 \cdot \pi \cdot \frac{D_{out}}{2} \cdot \left(L_t - t_f \cdot n_f\right) \tag{33}$$

The type of fins is selected depending on the kind of fluid which flows in contact with the fins. In the case of the air, a fluid with a small film coefficient and flowing under atmospheric pressure, it is common to employ cross fins [32].

III.1.3.3.3. Fans design

The fan is designed so that it generates enough power to overcome the pressure drop across the structure, namely, bundles of tubes, the fan itself and the base of the unit. To model a fan, a detailed characterization is required due to aerodynamic effects of the blade geometry, size, etc. However, such information is not typically available. For this case of study a particular fan has been selected whose characteristic curves can be found in the literature [24]. This section is divided in two parts: the development of a correlation to predict the power generated by the fan as a function of the flow rate, and the development of models for each one of the contributions to the pressure drop.

III.1.3.3.3.1. Power per fan

The power required by the fan is that needed to overcome the pressure drop, and can be obtained from Eq. (34):

$$P_{vent} = n_{fan} \cdot P_F = Q_{air} \cdot \Delta p_e \tag{34}$$

The power per fan depends on the geometry of the blade. For our case, Fig. 4 shows the profile for three blades angles, 14°-18°, due to the lack of further information [24].

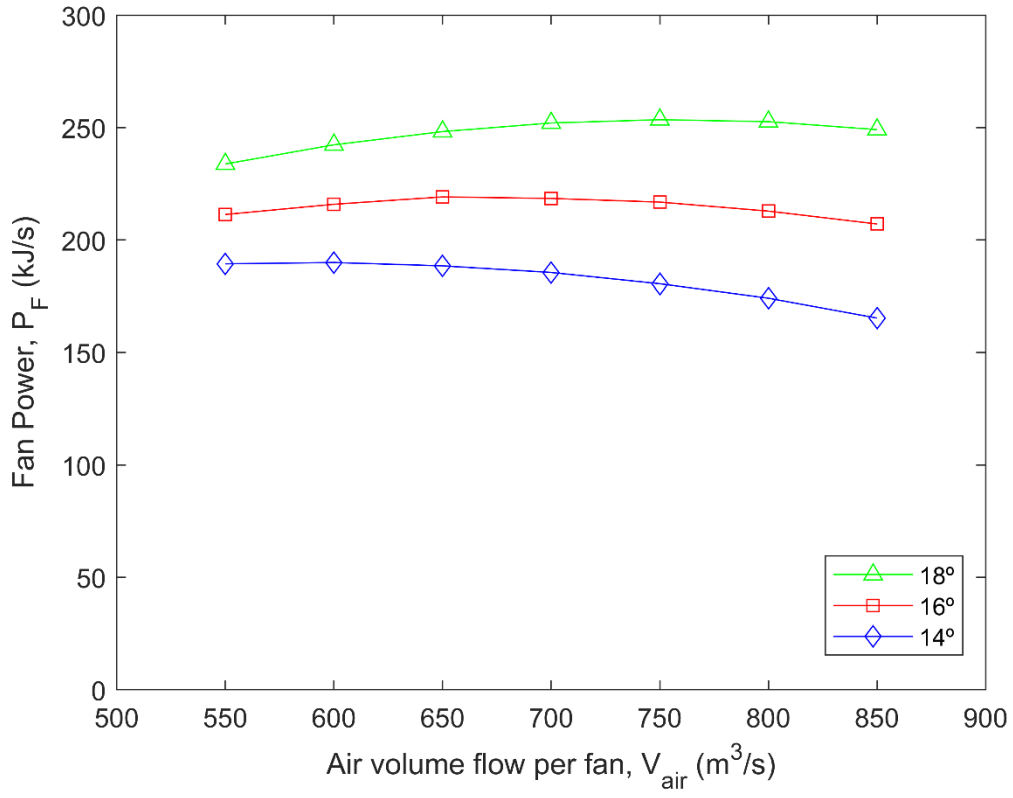

Fig. 4. Experimental data for the fan power.

A surrogate model is developed based on the typical power curves in the literature, see Fig. 4 to evaluate the power consumption as a function of the air flow. A two-stage fitting procedure is carried out to account for two effects, that of the air velocity and the one related to the blade geometry, in particular, the blade angle A second order polynomial is used to capture the effect of air flow on the power, assuming that there is no power consumed for no air flow rate, Eq. (35). There is typically a base consumption. To account for it, the minimum flowrate for a fan to operate will imposed as a lower bound, to avoid very small flows, and an additional base consumption is added if the fan is working.

$$\left(P_F\right)_n = \alpha_n \cdot V_a^{\,2} + \beta_n \cdot V_a + \varepsilon_n \tag{35}$$

To capture the effect of the blade geometry, the coefficients *α*, *β* and *ε* are a function of flowrate for each blade angle as seen in Table 1. Next, a correlation between their values and the blade angle is developed, see Eq. (36). It turns out that a linear relationship between coefficients α and β and the angle fits the results. Table 2 shows the parameters:

$$\alpha_n = p_\alpha \cdot \gamma_{bt} + m_\alpha$$
$$\beta_n = p_\beta \cdot \gamma_{bt} + m_\beta \quad (36)$$

Table 1. Effect of the blade angle on the power curve.

Angle γ_{pt}	α_n	β_n	ε_n
14	-4,9362.10^{-4}	6,1246.10^{-1}	0
16	-4,6668.10^{-4}	6,3963.10^{-1}	0
18	-4,4113.10^{-4}	6,6852.10^{-1}	0

Table 2. Coefficients for the effect of the angle on the second order polynomial fitting of the power curve.

Coefficient	p	m
α_n	1.3122·10^{-5}	-6.7710·10^{-4}
β_n	1.4015·10^{-2}	4.1596·10^{-1}
ε_n	0	0

Thus, by substituting Eq. (36) into Eq. (35), the expression for P_F becomes Eq. (37):

$$P_F = \left(1.3122 \cdot 10^{-5} \cdot \gamma_{pt} - 6.7710 \cdot 10^{-4}\right) \cdot V_{air}^2 + \left(1.4015 \cdot 10^{-2} \cdot \gamma_{pt} + 4.1596 \cdot 10^{-1}\right) \cdot V_{air} \quad (37)$$

The number of fans is computed as follows, Eq. (38):

$$Q_{air} = n_{fan} \cdot V_{air} \quad (38)$$

III.1.3.3.3.2. Pressure drop

The pressure drop across the system is the one responsible for the energy consumed by the fans. To compute it, different contributions such as the pressure drop at the entrance of the structure, before and after the fan and finally through the tubes bundles, apart from the pressure drop across the fan itself are considered, see Eq. (39) [33]:

$$\Delta p_e = -\left[\begin{array}{l} \dfrac{K_{ts}}{2\cdot\rho_{a56}}\left(\dfrac{m_{air}}{N_b\cdot A_{fr}}\right)^2 + \dfrac{K_{up}}{2\cdot\rho_{a3}}\left(\dfrac{m_{air}}{A_e}\right)^2 - \Delta p_{Fs} \\ + \dfrac{K_{do}}{2\cdot\rho_{a3}}\left(\dfrac{m_{air}}{A_e}\right)^2 + \dfrac{K_{\theta t}}{2\cdot\rho_{a56}}\left(\dfrac{m_{air}}{N_b\cdot A_{fr}}\right)^2 \end{array} \right] \tag{39}$$

Each of the contributions in Eq. (39) require a surrogate model to account for the blade geometry.

-The fan static pressure, Δp_{Fs}, is a function of the flow rate and the blade angle, see Fig. 5 developed from the data in Bredell and Kröger [24]. In order to formulate a one equation model to account for both variables, blade angle and air flow rate, the same two-stage procedure as before is used. The mathematical expression that captures the profiles for all angles is given by eq. (40). Next, the effect of the angles on the coefficients of the master correlation is determined. This correlation will only be valid for the fan whose characteristics have been analyzed. However, the model is flexible and if data for other fans is available, it can be easily updated.

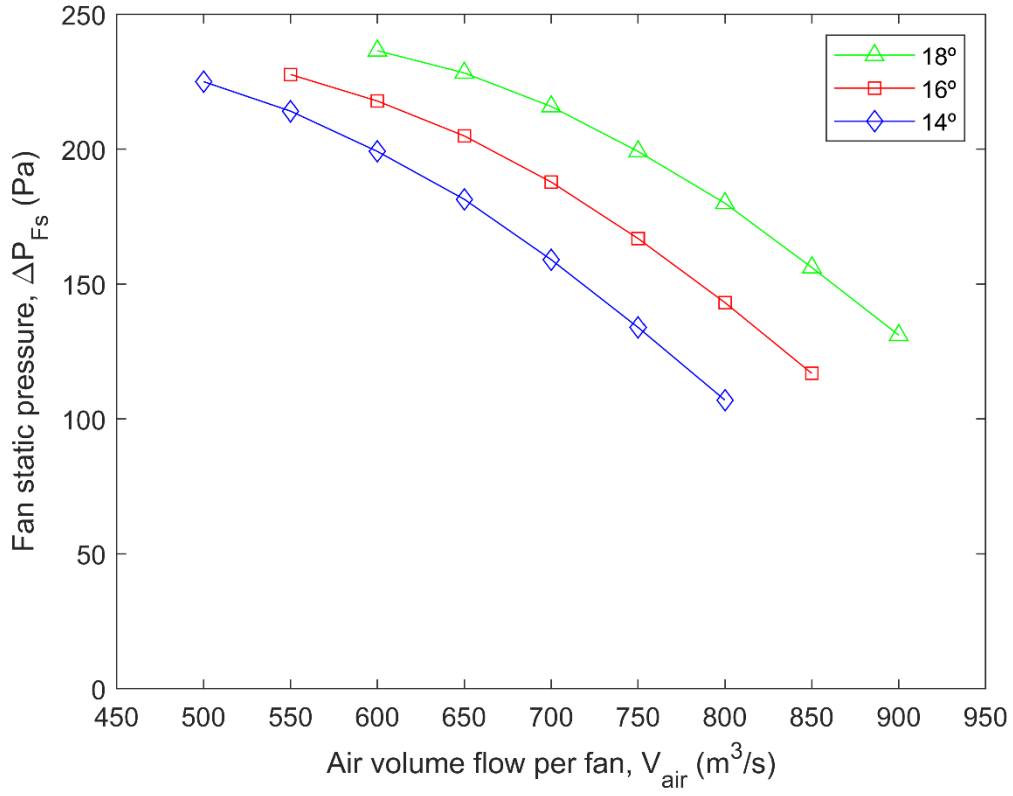

Fig. 5. Experimental fan static pressure.

$$\left(\Delta p_{Fs}\right)_n = \alpha_n \cdot V_a^2 + \beta_n \cdot \gamma_{pt} + \varepsilon_n \tag{40}$$

Again, it turns out that a linear regression, Eq. (41), fits the effect of the angle on coefficients *α*, *β* and *ε* of Eq. (40). Only data for 14°−18° are available in the literature to develop this model. Table 3 shows the fitting coefficients of Eq. (40) and Table 4 those of Eq. (41):

$$y = p \cdot \gamma_{pt} + m \tag{41}$$

Table 3. Coefficients of the second order polynomial for static pressure drop.

Blade angle γ_{pt}	α	β	ε
14	$-6.6721.10^{-4}$	$4.7129.10^{-1}$	$1.5645.10^{2}$
16	$-6.8507.10^{-4}$	$5.8780.10^{-1}$	$1.1178.10^{2}$
18	$-6.9630.10^{-4}$	$6.8986.10^{-1}$	$7.3628.10^{1}$

Table 4. Coefficients for the effect of the blades on the static pressure drop.

Coefficient	p	m
α	$-7.2725.10^{-6}$	$-5.6650.10^{-4}$
β	$5.4643.10^{-2}$	$-2.9130.10^{-1}$
ε	$-2.0706.10^{1}$	$4.4524.10^{2}$

The extended fitting is provided by Eq. (42):

$$\Delta p_{Fs} = \left(-7.2725\cdot10^{-6}\cdot\gamma_{pt} - 5.6650\cdot10^{-4}\right)\cdot V_{air}^2 + \left(5.4643\cdot10^{-2}\cdot\gamma_{pt} - 2.9130\cdot10^{-1}\right)\cdot V_{air} + \left(-2.0706\cdot10^{1}\cdot\gamma_{pt} + 4.4524\cdot10^{2}\right) \tag{42}$$

-Coefficient K_{ts} represents the pressure drop across fan's support platform, and it is computed using Eq. (43) [34]:

$$K_{ts} = \frac{C_{Dts} L_{ts} d_{ts} n_{ts}}{A_2} \tag{43}$$

The value of C_{Dts} depends on the support beam geometry and the Reynolds number. In this study, it is assumed to be 1.9 [35]. The area A_2 is not well defined because the orientation of the equipment is unknown, thus it is assumed that it corresponds to the rectangular frontal area of the support, Eq. (44):

$$A_2 = L_{ts} \cdot N_t \cdot X_t \tag{44}$$

The contribution of the support platform to the pressure drop is corrected by the frontal flow area of an A-frame. It is defined as the area without obstacles in each row of tubes. This area can be calculated using Eq. (45):

$$A_{fr} = \left[N_t \cdot \left(n_f \cdot t_f\right) \cdot \left(X_t - D_f\right) + N_t \cdot \left(X_t - D_{out}\right) \cdot \left(L_t - n_f \cdot t_f\right)\right] \cdot \sin(\theta) \tag{45}$$

-Coefficient K_{up} corresponds to the pressure drop across the obstacles before the fan, such as a protector screen. The value of K_{up} is presented in the literature in the form of figures [34]. A two-step modeling procedure is used to develop a one equation model for K_{up} as a function of the two ratios of variables involved, namely $A_{ob,up}/A_c$ and x_{up}/d_c. The general expression for K_{up} is given by Eq. (46). Table 5 collects the coefficients for various x_{up}/d_c ratios. In this case, the effect of the second variable on the coefficients of Eq. (46) is not linear but is given by Eq. (47) (See Table 6).

Table 5. Coefficients for correlation Eq. (46).

x_{up}/d_c	α	β	γ
0.05	14.7401	1.5868	-0.0001
0.10	6.7789	0.6917	0.0086
0.15	3.9267	0.5045	0.0012
0.20	2.1739	0.4121	-0.0035
0.30	0.9797	0.3280	-0.0059
0.40	0.5746	0.1598	0.0003

Table 6. Coefficients for correlation eq. (47).

Coefficient	p	m
α	0.1560	-1.5854
β	0.0782	-0.9947

$$K_{up} = \alpha_n \cdot \left(\frac{A_{ob,up}}{A_c}\right)^2 + \beta_n \cdot \left(\frac{A_{ob,up}}{A_c}\right) + \gamma_n \tag{46}$$

$$\alpha_n = p_\alpha \cdot \left(\frac{x_{up}}{d_c}\right)^{m_\alpha}$$
$$\beta_n = p_\beta \cdot \left(\frac{x_{up}}{d_c}\right)^{m_\beta} \tag{47}$$

The final expression is as follows, Eq. (48):

$$K_{up} = 0.1560 \cdot \left(\frac{x_{up}}{d_c} \right)^{-1.5854} \cdot \left(\frac{A_{ob,up}}{A_c} \right)^2 + 0.0782 \cdot \left(\frac{x_{up}}{d_c} \right)^{-0.9947} \cdot \left(\frac{A_{ob,up}}{A_c} \right) \tag{48}$$

This contribution to the pressure drop is corrected using the free area across the fan, computed using Eq. (49) [34]:

$$A_e = \frac{\pi}{4} \cdot \left(d_c^2 - d_{fh}^2 \right) \tag{49}$$

-Coefficient K_{do} corresponds to the pressure drop across the obstacles after the fan, such as the shaft. The value of K_{do} can be read in the figures presented by Kröger [34]. Similarly to previous coefficients, a one equation model is developed, Eq. (50), that includes the effect of $A_{ob,do}/A_c$ and x_{do}/d_c, whose relations are given by Eqs. (50), (51):

$$K_{do} = \alpha_n \cdot \left(\frac{A_{ob,do}}{A_c} \right)^2 + \beta_n \cdot \left(\frac{A_{ob,do}}{A_c} \right) + \gamma_n \tag{50}$$

$$\begin{aligned} \alpha_n &= p_\alpha \cdot \left(\frac{x_{do}}{d_c} \right) + m_\alpha \\ \beta_n &= p_\beta \cdot \left(\frac{x_{do}}{d_c} \right) + m_\beta \end{aligned} \tag{51}$$

Table 7 shows the original fitting parameters for Eq. (50) and Table 8 those that allow including the effect of the x_{do}/d_c ratio into the correlation. Again, it turned out to be a linear relationship as given by Eq. (51). Eq. (52) shows the final correlation.

$$\begin{aligned} K_{do} = &\left(-75.4268 \cdot \left(\frac{x_{do}}{d_c} \right) + 15.8845 \right) \cdot \left(\frac{A_{ob,do}}{A_c} \right)^2 \\ &+ \left(-18.2098 \cdot \left(\frac{x_{do}}{d_c} \right) + 3.6192 \right) \cdot \left(\frac{A_{ob,do}}{A_c} \right) \end{aligned} \tag{52}$$

Table 7. Fitting parameters for eq. (50).

x_{do}/d_c	α	β	γ
0.05	11.7438	2.9460	-0.0090
0.10	9.3812	1.4274	-0.0023
0.15	3.5998	0.9172	0.0062
0.20	1.0998	0.0811	-0.0017

Table 8. Fitting parameters for eq. (51).

Coefficient	p	m
α_n	-75.4268	15.8845
β_n	-18.2098	3.6192
γ_n	0	0

-Coefficient $K_{\theta\tau}$ represents the total pressure drop across the heat exchanger bundle and includes the kinetic energy losses across the heat exchanger. This coefficient can be calculated using Eq. (53) under isothermal flow conditions [33]:

$$K_{\theta t} = K_{he} + \left(\frac{1}{sin(\theta_m)} - 1 \right) \left(\frac{1}{sin(\theta_m)} - 1 + 2\sqrt{K_{ci}} \right) + K_{dj} + K_o \tag{53}$$

The function $\sin(\theta_m)$ is approximated by a second order polynomial, within the range of typical θ_m (0-90°), to avoid numerical issues. The polynomial obtained is Eq. (54):

$$\sin(\theta_m) = -1.0293 \cdot 10^{-4} \cdot \theta_m^2 + 2.0845 \cdot 10^{-2} \cdot \theta_m - 2.3441 \cdot 10^{-2} \tag{54}$$

The heat exchanger's pressure drop coefficient for normal isothermal flow, K_{he}, is defined by Heyns [20], Eq. (55):

$$K_{he} = 4177.08481 \cdot R_y^{-0.4392686} \tag{55}$$

The mean flow incident angle at the heat exchanger inlet, θ_m, is function of the A-frame half apex angle θ [33], Eq. (56):

$$\theta_m = 0.0019 \cdot \theta^2 + 0.9133 \cdot \theta - 3.1558 \tag{56}$$

The heat exchanger entrance contraction loss coefficient for normal flow, K_{ci}, is a function of the ratio of the minimum to free stream flow area through the heat exchanger bundle σ and the ratio of the minimum to free stream flow area at the bundle inlet σ_{21} [33]. These three variables can be calculated with Eq. (57), (58), (59), (60).

$$K_{ci} = \left(\frac{1 - \frac{1}{\sigma_c}}{\sigma} \right)^2 \tag{57}$$

$$\sigma_c = 0.6155417 + 0.04566493 \cdot \sigma_{21} - 0.336651 \cdot \sigma_{21}^2 + 0.4082743 \cdot \sigma_{21}^3 + 2.672041 \cdot \sigma_{21}^4 - 5.963169 \cdot \sigma_{21}^5 + 3.558944 \cdot \sigma_{21}^6 \tag{58}$$

$$\sigma_{21} = \frac{\left[X_l \cdot (N_r - 1) + D_f\right] \cdot \left[X_t \cdot (N_r - 1) + D_f\right] - \frac{\pi}{4} \cdot D_f^2 \cdot N_t \cdot N_r}{\left[X_l \cdot (N_r - 1) + D_f\right] \cdot \left[X_t \cdot (N_r - 1) + D_f\right]} \tag{59}$$

$$\sigma = \frac{N_t \cdot (X_t - D_f) \cdot L_t}{N_t \cdot X_t \cdot L_t} \tag{60}$$

Coefficients K_{dj} and K_o represent the kinetic energy loss at the heat exchanger outlet as a result of turbulent decay of the jet of air [20,33]. Fig. 6 shows the geometry configuration. Thus, K_{dj} can be computed by Eq. (61) while K_o is computed by Eq. (62):

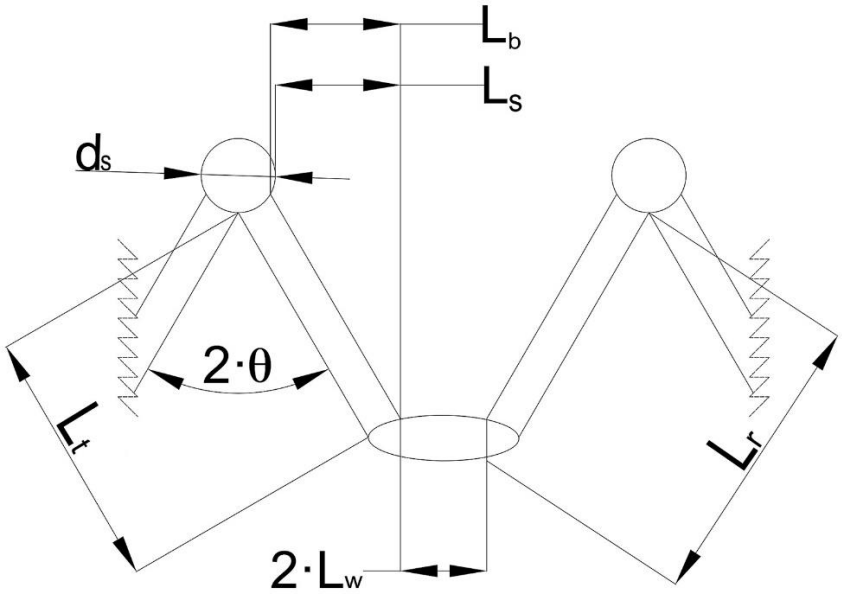

Fig. 6. Pipe configuration.

$$K_{dj} = \left[\begin{array}{l} \left\{ -2.89188 \cdot \left(\frac{L_w}{L_t} \right) + 2.93291 \cdot \left(\frac{L_w}{L_t} \right)^2 \right\} \cdot \left(\frac{L_t}{L_s} \right) \cdot \left(\frac{L_b}{L_s} \right) \cdot \left(\frac{28}{\theta} \right)^{0.4} + \\ + \left\{ \left(\frac{L_s}{L_b} \right) \cdot \exp\left(2.36987 + 5.8601 \cdot 10^{-2} \cdot \theta - 3.3797 \cdot 10^{-3} \cdot \theta^2 \right) \right\}^{0.5} \cdot \left(\frac{L_t}{L_r} \right) \end{array} \right]^2 \tag{61}$$

$$K_o = \left[\begin{array}{l} \left\{ -2.89188 \cdot \left(\frac{L_w}{L_t} \right) + 2.93291 \cdot \left(\frac{L_w}{L_t} \right)^2 \right\} \cdot \left(\frac{L_s}{L_b} \right)^3 + 1.9874 + \\ -3.02783 \cdot \left(\frac{d_s}{2 \cdot L_b} \right) + 2.0187 \cdot \left(\frac{d_s}{2 \cdot L_b} \right)^2 \end{array} \right] \cdot \left(\frac{L_t}{L_s} \right)^2 \quad (62)$$

The rest of the geometry features of the A-frame are computed using Eqs. (63), (64), (65), (66):

$$N_{Lr} = \frac{L_w}{cos(90 - \theta)} \quad (63)$$

$$L_r = N_{Lr} + L_t \quad (64)$$

$$L_b = L_r \cdot cos(90 - \theta) \quad (65)$$

$$L_s = \left(\frac{d_s}{2} + L_r \right) \cdot sin(\theta) - \frac{d_s}{2} \quad (66)$$

Furthermore, the bounds for the size of the fan are as follows, Eqs. (67), (68), (69), so that the fan can be allocated below the A-frame:

$$d_c \leq 2 \cdot \sin(\theta) \cdot L_t \quad (67)$$

$$n_{fan} \cdot d_c + Sep_{fan} \cdot (n_{fan} - 1) \leq X_t \cdot N_t \quad (68)$$

$$n_{fan} \cdot \frac{\pi}{4} \cdot d_c^2 + Sep_{fan} \cdot (n_{fan} - 1) \cdot 2 \cdot \sin(\theta) \cdot L_t \leq \frac{\pi}{4} \cdot 2 \cdot \sin(\theta) \cdot L_t \cdot \frac{N_b}{2} X_t \cdot N_t \quad (69)$$

The distance of upstream obstacles x_{up} and the distance of downstream obstacles x_{do} have to satisfy the following constraints, Eqs. (70), (71), (72), (73) [34]:

$$x_{up} \geq 0.05 \cdot d_c \quad (70)$$

$$x_{up} \leq 0.40 \cdot d_c \quad (71)$$

$$x_{do} \geq 0.05 \cdot d_c \quad (72)$$

$$x_{do} \leq 0.20 \cdot d_c \quad (73)$$

III.1.3.4. Ranges for variables and parameters

The ranges for the design variables are defined using the data from the literature to ensure representative solutions. These value ranges are collected in the supplementary material based on data from the literature for the pipes and the bundle, Table S1 [11,19,20,24,33], the characteristics of the fan in Table S2 [11,24,30], and the support geometry in Table S3 [36,37].

Some variables, i.e. fan diameter, are fixed based on data from the literature in order to solve it. However, these values can be replaced by variables if there exists information to build models that correlate them to the power consumption, etc. Some geometric variables are fixed based on typical standard values:

- The fan's specifications are defined by the manufacturer [24]. See Table S4 in the supplementary material.
- Some specifications of the bundles are fixed as seen in the supplementary material, Table S5. In this case, we used the following assumptions:
    - The pipe thickness is the standard value to the minimum inner pipe diameter [38]. This value has to be modified if the diameter takes distant values from the minimum inner diameter.
    - The fin thickness, t_f, is fixed [11].
    - The inner diameter of the steam pipe is fixed according to the maximum annual steam flow, the steam flow of the month July. In this case, the value of ds is the same as Heyns [20].
    - According to the small size of the facility of our case study, L_w takes the value of 0, because the tube bundles are distributed in a single street of bundles.

III.1.4. Optimization procedure

The link between design and seasonal operation is evaluated by proposing a two-step optimization procedure. The detailed model presented in Section 3 cannot be used

to evaluate the seasonal performance and a simplified model is developed based on the detailed design. This section is divided into two. Section 4.1 shows the objective function used to design the A-frame. Finally, Section 4.2 shows the model used to evaluate the operation of the plant over time.

III.1.4.1. Optimal equipment design

The model formulated in Section 3.3, an MINLP, is solved by using a tailor-made Branch and Bound method for the month of the largest cooling load. The objective function is based on the annualized cost of the unit including the cost of operation. The estimation of the cost of the units is based on the equipment cost to compute the facility investment cost, and the power consumed to run it, as the operating cost. The equipment cost can be divided into fan cost and A-frame heat exchanger cost. The equipment cost can be estimated using Eqs. (74), (75), (76) [26,42]:

$$C_{frame} = 3109 \cdot A^{0.40} \tag{74}$$

$$C_{fan} = K_2 \cdot 2.2 \cdot \left[1 + 0.2164 \cdot \ln\left(\Delta p_e\right)\right] \tag{75}$$

$$K_2 = 10^{2.9471+0.3302\cdot\log_{10}(v_{std})+0.1969\cdot\log_{10}(v_{std})^2} \tag{76}$$

The monthly amortization, Eq. (77), is determined considering that the expected life of the A-frame bundles is 25 years [19], while the fans lifespan is considered to be 18 years [43]:

$$Amort_{equipment} = \frac{C_{equipment}}{12 \cdot DeLi_{equipment}} \tag{77}$$

The cost for the power consumed is estimated using Eq. (78):

$$C_{elec} = \frac{1}{\eta_{fan}} \cdot P_F \cdot \left(744 \frac{kWh \cdot s}{kJ \cdot month}\right) \cdot C_{\$-kWh} \tag{78}$$

Thus, the objective function for the problem described in Section 3.3 becomes, Eq. (79):

$$Z = Amort_{frame} + Amort_{fan} + C_{elec} \tag{79}$$

The solution procedure is as follows. A deep first approach is implemented. The branching starts on the number of rows N_r, next the number of tubes per row N_t, subsequently the number of bundles of tubes, N_b. At this point the D_f is used as lower bound for X_t and X_l. The next level of the tree corresponds to the inner diameter and the outer diameter of the tube D_{in} and D_{out}. Subsequently, the tube length L_t is fixed using intervals of 0.15 m [44]. At this point the number of fins per tube length is already fixed, n_f, and the fins diameter D_f. Finally, the number of fans n_{fan} is computed.

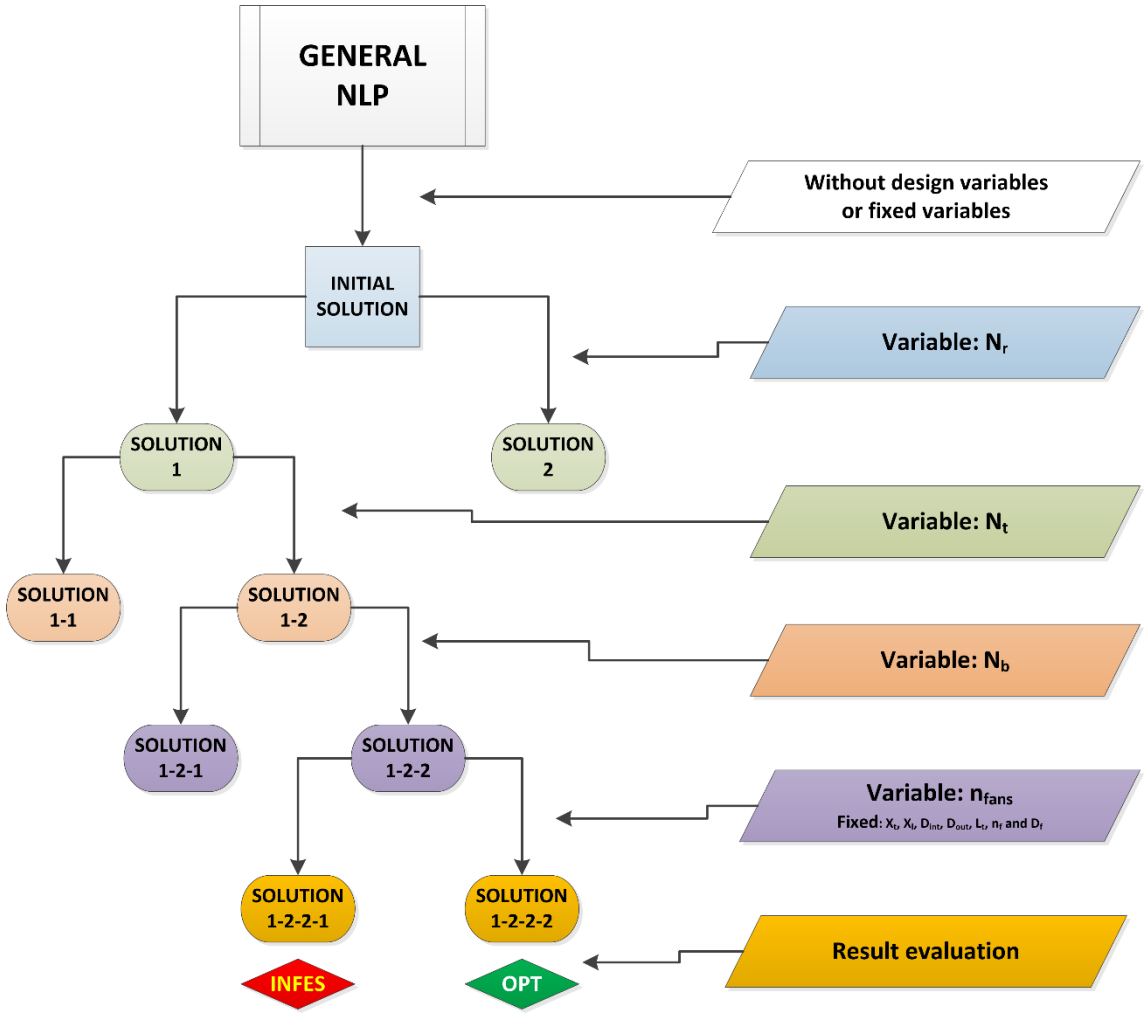

Fig. 7. Branch and Bound tree.

Each relaxed NLP problem at any node is solved using a multi-start initialization procedure. The problem size is about 150 eqs. and similar number of variables. It is also possible that some decision variables can be fixed at the same node because their values

are at integer values already, typically at the bounds. In each step of the procedure the objective function is compared to the other solutions of the branch and bound tree to decide how to continue. The resulting decision tree for this case can be seen in Fig. 7 below.

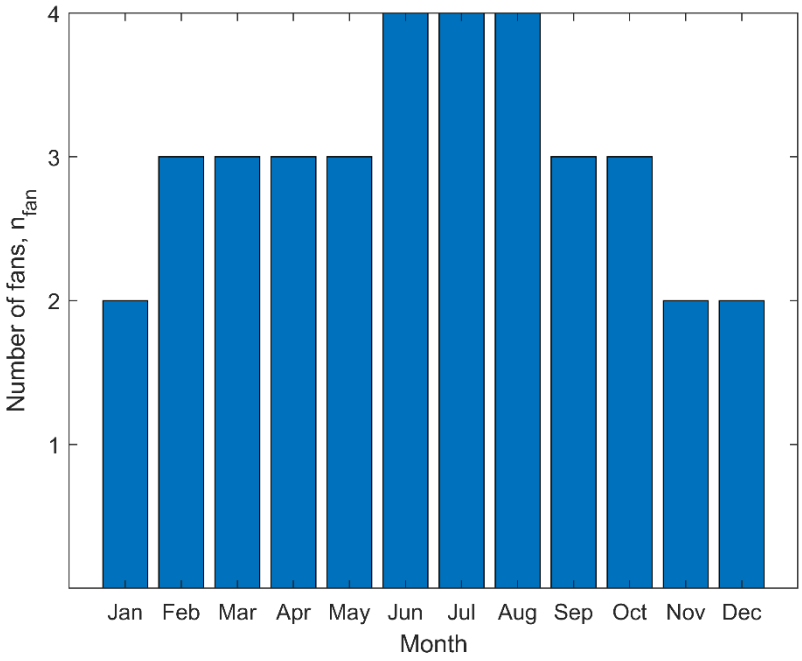

Fig. 8. Use of fans over the year.

III.1.4.2. Optimal operating conditions

The optimal geometric design provided by the previous problem is applied to study the unit operating conditions on a monthly basis. This part of the problem works as a recourse. The evaluation of monthly operating conditions is carried out by formulating a multi-period optimization model aiming at minimum the energy consumption over an entire year once the geometry is fixed. Hourly level operation is not considered a design but a control problem and it is not addressed in this work. However, for such a model to be solved, the highly non-linear equations of the design model must be simplified. First, all variables related to the mechanical design of the equipment (pipes, bundles, fans and support structure's specifications) are fixed using the results of the optimal design. Then, the coefficients that depend on those variables (K_{up}, K_{do} and K_{ts}) are computed and fixed. Air thermodynamic properties are also fixed to average annual values since there is not

much variation throughout the year. Next, the rest of the variables are transformed into monthly depended parameters or variables. For instance, the heat transfer coefficients are simplified considering an average global heat transfer coefficient, U , for each month (m). The values of U are obtained optimizing the operating conditions for each month individually. Table 9, Table 10 present the main operating and atmospheric conditions. Thus, the heat coefficient U becomes $U \rightarrow U(m)$. Table 11 shows the values of U .

Table 9. Atmospheric conditions [39-41].

MONTH	kWh/m²·day	Day	SUN (H)	Sun(h/day)	$T_{in,air}$ (ºC)	% Humidity
J	4.377	31	191	6.161	12.5	69
F	5.125	28	191	6.821	13.2	68
M	5.319	31	228	7.355	14.7	66
A	6.387	30	250	8.333	16.4	64
May	6.697	31	299	9.645	19.1	66
June	8.587	30	322	10.733	22.7	64
July	8.668	31	338	10.903	25.7	63
Aug	7.342	31	312	10.065	26.4	65
Sep	6.057	30	257	8.567	24.0	66
Oct	4.126	31	221	7.129	20.0	68
Nov	3.513	30	187	6.233	16.2	70
Dec	3.326	31	176	5.677	13.7	70
Average	5.794	30.4	248	8.13	18.7	66.6

Table 10. Monthly operation of the CSP plant [2].

	Jan	Feb	Mar	Apr	May	Jun
Q (kW)	18 650	21 610	22 460	27 120	28 400	36 450
$T_{in,air}$ (ºC)	12.5	13.2	14.7	16.4	19.1	22.7
T_v (ºC)	59.7	59.7	59.7	59.7	59.7	59.7
P_{gen} (kW)	12 623	14 632	15 206	18362	19 222	24 673

Table 10 (Continued). Monthly operation of the CSP plant [2].

	Jul	Aug	Sep	Oct	Nov	Dec
Q (kW)	36 870	30 940	25 850	17 380	14 830	13 990
$T_{in,air}$ (ºC)	25.7	26.4	24.0	20.0	16.2	13.7
T_v (ºC)	59.7	59.7	59.7	59.7	59.7	59.7
P_{gen} (kW)	24 959	20 943	17 201	11 763	10 042	9468

Table 11. U values per month.

Month	U (J/K m^2 s)
Jan	444
Feb	465
Mar	473
Apr	500
May	512
Jun	546
Jul	573
Aug	541
Sep	517
Oct	458
Nov	426
Dec	412

Similarly, other variables are also made monthly dependent: $A_{out}(m)$, $Q(m)$, $LMTD(m)$, $\Delta T_a(m)$, $\Delta T_b(m)$, $T_{out,air}(m)$, $T_{in,air}(m)$, $m_{air}(m)$, $m_w(m)$ and $Q_{air}(m)$. These variables cannot be fixed because the area required, the air flow and the energy balances change on a monthly basis.

Finally, the multi-period model involves the energy balances, the design equation for the heat exchanger and a set of equations grouped into four blocks as follows:

-Global equations: eqs. (80), (81):

$$n_b^{tot}(m) = \sum_{i=1}^{n_{fan}} n_b^i(m) \tag{80}$$

$$Q_{air}(m) = \sum_{i=1}^{n_{fan}} V_{air}^i(m) \tag{81}$$

-Fans equations: eqs. (82), (83), (84), (85):

$$V_{air}^i(m) \leq f^i(m) \cdot 700 \tag{82}$$

$$V_{air}^i(m) \geq f^i(m) \cdot 50 \tag{83}$$

$$f^i(m) \cdot b_{fan}(m) \geq n_b^i(m) \tag{84}$$

$$n_{fan}(m) = \sum_{i=1}^{n_{fan}} f^i(m) \tag{85}$$

Variable b_{fan} is defined considering that, after the design of the equipment, the pipes bundles will be distributed equitably among the fans.

-Power equation: eqs. (86), (87), (88):

$$P_{vent}(m) = \sum_{i=1}^{n_{fan}} P_F^i(m) \tag{86}$$

$$\begin{aligned}\Delta p_e^i(m) &= \Delta p_{Fs}^i(m) + 4.5922\cdot 10^{-8}\cdot\left(m_{fan}^i(m)\right)^2 + 4.5922\cdot 10^{-8}\cdot\left(m_{fan}^i(m)\right)^2 \\ &+9.38925\cdot 10^{-6}\cdot\left(m_{fan}^i(m)\right)^2 + 1.1207\cdot 10^{-5}\cdot\left(m_{fan}^i(m)\right)^2 \\ &+\left(-6.2129\cdot 10^{-8}\cdot V_{air}^i(m) + 1.3642\cdot 10^{-4}\right)\cdot\left(m_{fan}^i(m)\right)^2\end{aligned} \tag{87}$$

$$P_{vent}(m) = \sum_{i=1}^{n_{fan}} \left(\Delta p_e^i(m)\cdot m_{fan}^i(m)\right) \tag{88}$$

-Redefined equations: Eqs. (8), (30) are redefined using the variable n_b in order to calculate $A_{in}(m)$ and $A_{out}(m)$:

$$A_{in}(m) = n_b^{tot}(m)\cdot N_t \cdot N_r \cdot A_{in,pipe} \tag{8*}$$

$$A_{out}(m) = n_b^{tot}(m)\cdot N_t \cdot N_r \cdot A_{out,pipe} \tag{30*}$$

-The objective function is given by Eq. (89) aiming at the minimum annual consumption of energy Eq. (89). A base of 20 kW is assumed as the power required to switch on a fan:

$$Z = \sum_{m=1}^{12}\sum_{i=1}^{n_{fan}} \left(P_F^i(m) + 20000\cdot f^i(m)\right) \tag{89}$$

The problem size is 529 equations, 481 continuous and 120 discrete variables. Note that control is out of the scope of this paper.

III.1.5. Results

The case study of the Concentrated Solar Power facility developed in Martín and Martín [2] is used. This facility is based on an actual one in Spain. It is a small facility producing around 20 MW a year, located in a region where solar incidence is high and the

availability of water is becoming a challenge. The results section is divided into four parts. After describing the case of study, the geometric design of the unit for the month of the largest cooling load is presented. A sensitivity analysis evaluating the effect of the cost of electricity and the fan performance is carried out. Next, for a fixed geometry, the operation over a year is optimized. Finally, the economics and CO_2 emissions of dry and wet cooling systems are evaluated.

III.1.5.1. Operating data

The facility is located in the same region as the one in the work by Martín & Martín [2]. The operating conditions, weather data and plant operation are collected in Table 9, Table 10.

III.1.5.2. Equipment design

The Branch and Bound tree that leads to the solution is plotted in Fig. 7. Solution 1 had a value of the objective function Z equal to 84 958.09 $/month, and the Solution 2 of 107 366.80 $/month, thus the Solution 2 node was phantomed. At the second level, the Solution 1-1 had Z = 85 124.38 $/month and the Solution 1–2 Z = 84 958.09 $/month, thus the Solution 1-1 node was phantomed. Checking the solutions of the third level, it is noted that Solution 1-2-1, Z = 86 211.34 $/month, and Solution 1-2-2, Z = 85 659.96 $/month, suggest that the Solution 1-2-1 node to be phantomed. At the last level, Solution 1-2-2-1 was infeasible, thus the optimal solution for the case of study was Solution 1-2-2-2. The optimal design for the equipment is collected in the column labeled as *Values n°1* on Table 12.

The equivalent diameter was the same as D_{out}, which is due to the fact that the tubes only have a small number of fines. Using this result, the model is solved assuming $D_{eq} \approx D_{out}$. The results are shown on the column labeled as *Values n°2* on Table 12. The results presented in Table 12 are very similar. However, L_{ts} takes a different value in both solutions. The main reason for this difference is the fact that the variable is loosely

bounded. Nevertheless, the values of variables L_{ts} and d_{ts} need to be checked based on mechanical considerations of the support structure. The optimal apex angle is 62.93°, which is within the typical range. Most of the units are designed with an apex of 60° which was already obtained in the literature [27]. This result differs from typical air coolers where the pipes are horizontal [26]. Note that the model allowed that possibility, but the results showed otherwise. turned out to be 34.35 and the total number of fins per tube turned out to be 464; both values show that finned tubes are needed to provide enough transfer area, although the value of n_f is smaller than fully finned tubes as used previously. Fins increase the pressure drop at the cost of providing a larger contact area. As a result, the system tries to reduce the pressure drop and increases the number of tubes [24]. The value of n_f is small because there is no limit to the ground footprint of the units, and this is the option with the smallest pressure drop. Even though, the value is a tenth compared to the values in the literature, 393.7 fines per m [26]. A constraint about layout availability will modify the result, thus some variables as X_t, N_t or N_r could change since all the pipes needed are arranged in the same row and even the number of fins per unit length if more area is required. For instance, typically the number of rows of pipes is 2 [25,27] or 4 [26] even though this last design is not an A-Frame but the pipes are horizontal. The use of multiple rows increases the pressure drop and is meant to provide a larger heat transfer surface per cross sectional area. To reduce power consumption a single row of pipes is suggested. Furthermore, the number of tubes per row is also smaller, around 60 [25], or 56 for the horizontal design [26] and shorter tubes were installed, around 9 m [34] or 10.9 m [26] versus 13.5 m, see Table 12. The A-frame layout results in larger pipes compared to the design in Ref. [26]. Another interesting comparison is that the diameter of the tube obtained in previous work is 3.68 mm [27] while our results suggest smaller diameter, 3.3 mm. This fact results in larger heat transfer coefficients reducing the need for contact area. Finally the pitch distances are larger than the one in other designs [26,27], to reduce the pressure drop. Even though the design resulting from the optimization cannot be validated with a physical unit, the results obtained agree with the designs in the literature [24-27,34].

Table 12. Optimal design for July.

Variable	Values n^{o}1	Values n^{o}2	Variable	Values n^{o}1	Values n^{o}2
θ (°)	62.93	62.93	X_l (m)	0.15	0.15
L_t (m)	13.50	13.50	n_{fan}	4	4
D_{out} (m)	0.033	0.033	b_{fan}	4	4
D_{in} (m)	0.027	0.027	γ_{pt} (°)	16.38	16.38
D_{eq} (m)	0.033	0.033	L_{ts} (m)	9.47	6.00
N_t	75	75	d_{ts} (m)	0.10	0.10
N_r	1	1	x_{up} (m)	0.60	0.60
N_b	16	16	x_{do} (m)	1.50	1.50
D_f (m)	0.043	0.043	C_{frame} ($)	175,055	175,073
n_f	34.351	34.347	C_{fan} ($)	1,651,070	1,651,070
Fins per pipe	464	464	C_{elec} ($/month)	77,476	77,470
X_t (m)	0.15	0.15	**Z ($/month)**	**85 703.60**	**85 697.42**

One of the variables with larger uncertainty is the electricity cost, the second one is the fan performance. A sensitivity analysis is performed using a range of values from −20% to +20% of the original value were used. The results of the optimal design, following Section 4.1, are almost the same as those in Table 12, see Table 13. Slight differences can be found in one variable that is not tightly constrained and therefore the model has more freedom to select the final value such as L_{ts}. Even though, the result is close, 8.47 m–9.74 m. The rest values, but for the number of fines per pipe, are the same. In this case, the more common value obtained is 464 fines per pipe, but in the case of using an electricity cost 20% lower than the base case. However, the actual difference, 464 vs. 463, can be due to numerical issues. The second variable analyzed is the fan performance. The base case uses a value of 60% based on the literature [24]. In Table 13 the main characteristics of the A-frame are presented. Again, the only difference corresponds to the length of the support of the A-frame, L_{ts}, that is reduced to 7.93 m in case the performance is 40%. The fins per pipe are 465 instead of 464, that can be due to numerical issues more that an actual difference. Evaluating the results in Table 13 it is possible to conclude that the design is rather robust.

Table 13. Effect of electricity price on the design.

Variable	Original	Original	E_{cost}+20%	E_{cost}-20%	η=40%	η=90%
η	60	60	60	60	40	90
θ (°)	62.93	62.93	62.93	62.93	62.92	62.92
L_t (m)	13.50	13.50	13.50	13.50	13.50	13.50
D_{out} (m)	0.033	0.033	0.033	0.033	0.033	0.033
D_{in} (m)	0.027	0.027	0.027	0.027	0.027	0.027
D_{eq} (m)	0.033	0.033	0.033	0.033	0.033	0.033
N_t	75	75	75	75	75	75
N_r	1	1	1	1	1	1
N_b	16	16	16	16	16	16
D_f (m)	0.043	0.043	0.043	0.043	0.043	0.043
n_f	34.351	34.347	34.347	34.307	34.449	34.449
Fins per pipe	464	464	464	464	464	464
X_t (m)	0.15	0.15	0.15	0.15	0.15	0.15
X_l (m)	0.15	0.15	0.15	0.15	0.15	0.15
n_{fan}	4	4	4	4	4	4
b_{fan}	4	4	4	4	4	4
γ_{pt} (°)	16.38	16.38	16.38	16.38	16.38	16.38
L_{ts} (m)	9.47	6.00	9.47	8.68	7.93	9.47
d_{ts} (m)	0.10	0.10	0.10	0.10	0.10	0.10
x_{up} (m)	0.60	0.60	0.60	0.60	0.60	0.60
x_{do} (m)	1.50	1.50	1.50	1.50	1.50	1.50

III.1.5.3. Operation

For the optimal geometry of the unit defined in the previous stage, we optimize the operation of the system for minimum power consumption. This problem becomes a multi-period MINLP optimization one. It can be considered as a recourse where, it is up to the operation to decide the number of fans used, the outlet air temperature and the flow used per fan. It is assumed that for a fan to operate, a minimum flow rate of 50 m^3/s is required. Figs. 8-14 show the results obtained. In Fig. 8 it can be seen that the fans are fully used during summer, June to August. During winter, a fourth of the year, only half of the units are needed. The reason is that the CSP facility is producing less than haft power

than in winter and, in consequence, rejecting also less heat. As a result, assuming that it is possible to shut down some sections of bundles for better efficiency so that a decrease in the heat transfer coefficient due to low flow rates is avoided, Fig. 9 presents the actual area needed on a monthly basis. Again, winter time requires only half of the system available area, while during summer time there still exists a small margin of operation of about 5%. This margin is interesting for flexibility purposes. From the economic point of view, the investment in the A-frame is only fully used a quarter of the entire year, while the rest the units are underused, which is one the burdens for the operation of these plants. For half a year the area used is lower than 75% of that available. So far, the high costs of the solar field, representing almost 60% of the investment in units [2] mitigates the economic impact for under usage of the heat exchanger network of the plant the turbine and the cooling system. However, the solar field is the one that is currently improving its efficiency since the rest of the process is similar to current thermal power plants, therefore it is expected that idle units will show a larger contribution to the investment in the near future.

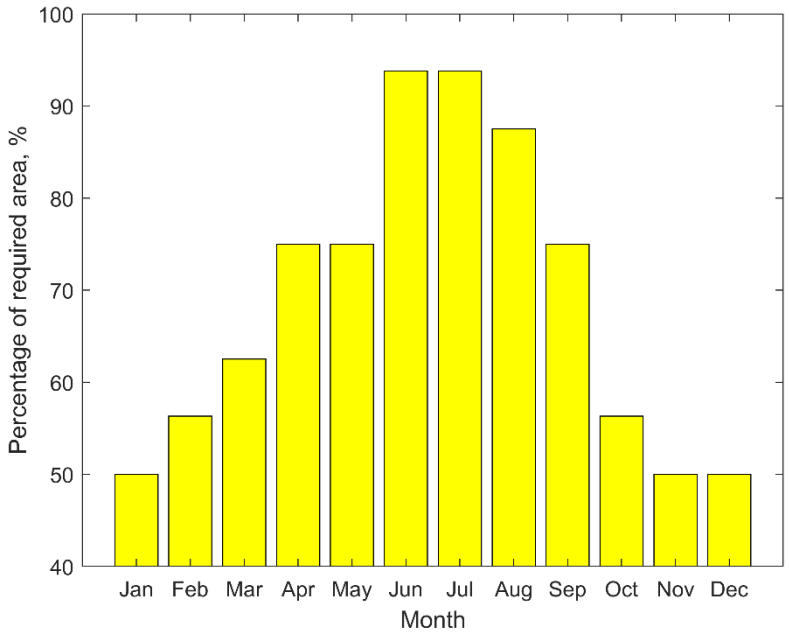

Fig. 9. Area used per month.

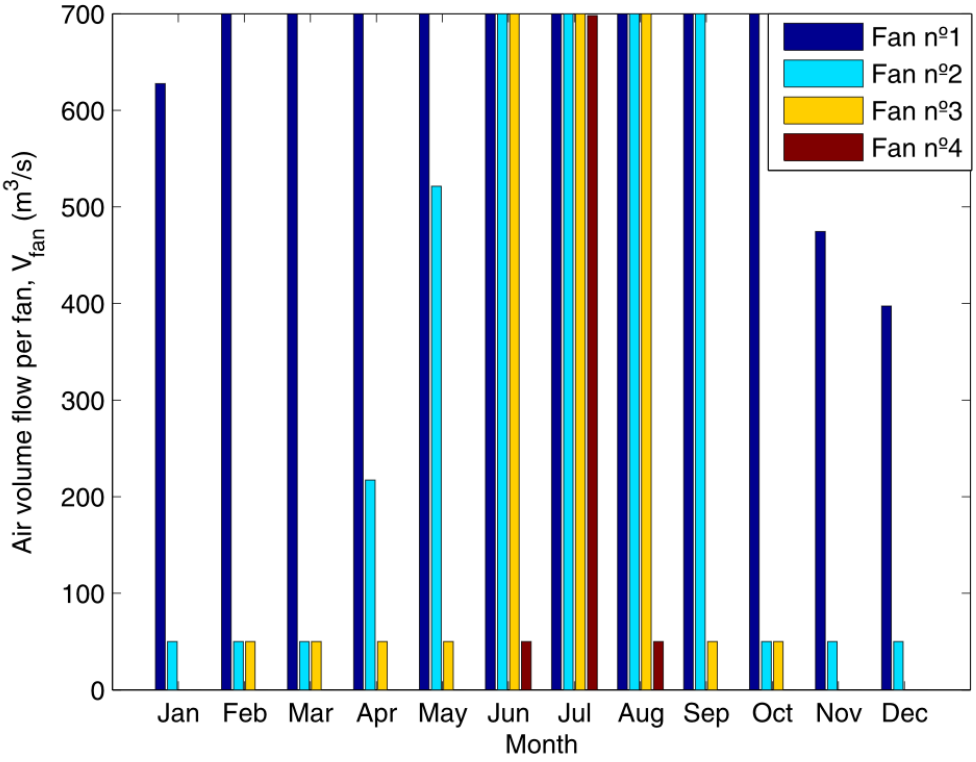

Fig. 10. Air volume flow rate used per fan and month.

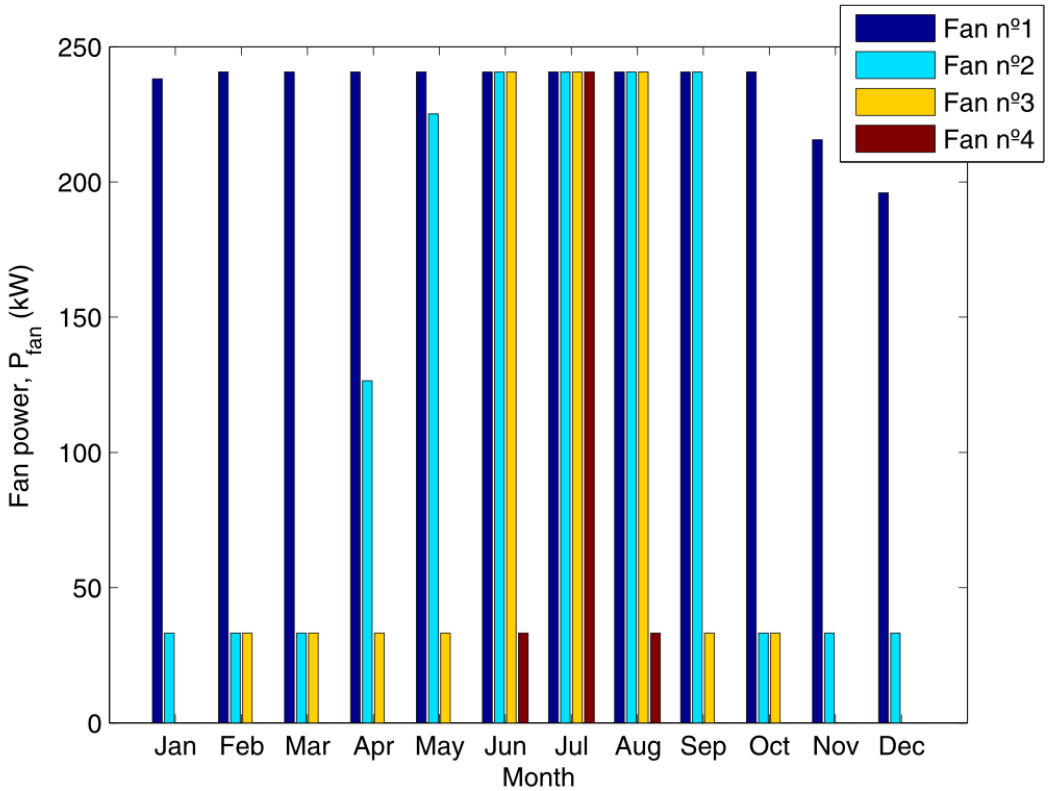

Fig. 11. Power used per fan and month.

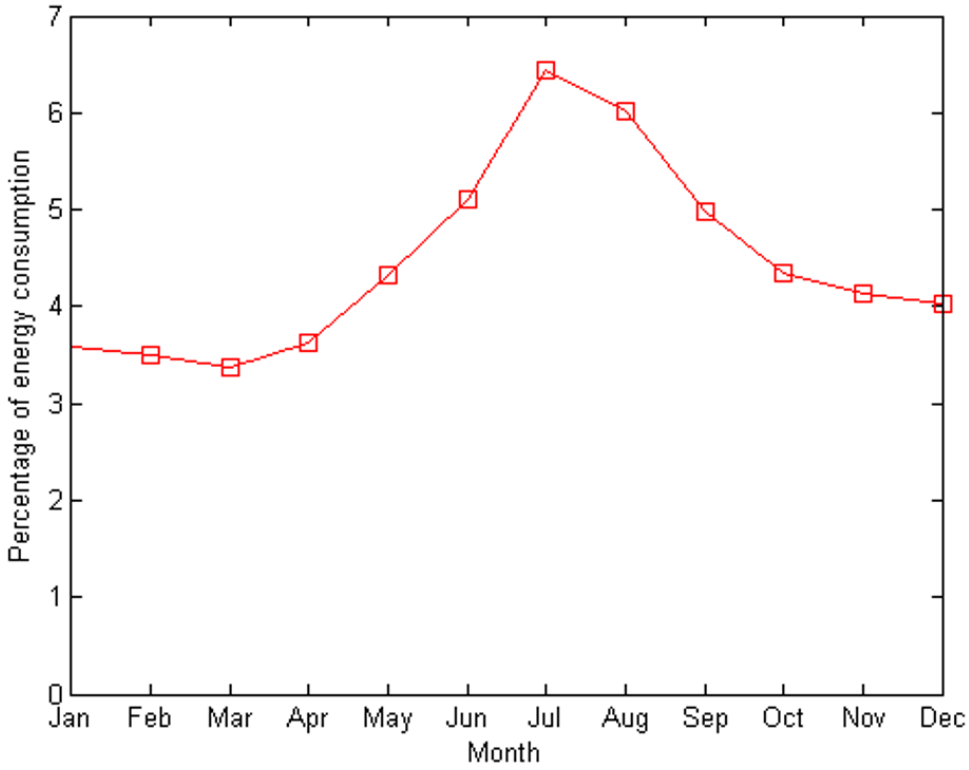

Fig. 12. Percentage of Energy consumption.

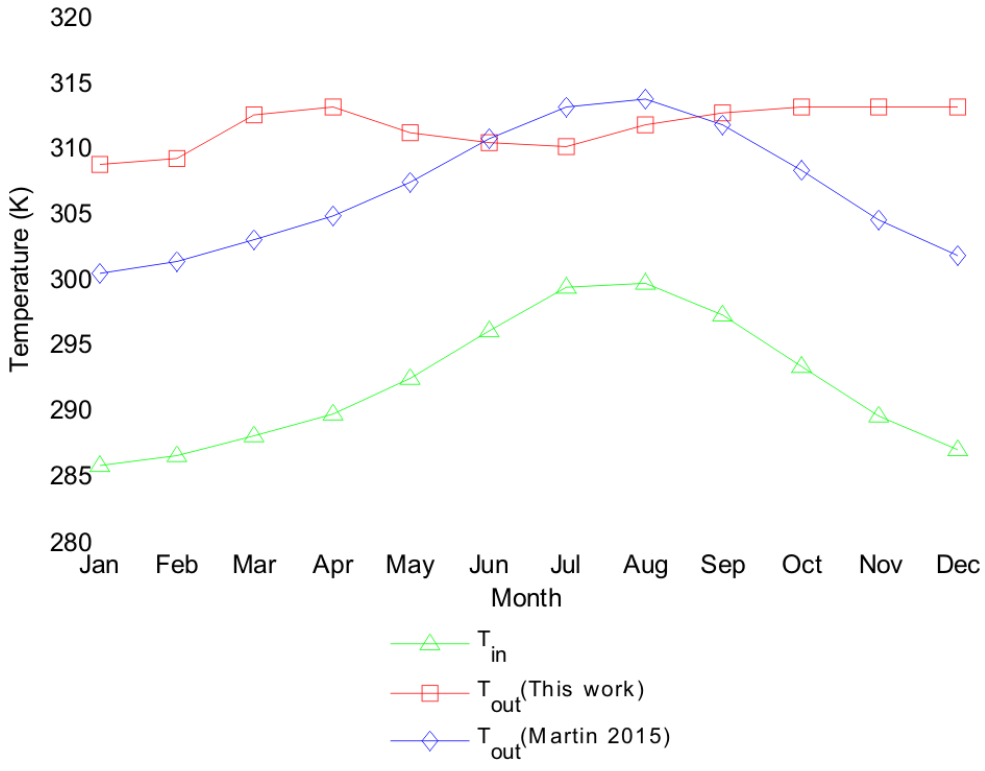

Fig. 13. Temperature gradient across the unit.

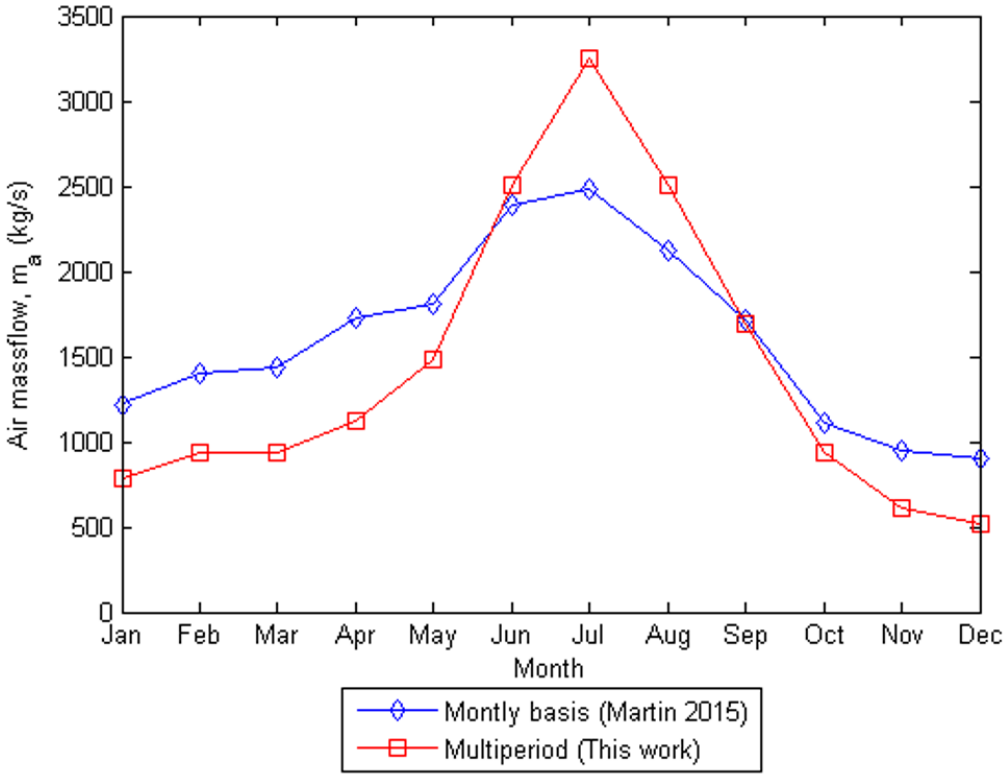

Fig. 14. Total mass flowrate used per month (Multiperiod, squares; Monthly basis, triangles).

The monthly operation also depends on the air flow used per fan and month. In principle, it is only when a fan is fully used when the second one enters in operation. However, that is not exactly correct in all cases. Sometimes, when only a small extra need is required from another fan, it is more efficient to use two fans at a lower flowrate, rather than only one using a larger flow, see Fig. 10. A minimum flow of 50 m^3/s is set for a second fan to operate. As a result of the economics, even if it would be possible to meet the cooling needs with one fan, every single month uses at least two fans, with one of them operating at the minimum load allowed. In January the first fan is operating close to its full capacity, around 625 m^3/s, so there is still margin to accommodate the rest of the air processes. November and December show a different behavior. In these two months a little over a half of the capacity of the first fan, 470 and 400 m^3/s, is used and yet a second one is in operation. It is possible to see that only July requires the full use of the 4 fans, while June and August have three fans operating at full capacity and the fourth one at the minimum. Similarly, for April and May a third fan is operating even though there is enough cooling capacity with two. The second fan in April is at one third of its full capacity while the second fan for May reaches three fourths of its full capacity. This can also be due to

the shape of the pressure drop curve as a function of the flow rate as well as the minimum air flow across a fan required for it to operate. Fig. 11 is similar to Fig. 10 where instead of presenting the air flow rate, power is shown. Around 1 MW of cooling power is needed during July compared to a little over 250 kW during winter.

The aim of this work is to reduce the energy consumption of dry cooling systems. The efficiency of the system is given by the fraction of the total energy produced by the CSP facility that needs to be diverted to the cooling system. Assuming that the fans have an efficiency of $\eta_{fan} = 60\%$ [24], Fig. 12 shows the percentage of energy consumed by the fans. We see that it is not constant over the year but there is a peak during summer, and in particular, in July. Note that the maximum power consumption takes place during that month, and that there is no proportionality between the power produced by the CSP facility and the power consumed by the cooling system. The A-frame system consumes from 3% in winter to 6.5% in August. This variation can be justified combining the information related to the fans operation in Figs. 10 and 11 with the one provided in Fig. 13. The cooler the temperature, the larger the driving force for heat transfer reducing the area needed and the pressure drop. Fig. 13 shows that the air temperature exiting the A-frame system is almost constant resulting in large temperature gradients of up to 25 K in winter, but a reduced 10 K in summer. As a result, the heat transfer area required in summer is not only due to the heat rejection, but also due to the reduced temperature gradient. Furthermore, in Fig. 14 it is possible to see that the air flow rate follows a profile similar to the one of the fraction of energy consumed, given by Fig. 12. There is a large increase in the mass flow rate used in June to August resulting in the need for the use of 4 fans to move that amount of air. Again, the reason is the need for larger contact areas due to a reduced heat transfer driving force. Furthermore, Fig. 13 also shows that if the system is optimized on a monthly basis, the ΔT is maintained constant over the months [11]; however, the multi-period optimization suggests using as much temperature difference as possible every single month, see Fig. 13, so that for most of the year the total mass flow rate used is smaller. As a result, the power required to move it also decreases compared to the standalone monthly operation. This is a particularly interesting result obtained by the multi-period optimization since it proves that the optimal operation of the units that use solar energy cannot be efficiently carried out on a

monthly basis or using a scenario based approach but a full year of operation must be considered. The use of a multiperiod approach makes the most of the resources available reducing the operating costs. This result also supports the use of the approach presented in this work.

The comparison of these results with the ones in the literature is not straightforward. In previous works a fan efficiency of 90%, $\eta_{fan} = 90\%$,was used. To compare the results of this work with the numbers presented in the previous one [11], the same fan efficiency must be considered. Using this efficiency, the energy consumption turns out to be 4.3%. The optimization of the unit allows reducing the energy consumption by 0.7% of the power produced by the facility corresponding to 10–20% savings with respect to other models and the literature. Note that the design provided by this work is a detailed one, unlike the one in Ref. [11] where the entire facility is considered. Fig. 15 shows the comparison between the power consumed by the fan in previous work [11] and that presented in this work considering $\eta_{fan} = 90\%$. During summer time, 20% savings are reported but for winter-spring time, almost half of the energy is saved.

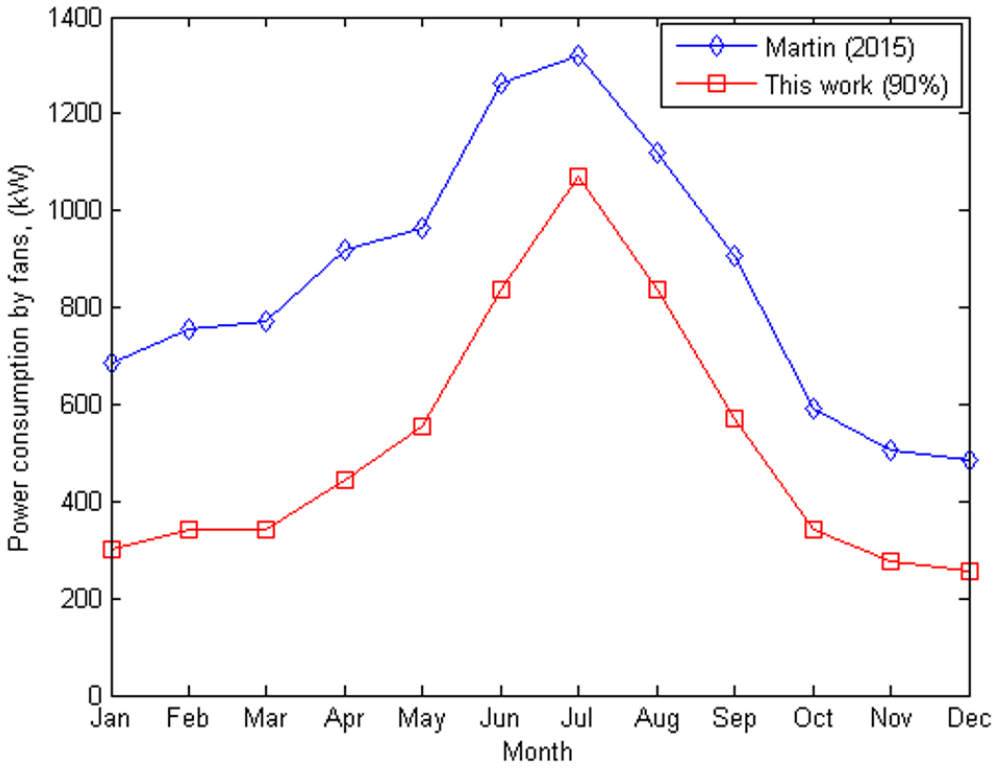

Fig. 15. Comparison of the multiperiod optimization and the monthly basis operation.

The variability in solar incidence and weather conditions constitutes a scheduling and control problem to be addressed at a more detailed time grid for the use of variable sources of energy. These issues will be addressed as future work by extending the model to deal with uncertain weather conditions at hourly or subhourly level, taking into account that they will also affect the operation of the plant that this cooling system serves and therefore an integrated solution is to be provided.

III.1.5.4. Economic and environmental evaluation

The assessment of A-frame systems is performed comparing the cost and emissions of the A-frame with those of a wet cooling tower.

1. The economic evaluation is divided into two parts: equipment cost and monthly operating cost.

The equipment cost of the A-frame, involving bundles and fans, is estimated using Eqs. (74-76), while eq. (90) is used to estimate the cost of the cooling tower [45]. In this case, a value of 800 m^3/s is considered for the variable v_{std} in order to take into account a fan with the manufacturer's characteristics.

$$C_{tower} = 101923 \cdot \left(Q \cdot 3.414 \cdot 10^{-6}\right)^{0.6} \quad (90)$$

The second part of economic evaluation is the operating cost. This cost is estimated as follows:

a. The amortization is calculated using Eq. (77), considering 25 years of expected life for the A-frame bundles [19], and 18 years are considered for the fans and the cooling tower [43].
b. The operating costs are estimated based on different factors for each system:
    - In the case of the A-frame this cost is due to the energy consumed by the fans, which can be calculated using eq. (78). The price of a kWh produced by a CSP plant is 0.083 $2013/kWh [46]. Part of that energy is consumed to operate the fans. The energy consumed considered has been computed in Section 4.2 for July.

- In the case of the cooling tower, the operating cost is due to the losses of water by evaporation. The monthly consumption of water for the CSP plant considered in the analysis is $7.70 \cdot 10^{-3}$ m^3/s [47]. The price of water in Almería, the location selected for the CSP plant, is 1.204 607 €/m^3 [48].

2. The environmental evaluation focuses on computing the CO2 emissions avoided by each of the systems. These emissions are calculated considering the equivalent amount of CO_2 generated if non-renewable resources had been used to produce the energy instead. However, from this value the generated by the fans consumption or by the water consumption must be subtracted. From the literature, it is assumed that each kWh obtained result in the emission of 0.632 kg CO_2 [49]:
    - In the case of the A-frame, the CO2 emissions avoided corresponds to that produced by the CSP facility discounting the energy consumed power the fans, Eq. (91):

$$Eco_{A-frame} = P_{gen} \cdot \left(744 \frac{kWh \cdot s}{kJ \cdot month}\right) \cdot \left(0.632 \frac{kgCO_2}{kWh}\right) \cdot \left(1 - \%_f\right) \quad (91)$$

    - In the case of the cooling tower, the emissions mitigated are given by the power produced by the CSP facility minus those related to water consumption as presented in eq. (92). We assume that each m3 of water used generates 0.30 kg CO_2 [50]:

$$Eco_{tower} = P_{gen} \cdot \left(744 \frac{kWh \cdot s}{kJ \cdot month}\right) \cdot \left(0.632 \frac{kgCO_2}{kWh} - C_{H_2O} \cdot 0.30 \frac{kgCO_2}{m^3 H_2O}\right) \quad (92)$$

Table 14. Economic and environmental evaluation.

Factor		**Refrigeration system**	
		A-frame	**Humidification tower**
Equipment cost	Core equipment ($\$_{2014}$)	175,078	1,854,379
	Fans ($\$_{2014}$)	2,053,355	-
Monthly equipment cost ($\$_{2014}$/month)		10,090	8,585
Water consumption ($\$_{2014}$/month)		-	33,035
Cost of energy consumption ($\$_{2014}$/month)		99,050	-
Total monthly cost ($\$_{2014}$/month)		109,140	41,620
CO_2 avoided emissions in July ($kgCO_2$)		10,981,823.98	11,724,338.72

The results obtained for July are used to compute the CO_2 emissions and water and energy consumptions, see Table 14.

The A-frame option is, nowadays and for the location considered, worse solution than cooling towers under both criteria, cost and CO_2 emissions. The A-frame is worse because the use of fans raises the cost above that of the cooling towers and its low efficiency results in lower mitigation of CO_2 emissions. These results could change in the future if the following scenarios take place:

- The economic results of A-frame could be improved in three ways: by decreasing investment cost of the fans, and/or by increasing the fan mechanical efficiency and, with it, the mitigated emissions of CO_2. However, the price of water will increase in the future, due to the desertification [51], reducing the advantage of using cooling towers.
- The environmental results of A-frame could be improved if the cooling tower needs an additional fan system, because the CO_2 avoided emissions of this refrigeration system will decrease and the difference with the A-frame system will be lower.

Furthermore, in a previous paper [11] a correlation to define the selection of the cooling technology as a function of the water consumption and the energy produced was developed to evaluate the regions where one technology is preferable. The results presented above are in line with the predictions provided by that correlation supporting the use of wet cooling in the region of study.

III.1.6. Conclusions

In this work a two-stage optimization procedure for the design and monthly operation of A-frame dry cooling systems within solar thermal power plants has been developed. The particular features of these systems are the fact that the availability of water is limited as well as the variable production capacity over time as a function of solar incidence. A detailed model is developed as the basis for the optimization of the geometry including pipe number, layout, diameter and length. A MINLP problem is formulated and

solved for the month of the largest cooling load, using a tailor-made branch and bound algorithm. In a second step, for the optimal geometry, we compute the optimal monthly use of the unit by formulating a multi-period MINLP. The solution of this problem indicates the use of number of fans, the air flowrate and its inlet and outlet temperature. The tool developed is detailed in the unit geometric characteristics and flexible to include new features or model for different fans.

The solution allows identifying several guidelines for the design of A-frames. It suggests an apex angle of 63°, one row of 75 pipes of 13.5 m long and with a diameter of 3.3 mm. A total of 4 fans are used but they only operate at full capacity during summer. This geometry shows a reduced consumption of energy by 0.7%, 20% less energy consumption that previous results, that within a power plant, results in a large energy savings. This two-step procedure reveals that multiperiod evaluation allows exploiting the design. It shows that it is recommendable to make full use of the temperature gradient to reduce the monthly air flow rate, saving energy on a monthly basis compared to a monthly optimization. Finally, the selection of cooling technology depends on the location because of water availability and weather conditions. Wet towers are quite competitive but CSP facilities are typically built in regions with limited water availability so that dry cooling systems are an interesting alternative.

III.1.7. Nomenclature

A_2 : Entrance area of support structure, m^2.

A_c : Total projected area of the fan, m^2.

A_e : Effective area across the fan, m^2.

A_f : Total outer fins' area, m^2.

A_{fr} : Total frontal flow area, m^2.

$A_{fr,bundle}$: Frontal flow area of a bundle, m^2.

A_{in} : Inside total area, m^2.

$A_{in,pipe}$: Inside area of a tube, m^2.

A_k : Logarithm mean area, m^2.

$A_{ob,do}$: Projected area of fan's downstream obstacles, m^2.

$A_{ob,up}$: Projected area of fan's upstream obstacles, m^2.

A_{out} : Outside total area, m^2.

$A_{out,fin}$: Outer fin area, m^2.

$A_{out,pipe}$: External total area of a pipe, m^2.

A_{tf} : Total fins area, m^2.

A_{smooth} : Smooth area of a tube, m^2.

$Amort_{equipment}$: Amortization of an equipment, $$_{2014}$/month.

b_{fan} : Bundles per fan.

$C_{\$-kWh}$: kWh price, $$_{2014}$/kWh.

C_{Dts} : Drag coefficient of support.

C_{elec} : Energy cost, $$_{2014}$/month.

$C_{equipment}$: Cost of an equipment, $$_{2014}$.

C_{fan} : Cost of a fan, $$_{2014}$.

C_{frame} : Heat exchanger cost, $$_{2014}$.

C_{H_2O} : CO_2 generated by water, kg/m^3.

$C_{p_{air}}$: Air heat capacity, kJ/(kg K).

$C_{p_{w,vap}}$: Water steam heat capacity, kJ/(kg K).

C_{tower} : Cost of a humidification tower, $$_{2014}$.

d_c : Inner fan diameter, m.

D_{eq} : Equivalent diameter, m.

D_f : Outer fin diameter, m.

d_{fh} : Diameter of fan shaft, m

D_{in} : Inner pipe diameter, m.

D_{out} : Outer pipe diameter, m.

d_s : Inlet steam duct diameter, m.

d_{ts} : Width of support beam, m.

$DeLi_{equipment}$: Expected life of an equipment, year.

e : Pipe mean thickness, m.

$Eco_{A-frame}$: Avoided CO_2 emissions by an A-frame, $kgCO_2$.

Eco_{tower} : Avoided CO_2 emissions by a humidification tower, $kgCO_2$.

f : Binary parameter of the fan during the month.

g : Gravitational acceleration, m/s^2.

H : Humidity of the air, kg/kg.

h_{air} : Air side coefficient, $kJ/(K\ m^2\ s)$.

h_c : Steam side coefficient, $kJ/(K\ m^2\ s)$.

$h_{ae}A_a$: hA steam term, kJ/(K s).

K_2 : K_2 term of fan cost.

k_{air} : Thermal conductivity of air, $kJ/(K\ m^2/m\ s)$.

k_c : Thermal conductivity of saturated liquid water on steam temperature, $kJ/(K\ m^2/m\ s)$.

K_{ci} : Heat exchanger entrance contraction loss coefficient for normal flow.

K_{dj} : Coefficient of losses due to the turbulent decay of the jet after the bundles.

K_{do} : Pressure drop coefficient of fan's downstream obstacles.

k_f : Thermal conductivity of fin, $kJ/(K\ m^2/m\ s)$.

K_{he} : Loss coefficient for normal isothermal flow through the finned-tube bundle

k_{mat} : Thermal conductivity of pipe material, $kJ/(K\ m^2/m\ s)$.

K_o : Coefficient of losses during the final mixing process as the flow leaves the A-frame .

K_{ts} : Pressure drop coefficient trough the support platform.

K_{up} : Pressure drop coefficient of fan's upstream obstacles.

$K_{\theta t}$: Total pressure drop coefficient across the heat exchanger bundles.

L_b : Projected total length of pipe, m.

L_r : Total bundle length, m.

L_s : Projected free length of pipe, m.

L_t : Pipe length, m.

L_{ts} : Length of support beam, m.

L_w : Walkway length, m.

$LMTD$: Logarithm mean temperature difference, K.

m : Dimensionless term m.

m_{air} : Air mass flow, kg/s.

m_{at} : Equivalent air mass flow per tube of a pair of rows, kg/s.

m_{fan} : Air mass flow per fan, kg/s.

m_w : Water vapor mass flow, kg/s.

N_b : Number of bundles.

n_b : Number of bundles working corresponding to the studied fan.

n_f : Number of fins per tube.

n_{fan} : Number of fans.

N_r : Number of rows per bundle.

N_t : Number of pipes per row.

n_{ts} : Number of support beams per side.

Nu : Nusselt number.

Ny : Characteristic heat transfer parameter of air, 1/m.

p_f : Separation between the same side of two adjacent fins, m.

P_F : Power supplied by a fan on his shaft, kJ/s.

P_{gen} : Energy produced by the CSP, kJ/s.

P_{vent} : Total power supplied by fans, kJ/s.

Pr : Prantl number.

Q : heat flow, kJ/s.

Q_{air} : Total air volume flow, m^3/s.

Re : Reynolds number.

Ry : Characteristic flow parameter of air, 1/m.

Sep_{fan} : Distance between fans, m.

$S_{\min-t}$: Minimum flow area, m^2.

t_f : Mean fin thickness, m.

$T_{in,air}$: Inlet air temperature, K.

$T_{out,air}$: Outlet air temperature, K.

T_v : Water steam temperature, K.

U : Overall heat transfer coefficient, kJ/(K m^2 s).

$U_c H_t L_t$: UHL steam term, kJ/(K s).

V_{air} : Air volume flow per fan, m^3/s.

v_{std} : Air volume flow at standard conditions, m^3/s.

x_{do} : Downstream obstacles from the fan, m.

X_l : Horizontal tube pitch, m.

x_{up} : Upstream obstacles from the fan, m.

X_t : Vertical tube pitch, m.

Z : Objective function, $\$_{2014}$/month.

$\%_f$: Percentage of energy consumed by fans.

Greek letters:

α_n : Generic alpha-n parameter.

β_n : Generic beta-n parameter.

Γ : Airflow across the minimum flow area, kg/s.

γ_{pt} : Fan blade's angle, º.

Δp_e : Total pressure drop across the system unit, Pa.

Δp_{Fs} : Fan static pressure, Pa.

ΔT_a : Temperature difference at the entrance of the heat exchanger, K.

ΔT_b : Temperature difference at the exit of the heat exchanger, K.

ε_n : Generic epsilon-n parameter.

η_0 : Outside area efficiency.

η_f : Fins' efficiency.

η_{fan} : Fan efficiency.

θ : A-frame apex angle, º.

θ_m : Mean flow incident angle, º.

λ_w : Latent heat of evaporation of the water steam, K.

μ_{air} : Air viscosity, kg/(m s).

μ_c : Saturated liquid water viscosity on steam temperature, kg/(m s).

ρ_{a3} : Mean air density trough the fan, kg/m^3.

ρ_{a56} : Mean air density across the heat exchanger bundles, kg/m^3.

ρ_c : Saturated liquid water density on steam temperature, kg/m^3.

σ : Ratio of the minimum to free stream flow area through the heat exchanger bundle.

σ_{21} : Ratio of the minimum to free stream flow area at the bundle inlet.

σ_c : Ratio of area related with K_{ci} .

φ : Dimensionless term phi.

Subscript:

(m) : month.

Superscript:

i : i-th element of the set.

tot : Total monthly value of a variable.

III.1.8. References

1. A. González-Finat, R. Liberali. **Concentrating solar power from research to implementation.** Office for Official Publications of the European Communities, Luxembourg, Luxembourg (2007).
2. L. Martín, M. Martín. **Optimal year-round operation of a concentrated solar energy plant in the south of Europe.** Appl Therm Eng, 59 (2013), pp. 627-633.
3. B. Kelly, H. Price. **Nexant parabolic trough solar power plant systems analysis task 2: comparison of wet and dry rankine cycle heat rejection**. Nexant Inc.: California, San Francisco (2006).
4. C.S. Turchi, M.J. Wagner, C.F. Kutscher. **Water use in parabolic trough power plants: summary results from WorleyParsons' analyses.** National Renewable Energy Laboratory, Colorado, Golden (2010).
5. H. Zhai, E.S. Rubin. **Performance and cost of wet and dry cooling systems for pulverized coal power plants with and without carbon capture and storage**. Energy Pol, 38 (2010), pp. 5653-5660.
6. G. Barigozzi, A. Perdichizzi, S. Ravelli. **Wet and dry cooling systems optimization applied to a modern waste-to-energy cogeneration heat and power plant**. Appl Energy, 88 (2011), pp. 1366-1376.
7. A.M. Blanco-Marigorta, M.V. Sánchez-Henríquez, J.A. Peña-Quintana. **Exergetic comparison of two different cooling technologies for the power cycle of a thermal power plant**. Energy, 36 (2011), pp. 1966-1972.
8. P. Habl, A.M. Blanco-Marigorta, B. Erlach. **Exergoeconomic comparison of wet and dry cooling technologies for the Rankine cycle of a solar thermal power plant**. Proceedings of ecos (2012) the 25th.
9. A.A.L.M. Liqreina. **Evaluation of dry cooling option for parabolic trough [CSP] plants including related technical and economic assessment: case of study CSP Plant in Ma'an/Jordan**. M.Sc. Thesis. Cairo University (2012).
10. P. Palenzuela, G. Zaragoza, D.C. Alarcón-Padilla, J. Blanco. **Evaluation of cooling technologies of concentrated solar power plants and their combination with desalination in the Mediterranean area**. Appl Therm Eng, 50 (2013), pp. 1514-1521.

11. M. Martín. **Optimal annual operation of the dry cooling system of a concentrated solar energy in the south of Spain**. Energy, 84 (2015), pp. 774-782.
12. Hikmet Esen, Mustafa Inalli, Mehmet Esen. **Technoeconomic appraisal of a ground source heat pump system for a heating season in eastern Turkey**. Energy Convers Manag, 47 (2006), pp. 1281-1297
13. Hikmet Esen, Mustafa Inalli, Mehmet Esen. **A techno-economic comparison of ground-coupled and air-coupled heat pump system for space cooling**. Build Environ, 42 (2007), pp. 1955-1965.
14. Mehmet Esen, Tahsin Yuksel. **Experimental evaluation of using various renewable energy sources for heating a greenhouse**. Energy Build, 65 (2013), pp. 340-351.
15. M.W. Rosegrant, X. Cai, S.A. Cline. **Global water outlook to 2025: averting an impending crisis**. International Food Policy Research Institute, Washington, DC (2002).
16. A. Dyreson, F. Miller. **Night sky cooling for concentrating solar power plants**. Appl Energy, 180 (2016), pp. 276-286.
17. L. Chen, L. Yang, Xm Du, Y. Yang. **A novel layout of air cooled condenser to improve thermo flow performances**. Appl Energy, 165 (2016), pp. 244-259.
18. L.J. Yang, M.H. Wang, X.Z. Du. **Yang YP Trapezoidal array of air-cooled condensers to restrain the adverse impacts of ambient winds in a power plant**. Appl Energy, 99 (2012), pp. 402-413.
19. K. Zammit. **Air-cooled condenser design, specification, and operation guidelines**. Electric Power Research Institute: California, Palo Alto (2005).
20. J.A. Heyns. **Performance characteristics of an air-cooled steam condenser incorporating a hybrid (dry/wet) dephlegmator**. M.Sc.E. Thesis. University of Stellenbosch, Stellenbosch, South Africa (2008).
21. Wolverine. **Wolverine Tube Inc. Chapter 6 Heat transfer to air cooled heat exchangers. Engineering data book III**. (2010) https://www.microcooling.com/wp-content/uploads/2012/09/DataBookIII.pdf, http://www.wlv.com/heat-transfer-databook/Last [Accessed Jun 2017].
22. C. Butler, R. Grimes. **The effect of wind on the optimal design and performance of a modular air-cooled condenser for a concentrated solar power plant**. Energy, 68 (2014), pp. 886-895.

23. L. Yang, X. Zhao, X. Du, Y. Yang. **Heat load capability matching principle and its applications to anti-freezing of air cooled** condenser. Appl Energy, 127 (2016), pp. 34-43.
24. J.R. Bredell, D.G. Kröger. **Numerical investigation of fan performance in a forced draft air-cooled steam condenser**. California Energy Commission, California (2006).
25. M. Pieve, G. Salvadori. **Performance of an air-cooled steam condenser for a waste-to-energy plant over its whole operating range**. Energy Convers Manag, 52 (2011), pp. 1908-1913.
26. J.I. Manassaldi, N.J. Scenna, S.F. Mussati. **Optimization mathematical model for the detailed design of air cooled heat exchangers**. Energy, 64 (2014), pp. 734-746.
27. A.E. Conradie, J.D. Buys. **Kroger DG Performance optimization of dry-cooling systems for power plants through sqp methods**. Appl Therm Eng, 18 (1–2) (1998), pp. 25-45.
28. I.E. Grossmann, K.P. Halemane, R.E. Swaney. **Optimization strategies for flexible chemical processes**. Comput Chem Eng, 7 (4) (1983), pp. 439-462.
29. S.T.W. Kuruneru, E. Sauret, S.C. Saha, Y. Gu. **Numerical investigation of the temporal evolution of particulate fouling in metal foams for air cooled heat exchangers**. Appl Energy, 184 (2016), pp. 531-547.
30. J.J. Chen. **Letter to the editor: comments on improvement on a replacement for the logarithmic mean**. Chem Eng Sci, 42 (1987), pp. 2488-2489.
31. G. Towler, R. Sinnott. **Chemical engineering design**. Elsevier Inc.: United States of America (2008).
32. D.Q. Kern. **Process de transferencia de calor (Process Heat Tansfer)**. Compañía Editorial Continental S.A.: México D.F. (1999).
33. M.T.F. Owen. **A numerical investigation of air-cooled steam condenser performance under windy conditions.** M.Sc.E. Thesis. University of Stellenbosch, Stellenbosch, South Africa (2010).
34. D.G. Kröger. Air-cooled heat exchangers and cooling towers: thermal-flow performance evaluation and design, vol. II, Pennwell: Oklahoma, Tulsa (2004).
35. R.L. Daugherty, J.B. Franzini. **Fluid mechanics with engineering applications** (seventh ed.), McGraw-Hill Inc., United States of America (1977).
36. https://www.gerdau.com.co/Portals/4/CatalogoVigas.pdf [accessed February 2016].
37. A. Llanos. **Personal communication**. (2015).

38. R.H. Perry, D.W. Green. **Chemical engineers handbook**. (eighth ed.), McGraw-Hill Education: United States of America (2007).
39. www.aemet.es/es/serviciosclimaticos/datosclimatologicos/valoresclimatologicos?l=6325O&k=and [accessed January 2013].
40. J.M. Sancho Ávila, J. Riesco Martín, C. Jiménez Alonso, M.C. Sánchez de Cos Escuin, J. Montero Cadalso, M. López Bartolomé. **Atlas de radiación solar AEMET (Spain) (AEMET solar radiation atlas: Spain)**. Agencia Estatal de Meteorología, Madrid, Madrid (2013).
41. www.agenciaandaluzadelaenergia.es/Radiacion/radiacion1.php [accessed January 2013].
42. http://www.matche.com/equipcost/Exchanger.html [accessed February 2016].
43. MPR, Ministerio de la Presidencia. **Ley 24/2014, de 24 de noviembre, del Impuesto sobre Sociedades**. Boletín Oficial del Estado, 288 (2014), pp. 96939-97097 [Accessed Feb 2016].
44. S.M. Walas. **Chemical process equipment: selection and design**. Butterworth-Heinemann, Boston (1988).
45. http://www.matche.com/equipcost/Cooling.html [accessed February 2016].
46. https://www.eia.gov/forecasts/aeo/electricity_generation.cfm [accessed March 2016].
47. L. Martín. **Planta de producción de energía por Concentración de energía Solar**. M.Sc.Eng Thesis. University of Salamanca, Salamanca, Spain (2013).
48. http://www.galasa.es/administracion/include/ficheros/documentos/20/Tarifas%20Galasa.pdf [accessed March 2016].
49. C. Thomas, T. Tennant, J. Rolls. **The GHG indicator: UNEP guidelines for calculating greenhouse gas emissions for businesses and non-commercial organisations**. United Nations Environment Programme (2000).
50. http://www.water.org.uk/news-water-uk/latest-news/water-industry-sustainability-latest-indicators [accessed March 2016].
51. http://www.eea.europa.eu//publications/europes-environment-aoa [accessed January 2016].

III.1.9. Supplementary data

Table S1. Pipes and bundle geometric characteristics [1-5]

Variable	Type	Symbol	Units	Lower bound	Upper bound
Pipes apex angle	Cont	$2.\theta$	º	45	160
Pipe Length	Cont	L_t	m	4	15
Pipe external diameter	Standard	D_{out}	m	0.03341	0.08
Piper internal diameter	Standard	D_{in}	m	0.02665	0.07324
Pipes per line	Integer	n_t	-	10	75
Lines per bundle	Integer	n_r	-	1	5
Number of bundles	Integer	n_b	-	2	16
Fins diameter	Cont	D_f	m	-	-
Fins per meter	Cont	n_f	-	10	591
Horizontal separation	Cont	X_t	m	0.03341	0.17
Vertical separation	Cont	X_l	m	0.03341	0.17

Table S2. Fan characteristics [1,4-5]

Variable	Type	Symbol	Units	Lower bound	Upper bound
Number of fans	Integer	n_{fan}	-	1	6
Air flow per fan	Cont	Q_{fan}	$m^3/(s)$	0	800
Upstream obstacle distance	Cont	x_{up}	m	0.5	0.6
Downstream obstacle distance	Cont	x_{do}	m	1.2	1.5

Table S3. Support geometry [6,7]

Variable	Type	Symbol	Units	Lower bound	Upper bound
Support structure length	Cont	L_{ts}	m	6	12
Support structure width	Cont	d_{ts}	m	0.1	0.4

Table S4. Fan characteristics [8]

Variable	Symbol	Value	Units
Shaft diameter	d_{fh}	1.399	m
Shell diameter	d_c	9.145	m
Fan distance	Sep_{Fan}	0.05	m
Efficiency	η_{fan}	60	%
Upstream obstacle area	$A_{ob,up}$	3.354839	m^2
Downstream obstacle area	$A_{ob,do}$	6.991921	m^2

Table S5. Bundle fixed parameters [1,9,10]

Variable	Symbol	Value	Units
Pipe thickness	e	0.0015	m
Fin thickness	t_f	0.000375	m
Steam pipe diameter	d_s	1.25	m
Street separation	L_w	0	m

References

1. Martín M. **Optimal annual operation of the dry cooling system of a concentrated solar energy in the south of Spain**. Energy 2015; 84: 774-82.
2. Esen, Hikmet, Inalli, Mustafa, Esen, Mehmet. **A techno-economic comparison of ground-coupled and air-coupled heat pump system for space cooling**. Building and Environment 2007; 42: 1955-65.
3. Esen, Mehmet, Yuksel, Tahsin. **Experimental evaluation of using various renewable energy sources for heating a greenhouse**. Energy and Buildings 2013; 65: 340-51.
4. Chen L, Yang L, Du Xm Yang Y **A novel layout of air cooled condenser to improve thermo flow performances**. Appl. Energy 2016, 165, 244-259
5. Yang L, Zhao X, Du X, Yang Y. **Heat load capability matching principle and its applications to anti-freezing of air cooled condenser**. Appl. Energy 2016, 127, 34-43
6. Manassaldi JI, Scenna NJ, Mussati SF. **Optimization mathematical model for the detailed design of air cooled heat exchangers**. Energy 2014; 64: 734-46.
7. Conradie AE, Buys JD, Kroger DG. **Performance optimization of dry-cooling systems for power plants through sqp methods**. Appl. Thermal Engineering 1998, 18 (1-2), 25-45
8. Bredell JR, Kröger DG. **Numerical investigation of fan performance in a forced draft air-cooled steam condenser**. California Energy Commission: California, 2006.
9. Heyns JA. **Performance characteristics of an air-cooled steam condenser incorporating a hybrid (dry/wet) dephlegmator**. M.Sc.E. Thesis, University of Stellenbosch, Stellenbosch, South Africa, 2008.
10. Perry RH, Green DW. **Chemical Engineers Handbook**. Eighth Edition. McGraw-Hill Education: United States of America, 2007.

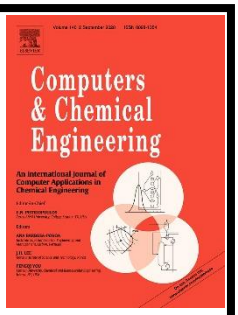

Optimal design of aging systems: A-frame coolers design under fouling

Luceño, J.A. and Martín, M.

Computers and Chemical Engineering, **2019**, *122*, 47-58

DOI: 10.1016/j.compchemeng.2018.05.015

III.2.1. Introduction

Everyday operation causes fatigue to materials and dirt deposits build on the surface of equipment. As a result, these units suffer losses in performance over time that affect the overall yield of the unit and of the facility. Beyond the lost in performance, failures may occur if the units operate for longer periods. Eventually, some of the units or sections must be replaced or repaired. It is estimated that $20,000–$30,000 of losses per hour can occur in refineries due to failures due to lack of proper maintenance (Tan and Kramer, 1997). Industry schedules maintenance shutdowns to evaluate the status, mitigate risks, clean and repair sections and entire units. In the literature, there is a large number of methods to evaluate maintenance strategies, most of them in the field of chemical and mechanical engineering, but also in logistics, where planes, train, trucks or ships are subjected to regular maintenance (Dekker, 1996). However, the most common optimization is minimum cost subject to average uptime or downtime (Mukerji et al., 1991; Wang, 2002) and mitigation strategies are developed based on the performance decay or the aging process (Kijima and Sumita, 1986; Damaso and García, 2009; Beaurepaire et al., 2012). Different tools have been developed to help schedule maintenance (Nguyen et al., 2008). To the best of our knowledge, simultaneous design and operation of the units considering performance decay is not addressed, although for instance the design of structures considers aging (Dekker, 1996).

Concentrated solar power (CSP) plants are typically located in regions with high solar incidence but limited water availability (Martín and Martín, 2013). For years, water consumption was not an issue in industry. However, it is no longer the case (Rosegrant, 2002). Wet cooling towers have been used and proved efficient, but the consumption of water adds up to around 2 L per kWh produced, a luxury that desert regions cannot afford (Martín and Martín, 2017). The large cooling needs required by any thermal plant using wet cooling systems are responsible for the water-energy nexus involved in power production (DOE, 2018). A large Energy–Water–Food initiative is being put together to address inefficiencies that lead to unsustainable operation of industrial and agricultural systems (FAO, 2018). Lately, several efforts have been carried out to limit the consumption of water using a particular design of air coolers, A-frames. These units are

characterized by their pipe configuration in the form of an "A", and promising cooling efficiencies (Martín, 2015). However, the consumption of up to 10% of the power generated in the facility to operate the fans is an important drawback. The design of such units has typically been carried out based on heuristics (Kröger, 2004; Heyns, 2008) and optimization studies for the design were limited to a small number of variables (Bredell and Kröger, 2006). Recently, Luceño and Martín (2018) developed a detailed mathematical optimization framework for the optimal design and annual operation of an A-frame cooling systems. The work reported promising savings in the operation of these units.

A-frame units are located in open air and fouling, in particular, particle fouling is an important issue for their operation and performance. Fouling phenomena have been long studied for heat exchangers (Kern and Seaton, 1959) and the rate of deposition and fouling have been modelled in the literature (Muller-Steinhagen et al., 1988; Muller-Steinhagen et al., 2005). Design books present characteristic factors to estimate the effect of fouling on the loss of heat transfer efficiency due to the deposition of dirt on the pipes (Coker, 2007; Walas, 1988; Zammit, 2005; GEA 2008; Towler and Sinnott, 2008). Müller-Steinhagen et al. (2011) stated that conservative designs represent 0.25% of the gross domestic product of industrialized countries and several cleaning strategies were discussed. However, from the design perspective the effect of deposits nature and building-up have not been evaluated until recently. The synthesis of heat exchanger networks under fouling conditions has been addressed at design level by Liu et al. (2015) and at control level by Luo et al. (2013) to mitigate the performance decay. Díaz-Bejarano et al. (2017) developed a systematic approach for the analysis and characterization of fouling and cleaning in refinery heat exchangers. In the case of air coolers, particle deposition is the main issue (Ahn et al., 2006).

When operating A-frames, fouling does not only affect the heat transfer coefficient, but deposits also block the cross sectional area, generating an additional pressure drop across the bundle of pipes (Pu et al., 2009; Sarfraz and Bach, 2016). An experimental example that determined the effect of particle fouling on the global heat transfer coefficient and the pressure drop showed that for single-row heat exchangers, the pressure drop increased by 28–31%, while the heat transfer performance decreased

by 7–12% when 300 g of standard dust was sprayed (Pak et al., 2003). Therefore, the share of the power produced by the facility to be devoted to operating the fans increases with time. Several lab scale studies have been developed showing the effect of particle deposition on pressure drop for air coolers (Ahn et al., 2006) as well as that on the heat transfer coefficient (Haghighi-Khoshkhoo and McCluskey, 2007) or considering the effect of fouling on both (Bell et al., 2009).

In this work we present a general methodology for the simultaneous optimal design and operation of units or processes whose yield is affected by aging or performance decays. In this case aging refers to the loss of efficiency due to fouling. We propose a parametric programming design procedure to determine the design and the cleaning/maintenance schedule. We use it for the design of A-frames under fouling conditions. We extend the previous model of an A-frame developed by Luceño and Martín (2018) to account for the effect of fouling on both, the heat transfer resistance and the pressure drop. The paper is organized as follows: In Section 2, the methodology is described. In Section 3 the modelling features of the case of study are presented focusing on the effect of particle fouling on the pressure drop across the pipe bundle and on the heat transfer coefficient. Next, in Section 4 the case study and the main results are discussed such as design features comparing the clean and the dirty designs, and major operating conditions including the power consumed by the cooling system, as well as the usage of area and number of fans. Finally, Section 5 draws some conclusions.

III.2.2. Unit design and operation under aging

This methodology is generic for any phenomenon that decreases the yield or performance of a unit or a process over time. It is based on a parametric optimization approach for the simultaneous design and operation of the unit. The parameter is the cycle time, the years of operation before a maintenance shutdown. First, a detail model of the unit or facility is to be developed. Special attention is to be paid to identify the performance/yield variables. Next, the yield decay must be characterized and its effect on the operating variables must be modelled. Before applying the methodology, the lifetime of the plant is to be estimated to determine the operating horizon.

The methodology consists of two stages. The length of the operating cycle is an optimization parameter. For a fixed cycle time period before maintenance, the unit is designed to operate under the worst conditions, those corresponding to just before cleaning, a robust design. The variables affected by aging are estimated from the decay laws under these conditions. Then, the design of the unit is optimized by solving the detail mathematical model using the operating costs, OPEX, as objective function.

For the fixed design determined by a particular length cycle, we formulate a multiperiod optimization problem. The variables affected by aging are computed beforehand using the decay laws. The time step is variable depending on the operating horizon. The objective function is the OPEX over the entire operating period. Cleaning steps may have a cost. It can be estimated as the profit that is not obtained during the cleaning stage assuming the production capacity of the month/months before cleaning, depending on the performance of the plant, or it can be fixed. The cleaning or maintenance costs are added to the objective function for as many stops as needed along the entire lifetime of the unit. If there is not an integer number of operating periods to cover the entire lifetime, a fraction is added and so its cost, to the OPEX for comparison among cleaning schedules.

A different operating horizon is fixed, and the procedure is repeated until the OPEX does not longer decreases. Therefore, the worst case is optimized.

By solving this two-stage problem for different operating horizons, the optimal operating horizon before cleaning is computed so that both the maintenance schedule and unit design are simultaneously addressed. Fig. 1 shows a generic scheme of the procedure. In dashed lines the data computed for the particular example described below, that can be substituted by the operating variables subjected by aging in the particular case.

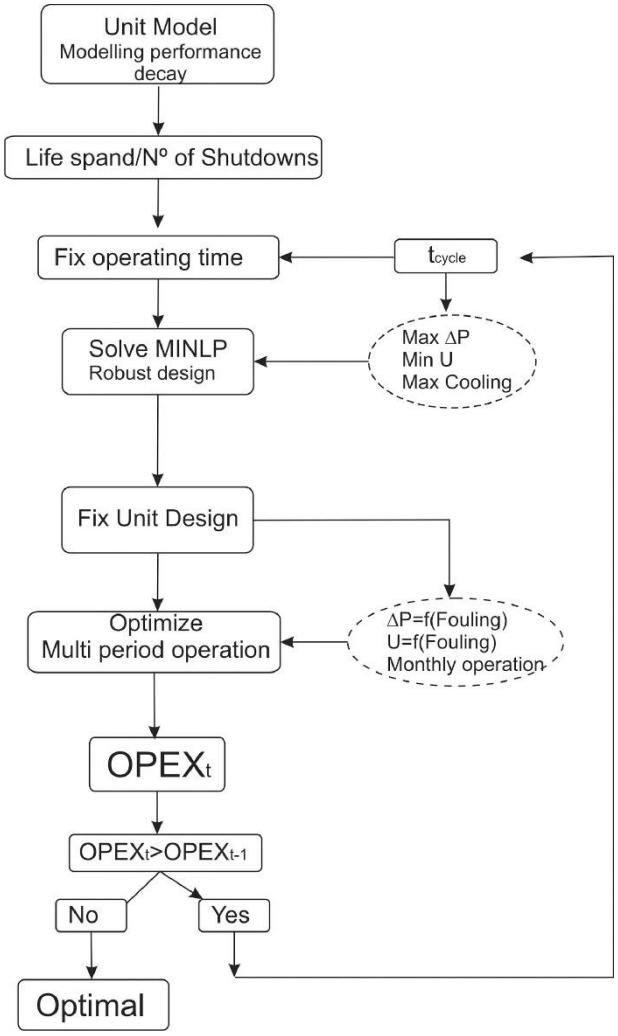

Fig. 1. Scheme of the algorithm.

III.2.3. Case of study

We consider the case of the optimal design of A-frame systems under fouling conditions within the operation of CSP plants. These units are located in the open air, and therefore subjected to weather conditions. In particular, deposits build on the heat exchanger pipes affecting both the pressure drop and the heat transfer coefficient. Thus, the aging variables are the global heat transfer coefficient and the pressure drop.

III.2.3.1. CSP facility description

The plant consists of three sections: the heliostat field, including the collector and the molten salts storage tanks, the steam turbine and the air cooler steam condenser. Fig. 1S in the supplementary material presents the flowsheet for the process. This process is based on the use of a tower to collect the solar energy and a regenerative Rankine cycle. The steam is generated in a system of three heat exchangers where water is heated up to saturation and then evaporated using the total flow of molten salts. However, only a fraction of the flow of salts is used to superheat the steam before it is fed to the first body of the turbine. The rest is used to reheat up the steam before it is fed to the medium pressure turbine. In the medium pressure turbine, part of the steam is extracted and it is used to heat up the condensate. The rest of the steam is finally expanded to an exhaust pressure, condensed and recycled. For the condensation of the steam we propose the use of a direct air cooler system, an A-frame. For the detailed information on the modelling features of the heliostat field and the steam turbine, we refer to previous work (Martín and Martín, 2013; Martín, 2015).

III.2.3.2. Air cooling system

The exhaust steam from the turbine circulates along a large pipe and it is distributed into the inclined pipes that form a roof over a system of fans in the form of an A. The steam is condensed in the tubes as it descends. Fig. 2S shows a scheme of a typical A-frame condenser.

III.2.3.3. A-frame model structure

The model extends previous work to include the effect of fouling on the heat transfer coefficient and on the pressure drop. Thus, the model is divided in 3 sections: mass and energy balances, A-frame design, and fans design. For the sake of the length of the paper we focus on modelling the effect of fouling on the global heat transfer coefficient and the pressure drop. The details of the geometry of the A-frame can be

found in the supplementary material as well as in previous work (Luceño and Martín, 2018).

III.2.3.3.1. Mass and energy balances

Two energy balances are formulated, one for the air flow and another one for the steam. The first one determines the air flow required for the operation, and is given by Eq. (1):

$$Q = m_{air} \cdot \left[C_{p_{air}} \cdot \left(T_{out,air} - T_{in,air} \right) + H \cdot C_{p_{w,vap}} \cdot \left(T_{out,air} - T_{in,air} \right) \right] \quad (1)$$

The energy that has to be rejected, Q, is computed from the energy balance to the steam, as given by Eq. (2) and the data of the operation of the CSP plant (Martín and Martín, 2013).

$$Q = m_w \cdot \lambda_w \quad (2)$$

III.2.3.3.2. A-frame design

The general design equation of any heat exchanger is Eq. (3):

$$Q = U \cdot A_{out} \cdot LMTD \quad (3)$$

LMTD is computed using Chen's approximation (Chen, 1987). A_{out} is that given by finned pipes. The total area, A_{out}, is computed by the number of pipes per row and bundle and the fines that they have, see supplementary material.

The global heat transfer coefficient, U, is affected by fouling. Therefore, we need to correct it as follows:

$$\frac{1}{U} = f_{air} + R_{air} + f_{tube} + f_{steam} + R_{steam} \quad (4)$$

The terms related to the air and steam sides, f_{air}, f_{steam}, and that of the tube, f_{tube}, remain the same as previous work (Luceño and Martín, 2018). However, to account for fouling we assume that the resistance to the air side as a function of time increases. There

are a number of typical trends depending on the type of deposit from linear (Al-Haj Ibrahim, 2012) to logarithmic based. Typically, the thickness of a deposit is a measure of the resistance of the deposit to the transfer of heat. Therefore, based on the results for particle deposition in air coolers by Ahn et al. (2006), we assume that the resistance to heat transfer due to fouling follows the same profile as that of the pressure drop. We use values from tables in design books for the actual final value and, according to the profile for deposition (Ahn et al., 2006; Yang et al., 2007; The Engineering Toolbox 2018), it is assumed that the resistance to fouling is reached after 8 years. Fig. 2 shows the increase in the fouling resistance to heat transfer over time. Eq. (5) presents the fitting correlation. The increase in the resistance due to fouling on the steam side, Eq. (6), is assumed to be linear with time.

$$R_{air} \cdot 10^{4} = \frac{9.379}{1+e^{5.091-1.020 \cdot t}} - 2.400 \cdot 10^{-2} \tag{5}$$

$$R_{ws} = 1.1250 \cdot 10^{-5} \cdot t(years) \tag{6}$$

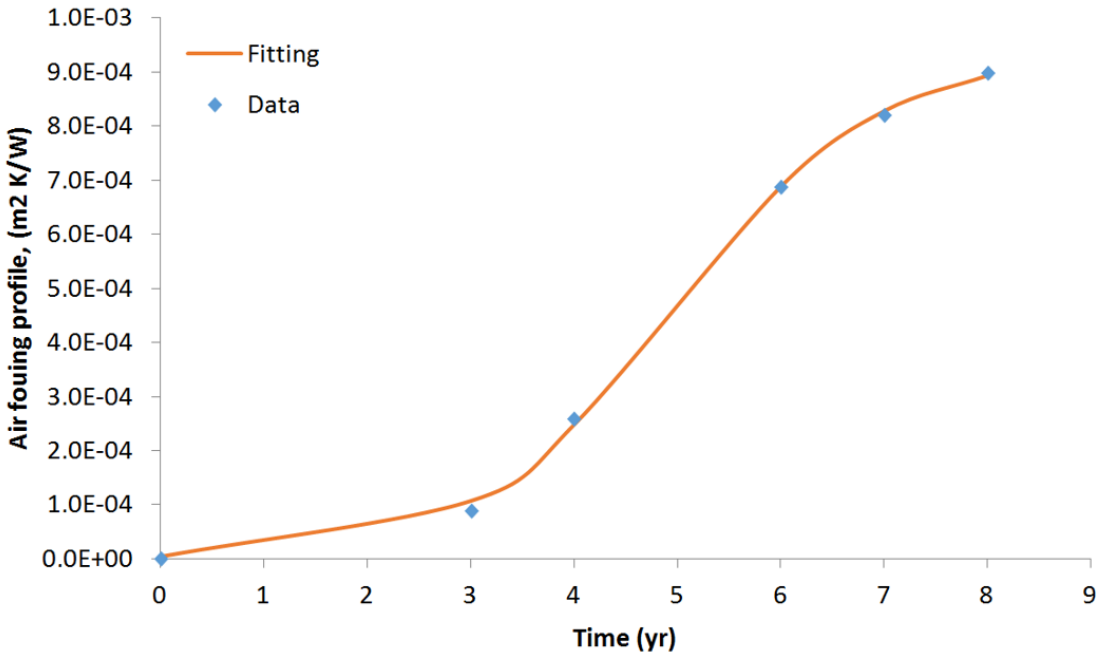

Fig. 2. Fouling resistance of in the air side over time.

III.2.3.3.3. Fans design

The deposition of dust on the pipes increases the pressure drop across the pipe bundle. As a result, the energy consumption increases so as to be able to move the air

flow to condense the exhaust steam. In this model we use the same blade designs as in a previous work (Luceño and Martín, 2018).

III.2.3.3.3.1. Power per fan

The power required by the fan is that needed to overcome the pressure drop, and can be obtained from Eq. (7):

$$P_{vent} = n_{fan} \cdot P_F = Q_{air} \cdot \Delta p_e \tag{7}$$

Where P_F is given by Luceño and Martín (2018)

$$P_F = \left(1.3122 \cdot 10^{-5} \cdot \gamma_{pt} - 6.7710 \cdot 10^{-4}\right) \cdot V_{air}^2 + \left(1.4015 \cdot 10^{-2} \cdot \gamma_{pt} + 4.1596 \cdot 10^{-1}\right) \cdot V_{air} \tag{8}$$

The number of fans is computed as follows, Eq. 9:

$$Q_{air} = n_{fan} \cdot V_{air} \tag{9}$$

III.2.3.3.3.2. Pressure drop

The pressure drop across the system is the one responsible for the energy consumed by the fans. To compute it, we need to account for the different contributions such as the pressure drop at the entrance of the structure, f_s, before, f_{bfans}, and after the fan, f_{afans}, and finally across the tubes bundles, f_{bundle}, apart from the pressure drop across the fan itself, Δp_{Fs} see Eq. (10). The details of each one of the terms can be seen in the supplementary material or in previous work (Luceño and Martín, 2018). However, fouling modifies the pressure drop across the pipes bundle.

$$\Delta p_e = -\left[f_f + f_{bfans} - \Delta p_{Fs} + f_{afans} + f_{bundle} \cdot Fouling \right] \tag{10}$$

In order to compute the increase in the pressure drop generated in the bundles of tubes over time, experimental data from the literature have been used. Bell (2007) shows experimental data for three levels of fouling for different velocities. Based on those values, we see that the effect of velocity on the contribution of fouling to pressure drop is already considered within the clean model. Kern and Seaton (1959) proved that there is an asymptotic thickness of the fouling layer. It is expected that pressure drop will follow the same trend. Using the experimental data from Ahn et al. (2006), it is possible to fit the

increase in the pressure drop as a result of particle fouling over time. Fig. 3 shows the profile of the increase in the pressure drop due to fouling. Rhombus represent the experimental dada and the line plots the model given by Eq. (11).

$$Fouling = 0.01\left(\frac{26.891}{1+e^{4.806+0.973\cdot t(years)}}+126.172\right) \tag{11}$$

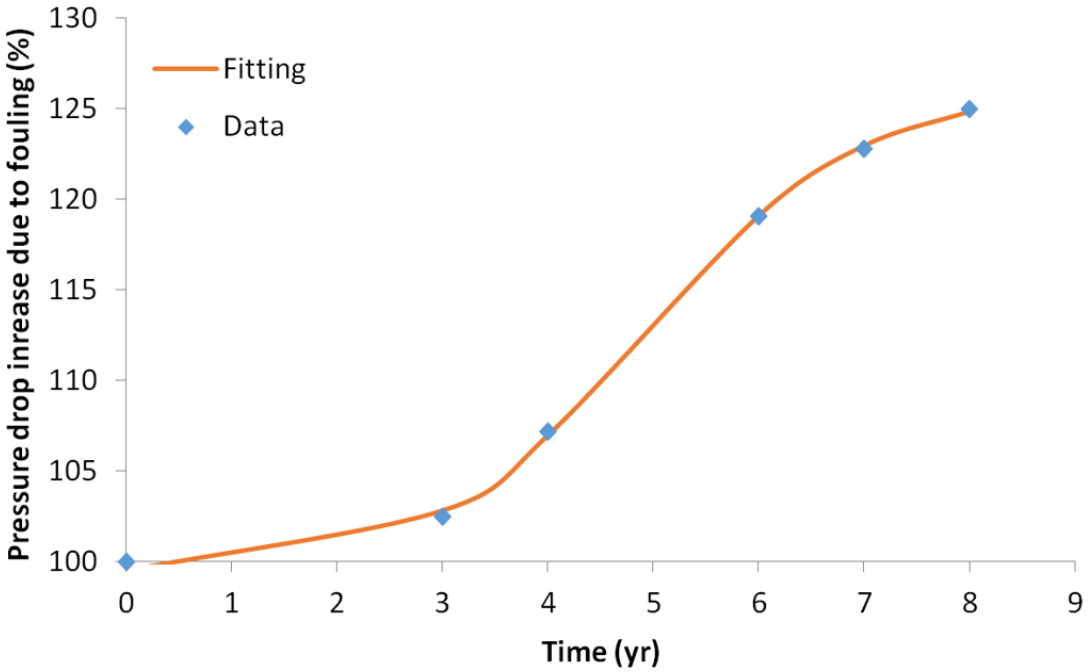

Fig. 3. Pressure drop increase over time under fouling conditions.

III.2.3.4. Design of A-frames under fouling conditions

To determine the optimal design and cleaning scheme a parametric optimization framework is proposed, see Fig. 1. The parameter is the number of years before cleaning, always above 3 years and typically below half-life of the unit, 8 years. In general, the cycle time could be extended up to the lifetime. However, we assumed at least one maintenance shutdown and the fact that by the time the unit is decommissioned it should to be left clean. Thus, from 8 years to a maximum of 13 years would have been possible, based on the fact that for 3 years fouling does not present performance decays. The algorithm works as follows. For the maximum dirty conditions, by the end of the cycle, we design the unit for the month of the maximum cooling load. We solve an MINLP using a

Taylor made Branch and Bound algorithm to determine the number of bundles, pipes, fans and the geometry of the unit.

The accumulation of dust reduces *U* and increases the pressure drop as presented in the model above. Over the horizon period before the next maintenance shutdown for cleaning we optimize the operation and determine the costs. With the geometrical design already fixed, we compute *U* clean for the different months along that final year of operation. Each of them is used as reference to compute the clean ones of the corresponding months of the first year of operation by removing the contribution of the fouling. With the clean *U*, we finally recompute *U* for all other months of the operating period. We also compute a coefficient, the increase of the pressure drop on a monthly basis using Eq. (11). We assume that the solar profile will be similar over the years, but that can be updated using prediction algorithms i.e. ARIMA. We solve the MINLP for the number of months corresponding with the operation before cleaning. Multiperiod optimization is required. If the problem becomes large, a rolling horizon scheme can be implemented. The solution to this problem provides an operating cost for this period. We compute the number of cleaning stages and provide a cost for cleaning. Several costs are considered, including no cleaning costs and three different costs. The cleaning costs considered correspond to the production capacity of one month of operation. That does not mean that it takes one entire month for maintenance. We use the monthly maximum, minimum and average production capacities over a year to evaluate the effect of cleaning costs on the solution performing a sensitivity analysis. Finally, since the life time of the unit is assumed to be 16 years (MPR, 2014; MPR, 2014), there is an additional cost for the additional years until the unit is to be decommissioned as a fraction of the operating cost of the entire period computed by the MINLP problem.

III.2.3.4.1. Optimal equipment design

The objective function is based on the annualized cost of the unit including the cost of operation. The estimation of the cost of the units is based on the equipment cost to compute the facility investment cost, and the power consumed to run it, as the operating cost. The equipment cost can be divided into fan cost and A-frame heat

exchanger cost. The equipment cost can be estimated using Eqs. (12)–(14) (Manassaldi et al., 2014; Matche 2014):

$$C_{frame} = 3109 \cdot A^{0.40} \tag{12}$$

$$C_{fan} = K_2 \cdot 2.2 \cdot \left[1 + 0.2164 \cdot \ln\left(\Delta p_e\right)\right] \tag{13}$$

$$K_2 = 10^{2.9471+0.3302\cdot\log_{10}(v_{std})+0.1969\cdot\log_{10}(v_{std})^2} \tag{14}$$

The monthly amortization, Eq. (15), is determined considering that the expected life of the A-frame bundles and the fans, both assumed to be 16 years (MPR, 2014):

$$Amort_{equipment} = \frac{C_{equipment}}{12 \cdot DeLi_{equipment}} \tag{15}$$

The cost for the power consumed is estimated using Eq. (16):

$$C_{elec} = \frac{1}{\eta_{fan}} \cdot P_F \cdot \left(744 \frac{kWh \cdot s}{kJ \cdot month}\right) \cdot C_{\$-kWh} \tag{16}$$

Finally, cleaning cost is added and is multiplied by the number of cleaning instances over the lifespan on the unit. Thus, the objective function becomes, Eq. (17):

$$Z = Amort_{frame} + Amort_{fan} + C_{elec} + n_{ckeaning} \cdot C_{cleaning} \tag{17}$$

Subject to the model is described in Section 3.3. See supplementary material for further details.

A Taylor made Branch and Bound method is used to solve the MINLP based on a deep first approach. We start by branching on the number of rows N_r, next the number of tubes per row N_t, subsequently the number of bundles of tubes, N_b. At this point we use the Df as lower bound for X_t and X_l. The next level of the tree corresponds to the inner diameter and the outer diameter of the tubes D_{in} and D_{out}. Subsequently, the tube length L_t is fixed using intervals of 0.15 m (Wallas, 1990). At this point we already fix the number of fins per tube length, n_f, and the fins diameter D_f. Finally, the number of fans n_{fan} is computed. Each relaxed NLP problem at any node corresponds to a highly nonlinear,

non convex model of about 150 eqs. and variables. It is solved using a multi-start initialization procedure using CONOPT as preferred solver.

III.2.3.4.2. Optimal operating conditions

The optimal geometric design provided by the previous problem is applied to evaluate the unit operating conditions on a monthly basis. The monthly operating conditions are determined by solving a multi-period optimization model. The objective function is the minimization of the energy consumption. However, for such a model to be solved, the highly non-linear equations of the design model must be simplified. First, all variables related to the mechanical design of the equipment (pipes, bundles, fans and support structure's specifications) are fixed using the results of the optimal design. Then, the coefficients that depend on the geometry are also computed and fixed. Air thermodynamic properties are also fixed to average annual values since there is not much variation throughout the year.

Next, the variables are transformed into monthly depended parameters or variables. In particular, the fouling coefficient to compute the pressure drop and the global heat transfer coefficient as described above. Fig. 5 shows the values of U that have been included in the formulation. Similarly, using the deposit growing rate, we compute the profile of increase in the pressure drop as a function of time, see Fig. 6.

Finally, we also have: $A_{out}(m)$, $Q(m)$, $LMTD(m)$, $\Delta T_a(m)$, $\Delta T_b(m)$, $T_{out,air}(m)$, $T_{in,air}(m)$, $m_{air}(m)$, $m_w(m)$ and $Q_{air}(m)$. These variables cannot be fixed because the area used or needed, the air flow and the energy balances change on a monthly basis.

Thus, the multi-period model involves the energy balances, the design equation for the heat exchanger and a set of equations grouped into four blocks as follows:

–**Global equations**: the Eqs. (18) and (19):

$$n_b^{tot}(m) = \sum_{i=1}^{n_{fan}} n_b^i(m) \tag{18}$$

$$Q_{air}(m) = \sum_{i=1}^{n_{fan}} V_{air}^i(m) \tag{19}$$

–**Fan's equations**: the Eqs. (20)–(23):

$$V_{air}^{i}(m) \leq f^{i}(m) \cdot 700 \tag{20}$$

$$V_{air}^{i}(m) \geq f^{i}(m) \cdot 50 \tag{21}$$

$$f^{i}(m) \cdot b_{fan}(m) \geq n_{b}^{i}(m) \tag{22}$$

$$n_{fan}(m) = \sum_{i=1}^{n_{fan}} f^{i}(m) \tag{23}$$

Variable b_{fan} is defined considering that, after the design of the equipment, the pipes bundles will be distributed equitably among the fans.

–**Power's equation**: the Eqs. (24) and (25):

$$P_{vent}(m) = \sum_{i=1}^{n_{fan}} P_{F}^{i}(m) \tag{24}$$

$$\begin{aligned}\Delta p_{e}^{i}(m) = {} & \Delta p_{Fs}^{i}(m) + 4.5922 \cdot 10^{-8} \cdot \left(m_{fan}^{i}(m)\right)^{2} + 4.5922 \cdot 10^{-8} \cdot \left(m_{fan}^{i}(m)\right)^{2} \\ & + 9.38925 \cdot 10^{-6} \cdot \left(m_{fan}^{i}(m)\right)^{2} + 1.1207 \cdot 10^{-5} \cdot \left(m_{fan}^{i}(m)\right)^{2} \\ & + \left(-6.2129 \cdot 10^{-8} \cdot V_{air}^{i}(m) + 1.3642 \cdot 10^{-4}\right) \cdot \left(m_{fan}^{i}(m)\right)^{2}\end{aligned}$$

$$P_{vent}(m) = \sum_{i=1}^{n_{fan}} \left(\Delta p_{e}^{i}(m) \cdot m_{fan}^{i}(m)\right) \tag{25}$$

–**Redefined equations**: the Eqs. (26) and (27) are defined using the variable n_b in order to calculate $A_{in}(m)$ and $A_{out}(m)$:

$$A_{in}(m) = n_{b}^{tot}(m) \cdot N_{t} \cdot N_{r} \cdot A_{in,pipe} \tag{26}$$

$$A_{out}(m) = n_{b}^{tot}(m) \cdot N_{t} \cdot N_{r} \cdot A_{out,pipe} \tag{27}$$

–**The objective function** is given by Eq. (28) aiming at the minimum annual consumption of energy. We consider a base of 20 kW as the power required to switch on a fan:

$$Z = P_{Electricity} \cdot n_{cycles} \left(\sum_{m=1}^{12} \sum_{i=1}^{n_{fan}} \left(P_{F}^{i}(m) + 2000 \cdot f^{i}(m) \right) \right) + n_{cleaning} \cdot C_{cleaning} \tag{28}$$

The problem size depends on the years of continuous operation up to 6350 equations, 5800 continue and 1440 discrete variables. We use a commercial MINLP solver DICOPT, but if no integer solutions are reported, an approximation method is used instead by using the continuous solution provided and rounding the continuous solutions up. Alternatively, a rolling horizon kind of scheme can be implemented.

III.2.4. Results

We use as a case study the Concentrated Solar Power facility developed in Martín and Martín (2013) based on an actual facility in Spain. It is a small facility producing around 20 MW a year, located in a region where solar incidence is high and the availability of water is becoming a challenge. Results section is divided into three subsections. In Section 4.1 we present the cooling needs of the CSP plant and the monthly atmospheric data. Section 4.2 discusses the main design features of the unit. Finally, Section 4.3 presents the operation and optimal cleaning instances.

III.2.4.1. Operating data

The facility is located in the same region as the one in the work by Martín and Martín (2013). The operating conditions, weather data and plant operation are collected and summarized in Tables 1 and 2. We assume that over the time horizon the average monthly conditions are the same every year. Further studies on the effect of uncertainty are out of the scope of this work.

Table 1. Atmospheric conditions (Martín and Martín, 2013).

MONTH	kWh/(m²·day)	Day	SUN (H)	Sun (h/day)	$T_{in,air}$ (ºC)	% Humidity
January	4.377	31	191	6.161	12.5	69
February	5.125	28	191	6.821	13.2	68
March	5.319	31	228	7.355	14.7	66
April	6.387	30	250	8.333	16.4	64
May	6.697	31	299	9.645	19.1	66
June	8.587	30	322	10.733	22.7	64
July	8.668	31	338	10.903	25.7	63

Table 1 (Continued). Atmospheric conditions (Martín and Martín, 2013).

MONTH	kWh/m²·day	Day	SUN (H)	Sun(h/day)	$T_{in,air}$ (ºC)	% Humidity
August	7.342	31	312	10.065	26.4	65
September	6.057	30	257	8.567	24.0	66
October	4.126	31	221	7.129	20.0	68
November	3.513	30	187	6.233	16.2	70
December	3.326	31	176	5.677	13.7	70
Average	5.794	30.4	248	8.13	18.7	66.6

Table 2. Monthly operation of the CSP plant (Martín and Martín, 2013).

	Jan	Feb	Mar	Apr	May	Jun
Q **(kW)**	18,650	21,610	22,460	27,120	28,400	36,450
$T_{in,air}$ **(ºC)**	12.5	13.2	14.7	16.4	19.1	22.7
T_v **(ºC)**	59.7	59.7	59.7	59.7	59.7	59.7
P_{gen} **(kW)**	12,623	14,632	15,206	18,362	19,222	24,673

Table 2 (Continued). Monthly operation of the CSP plant (Martín and Martín, 2013).

	Jul	Aug	Sep	Oct	Nov	Dec
Q **(kW)**	36,870	30,940	25,850	17,380	14,830	13,990
$T_{in,air}$ **(ºC)**	25.7	26.4	24.0	20.0	16.2	13.7
T_v **(ºC)**	59.7	59.7	59.7	59.7	59.7	59.7
P_{gen} **(kW)**	24,959	20,943	17,201	11,763	10,042	9,468

III.2.4.2. Equipment design

A Branch and Bound method was applied for the design of units for different years of operation before the removal of the deposits. The solution of each design takes about 30 min of CPU time in an Intel i5 core running under Windows 10. Based on a life span of the unit of 16 years, the number of maintenance shutdowns determines the length of the cycle. We consider at least one and a maximum of 3 shutdowns since for 3 years fouling does not show performance decays and a minimum cycle of 4 years is considered. Table 3 shows the designs resulting for 4, 5, 6, 8 and 12 years of operation for 1 to 3 maintenance shutdowns. We can see that most of the characteristics are the same. The fan blades angles are within 16° and 16.5°. The general trend is that the blade angle slightly increases

with the length of the operating cycle. Small differences can also be seen in the angle of the A-frame, from 63.8° to 64.3°, which can be due to numerical issues. Most of the units are designed with an apex of 60°, a result that has already been obtained in the literature (Conradie et al.,1998). Furthermore, the bundle of pipes consists of a single line of 75 pipes in all cases. The number of tubes per row is larger compared to typical designs in the literature, around 60 (Pieve and Salvadori, 2011) or 56 for the horizontal design (Manassaldi, 2014). Note that those studies do not consider fouling. A total number of 8 two-side bundles is to be installed to reject the heat during the month of the largest power production capacity, July. The diameter of the pipes is the same in all cases as well as its length, 15 m. However, in the literature shorter tubes are typically installed, 9 m (Kröger, 2004) or 10.9 m (Manassaldi, 2014). The only major difference between the designs for the different operating cycle lengths is given by the tube fines. It increases with the number of years of continuous operation. This can be due to the fact that the longer the operation period the lower the heat transfer coefficients due to the fouling resistance, and larger heat transfer areas are required. As a result of the larger number of fines, the area available increases from 2000 m^2 to 5000 m^2 when the operating period reaches 12 years. The size of the fines also changes with the operating period before cleaning, but there is no clear trend, mostly due to the large number of degrees of freedom. In the literature, the typical number of fines is around 393.7 fines per m (Manassaldi, 2014). The difference between this value and our results is due to the lack of constraints on the projected area of the unit. Aiming at lower pressure drop results in a design that increases the open area in the pipe layout.

Table 3. Major design characteristics of the A frame design for different years of continuous operation.

Variable	Years of operation				
	12	**8**	**6**	**5**	**4**
Air flow (kg/s)	2,641.83	2,641.83	2,641.83	2,641.83	2,641.83
T_{out} (K)	313.00	313.00	313.00	313.00	313.00
Apex. (°)	64.15	63.89	63.87	63.82	64.30
L (m)	15.00	15.00	15.00	15.00	15.00
D_{ext} (m)	0.033	0.033	0.033	0.033	0.034
D_{int} (m)	0.027	0.027	0.027	0.027	0.028
N_t	75	75	75	75	75
N_r	1	1	1	1	1
n_b	16	16	16	16	16

Table 3 (Continued). Major design characteristics of the A frame design for different years of continuous operation.

Variable	Years of operation				
	12	**8**	**6**	**5**	**4**
D_f (m)	0.053	0.053	0.056	0.061	0.044
n_f	64.918	58.963	39.957	19.62	10
Number of fines per tube	974	884	599	294	150
X_t (m)	0.15	0.15	0.15	0.15	0.15
X_l (m)	0.15	0.15	0.15	0.15	0.15
n_{fans}	4	4	4	4	4
Beta (°)	16.54	16.52	16.38	16.24	16.14
Q_{fan} (m^3/s)	557.82	557.82	557.82	557.82	557.82
L_{ts} (m)	6.00	6.00	6.00	6.00	11.12
d_{ts} (m)	0.10	0.10	0.10	0.10	0.10
x_{up} (m)	0.60	0.60	0.60	0.60	0.60
x_{do} (m)	1.50	1.50	1.50	1.50	1.50
A_{ext} (m^2)	5,095.777	4,889.542	4,220.582	3,376.233	2,191.516
Coste vent ($)	1,651,970	1,651,820	1,651,090	1,650,340	1,649,770
Men_{Vent} ($/month)	7,648	7,647	7,644	7,640	7,638
Cost ($)	91,401	89,917	84,827	77,649	65,433
Men_{Aframe} ($/month)	305	300	283	259	218
Cost ener ($/month)	78,190	78,071	77,487	76,897	76,446
Power (W)	9.46E+5	9.44E+05	9.37E+05	9.30E+05	9.25E+05
Z ($/month)	**86,142.60**	**86,018.20**	**85,414.10**	**84,796.00**	**84,302.00**

The comparison between the design under no fouling conditions (Luceño and Martín, 2018) with the results in this work is not a fair one. However, it is interesting to see the changes in the geometric characteristics as a result of fouling. The length of the pipes is larger when fouling is considered, from 13.5 m in case of a clean design to 15 m in case of considering fouling. The number of fines selected for the clean operation corresponds to a value in between those corresponding to 5 and 6 years of operation under fouling conditions, and the apex angle is a little smaller, around 62°. Finally the pitch distances are larger than the one in other designs (Manassaldi et al., 2014; Conradie et al., 1998), to reduce the pressure drop. In general, larger areas will be required when fouling is considered and therefore the changes in the designs are related to that.

III.2.4.3. Operation

For the optimal geometry of the unit obtained for each cycle time, we optimize the operation of the system for minimum power consumption. Therefore, the problem becomes a multi-period MINLP optimization problem. The multiperiod problem for each cycle time takes from 25 min to 30 min depending on its length in an Intel i5 computer running under Windows 10. Thus, it is up to the operation to decide the number of fans used, the outlet air temperature and the flow used per fan. We assume that for a fan to operate, a minimum flow rate of 50 m^3/s is required. 4 and 5 years cycle length can be solved to integral solutions, but longer cycles needed for the continuum solution to be rounded up. We also tried BARON, but reducing the optimality gap below 10% was rather difficult and the solutions obtained were similar to the approximated ones. It is out of the scope of this work to pursue a more accurate solution method. However, it will be an interesting future work.

Fig. 4 shows the results of the comparison of the operation over 4, 5, 6, 8 and 12 years. When no cleaning costs are considered, or if cleaning can be performed during non-operating periods when solar is not included in the energy mix, there is an optimum value of 6 years of operation before cleaning. Beyond 6 years the operating cost increases slightly. However, the cost savings when operating in 6 years cycles compared to operating for 8 years are small. Over 8 years the operation cost slightly increases. Next, the cleaning costs are assumed to be between the energy not produced in January, the month with the lowest power production, and July, the month of the largest power produced. Furthermore a third value, the average production of the facility over a year is assumed too, see Table 2 for the actual values. Note that this does not mean that the plant will stop for an entire month for cleaning. When different costs for cleaning are added, it turns out that longer operating periods are favored. However, for 12 years of operation before cleaning the operating costs increase with or without considering cleaning costs. Thus, we consider that the optimal cycle time is 8 years. The particular fouling building-up profile results in the fact that there are small additional losses of efficiency over 8 years while the number of shutdowns is just one instead of 2 in case 6 years is selected as cycle time and therefore, the operating cycle of 8 years is preferred. However, if a different profile is found, the results may be affected and shorter or longer

cycle times would be selected since a minimum would have been found in the parametric optimization approach.

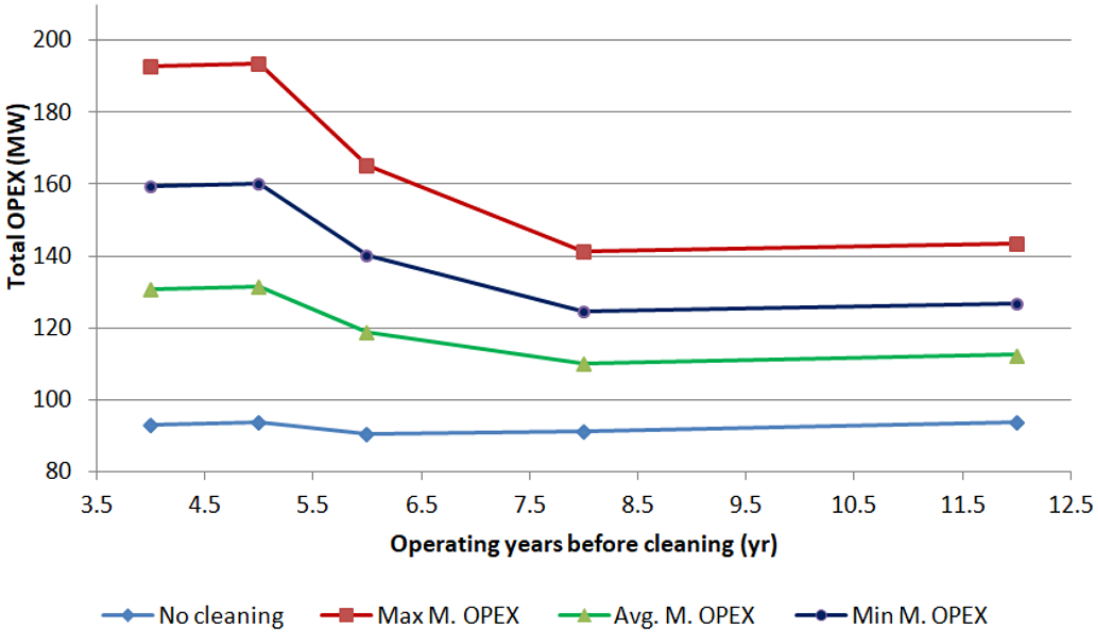

Fig. 4. Operating cost over time under fouling conditions.

Next, we present the results of the operation for cycle lengths of 4, 5, 6 and 8 years. Fig. 5 shows the profile of the global heat transfer coefficient over time. The shorter the cycle, the larger the U. The global heat transfer coefficients are larger for cleaner pipes since deposits have not had the time to build-up. To provide additional transfer area to mitigate the smaller U's when the operating cycle is longer, a larger number of fines are required. If we operate for 8 years, the number of fines is around six times the ones suggested for an operating cycle of 4 years. Fig. 6 shows the increase in the pressure drop due to fouling over time. Note that this increment only affects one of the terms of Eq. (10), and that at most this term only increases up to 25% by the end of the operating cycle. The plateau reached by the pressure drop results in the fact that longer operating times are reasonable to operate. A different profile, linear for instance, would have changed the decision over the operating cycle time since a clear minimum is expected to have appeared.

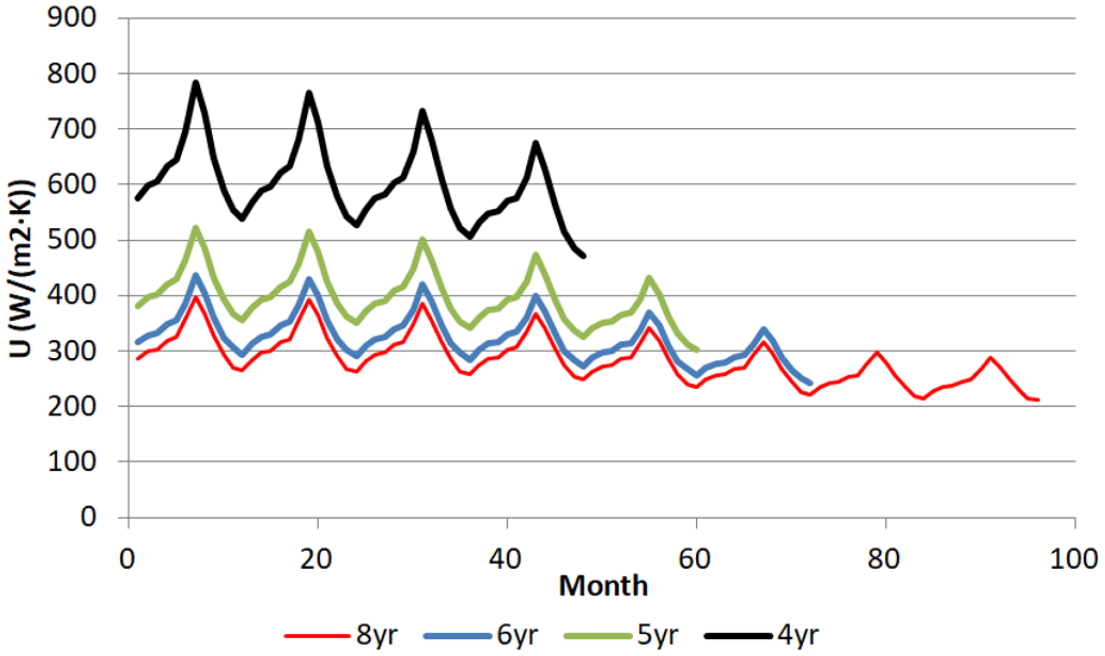

Fig. 5. Profile of the global heat transfer coefficient under fouling conditions.

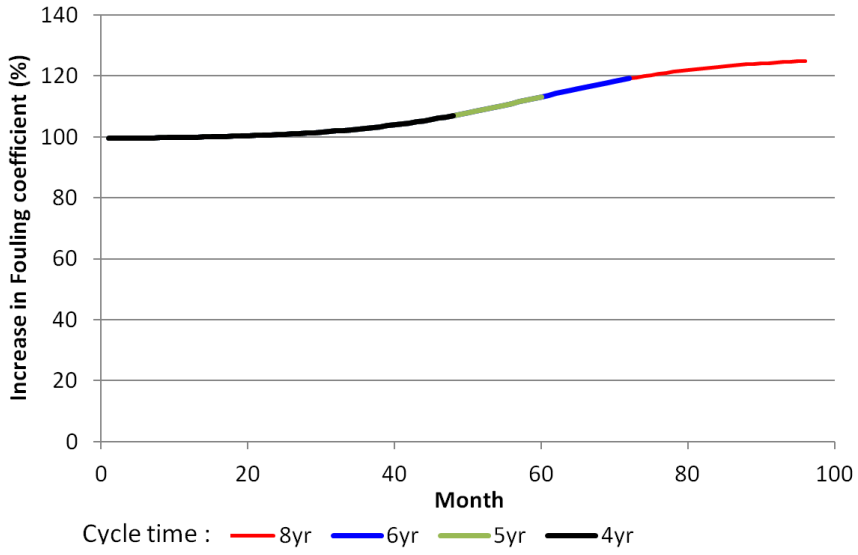

Fig. 6. Profile of the fouling coefficient.

The operating results for the different cycle lengths considered including the effect of fouling on the heat transfer resistance and the pressure drop are presented in Figs. 7–12. Fig. 7 shows the fraction of area used for all four cycle lengths. The area required increases over time. The shorter the cycle, the smaller the increase in the area needed before cleaning. A merely 10% additional area is needed if we operate in a 4 year cycle, but it goes over 20% increase for the optimal case of 8 years of continuum operation. The cycle length is identified easily. By the end of the cycle the maximum area is used, typically

almost the entire area available by design. Furthermore, after cleaning, the area usage is reduced again. Only in the case of 5 years the available area is not fully used.

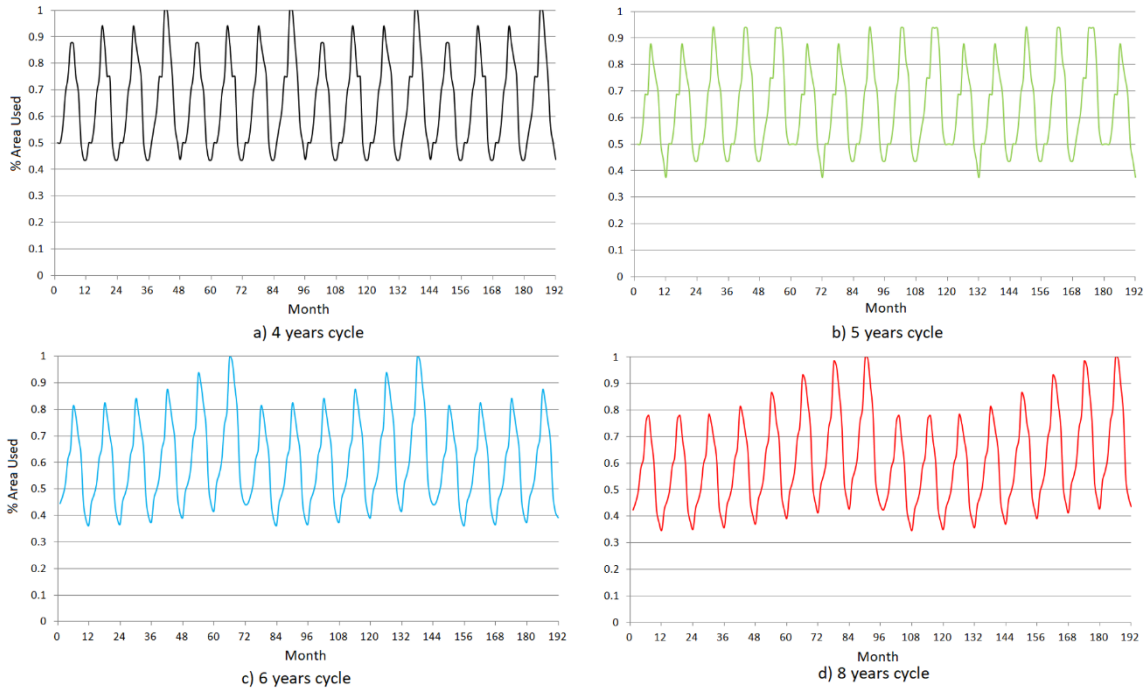

Fig. 7. Fraction of area used over time.

Fig. 8 shows the number of fans in operation over time. We see that as the cycle time before cleaning increases, the usage of the fans increases too. Over summer time, it is necessary to use 3 and 4 fans over longer periods of time due to the increase in the pressure drop and the need to move a larger air flow rate. Just before cleaning the fans capacity is fully used, the peaks of use are wider in Fig. 8. This poses a high stress on the fan system. However, the fans are a more efficiently used for larger operating cycles, otherwise, a large section of the unit remains idle for longer periods of time. Idle units are a burden for the economy of these facilities.

Fig. 9 shows the power production over time. It is not easy to see that the longer the cycle the higher the power consumed due to fouling resistance to the air flow. The reason is the relatively small increase in power consumption due to fouling. To present that effect more clearly, for the optimal solution, 8 years of operation, Fig. 10 compares the power consumed every January over the entire cycle. It shows the effect of building up in the pressure drop and the increase in the power consumed. The increase follows the sigmoid that represents the increase in pressure drop due to fouling.

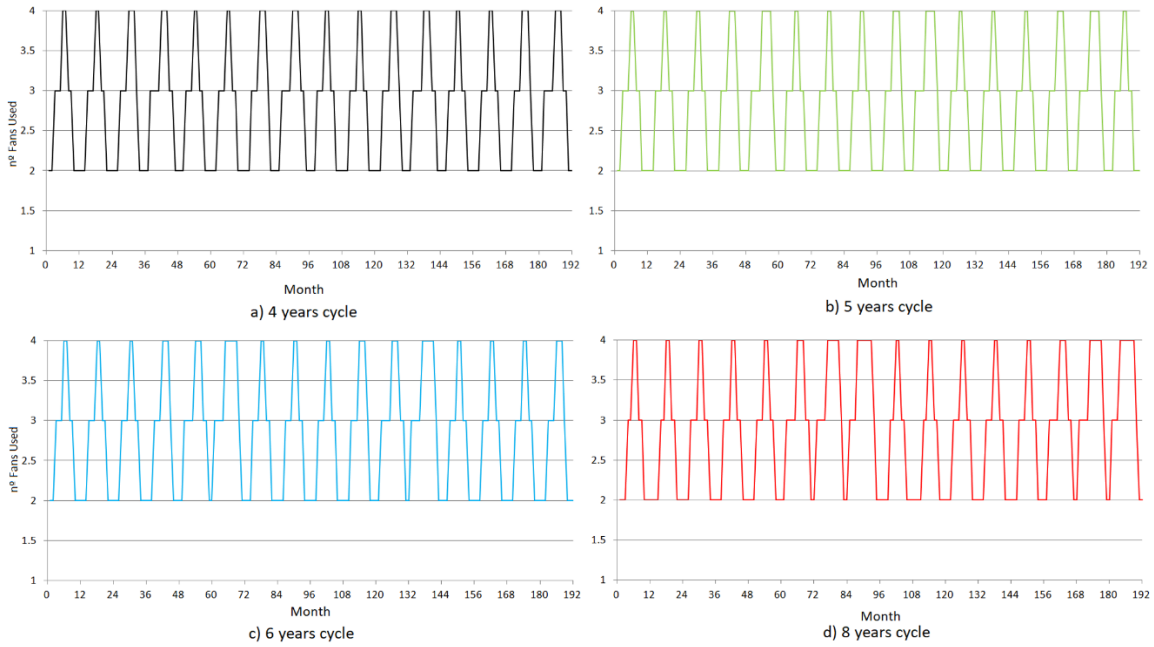

Fig. 8. Number of fans of operation over time.

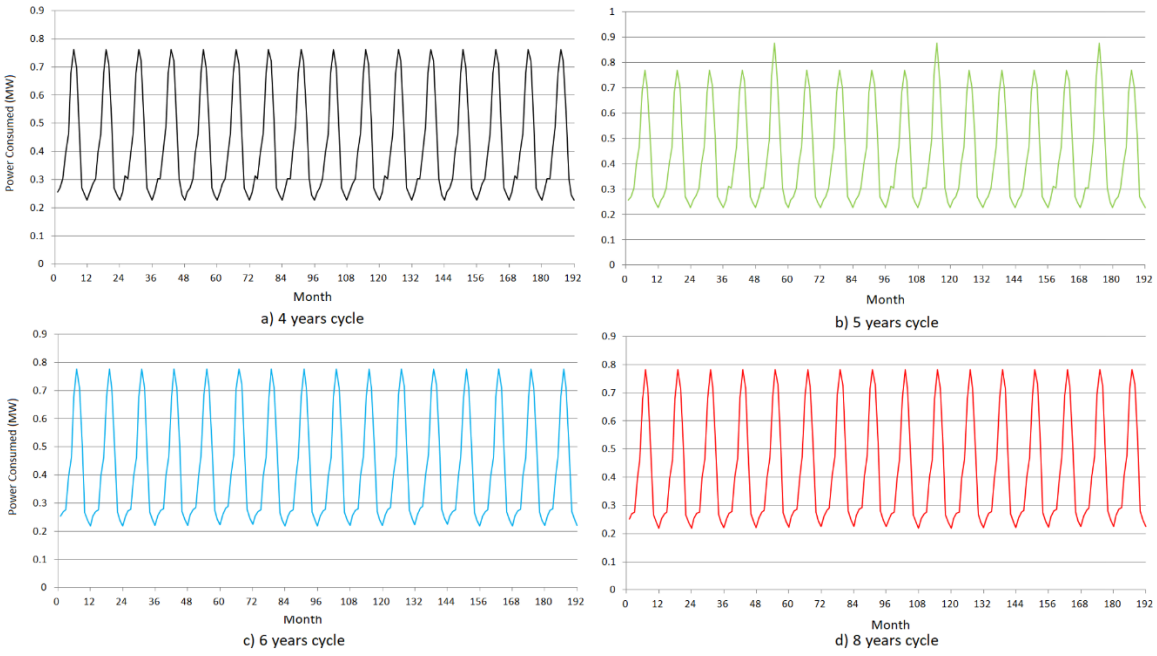

Fig. 9. Power consumption over time.

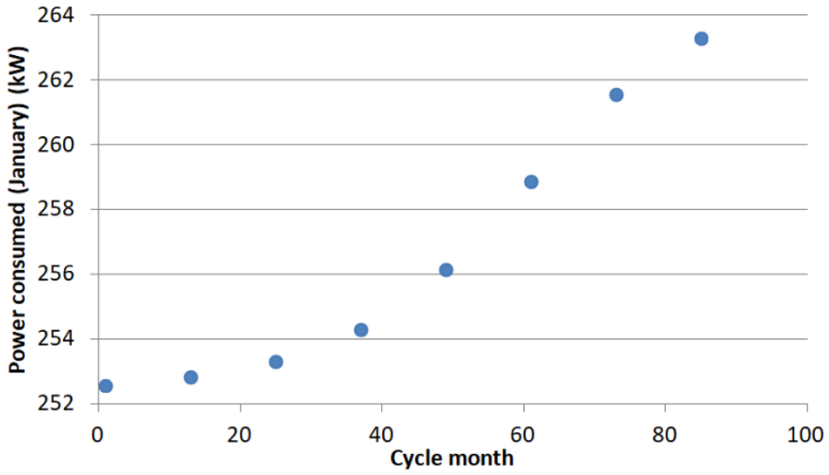

Fig. 10. Increase in power consumption over time for a cycle. 8 years of cleaning cycle.

For the sake of the length of the work we only present the flow rates per fan for the optimal case, an operating cycle of 8 years. Based on the assumption that every year the plant operation is the same, the air flow rate across the system for any particular month is the same over the horizon studied. The particular power curves of the fans suggest the use of a second fan even before the first one reaches it full capacity. In spite of the increase in the pressure drop, typically the operation of the fan is symmetric over time. We cannot ascertain that the differences are not related to numerical issues, see Fig. 11. Four subplots are show (a)–(d) to present a 2 year period for plot for clarity.

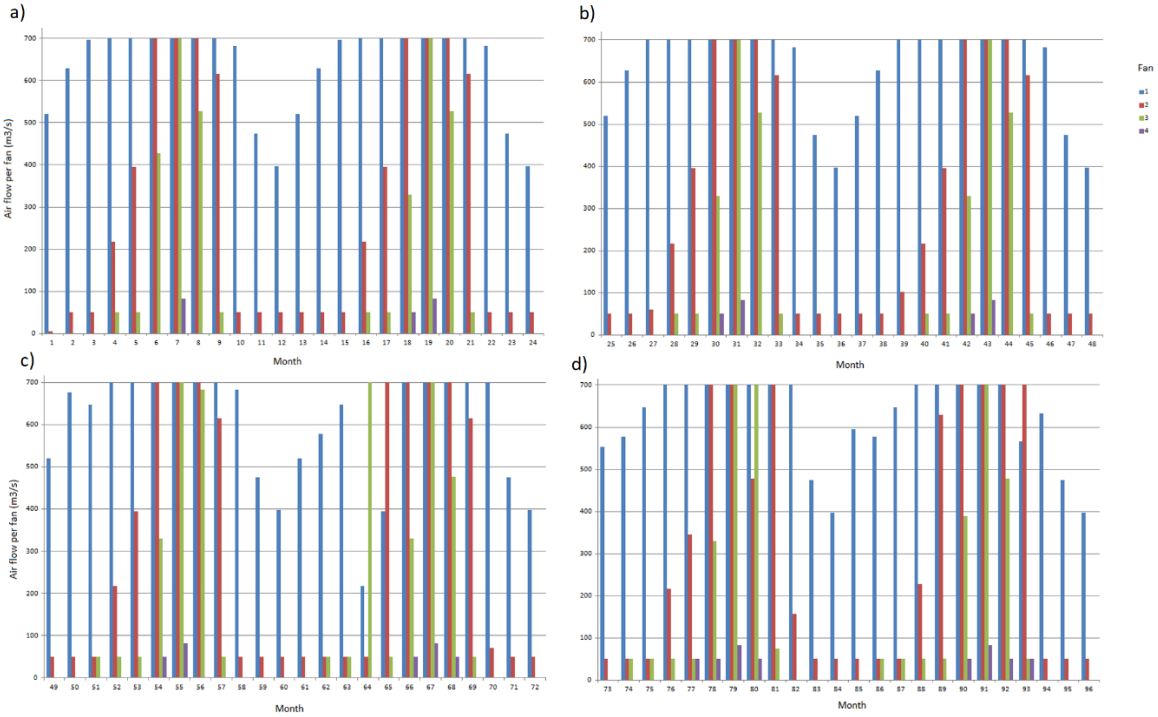

Fig. 11. Air flow across each of the operating fans. 8 years cycle. (a) 0–2 years; (b) 2–4 years; (c) 4–6 years; (d) 6–8 years.

Finally, Fig. 12 shows the percentage of the produced energy used over time to power the fans. A maximum of 3.5% is found using summer periods, but the range is from 2% in winter to 3.5% in July. We see that the power consumed fraction increases slightly over time between cleaning stages, but the increase is not large since, as we saw in Fig. 9, the total power consumption only increases slightly due to fouling.

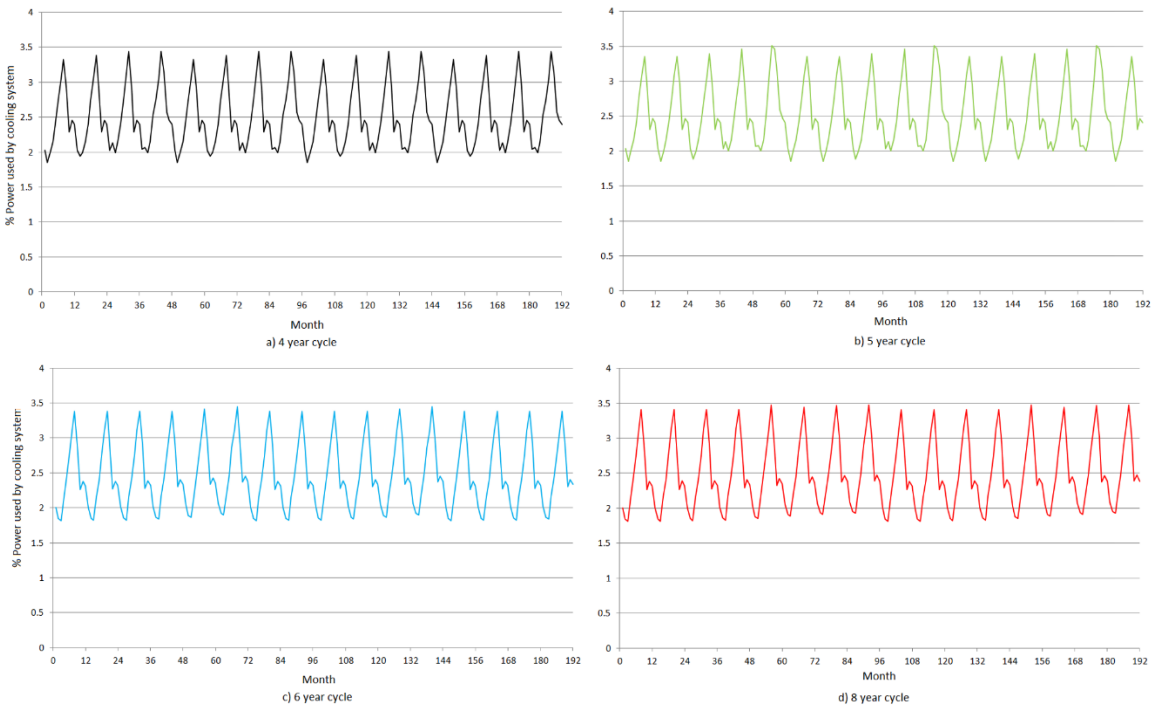

Fig. 12. Fraction of power used by fans.

The operation of solar based facilities shows high dependency with the weather conditions on both the energy source and the cooling devices. So far deterministic designs have been evaluated (Luceño and Martín, 2018) and this work. However, the operation of the system must include solar incidence variability and weather conditions. Future work will focus on addressing uncertainty in the design of air cooling systems and its integration with CSP facilities.

III.2.5. Conclusions

In this work we have presented a parametric optimization framework for the optimal design and operation of units subjected to performance decays over time. We have applied it to the design of A-frame dry cooling systems under fouling conditions. The

model for the A-frame is detailed following the typical design of heat exchangers including pipes layout and size and fans performance. The particular feature is the addition of a model to evaluate the effect of particle deposition on the pipes of the A-frame on both the pressure drop and the resistance to the heat transfer. A two-stage procedure is proposed for the optimal design, and unit operation to evaluate the operating time before cleaning. The unit is designed by solving an MINLP problem including the geometry of the A-frame for the month of the largest cooling load between 3 and half the unit life. We compute the monthly *U* for that configuration in the last year of operation and with that as reference, the *U* for each month of the operating cycle. In a second step, we optimized the monthly operation of the unit by formulating a multi-period MINLP for the various cycle lengths. Cleaning costs are added in terms of power not produced. The solution of this problem indicates not only the optimal cleaning schedule, but also the use of the number of fans, the air flowrate and its inlet and outlet temperature.

The solution suggested an operating cycle of 8 years for the case of a sigmoid profile for dust deposition. The units main characteristics are an apex angle of 63.8°, one row of 75 pipes of 15 m long and with a diameter of 3.3 mm. A total of 4 fans are used but they only operate at full capacity during summer. The number of fans in operation increases for the central months of the years by the end of the cycle time. The optimization allows a reduced power usage to operate the fans, always below 4%, even though this value increases over the operating cycle before the next cleaning stage. For larger cycle lengths the solution is to be approximated from the continuous one due to the size of the model. A more accurate problem reformulation can help solve the problem such as the use of a rolling horizon framework.

III.2.6. Nomenclature

A_{in} : Inside total area, m^2.

A_{out} : Outside total area, m^2.

$Amort_{equipment}$: Amortization of an equipment, $\$_{2014}$/month.

$C_{\$-kWh}$: kWh price, $\$_{2014}$/kWh.

C_{elec} : Energy cost, $\$_{2014}$/month.

$C_{equipment}$: Cost of an equipment, $\$_{2014}$.

C_{fan}: Cost of a fan, $\$_{2014}$.

C_{frame} : Heat exchanger cost, $\$_{2014}$.

$C_{cleaning}$: Cost of a cleaning stage, $\$_{2014}$.

$C_{p_{air}}$: Air heat capacity, kJ/(kg K).

$C_{p_{w,vap}}$: Water steam heat capacity, kJ/(kg K).

D_f : Outer fin diameter, m.

d_{ts} : Width of support beam, m.

$DeLi_{equipment}$: Expected life of an equipment, year.

f : Binary parameter of the fan during the month.

f_j: Resistance to the heat trasnfer in side j, (K m^2 s)/ kJ

Fouling: Increase in the pressure drop due to fouling

H : Humidity of the air, kg/kg.

K_2 : K_2 term of fan cost.

L_t : Pipe length, m.

L_{ts} : Length of support beam, m.

$LMTD$: Logarithm mean temperature difference, K.

m_{air} : Air mass flow, kg/s.

m_{fan} : Air mass flow per fan, kg/s.

m_w : Water vapor mass flow, kg/s.

n_b : Number of bundles working corresponding to the studied fan.

n_f : Number of fins per tube.

n_{fan}: Number of fans.

$n_{cleaning}$ Number of cleaning stages

n_{cycles} Number of operating cycles

N_r : Number of rows per bundle.

N_t : Number of pipes per row.

P_F : Power supplied by a fan on his shaft, kJ/s.

P_{vent} : Total power supplied by fans, kJ/s.

Q : heat flow, kJ/s.

Q_{air} : Total air volume flow, m^3/s.

R: Fouling resistance (K m^2 s)/ kJ

$T_{in,air}$: Inlet air temperature, K.

$T_{out,air}$: Outlet air temperature, K.

t: time (years)

U : Overall heat transfer coefficient, kJ/(K m^2 s).

V_{air} : Air volume flow per fan, m^3/s.

v_{std} : Air volume flow at standard conditions, m^3/s.

x_{do} : Downstream obstacles from the fan, m.

x_{up} : Upstream obstacles from the fan, m.

Greek letters:

γ_{pt} : Fan blade's angle, °.

Δp_e : Total pressure drop across the system unit, Pa.

ΔT_a : Temperature difference at the entrance of the heat exchanger, K.

ΔT_b : Temperature difference at the exit of the heat exchanger, K.

λ_w : Latent heat of evaporation of the water steam, (kJ/kg)

Subscript:

(m) : month.

Superscript:

i : i-th element of the set.

tot : Total monthly value of a variable.

III.2.7. References

Ahn et al., 2006

Y. Ahn, S. Cheong, Y. Jung, J. Lee. **An experimental study of the air-side particulate fouling in fin-and-tube heat exchangers of air conditioners**. International Refrigeration and Air Conditioning Conference. Paper 818 (2006).

Al-Haj Ibrahim, 2012

Al-Haj Ibrahim, H., 2012 Fouling in Heat Exchangers. MATLAB – A Fundamental Tool for Scientific Computing and Engineering Applications – Volume 3.

Beaurepaire et al., 2012

P. Beaurepaire, M.A. Valdebenito, G. Schueller, H.A. Jensen. **Reliability –based optimization of maintenance scheduling of mechanical components under fatigue**. Compt. Methods. Appl. Mech Eng., 1 (221–222) (2012), pp. 24-40.

Bell et al., 2009

IH. Bell, E.A. Groll, H. Koning, T. Odrich. **Experimental analysis of the effects of particulate fouling on heat exchanger heat transfer and air side pressure drop for a hybrid dry cooler**. Proc. Int. Conf. Heat Exchanger Fouling and Cleaning. 2009, Austria (2009).

Bredell and Kröger, 2006

J.R. Bredell, D.G. Kröger. **Numerical Investigation of Fan Performance in a Forced Draft Air-Cooled Steam Condenser**. California Energy Commission, California (2006).

Chen, 1987

J.J. Chen. **Letter to the editor: Comments on improvement on a replacement for the logarithmic mean**. Chem. Eng. Sci., 42 (1987), pp. 2488-2489.

Coker, 2007

A.K. Coker. **Ludwig's Applied Process Design for Chemical and Petrochemical Plants.** (4th ed.), Elsevier, Oxford (2007).

Conradie et al., 1998

A.E. Conradie, J.D. Buys, D.G. Kroger. **Performance optimization of dry-cooling systems for power plants through sqp methods**. Appl. Therm. Eng., 18 (1–2) (1998), pp. 25-45.

Damaso and García, 2009

V.C. Damaso, P.A.A. García. **Testing and preventive maintenance scheduling optimization for aging systems modeled by generalized renewal process**. Pesquisa Oper., 29 (3) (2009), pp. 563-576.

Dekker, 1996

R. Dekker. **Application of maintenance optimization models: a review and analysis**. Rel. Eng. Sys. Saf., 51 (1996), pp. 229-240.

Díaz-Bejarano et al., 2017

E. Díaz-Bejarano, F. Coletti, S. Macchietto. **Thermo-hydraulic analysis of refinery heat exchangers undergoing fouling**. AIChE J., 63 (3) (2017), pp. 984-1001.

DOE, 2018

DOE. https://energy.gov/under-secretary-science-and-energy/downloads/water-energy-nexus-challenges-and-opportunities (2018). Last accessed January 2018.

FAO 2018

FAO. http://www.fao.org/energy/water-food-energy-nexus/en/ (2018). [last accessed February 2018]

GEA 2008

GEA 2008. Industrial air-cooled heat exchangers, and the effects of air side fouling 207-211.

Haghighi-Khoshkhoo and McCluskey, 2007

R. Haghighi-Khoshkhoo, F.M.J. McCluskey. **Air-side fouling of compact heat exchangers for discrete particle size ranges**. Heat Transf. Eng., 28 (1) (2007), pp. 58-64.

Heyns, 2008

J.A. Heyns. **Performance Characteristics of an Air-Cooled Steam Condenser Incorporating a Hybrid (Dry/Wet) Dephlegmator**. M.Sc. Thesis. University of Stellenbosch, Stellenbosch, South Africa (2008).

Kern and Seaton, 1959

D.Q. Kern, R.E. Seaton. **A theoretical analysis of thermal surface fouling**. Br. Chem. Eng., 4 (5) (1959), pp. 258-262.

Kijima and Sumita, 1986

M. Kijima, N. Sumita. **A useful generalization of renewal theory: counting process governed by non-negative Markovian increments**. J. Appl. Probab., 23 (1986), pp. 71-88.

Kröger, 2004

D.G. Kröger. Air-Cooled Heat Exchangers and Cooling Towers: Thermal-Flow Performance Evaluation and Design, II, Pennwell, Oklahoma, Tulsa (2004).

Liu et al., 2015

L.L. Liu, J. Fan, P.P. Chen, J. DU, F-L. Yang. **Synthesis of heat exchanger networks considering fouling, ageing and cleaning**. Ind. Eng. Chem. Des, 54 (1) (2015), pp. 296-306.

Luceño and Martín, 2018

J.A. Luceño, M. Martín. **Optimal design and operation of A-frame systems for solar power plants**. in press. Energy (2018).

Luo et al., 2013

X. Luo, C. Xia, L. Sun. **Margin design, online optimization, and control approach to heat exchanger network with bypasses**. Comp. Chem. Eng., 53 (2013), pp. 102-121.

Manassaldi et al., 2014

J.I. Manassaldi, N.J. Scenna, S.F. Mussati. **Optimization mathematical model for the detailed design of air cooled heat exchangers**. Energy, 64 (2014), pp. 734-746.

Martín, 2015

M. Martín. **Optimal annual operation of the dry cooling system of a concentrated solar energy in the South of Spain**. Energy, 84 (2015), pp. 774-782.

Martín and Martín, 2013

L. Martín, M. Martín. **Optimal year-round operation of a concentrated solar energy plant in the South of Europe**. App. Therm. Eng., 59 (2013), pp. 627-633.

Martin and Martín, 2017

M. Martin, M. Martín. **Cooling limitations in power plants: optimal multiperiod design of natural draft cooling towers**. Energy, 135 (2017), pp. 625-636.

Matche 2014

Matche. http://www.matche.com/equipcost/Exchanger.html (2014). [last accessed February 2018]

MPR 2014

MPR, Ministerio de la Presidencia**. Ley 24/2014, de 24 de noviembre, del Impuesto sobre Sociedades**. Boletín Oficial del Estado, 288 (2014), pp. 96939-97097. [last accessed February 2016].

Mukerji et al., 1991

R. Mukerji, H.M. Merrill, B.W. Erickson, J.H. Parker, R.E. Friedman. **Power plant maintenance scheduling: optimizing economics and reliability**. IEEE Trans. Power Syst., 6 (2) (1991), pp. 476-483.

Muller-Steinhagen et al., 1988

H Muller-Steinhagen, F Reif, N Epstein, AP Watkinson. **Influence of operating conditions on particulate fouling**. Can. J. Chem. Eng., 66 (1988), pp. 42-50.

Muller-Steinhagen et al., 2005

H. Muller-Steinhagen, M.R. Malayeri, A.P. Watkinson. **Fouling of heat exchanger-new approaches to solve old problem**. Heat Transf. Eng., 26 (2) (2005), pp. 1-4.

Müller-Steinhagen et al., 2011

H. Müller-Steinhagen, M.R. Malayeri, P. Watkinson. **Heat exchanger fouling: mitigation and cleaning strategies**. Heat Trans. Eng., 32 (3–4) (2011), pp. 189-196.

MPR 2014

MPR, Ministerio de la Presidencia. **Ley 24/2014, de 24 de noviembre, del Impuesto sobre Sociedades**. Boletín Oficial del Estado, 288 (2014), pp. 96939-97097. [last accessed February 2016].

Nguyen et al., 2008

D.Q. Nguyen, C. Brammer, M. Bagajewicz. **New tool for the evaluation of the scheduling of preventive maintenance for chemical process plants**. Ind. Eng. Chem Res., 47 (6) (2008), pp. 1910-1924.

Pak et al., 2003

B.C. Pak, B.J. Baek, E.A. Groll. **Impacts of fouling and cleaning on the performance of plate fin and spine fin heat exchangers**. KSME Int. J., 17 (11) (2003), pp. 1801-1811.

Pieve and Salvadori, 2011

M. Pieve, G. Salvadori. **Performance of an air-cooled steam condenser for a waste-to-energy plant over its whole operating range**. Energy Conv. Manag., 52 (2011), pp. 1908-1913.

Pu et al., 2009

H. Pu, G.-l. Ding, X.-K. Ma, H.-T. Hu, Y.F. Gao. **Effects of biofouling on air-side heat transfer and pressure drop for finned tube heat exchangers**. Int. J. Refrig., 32 (5) (2009), pp. 1032-1040.

Rosegrant et al., 2002

M.W. Rosegrant, X. Cai, S.A. Cline. **Global Water Outlook to 2025: Averting an Impending Crisis**. International Food Policy Research Institute, Washington, DC (2002).

Sarfraz and Bach, 2016

O. Sarfraz, C. Bach. **A literature review on heat exchanger air side fouling in heating, ventilation and air conditioning (HVAC) applications**. International Refrigeration and Air Conditioning Conference. Paper 1663 (2016).

Tan and Kramer, 1997

J.S. Tan, M.A. Kramer. **A general framework for preventive maintenance optimization in chemical process operations**. Comput. Chem. Eng., 21 (12) (1997), pp. 1451-1469.

The Engineering Toolbox 2018

The Engineering Toolbox. https://www.engineeringtoolbox.com/fouling-heat-transfer-d_1661.html (2018). [last accessed February 2018].

Towler and Sinnott, 2008

G. Towler, R. Sinnott. **Chemical Engineering Design**. Elsevier, Oxford. UK (2008).

Walas, 1988

S.M. Walas. **Chemical Process Equipment: Selection and Design**. Butterworth-Heinemann, Boston. USA (1990).

Wang, 2002

H. Wang. **A survey of maintenance policies of deteriorating systems**. Eur. J. Oper. Res., 139 (3) (2002), pp. 469-489.

Yang et al., 2007

L. Yang, J.E. Braun, E.A. Groll. **The impact of evaporator fouling and filtration on the performance of packaged air conditioners**. Int. J. Refrig., 30 (3) (2007), pp. 506-514.

Zammit, 2005

K. Zammit. **Air-Cooled Condenser Design, Specification, and Operation Guidelines**. Electric Power Research Institute, California, Palo Alto (2005).

III.2.8. Supplementary Material

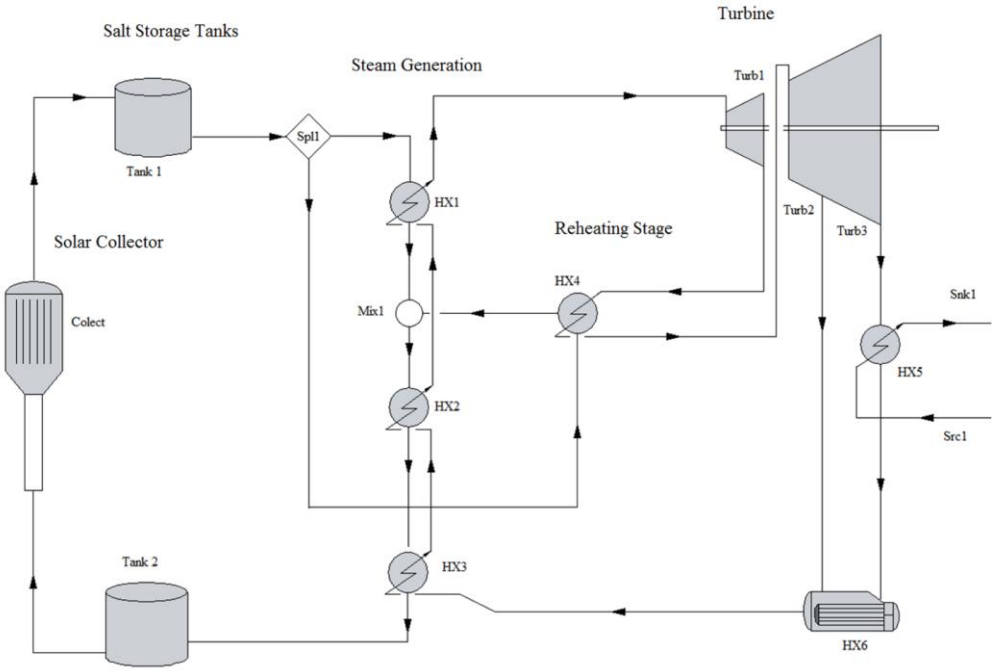

Figure S1. Scheme of the CSP flowsheet.

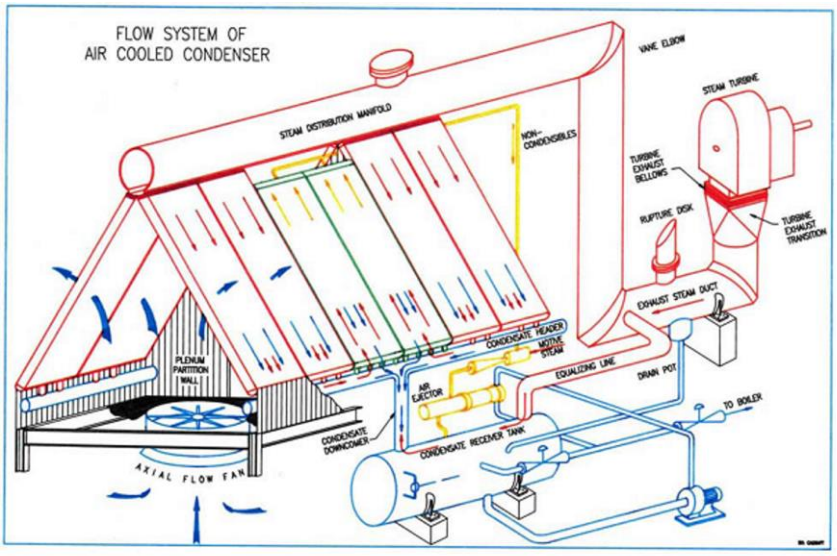

Figure S2. Scheme of an A-frame.

III.2.8.1.-A-frame design

III.2.8.1.1.-Heat exchanger design

The general design equation of any heat exchanger is eq. (S1):

$$Q = U \cdot A_{out} \cdot LMTD \tag{S1}$$

This equation has three terms that must be analyzed separately: the logarithmic mean temperature difference LMTD, the outside contact area A_{out}, and the global heat transfer coefficient U.

-The logarithmic mean temperature difference LMTD is calculated using eq. (S2):

$$LMTD = \frac{\left(\Delta T_a - \Delta T_b\right)}{ln\left(\Delta T_a / \Delta T_b\right)} \tag{S2}$$

However, eq. (S2) is a complex mathematical expression that is typically approximated using Chen approximation within optimization formulations to avoid numerical issues Chen (1987), eq. (S3):

$$LMTD \approx \left[\Delta T_a \cdot \Delta T_b \cdot \frac{\left(\Delta T_a + \Delta T_b\right)}{2}\right]^{1/3} \tag{S3}$$

The temperature's increments ΔT_a and ΔT_b are calculated using eqs. (S4)-(S5) where T_v is the steam temperature and $T_{in,air}$ and $T_{out,air}$ the air inlet and outlet temperature:

$$\Delta T_a = T_v - T_{in,air} \tag{S4}$$

$$\Delta T_b = T_v - T_{out,air} \tag{S5}$$

-The external contact area of the heat exchanger A_{out} is the area exposed to the heat flow and it is given by the number of pipes per row and bundle, N_t and N_r, and the number of bundles, N_b, eq. (S6).

$$A_{out} = N_b \cdot N_t \cdot N_r \cdot A_{out,pipe} \tag{S6}$$

-**The global heat transfer coefficient** referred to A_{out}, U, can be computed using the equation presented by Pieve and Salvadori (2011). This equation considers the resistances to heat transfer related to steam condensation and the convective heat transfer on the air side; we include also a term that considers the heat transfer resistance due to the conduction heat across the pipes wall. Thus, U is computed as eq. (S7):

$$\frac{1}{U} = \frac{A_{out}}{\eta_0 \cdot h_{air} \cdot A_{out}} + \frac{e \cdot A_{out}}{k_{mat} \cdot A_k} + \frac{A_{out}}{h_c \cdot A_{in}} \tag{S7}$$

We need to compute a large number of variables with remarkable mathematical complexity. The external area efficiency, η_0, is given by the eq. (S8), Pieve and Salvadori (2011):

$$\eta_0 = 1 - \frac{A_{tf}}{A_{out}}\left(1 - \eta_f\right) \tag{S8}$$

where A_{tf} is defined with the eq. (S9):

$$A_{tf} = A_f \cdot N_t \cdot N_r \cdot N_b \tag{S9}$$

where N_t, N_r and N_b are the number of pipes, the number of rows and the number of bundles respectively. The total fins area, A_f, is computed using the outer fin area $A_{out,fin}$ and eqs. (S10) and (S11):

$$A_{out,fin} = \pi \cdot D_f \cdot t_f + \frac{\pi}{2} \cdot \left(D_f^2 - D_{out}^2 \right) \quad \text{(S10)}$$

$$A_f = n_f \cdot A_{out,fin} \quad \text{(S11)}$$

The fins efficiency is given by eq. (S12), Pieve and Salvadori (2011):

$$\eta_f = \frac{tanh\left(m\varphi\right)}{m\varphi} \quad \text{(S12)}$$

where m and φ are calculated using eqs. (S13) and (S14) respectively, Pieve and Salvadori (2011)., as a function of the pipe geometry, lay out (D_f, D_{out} and t_f) and material (k_f) and the heat transfer coefficient, h_{air}:

$$m = \left(\frac{2 \cdot h_{air}}{k_f \cdot t_f} \right)^{1/2} \quad \text{(S13)}$$

$$\varphi = 0.5 \cdot \left[D_f - D_{out} + t_f \right] \cdot \left(\frac{D_f}{D_{out}} \right)^{\exp\left[0.065 \cdot m \cdot \left(D_f - D_{out} + t_f\right) - 1.3863\right]} \quad \text{(S14)}$$

The *air side coefficient*, h_{air}, is calculated using the air Nusselt number. The Nusselt number is defined as presented by Heyns (2008) by eq. (S15):

$$Nu = \frac{h_{air} \cdot D_{eq}}{k_{air}} \quad \text{(S15)}$$

We use Pieve and Salvadori's equation to include the effect of the geometry of the pipes and its lay out (D_f, D_{out} , p_f and t_f) on Nu , eq. (S16), Pieve and Salvadori (2011):

$$Nu = 0.134 \cdot \mathrm{Re}^{0.681} \cdot \mathrm{Pr}^{1/3} \cdot \left(\frac{p_f - t_f}{0.5 \cdot \left(D_f - D_{out}\right)} \right)^{0.2} \cdot \left(\frac{p_f - t_f}{t_f} \right)^{0.11} \quad \text{(S16)}$$

where Reynolds and Prandtl numbers are computed as per eqs. (S17) and (S18), Pieve and Salvadori (2011):

$$\mathrm{Re} = \frac{\Gamma \cdot D_{eq}}{\mu_{air}} \quad \text{(S17)}$$

$$\mathrm{Pr} = \frac{\mu_{air} \cdot C_{p_{air}}}{k_{air}} \tag{S18}$$

Variable Γ is the airflow across the minimum flow area and the rest are air properties and the equivalent diameter, D_{eq}, for flow purposes. The minimum flow area is computed using eq. (S19), Pieve and Salvadori (2011):

$$S_{\min-t} = \left[X_t - D_{out} - \frac{t_f}{p_f} \cdot \left(D_f - D_{out} \right) \right] \cdot L_t \cdot N_t \tag{S19}$$

Equation (S19) can be used only if equation (S20) is satisfied:

$$\frac{X_l}{D_{out}} > 0.5 \sqrt{1 + \frac{2X_t}{D_{out}}} \tag{S20}$$

However, in our case, the equation (S20) is always satisfied because we use a pipe isosceles triangle layout, see Figure 3, $X_t = X_l \geq D_{out}$; Thus, eq. (S16) can be used without formulating a disjunction.

The *steam side film coefficient, h_c,* is computed using eq. (S21), as suggested by Heyns (2008):

$$h_c = 0.9245 \cdot \left\{ \frac{L_t \cdot \rho_c^2 \cdot k_c^3 \cdot g \cdot \cos(90 - \theta) \cdot \lambda_w}{\mu_c \cdot m_{at} \cdot C_{p_{air}} \cdot \left(T_v - T_{in,air} \right) \cdot \left(1 - \exp\left[-U_c H_t L_t / \left(m_{at} \cdot C_{p_{air}} \right) \right] \right)} \right\}^{0.25} \tag{S21}$$

where m_{at} and $U_c H_t L_t$ can be computed as per eqs. (S22) and (S23) respectively (Chen et al 2016):

$$m_{at} = \frac{m_{air}}{2 \cdot N_t \cdot N_b} \tag{S22}$$

$$U_c H_t L_t = \frac{h_{ae} A_a}{2 \cdot N_t \cdot N_b} \tag{S23}$$

The $h_{ae} A_a$ term can be computed as follows, eq. (24) (Heyns, 2008):

$$h_{ae} A_a = k_{air} \cdot \mathrm{Pr}^{0.33} \cdot N_b \cdot A_{fr} \cdot Ny \tag{S24}$$

where Ny is computed using eq. (S25), Heyns, (2008):

$$Ny = 366.007945 \cdot Ry^{0.433256} \tag{S25}$$

and Ry by eq. (S26), Heyns, (2008):

$$Ry = \frac{m_{air}}{\mu_{air} \cdot N_b \cdot A_{fr}} \tag{S26}$$

Finally, the *material resistance to the heat transfer* depends on the thermal conductivity of the pipe, k_{mat}. It is estimated as an average for the range of working temperature ranges (Towler and Sinnot, 2008) so that a value of k_{mat} equal to $45 \cdot 10^{-3}$ kJ/(K m^2/m s) is used.

The mean area A_k is computed using eq. (S27):

$$A_k = \frac{\left(A_{out} - A_{in}\right)}{\ln\left(\frac{A_{out}}{A_{in}}\right)} \tag{S27}$$

where A_{in} and A_{out} are calculated as in eqs. (S6) and (S28):

$$A_{in} = N_b \cdot N_t \cdot N_r \cdot A_{in,pipe} \tag{S28}$$

III.2.8.1.2.-Pipes design for area availability

The pipes are the units that provide the contact area for heat transfer. For an enhanced area, these pipes present fins. The design variables and geometry of pipes are plotted in Figure S3.

The inside area of a pipe $A_{in,pipe}$ is the area of a cylinder of diameter D_{in} and length L_t. Thus, the area is given as presented in eq. (S29):

$$A_{in,pipe} = \pi \cdot L_t \cdot D_{in} \tag{S29}$$

The outside area of a pipe is the sum of fins area A_f and the smooth tube area A_{smooth}, and can be calculated as eq. (S30):

$$A_{out,pipe} = A_f + A_{smooth} \tag{S30}$$

Where the smooth area is computed by eq. (S31) with is the number of fins per tube length n_{fins} and the mean fin thickness t_f :

$$A_{smooth} = 2 \cdot \pi \cdot \frac{D_{out}}{2} \cdot \left(L_t - t_f \cdot n_f \right) \tag{S31}$$

The type of fins is selected depending on the kind of fluid which flows in contact with the fins. In the case of the air, a fluid with a small film coefficient and flowing under atmospheric pressure, it is common to employ cross fins (Kern, 1999).

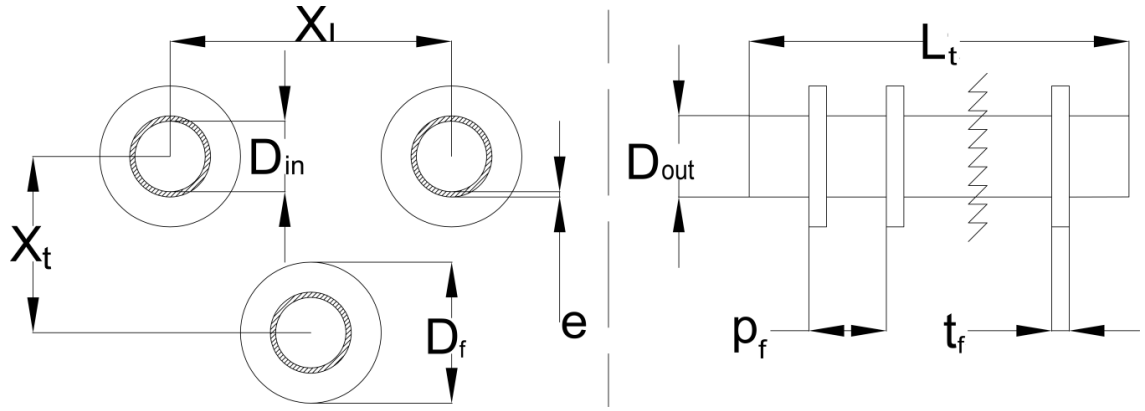

Figure S3. Geometry of pipes.

III.2.8.2.-Fans design

A fan is designed so that it generates enough power to overcome the pressure drop across the structure, namely, bundles of tubes, the fan itself and the base of the unit. Thus, to model a fan a detailed characterization is required due to aerodynamic effects of the blade geometry, size, etc. However, such information is not typically available. Therefore, for this formulation we rely on a particular fan whose charactersitic curves can be found in the literature (Bredell and Kriger, 2006). This section is divided in two parts: the development of a correlation to predict the power generated by the fan as a function of the flow rate, and the models for all the contributions to the pressure drop.

III.2.8.2.1.-Power per fan

The power required by the fan is that needed to overcome the pressure drop, and can be obtained from eq. (S32):

$$P_{vent} = n_{fan} \cdot P_F = Q_{air} \cdot \Delta p_e \qquad \text{(S32)}$$

The power per fan depends on the geometry of the blade. For our case, Figure S4 shows the profile for three blades angles, 14º-18º, due to the lack of further information (Bredell and Kriger, 2006).

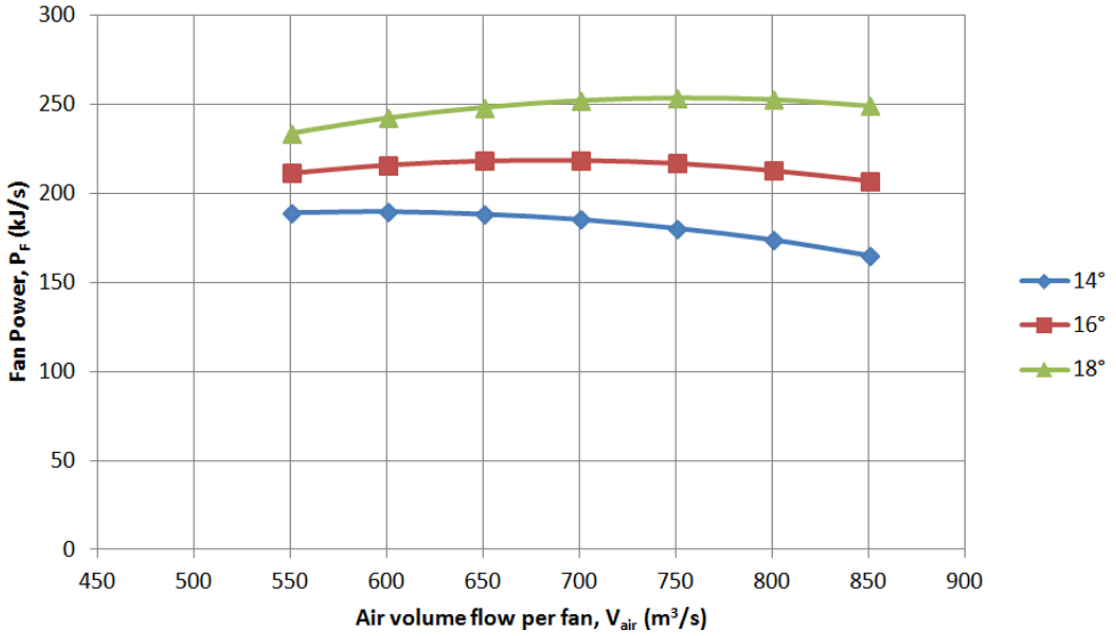

Figure S4. Experimental data for the fan power.

However, sometimes the fan may operate below this range of flowrates. Based on typical power curves in the literature, we fit the profiles in Figure S4, using a second order polynomial assuming that there is no power consumed for no air flow rate. There is typically a base consumption, but we will later limit the minimun flowrate for a fan to operate to avoid very small flows, and we will sum an additional base consumption if the fan is working. In order to capture the effect of the blade angle and that of the air flow within the model, we correlate the fan power vs the air flow in the form given by eq. (S33)

$$\left(P_F\right)_n = \alpha_n \cdot V_a^{\,2} + \beta_n \cdot V_a + \varepsilon_n \qquad \text{(S33)}$$

where the coefficients α_n, β_n and ε_n are a function of flowrate for each blade angle as seen in Table S1. Next, we look for a correlation between their values and the blade angle, see eq. (S34). It turns out that a linear relation between coefficients α_n and β_n and the angle fits the results. Table S2 shows the parameters:

$$\alpha_n = p_\alpha \cdot \gamma_{bt} + m_\alpha$$
$$\beta_n = p_\beta \cdot \gamma_{bt} + m_\beta \quad \text{(S34)}$$

Table S1. Effect of the blade angle on the power curve

Angle γ_{bt}	α_n	β_n	ε_n
14	-4,9362.10^{-4}	6,1246.10^{-1}	0
16	-4,6668.10^{-4}	6,3963.10^{-1}	0
18	-4,4113.10^{-4}	6,6852.10^{-1}	0

Table S2. Coefficients for the effect of the angle on the second order polynomial fitting of the power curve

Coefficient	p	m
α_n	1.3122·10^{-5}	-6.7710·10^{-4}
β_n	1.4015·10^{-2}	4.1596·10^{-1}
ε_n	0	0

Thus, by substituting eq. (S34) into eq. (S33), the expression for P_F becomes eq. (S35):

$$P_F = \left(1.3122 \cdot 10^{-5} \cdot \gamma_{pt} - 6.7710 \cdot 10^{-4}\right) \cdot V_{air}^2 + \left(1.4015 \cdot 10^{-2} \cdot \gamma_{pt} + 4.1596 \cdot 10^{-1}\right) \cdot V_{air} \quad \text{(S35)}$$

The number of fans is computed as follows, eq. (S36):

$$Q_{air} = n_{fan} \cdot V_{air} \quad \text{(S36)}$$

III.2.8.2.2.-Pressure drop

The pressure drop across the system is the one responsible for the energy consumed by the fans. To compute it, we need to account for the different contributions such as the pressure drop at the entrance of the structure, before and after the fan and finally through the tubes bundles, apart from the pressure drop across the fan itself, see eq. (S37) (Owen, 2010):

$$\Delta p_e = -\left[\begin{array}{l} \dfrac{K_{ts}}{2\cdot\rho_{a56}}\left(\dfrac{m_{air}}{N_b\cdot A_{fr}}\right)^2+\dfrac{K_{up}}{2\cdot\rho_{a3}}\left(\dfrac{m_{air}}{A_e}\right)^2 \\ -\Delta p_{Fs}+\dfrac{K_{do}}{2\cdot\rho_{a3}}\left(\dfrac{m_{air}}{A_e}\right)^2+\dfrac{K_{\theta t}}{2\cdot\rho_{a56}}\left(\dfrac{m_{air}}{N_b\cdot A_{fr}}\right)^2 \end{array}\right] \quad \text{(S37)}$$

We are going to model each of the contributions in eq. (S37) starting by the fan static pressure.

-The fan static pressure, Δp_{Fs}, is a function of the flow rate and the blade angle, see Figure S5 developed from the data in Bredell and Kröger (2004). In order to formulate a one equation model to account for both variables, blade angle and air flow rate, we follow the same procedure as before. We look for the mathematical expression, eq. (S38), that models all angles and evalute the effect of the angles on the coefficients of the master correlation.

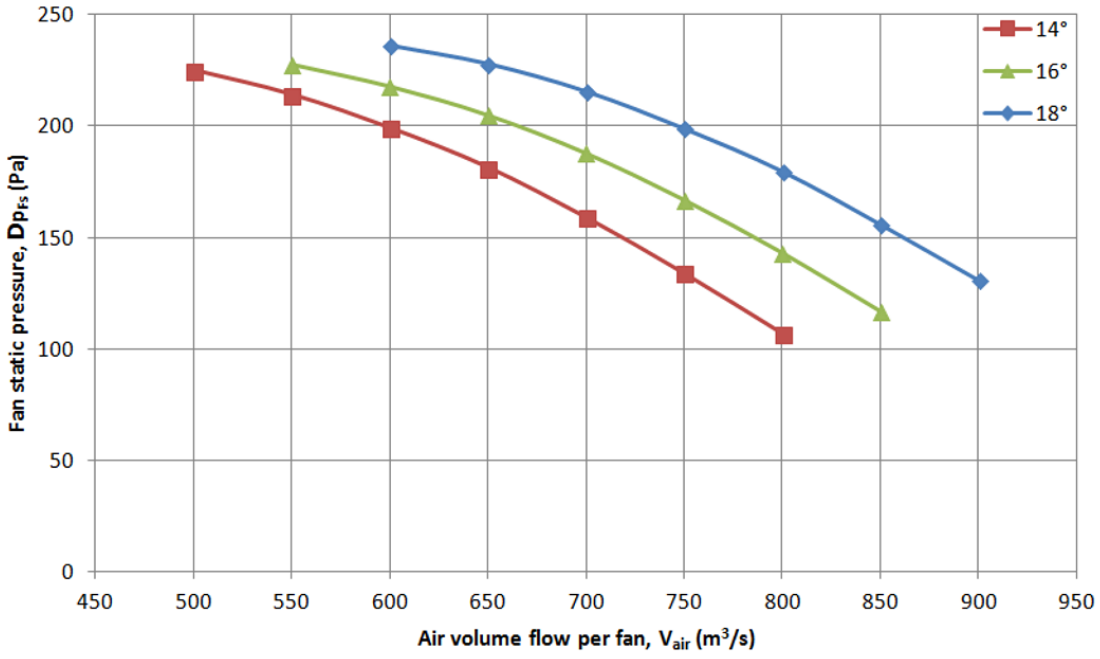

Figure S5. Experimental fan static pressure.

$$\left(\Delta p_{Fs}\right)_n = \alpha_n\cdot V_a^2+\beta_n\cdot\gamma_{pt}+\varepsilon_n \quad \text{(S38)}$$

Again, it turns out that a linear regression, eq. (S39), fits the effect of the angle on coefficients α, β and ε of eq. (S38). Only data for 14°-18° are available in the literature

to develop this model. Table S3 shows the fitting coefficients of eq. (S38) and Table S4 those of eq. (S39):

$$y = p \cdot \gamma_{pt} + m \tag{S39}$$

The extended fitting is provided by eq. (S40):

$$\begin{aligned}\Delta p_{Fs} = &\left(-7.2725\cdot10^{-6}\cdot\gamma_{pt} - 5.6650\cdot10^{-4}\right)\cdot V_{air}^2 \\ &+\left(5.4643\cdot10^{-2}\cdot\gamma_{pt} - 2.9130\cdot10^{-1}\right)\cdot V_{air} \\ &+\left(-2.0706\cdot10^{1}\cdot\gamma_{pt} + 4.4524\cdot10^{2}\right)\end{aligned} \tag{S40}$$

Table S3. Coefficients of the second order polynomial for static pressure drop

Blade angle γ_{pt}	α	β	ε
14	$-6.6721\cdot10^{-4}$	$4.7129\cdot10^{-1}$	$1.5645\cdot10^{2}$
16	$-6.8507\cdot10^{-4}$	$5.8780\cdot10^{-1}$	$1.1178\cdot10^{2}$
18	$-6.9630\cdot10^{-4}$	$6.8986\cdot10^{-1}$	$7.3628\cdot10^{1}$

Table S4. Coefficients for the effect of the blades on the static pressure drop

Coefficient	p	m
α	$-7.2725\cdot10^{-6}$	$-5.6650\cdot10^{-4}$
β	$5.4643\cdot10^{-2}$	$-2.9130\cdot10^{-1}$
ε	$-2.0706\cdot10^{1}$	$4.4524\cdot10^{2}$

-Coefficient K_{ts} represents the pressure drop across fan's support platform, and it is computed using eq. (S41) (Kroger, 2004):

$$K_{ts} = \frac{C_{Dts} L_{ts} d_{ts} n_{ts}}{A_2} \tag{S41}$$

The value of C_{Dts} depends on the support beam geometry and the Reynolds number. In this study, it is assumed to be 1.9 (Daugherty et al 1977). The area A_2 is not well defined because the orientation of the equipment is unknown, thus it is assumed that it corresponds to the rectangular frontal area of the support, eq. (S42):

$$A_2 = 2 \cdot \sin(\theta) \cdot L_{ts} \cdot L_t \tag{S42}$$

The contribution of the support platform to the pressure drop is corrected by the frontal flow area of an A-frame. It is defined as the area without obstacles in each row of tubes. This area can be calculated using eq. (S43):

$$A_{fr} = \left[N_t \cdot \left(n_f \cdot t_f\right) \cdot \left(X_t - D_f\right) + N_t \cdot \left(X_t - D_{out}\right) \cdot \left(L_t - n_f \cdot t_f\right)\right] \cdot \sin(\theta) \quad \text{(S43)}$$

-Coefficient K_{up} corresponds to the pressure drop across the obstacles before the fan, such as a protector screen. The value of K_{up} is presented in the literature in the form of figures (Kroger, 2004). We follow the same two stage procedure to develop a one equation model as a function of the two ratios of variables involved, namely $A_{ob,up}/A_c$ and x_{up}/d_c. The general expression for K_{up} is given by eq. (S44). Table S5 collects the coefficients for various x_{up}/d_c ratios. In this case, the effect of the second variable on the coefficients of eq. (S44) is not linear but is given by eq. (S45).

$$K_{up} = \alpha_n \cdot \left(\frac{A_{ob,up}}{A_c}\right)^2 + \beta_n \cdot \left(\frac{A_{ob,up}}{A_c}\right) + \gamma_n \quad \text{(S44)}$$

$$\alpha_n = p_\alpha \cdot \left(\frac{x_{up}}{d_c}\right)^{m_\alpha}$$
$$\beta_n = p_\beta \cdot \left(\frac{x_{up}}{d_c}\right)^{m_\beta} \quad \text{(S45)}$$

The final expression is as follows, eq. (46):

$$K_{up} = 0.1560 \cdot \left(\frac{x_{up}}{d_c}\right)^{-1.5854} \cdot \left(\frac{A_{ob,up}}{A_c}\right)^2 + 0.0782 \cdot \left(\frac{x_{up}}{d_c}\right)^{-0.9947} \cdot \left(\frac{A_{ob,up}}{A_c}\right) \quad \text{(S46)}$$

Table S5. Coefficients for correlation eq. (S44)

x_{up}/d_c	α	β	γ
0.05	14.7401	1.5868	-0.0001
0.10	6.7789	0.6917	0.0086
0.15	3.9267	0.5045	0.0012
0.20	2.1739	0.4121	-0.0035
0.30	0.9797	0.3280	-0.0059
0.40	0.5746	0.1598	0.0003

Table S6. Coefficients for correlation eq. (S45)

Coefficient	p	m
α	0.1560	-1.5854
β	0.0782	-0.9947

This contribution to the pressure drop is corrected using the free area across the fan, computed using eq. (S47) [34]:

$$A_e = \frac{\pi}{4} \cdot \left(d_c^2 - d_{fh}^2 \right) \tag{S47}$$

-Coefficient *K_{do} corresponds to the pressure drop across the obstacles after the fan*, such as the shaft. The value of K_{do} can be read in the figures presented by Kröger (2004). Similarly to previous coefficients, we developed a one equation model, eq. (S48), that includes the effect of $A_{ob,do}/A_c$ and x_{do}/d_c, whose relations are given by eqs. (S48)-(S49):

$$K_{do} = \alpha_n \cdot \left(\frac{A_{ob,do}}{A_c} \right)^2 + \beta_n \cdot \left(\frac{A_{ob,do}}{A_c} \right) + \gamma_n \tag{S48}$$

$$\begin{aligned} \alpha_n &= p_\alpha \cdot \left(\frac{x_{do}}{d_c} \right) + m_\alpha \\ \beta_n &= p_\beta \cdot \left(\frac{x_{do}}{d_c} \right) + m_\beta \end{aligned} \tag{S49}$$

Table S7 shows the original fitting parameters for eq. (S48) and Table S8 those that include the effect of the x_{do}/d_c ratio into the correlation. Again, it turned out to be a linear relationship as given by eq. (S49). Eq. (S50) shows the final correlation.

$$\begin{aligned} K_{do} = &\left(-75.4268 \cdot \left(\frac{x_{do}}{d_c} \right) + 15.8845 \right) \cdot \left(\frac{A_{ob,do}}{A_c} \right)^2 \\ &+ \left(-18.2098 \cdot \left(\frac{x_{do}}{d_c} \right) + 3.6192 \right) \cdot \left(\frac{A_{ob,do}}{A_c} \right) \end{aligned} \tag{S50}$$

Table S7. Fitting parameters for eq. (S48)

x_{do}/d_c	α	β	γ
0.05	11.7438	2.9460	-0.0090
0.10	9.3812	1.4274	-0.0023
0.15	3.5998	0.9172	0.0062
0.20	1.0998	0.0811	-0.0017

Table S8. Fitting parameters for eq. (S49)

Coefficient	p	m
α_n	-75.4268	15.8845
β_n	-18.2098	3.6192
γ_n	0	0

-Coefficient $K_{\theta t}$ *represents the total pressure drop across the heat exchanger bundle* and includes the kinetic energy losses across the heat exchanger. This coefficient can be calculated using eq. (S51) under isothermal flow conditions (Heyns, 2002; Owen, 2010):

$$K_{\theta t} = K_{he} + \left(\frac{1}{sin(\theta_m)} - 1\right)\left(\frac{1}{sin(\theta_m)} - 1 + 2\sqrt{K_{ci}}\right) + K_{dj} + K_o \quad \text{(S51)}$$

The function $\sin(\theta_m)$ is approximated by a second order polynomial, within the range of typical θ_m (0-90°), to avoid numerical issues. The polynomial obtained is eq. (S52):

$$\sin(\theta_m) = -1.0293 \cdot 10^{-4} \cdot \theta_m^2 + 2.0845 \cdot 10^{-2} \cdot \theta_m - 2.3441 \cdot 10^{-2} \quad \text{(S52)}$$

The heat exchanger's pressure drop coefficient for normal isothermal flow, K_{he}, is defined by Heyns (2002), eq. (S53):

$$K_{he} = 4177.08481 \cdot R_y^{-0.4392686} \quad \text{(S53)}$$

The mean flow incident angle at the heat exchanger inlet, θ_m, is function of the A-frame half apex angle θ (Owen, 2010), eq.(S54):

$$\theta_m = 0.0019 \cdot \theta^2 + 0.9133 \cdot \theta - 3.1558 \quad \text{(S54)}$$

The heat exchanger entrance contraction loss coefficient for normal flow, K_{ci}, is a function of the ratio of the minimum to free stream flow area through the heat exchanger bundle σ and the ratio of the minimum to free stream flow area at the bundle inlet σ_{21} (Owen, 2010). These three variables can be calculated with eq. (S55)-(S58).

$$K_{ci} = \left(\frac{1 - \frac{1}{\sigma_c}}{\sigma} \right)^2 \quad \text{(S55)}$$

$$\sigma_c = 0.6155417 + 0.04566493 \cdot \sigma_{21} - 0.336651 \cdot \sigma_{21}^2 + 0.4082743 \cdot \sigma_{21}^3 + 2.672041 \cdot \sigma_{21}^4 - 5.963169 \cdot \sigma_{21}^5 + 3.558944 \cdot \sigma_{21}^6 \quad \text{(S56)}$$

$$\sigma_{21} = \frac{\left[X_l \cdot (N_r - 1) + D_f\right] \cdot \left[X_t \cdot (N_r - 1) + D_f\right] - \frac{\pi}{4} \cdot D_f^2 \cdot N_t \cdot N_r}{\left[X_l \cdot (N_r - 1) + D_f\right] \cdot \left[X_t \cdot (N_r - 1) + D_f\right]} \quad \text{(S57)}$$

$$\sigma = \frac{N_t \cdot (X_t - D_f) \cdot L_t}{N_t \cdot X_t \cdot L_t} \quad \text{(S58)}$$

C*oefficients* K_{dj} *and* K_o represent the kinetic energy loss at the heat exchanger outlet as a result of turbulent decay of the jet of air (Heyns, 2002, Owen, 2010). Figure S6 shows the geometry configuration. Thus, K_{dj} can be computed by eq. (S59) while K_o is computed by eq. (S60).

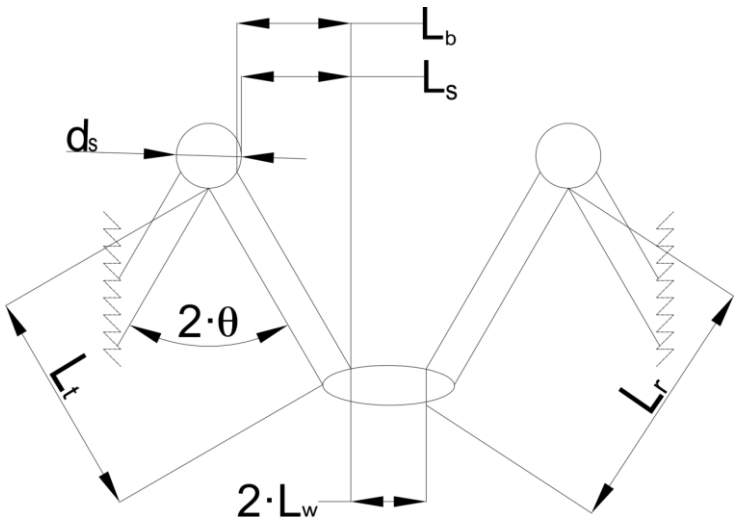

Figure S6. Pipe configuration

$$K_{dj} = \left[\begin{array}{l} \left\{ -2.89188 \cdot \left(\frac{L_w}{L_t} \right) + 2.93291 \cdot \left(\frac{L_w}{L_t} \right)^2 \right\} \cdot \left(\frac{L_t}{L_s} \right) \cdot \left(\frac{L_b}{L_s} \right) \cdot \left(\frac{28}{\theta} \right)^{0.4} + \\ + \left\{ \left(\frac{L_s}{L_b} \right) \cdot \exp\left(2.36987 + 5.8601 \cdot 10^{-2} \cdot \theta - 3.3797 \cdot 10^{-3} \cdot \theta^2 \right) \right\}^{0.5} \cdot \left(\frac{L_t}{L_r} \right) \end{array} \right]^2 \quad \text{(S59)}$$

$$K_o = \left[\begin{array}{l} \left\{ -2.89188 \cdot \left(\frac{L_w}{L_t} \right) + 2.93291 \cdot \left(\frac{L_w}{L_t} \right)^2 \right\} \cdot \left(\frac{L_s}{L_b} \right)^3 + 1.9874 + \\ -3.02783 \cdot \left(\frac{d_s}{2 \cdot L_b} \right) + 2.0187 \cdot \left(\frac{d_s}{2 \cdot L_b} \right)^2 \end{array} \right] \cdot \left(\frac{L_t}{L_s} \right)^2 \quad \text{(S60)}$$

The rest of the geometry features of the A-frame are computed using eqs. (S61)-(S64):

$$N_{Lr} = \frac{L_w}{cos\left(90 - \theta\right)} \quad \text{(S61)}$$

$$L_r = N_{Lr} + L_t \quad \text{(S62)}$$

$$L_b = L_r \cdot cos\left(90 - \theta\right) \quad \text{(S63)}$$

$$L_s = \left(\frac{d_s}{2} + L_r \right) \cdot sin\left(\theta\right) - \frac{d_s}{2} \quad \text{(S64)}$$

Furthermore, the bounds for the size of the fan are as follows, eqs. (S65)-(S67), so that the fan can be allocated below the A-frame:

$$d_c \leq 2 \cdot \sin\left(\theta\right) \cdot L_t \quad \text{(S65)}$$

$$n_{fan} \cdot d_c + Sep_{fan} \cdot \left(n_{fan} - 1\right) \leq X_t \cdot N_t \quad \text{(S66)}$$

$$n_{fan} \cdot \frac{\pi}{4} \cdot d_c^2 + Sep_{fan} \cdot \left(n_{fan} - 1\right) \cdot 2 \cdot \sin\left(\theta\right) \cdot L_t \leq \frac{\pi}{4} \cdot 2 \cdot \sin\left(\theta\right) \cdot L_t \cdot \frac{N_b}{2} X_t \cdot N_t \quad \text{(S67)}$$

The distance of upstream obstacles x_{up} and the distance of downstream obstacles x_{do} have to satisfy the following constraints, eqs. (S68)-(S71) (Kroger, 2004):

$$x_{up} \geq 0.05 \cdot d_c \quad \text{(S68)}$$

$$x_{up} \leq 0.40 \cdot d_c \quad \text{(S69)}$$

$$x_{do} \geq 0.05 \cdot d_c \quad \text{(S70)}$$

$$x_{do} \leq 0.20 \cdot d_c \quad \text{(S71)}$$

III.2.8.3.Ranges for variables and parameters

The ranges for the design variables are defined using the data from the literature. These value ranges are collected in Tables S9-S11 for the pipes, the fan and the structure respectively:

Table S9. Pipes and bundle geometric characteristics (Martín, 2015, Chen et al, 2016; Esen, 2007; Esen et al 2014; Yang et al 2016, Zammit, 2005)

Variable	Type	Symbol	Units	Lower bound	Upper bound
Pipes apex angle	Cont	$2.\theta$	º	45	160
Pipe Length	Cont	L_t	m	4	15
Pipe external diameter	Standard	D_{out}	m	0.03341	0.08
Piper internal diameter	Standard	D_{in}	m	0.02665	0.07324
Pipes per line	Integer	n_t	-	10	75
Lines per bundle	Integer	n_r	-	1	5
Number of bundles	Integer	n_b	-	2	16
Fins diameter	Cont	D_f	m	-	-
Fins per meter	Cont	n_f	-	10	591
Horizontal separation	Cont	X_t	m	0.03341	0.17
Vertical separation	Cont	X_l	m	0.03341	0.17

Table S10. Fan characteristics (Martín, 2015, Chen et al, 2016; Yang et al 2016)

Variable	Type	Symbol	Units	Lower bound	Upper bound
Number of fans	Integer	n_{fan}	-	1	6
Air flow per fan	Cont	Q_{fan}	$m^3/(s)$	0	800
Upstream obstacle distance	Cont	x_{up}	m	0.5	0.6
Downstream obstacle distance	Cont	x_{do}	m	1.2	1.5

Table S11. Support geometry (Manassaldi et al 2014; Conradie et al 1998)

Variable	Type	Symbol	Units	Lower bound	Upper bound
Support structure length	Cont	L_{ts}	m	6	12
Support structure width	Cont	d_{ts}	m	0.1	0.4

Some variables, i.e. fan diameter, are fixed based on data from the literature in order to solve it. However, these values can be replaced by variables if there exists information to build models that correlate them to the power consumption, etc. Some geometric variables are fixed based on typical standard values:

- The fan's specifications are defined by the manufacturer (Bredell and Kroger, 2006). See Table S12.
- Some specifications of the bundles are fixed as seen in Table S13. In this case, we used the following assumptions:
  - The pipe thickness is the standard value to the minimum inner pipe diameter (Perry and Green 2007). This value has to be modified if the diameter takes distant values from the minimum inner diameter.
  - The fin thickness, t_f, is fixed (Martín, 2015).
  - The inner diameter of the steam pipe is fixed according to the maximum annual steam flow, the steam flow of the month July. In this case, the value of d_s is the same as Heyns (2002).
  - According to the small size of the facility of our case study, L_w takes the value of 0, because the tube bundles are distributed in a single street of bundles.

Table S12. Fan characteristics

Variable	Symbol	Value	Units
Shaft diameter	d_{fh}	1.399	m
Shell diameter	d_c	9.145	m
Fan distance	Sep_{Fan}	0.05	m
Efficiency	η_{fan}	60	%
Upstream obstacle area	$A_{ob,up}$	3.354839	m^2
Downstream obstacle area	$A_{ob,do}$	6.991921	m^2

Table S13. Bundle fixed parameters

Variable	Symbol	Value	Units
Pipe thickness	e	0.0015	m
Fin thickness	t_f	0.000375	m
Steam pipe diameter	d_s	1.25	m
Street separation	L_w	0	m

III.2.8.4. Nomenclature

A_2 : Entrance area of support structure, m^2.

A_c : Total projected area of the fan, m^2.

A_e : Effective area across the fan, m^2.

A_f : Total outer fins' area, m^2.

A_{fr} : Total frontal flow area, m^2.

$A_{fr,bundle}$: Frontal flow area of a bundle, m^2.

A_{in} : Inside total area, m^2.

$A_{in,pipe}$: Inside area of a tube, m^2.

A_k : Logarithm mean area, m^2.

$A_{ob,do}$: Projected area of fan's downstream obstacles, m^2.

$A_{ob,up}$: Projected area of fan's upstream obstacles, m^2.

A_{out} : Outside total area, m^2.

$A_{out,fin}$: Outer fin area, m^2.

$A_{out,pipe}$: External total area of a pipe, m^2.

A_{tf} : Total fins area, m^2.

A_{smooth} : Smooth area of a tube, m^2.

$Amort_{equipment}$: Amortization of an equipment, $\$_{2014}$/month.

b_{fan} : Bundles per fan.

$C_{\$-kWh}$: kWh price, $\$_{2014}$/kWh.

C_{Dts} : Drag coefficient of support.

C_{elec} : Energy cost, $\$_{2014}$/month.

$C_{equipment}$: Cost of an equipment, $\$_{2014}$.

C_{fan} : Cost of a fan, $\$_{2014}$.

C_{frame} : Heat exchanger cost, $\$_{2014}$.

C_{H_2O} : CO_2 generated by water, kg/m^3.

$C_{p_{air}}$: Air heat capacity, kJ/(kg K).

$C_{p_{w,vap}}$: Water steam heat capacity, kJ/(kg K).

C_{tower} : Cost of a humidification tower, $\$_{2014}$.

d_c : Inner fan diameter, m.

D_{eq} : Equivalent diameter, m.

D_f : Outer fin diameter, m.

d_{fh} : Diameter of fan shaft, m

D_{in} : Inner pipe diameter, m.

D_{out} : Outer pipe diameter, m.

d_s : Inlet steam duct diameter, m.

d_{ts} : Width of support beam, m.

$DeLi_{equipment}$: Expected life of an equipment, year.

e : Pipe mean thickness, m.

$Eco_{A-frame}$: Avoided CO_2 emissions by an A-frame, $kgCO_2$.

Eco_{tower} : Avoided CO_2 emissions by a humidification tower, $kgCO_2$.

f : Binary parameter of the fan during the month.

g : Gravitational acceleration, m/s^2.

H : Humidity of the air, kg/kg.

h_{air} : Air side coefficient, $kJ/(K\ m^2\ s)$.

h_c : Steam side coefficient, $kJ/(K\ m^2\ s)$.

$h_{ae}A_a$: hA steam term, kJ/(K s).

K_2 : K_2 term of fan cost.

k_{air} : Thermal conductivity of air, $kJ/(K\ m^2/m\ s)$.

k_c : Thermal conductivity of saturated liquid water on steam temperature, $kJ/(K\ m^2/m\ s)$.

K_{ci} : Heat exchanger entrance contraction loss coefficient for normal flow.

K_{dj} : Coefficient of losses due to the turbulent decay of the jet after the bundles.

K_{do} : Pressure drop coefficient of fan's downstream obstacles.

k_f : Thermal conductivity of fin, kJ/(K m^2/m s).

K_{he} : Loss coefficient for normal isothermal flow through the finned-tube bundle

k_{mat} : Thermal conductivity of pipe material, kJ/(K m^2/m s).

K_o : Coefficient of losses during the final mixing process as the flow leaves the A-frame .

K_{ts} : Pressure drop coefficient trough the support platform.

K_{up} : Pressure drop coefficient of fan's upstream obstacles.

$K_{\theta t}$: Total pressure drop coefficient across the heat exchanger bundles.

L_b : Projected total length of pipe, m.

L_r : Total bundle length, m.

L_s : Projected free length of pipe, m.

L_t : Pipe length, m.

L_{ts} : Length of support beam, m.

L_w : Walkway length, m.

$LMTD$: Logarithm mean temperature difference, K.

m : Dimensionless term m.

m_{air} : Air mass flow, kg/s.

m_{at} : Equivalent air mass flow per tube of a pair of rows, kg/s.

m_{fan} : Air mass flow per fan, kg/s.

m_w : Water vapor mass flow, kg/s.

N_b : Number of bundles.

n_b : Number of bundles working corresponding to the studied fan.

n_f : Number of fins per tube.

n_{fan} : Number of fans.

N_r : Number of rows per bundle.

N_t : Number of pipes per row.

n_{ts} : Number of support beams per side.

Nu : Nusselt number.

Ny : Characteristic heat transfer parameter of air, 1/m.

p_f : Separation between the same side of two adjacent fins, m.

P_F : Power supplied by a fan on his shaft, kJ/s.

P_{gen} : Energy produced by the CSP, kJ/s.

P_{vent} : Total power supplied by fans, kJ/s.

Pr : Prantl number.

Q : heat flow, kJ/s.

Q_{air} : Total air volume flow, m^3/s.

Re : Reynolds number.

Ry : Characteristic flow parameter of air, 1/m.

Sep_{fan} : Distance between fans, m.

$S_{\min -t}$: Minimum flow area, m^2.

t_f : Mean fin thickness, m.

$T_{in,air}$: Inlet air temperature, K.

$T_{out,air}$: Outlet air temperature, K.

T_v : Water steam temperature, K.

U : Overall heat transfer coefficient, kJ/(K m^2 s).

$U_c H_t L_t$: UHL steam term, kJ/(K s).

V_{air} : Air volume flow per fan, m^3/s.

v_{std} : Air volume flow at standard conditions, m^3/s.

x_{do} : Downstream obstacles from the fan, m.

X_l : Horizontal tube pitch, m.

x_{up} : Upstream obstacles from the fan, m.

X_t : Vertical tube pitch, m.

Z : Objective function, $\$_{2014}$/month.

$\%_f$: Percentage of energy consumed by fans.

Greek letters:

α_n : Generic alpha-n parameter.

β_n : Generic beta-n parameter.

Γ : Airflow across the minimum flow area, kg/s.

γ_{pt} : Fan blade's angle, º.

Δp_e : Total pressure drop across the system unit, Pa.

Δp_{Fs} : Fan static pressure, Pa.

ΔT_a : Temperature difference at the entrance of the heat exchanger, K.

ΔT_b : Temperature difference at the exit of the heat exchanger, K.

ε_n : Generic epsilon-n parameter.

η_0 : Outside area efficiency.

η_f : Fins' efficiency.

η_{fan} : Fan efficiency.

θ : A-frame apex angle, º.

θ_m : Mean flow incident angle, º.

λ_w : Latent heat of evaporation of the water steam, K.

μ_{air} : Air viscosity, kg/(m s).

μ_c : Saturated liquid water viscosity on steam temperature, kg/(m s).

ρ_{a3} : Mean air density trough the fan, kg/m^3.

ρ_{a56} : Mean air density across the heat exchanger bundles, kg/m^3.

ρ_c : Saturated liquid water density on steam temperature, kg/m^3.

σ : Ratio of the minimum to free stream flow area through the heat exchanger bundle.

σ_{21} : Ratio of the minimum to free stream flow area at the bundle inlet.

σ_c : Ratio of area related with K_{ci} .

φ : Dimensionless term phi.

Subscript:

(m) : month.

Superscript:

i : i-th element of the set.

tot : Total monthly value of a variable.

III.2.8.5. References

Bredell and Kröger, 2006

J.R. Bredell, D.G. Kröger. **Numerical Investigation of Fan Performance in a Forced Draft Air-Cooled Steam Condenser**. California Energy Commission, California (2006).

Chen, 1987

J.J. Chen. **Letter to the editor: Comments on improvement on a replacement for the logarithmic mean**. Chem. Eng. Sci., 42 (1987), pp. 2488-2489.

Conradie et al., 1998

A.E. Conradie, J.D. Buys, D.G. Kroger. **Performance optimization of dry-cooling systems for power plants through sqp methods**. Appl. Therm. Eng., 18 (1–2) (1998), pp. 25-45.

Chen et al., 1987

L Chen, L. Yang, Y. Du Xm Yang. **A novel layout of air cooled condenser to improve thermo flow performances**. Appl. Energy, 165 (2016), pp. 244-259.

Daugherty et al., 1977

R.L. Daughery, J.B. Franzini. **Fluid Mechanics With Engineering Applications**. Seventh Edition. McGraw-Hill Inc.: United States of America, 1977.

Esen et al., 2007

H. Esen, M.Inalli, M. Esen. **A techno-economic comparison of ground-coupled and air-coupled heat pump system for space cooling**. Building and Environment, 42 (2007), pp. 1955-1965.

Esen et al., 2014

M- Esen, T. Yuksel. **Experimental evaluation of using various renewable energy sources for heating a greenhouse**. Energy and Buildings, 65 (2013), pp. 340-351.

Heyns, 2008

J.A. Heyns. **Performance Characteristics of an Air-Cooled Steam Condenser Incorporating a Hybrid (Dry/Wet) Dephlegmator**. M.Sc. Thesis. University of Stellenbosch, Stellenbosch, South Africa (2008).

Kern, 1999

D.Q. Kern. **Procesos de transferencia de calor (Process Heat Tansfer)**. Compañía Editorial Continental S.A.: México D.F., 1999.

Kröger, 2004

D.G. Kröger. Air-Cooled Heat Exchangers and Cooling Towers: Thermal-Flow Performance Evaluation and Design, II, Pennwell, Oklahoma, Tulsa (2004).

Manassaldi et al., 2014

J.I. Manassaldi, N.J. Scenna, S.F. Mussati. **Optimization mathematical model for the detailed design of air cooled heat exchangers**. Energy, 64 (2014), pp. 734-746.

Martín, 2015

M. Martín. **Optimal annual operation of the dry cooling system of a concentrated solar energy in the South of Spain**. Energy, 84 (2015), pp. 774-782.

Owen, 2010

M.T.F. Owen. **A numerical investigation of air-cooled steam condenser performance under windy conditions**. M.Sc.E. Thesis, University of Stellenbosch, Stellenbosch, South Africa, 2010.

Perry and Green, 2007

R.H. Perry, D.W. Green. **Chemical Engineers Handbook**. Eighth Edition. McGraw-Hill Education: United States of America, 2007.

Pieve and Salvadori, 2011

M. Pieve, G. Salvadori. **Performance of an air-cooled steam condenser for a waste-to-energy plant over its whole operating range**. Energy Conv. Manag., 52 (2011), pp. 1908-1913

Towler and Sinnott, 2008

G. Towler, R. Sinnott. **Chemical Engineering Design**. Elsevier, Oxford. UK (2008).

Yang et al., 2016

L. Yang, X. Zhao, X. Du, Y. Yang. **Heat load capability matching principle and its applications to anti-freezing of air cooled condenser**. Appl. Energy, 127 (2016), pp. 34-40.

Zammit, 2005

K. Zammit. **Air-Cooled Condenser Design, Specification, and Operation Guidelines**. Electric Power Research Institute, California, Palo Alto (2005).

CAPíTVLO iV

CALENTAMiENTO DE SALES FVNDiDAS: COLECTOR SOLAR

ACS Publications
Most Trusted. Most Cited. Most Read.

I&EC research
Industrial & Engineering Chemistry Research

Optimal Design of Solar Receivers in CSP Plants: Effects of Facility Location

Luceño, J.A.; de la Fuente, E.; and Martín, M.

Ind. Eng. Chem. Res., **2021**, *XXXX*, XXX-XXX

(Article ASAP)

DOI: 10.1021/acs.iecr.0c05383

IV.1.1. Introduction

Current society relies on electricity. Electricity, or electrical energy, is a key element for progress and development, increasing its demand with the growth of the population[1] or when new industries and technologies are developed, such as, data centers.[2] This form of energy can be obtained from the conversion of other sources, such as, combustion of fossil fuels (coal, gas, etc.), nuclear reactions, or employing renewable resources (wind, solar radiation, biomass, etc.). Renewable energies are the most interesting choice to produce electricity nowadays because they provide an alternative to increase the production of electricity[3] and represent the technologies that allow reducing greenhouse gas emissions.[4,5] Solar energy is the only energy source that the Earth receives, but it is more than enough to supply mankind needs. This work focuses on concentrated solar power (CSP) technologies that have received a lot of attention lately but still require additional development to improve the process efficiency to be installed across countries.[6] CSP technologies usually involve heat-transfer fluids (HTFs), used to capture solar energy for its use toward the production of energy via steam generation as well as a means to store thermal energy, enabling the overnight operation of the CSP plants.[7,8] HTFs are usually a mixture of two or more compounds; in previous works, molten salts[9] and synthetic fluids[10] were considered as HTFs.

CSP plants present three different sections: (1) the HTF circuit, which involves the heliostat field, the concentrating technology, and the thermal energy storage, if the facility has one of them; (2) the water–steam circuit, which comprises a heat exchanger network (to heat and evaporate the water stream) and a steam turbine (to produce electricity); and (3) the cooling system. There are different types of concentrating technologies, each one with a specific heliostat layout, but there are four main options nowadays: parabolic dish, parabolic trough, linear Fresnel reflector, and central receiver.[11–13] Section 2 is similar to traditional thermal power plants, where the difference is the use of HTFs and radiation to obtain the thermal energy employed to produce steam instead of the combustion of coal in a furnace. It consists of (1) a series of shell-and-tube heat exchangers to produce the steam and (2) high-, medium- and low-pressure turbines to generate electricity out of it.[13] Section 3 can present different cooling technologies, but

in the case of CSP, there are two main technologies, wet cooling and dry cooling,[9,14,15] and an intermediate option (hybrid cooling).[16]

There are different designs of solar receivers, such as the open volumetric air receiver,[17–19] the porous cavity receiver,[20] the particle solar receiver,[21] and the central or tubular receiver.[22] Each technology has its own characteristics, such as the need to study the influence of critical parameters in porous cavity receivers to improve efficiency,[20] the analysis of different kinds of materials and its effect on the absorption in particle solar receivers,[21] or the importance of correct simulation of the return air flow chamber in open volumetric air receivers;[17] furthermore, some works use CFD modeling applied to the analysis and optimization for some technologies, such as porous volumetric receivers.[18] Each of these technologies have been studied by different authors, but in this work, the technology studied is the central tube receiver because it is the most used at a commercial scale.[22]

Previous studies presented design methodologies for this equipment,[23,24] the evaluation of the peak temperature that takes place on the tubes applying an optimization of fluid distribution,[25] the importance of a flux map calculus and an optimal distribution of the heliostat field to reduce thermal stress in the receiver,[26] the simultaneous lay out optimization of the central receiver (horizontal distribution) and heliostat field,[27] a methodology to control the energy reached by the receiver,[28] and even parametric studies about the design and operation of molten salt receivers.[29,30] However, most of the studies focused on the relative location of the receiver without paying that much attention to its purpose as a heat-transfer unit while the ones dealing with this aspect present a procedural and/or simulation-based design, where the effects of facility location on the design feature and its performance have not been reported in the literature. In addition, the various radiation profiles that the locations of the CSP facilities may present, results in the need for evaluating the effect of different facility locations, with different radiation and weather data, on the design and heat-transfer features of the receiver.

This work presents a two-step methodology for the optimal design and the evaluation of the performance of central tube receivers. In the first step, a mathematical formulation is developed for the sizing of the unit that simultaneously considers the trade-offs related to individual element sizing and layout. In a second step, the performance of

the unit is evaluated over time. To address the location dependency on the unit design, different locations with their own weather data and two scenarios: same heliostat field (SHF) for all locations (resulting in different electricity production capacities) and different heliostat fields for each location [giving the same mean production (SMP) capacity] are evaluated. The receivers are optimally designed for each location and different scenarios. The work is organized in five sections: in the first section, the equations to design the equipment are presented; the second section deals with the framework used to design and evaluate each case; the third section presents the cases of study and the two scenarios and the value of some specific variables for the model; in the fourth section, the results are exposed and analyzed for both scenarios and cases. Finally, the conclusions of the work are drawn in section five.

IV.1.2. Model Formulation

In this work, a central receiver CSP plant is considered. These facilities have a solar field surrounding a central structure, commonly a tower built with cement or iron,[31] on top of which the receiver is placed. The receiver is set considering that the entire external surface is exposed to solar radiation. Furthermore, the path of the HTF across the receiver will determine some design variables.[24]

The modeling section is divided into two main subsections. The first one is related to the detailed design of the receiver, considering three different aspects: mechanical design, thermal design, and pressure drop evaluation. Each section has its own subsections, where the equations used to calculate the design parameters of the unit are presented. The second subsection is focused on the study of the performance over time of the design obtained in the previous module.

IV.1.2.1. Mechanical Design

The mechanical design comprises pipe selection, tower sizing, receiver design, and fluid flow path determination. It is recommended to choose the fluid flow path

considering the hemisphere where the facility is located, in order to feed the fluid to the most convenient bundle, reducing the pressure drop and increasing the fluid velocity.[24] In this work, the consideration will be the same as previous work which recommends two parallel flow paths without considering which is the initial bundle,[32] in order to present a general design case.

IV.1.2.1.1. Tube Selection

The tube external diameter (d_{ex}) and inner diameter (d_{in}) are selected according to standard sizes. In this work, the formulation used for the selection of the diameter of the pipe is presented in eqs 1–4.[33] Furthermore, the following sets of variables are introduced to simplify the nomenclature:

- number of external diameters is denoted $M = \{1, 2, ..., n_M\}$. It represents the number of external diameters that are considered as possible design values.
- number of internal diameters is denoted $J = \{1, 2, ..., n_J\}$. It corresponds to the number of possible internal diameters that are available for a specific M-external diameter. J can take different values across the set of external diameters.

$$d_{ex} = \sum_m d_{ex,m} \cdot y_{de,m} \qquad \forall m \in M \tag{1}$$

$$\sum_m y_{de,m} = 1 \qquad \forall m \in M \tag{2}$$

$$d_{in} = \sum_m \sum_j \left(d_{\mathbf{in},j,m} \cdot y_{\mathbf{di},j,m} \right) \qquad \forall m, j \in M, J \tag{3}$$

$$\sum_m \sum_j y_{di,j} = 1 \qquad \forall m, j \in M, J \tag{4}$$

Typically, the values of the diameter considered for the design of heat exchangers are presented in TEMA standard diameter value tables.[34] For this case, a total of five different external diameters (d_{ex}) are considered, following the typical range of design.[24] Each external diameter has different inner diameter (d_{in}) combinations, between 4 and

10 choices of thickness, see Supporting Information. Only one diameter and one thickness must be selected.

In solar central receivers, the tube length, H_{req}, corresponds to the linear section that is exposed to solar radiation. The connections between bundles and inlet and outlet pipes are covered by a screen or a small wall;[35] meanwhile, the linear section is still exposed to the Sun. Thus, the tube length considered is usually the linear section (Figure 1a). In the model, the tube junctions are not considered as tube length; thus, the tube length (H_{req}) can be determined by the height-diameter ratio of the collector (HD_{ratio}), as eq 5,[24] where D_{req} is the diameter of the receiver (m); as a recommendation, the ratio HD_{ratio} should be between 1 and 2.[24]

$$HD_{ratio} = \frac{H_{req}}{D_{req}} \tag{5}$$

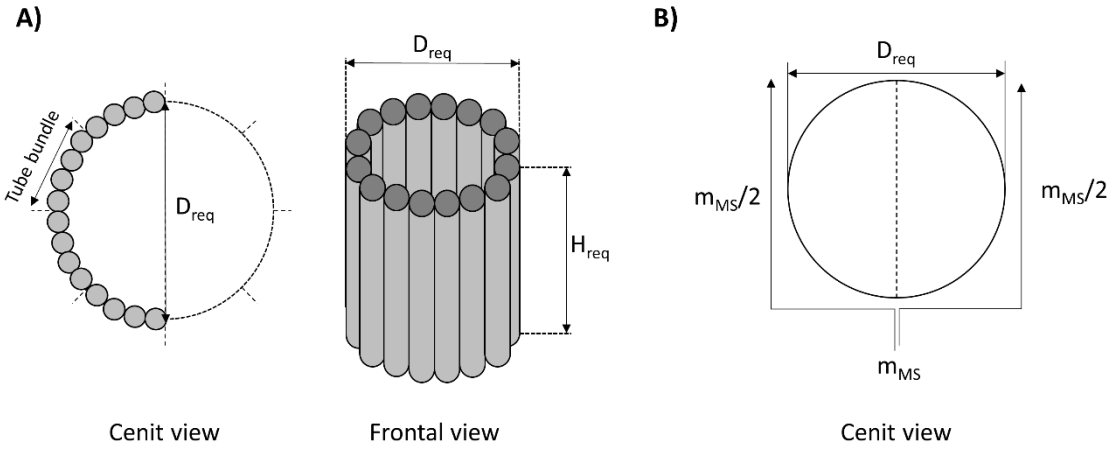

Figure 1. Central receiver scheme: (A) tube distribution and characteristic lengths; (B) flow splitting considered.

IV.1.2.1.2. Tower Design and Rescaled Wind Speed

The tower height (H_{tower}) affects the value of wind speed and, as a result, the heat transfer. This height is employed to rescale wind speed literature data due to the dependence of the wind speed on the separation and the orography of the location.[36] In this work, eq 6 is used to estimate H_{tower}:[24]

$$H_{tower} = 82.60 + 0.2552 \cdot \left(Q_{req} \cdot 10^{-3} \right) \quad (6)$$

where Q_{req} is the required heat to be absorbed by the HTF molten salts (kW). For a given value of H_{tower}, the Hellman law equation, eq 7,[37] is employed to determine the wind speed value at the desired height:

$$v_{Ht} = v_{meas} \cdot \left(\frac{H_{tower}}{H_{meas}} \right)^{\omega} \quad (7)$$

where v_{Ht} is the wind speed value at tower height (m/s), v_{meas} is the wind speed reported in the literature (m/s), H_{meas} is the height at which v_{meas} was measured (m), and ω is the friction coefficient or Hellman exponent. The ω value is tabulated, and it is a function of the ground topography. In this work, the value of 0.20 for ω was considered;[37] other values of ω can be consulted in Table S1 of the Supporting Information.

IV.1.2.1.3. Receiver Design

The mechanical design of the receiver involves the definition of the geometry of the equipment. This geometry is related to the number of tubes that provide the contact area and guide the molten salts through the receiver. The areas involved are $A_{req,\min}$, A_{flow}, A_{ob}, and A_{proj}.

The minimum total area required ($A_{req,\min}$) can be determined according to the incoming irradiation and the maximum heat flow across the wall of the tubes, as shown in eq 8:[24]

$$A_{req,\min} = \frac{Q_{req}}{HF_{\max}} \quad (8)$$

where $HF_{\max}$ is the maximum heat flow across tube wall (kW/m^2). The value of $A_{req,\min}$ is the lower bound for the design area A_{ob} that must be satisfied during the entire cycle.

The flow section required across a tube bundle (A_{flow}) is obtained using eq 9, where n_{path} is the number of splits for the m_{MS} . In this work, it is considered that the molten salt stream is split in two streams, so each stream will go over the half receiver, and n_{path} is equal to 2 (Figure 1b).

$$A_{flow} = \frac{\left(m_{MS} / n_{path}\right)}{\rho_{MS} \cdot v_{MS}} \tag{9}$$

where ρ_{MS} is the density (kg/m^3), m_{MS} is the total flow (kg/s), and v_{MS} is the velocity (m/s) of molten salts inside tubes (see Table S2 for the bounds).

The designed area (A_{ob}) and the projected area (A_{proj}) must be calculated using the design variables H_{req} and D_{req} , as shown in eqs 10 and 11:[24]

$$A_{ob} = \pi \cdot \frac{\pi}{2} \cdot H_{req} \cdot D_{req} \tag{10}$$

$$A_{proj} = \pi \cdot H_{req} \cdot D_{req} \tag{11}$$

The value of D_{req} can be obtained from the layout of the tubes so that the entire bundle has enough area as presented in eq 12:[23]

$$D_{req} \cdot \pi = N_{bundle} \cdot \left[B_{bundle} + B_{tube} \cdot \left(N_{tb} - 1 \right) + N_{tb} \cdot d_{ex} \right] \tag{12}$$

where N_{bundle} is the number of bundles, B_{bundle} is the separation between bundles (m), B_{tube} is the separation between tubes (m), and N_{tb} is the number of tubes per bundle. The value of N_{tb} is determined starting using A_{flow} and the flow section of one tube, as seen in eq 13:

$$N_{tb} = \frac{A_{flow}}{\frac{\pi}{4} \cdot \left(d_{in} \right)^2} \tag{13}$$

As $n_{path} = 2$, the value of N_{bundle} must be an even number. This constraint can be satisfied considering that the rest of N_{bundle} / n_{path} must be an integer positive value. If it is

required, this rest can be defined as an additional equation in the model, adding a new discrete variable.

IV.1.2.2. Thermal Design of the Receiver

The thermal design of the equipment is focused on the variables that are involved in heat transfer, such as temperatures and heat flows.

IV.1.2.2.1. Thermal Flows

The thermal design section presents the equations related to temperatures, fluid properties, dimensionless numbers, and heat-transfer coefficients. An energy balance to the molten salts is employed to determine the flow of molten salts required (m_{MS}), according to eq 14:

$$Q_{req} \cdot \eta_{ther} = m_{MS} \cdot Cp_{MS} \cdot \left(T_{out} - T_{in}\right) \tag{14}$$

where η_{ther} is the thermal efficiency of the receiver, Cp_{MS} is the specific heat [kJ/(kg·K)], T_{out} is the outlet temperature (K), and T_{in} is the inlet temperature (K) of the molten salts. The values of T_{in} and T_{out} are usually fixed depending on the HTF stability and flow properties, and m_{MS} changes each time period[9] so that the temperature of the molten salts stored is maintained over time. In this work, the values of Tin and Tout are taken to be 563.15 and 838.15 K, respectively, from previous works.[9,14]

Another important factor related to the operating temperatures is the heat flow across the tube wall (HF_{tube}). The tubes must be able to bear with the conduction heat transfer. The value of HF_{tube} can be determined using eq 15:[24]

$$HF_{tube} = \frac{\left(m_{MS} / n_{path}\right) \cdot Cp_{MS} \cdot \Delta T_{bundle}}{N_{tb}} \tag{15}$$

where ΔT_{bundle} is the temperature increment in each bundle (K), considering that it is equal in each bundle. It is computed using eq 16:

$$\Delta T_{bundle} = \frac{\left(T_{out} - T_{in}\right)}{\left(N_{bundle}/n_{path}\right)} \tag{16}$$

HF_{tube} has to be lower than the maximum heat flow across tube wall used ($HF_{\max}$, kW/m^2) for safety purposes and to ensure that tubes resist the thermal operating conditions. The value of $HF_{\max}$ is provided by the manufacturer. In the case of Incoloy steel, the value of $HF_{\max}$ is 1000 kW/m^2.[24] The constraint for $HF_{\max}$ is formulated as eq 17:

$$HF_{tube} \leq HF_{\max} \cdot \pi \cdot H_{req} \cdot d_{ex} \tag{17}$$

HF_{tube} is involved in the calculation of the tube surface mean temperature [$\overline{T}_s$, (K)], as seen in eq 18:

$$\overline{T}_s = \overline{T}_{MS} + HF_{tube} \cdot \left(\mathrm{R}_{cond} + \mathrm{R}_{conv}\right) \tag{18}$$

where $\overline{T}_{MS}$ is the molten salt mean temperature (K); this temperature is calculated as the average between the inlet and outlet molten salt temperature. R_{cond} is the heat resistance due to the conduction across the tube material (K/kW), and R_{conv} is the convection heat resistance of the HTF and the molten salts (K/kW). Thermal resistances can be determined using eqs 19 and 20:

$$\mathrm{R}_{cond} = \frac{\log\left(d_{ex}/d_{in}\right)}{k_{tube} \cdot 2\pi \cdot H_{req}} \tag{19}$$

$$\mathrm{R}_{conv} = \frac{1}{h_{in} \cdot d_{in} \cdot H_{req} \cdot \frac{\pi}{2}} \tag{20}$$

where k_{tube} is the thermal conductivity of the tube material [kW/((m^2/m)·K)] and h_{in} is the convective heat-transfer coefficient of the molten salts [kW/(m^2·K)]. The value of h_{in} can be calculated with eq 21, where the Nusselt number of the molten salts (Nu_{MS}) is determined using dimensionless numbers as shown in eqs 22–24:[24]

$$h_{in} = \frac{Nu_{MS} \cdot k_{MS}}{d_{in}} \tag{21}$$

$$Nu_{MS} = 0.023 \cdot \left(\mathrm{Pr}_{MS}\right)^{0.4} \cdot \left(\mathrm{Re}_{MS}\right)^{0.8} \tag{22}$$

$$\mathrm{Pr}_{MS} = \frac{Cp_{MS} \cdot \mu_{MS}}{k_{MS}} \tag{23}$$

$$\mathrm{Re}_{MS} = \frac{\rho_{MS} \cdot v_{MS} \cdot d_{in}}{\mu_{MS}} \tag{24}$$

where Pr_{MS} is the Prandtl number, μ_{MS} is the viscosity [kg/(m·s)], k_{MS} is the thermal conductivity [kW/((m^2/m)·K)], and Re_{MS} is the Reynolds number of the molten salts.

IV.1.2.2.2. Thermal Efficiency

The thermal efficiency of the equipment (η_{therm}) is considered to obtain more accurate results. This efficiency is calculated as the ratio between the total energy received and the energy lost by heat-transfer mechanisms (Q_{loss} (kW)), as presented in eq 25:

$$\eta_{therm} = 1 - \frac{Q_{loss}}{Q_{req}} \tag{25}$$

The variable Q_{loss} can be determined applying eq 26, where $Q_{l.refl}$, $Q_{l.rad}$, and $Q_{l.conv}$ are the heat losses (kW) due to reflection, radiation, and convection mechanisms, respectively.

$$Q_{loss} = Q_{l.refl} + Q_{l.rad} + Q_{l.conv} \tag{26}$$

Each of their values are determined using a different set of equations:

- The reflection losses $Q_{l.refl}$ can be calculated considering a linear dependency with Q_{req}, as seen in eq 27. The receiver effective absorbance (α_{eff}) is determined with

the receiver absorbance (α), as shown in eq 28; α is a characteristic of the chosen material. In this case, a value of 0.95 is considered.[24]

$$Q_{l.refl} = \left(1-\alpha_{eff}\right)\cdot Q_{req} \tag{27}$$

$$\alpha_{eff} = \frac{\alpha}{\alpha+\left(1-\alpha\right)\cdot\frac{\pi}{2}} \tag{28}$$

- The radiation losses $Q_{l.rad}$ are calculated applying the expression for radiation transfer, as seen in eq 29:

$$Q_{l.rad} = \sigma_{SB}\cdot\varepsilon_{eff}\cdot A_{proj}\cdot\left(\overline{T}_s^4-\overline{T}_{env}^4\right) \tag{29}$$

where σ_{SB} is the Stefan–Boltzmann constant [5.6704·10^{-11} kW/(m^2·K^4)], ε_{eff} is the receiver effective emissivity, and $\overline{T}_{env}$ is the mean atmospheric temperature (K). As in the case of α_{eff}, ε_{eff} can be determined with the receiver emissivity ε using eq 30. Furthermore, the value ε is material-dependent, and it is also affected by the tube coating chosen. In this work, ε values are estimated by a $\overline{T}_s$-based function obtained using literature data,[35] as seen in eq 31, where temperature T is introduced in K.

$$\varepsilon_{eff} = \frac{\varepsilon}{\varepsilon+\left(1-\varepsilon\right)\cdot\frac{\pi}{2}} \tag{30}$$

$$\varepsilon = 3.5746\cdot10^{-7}\cdot\left(T^2\right)-1.0557\cdot10^{-4}\cdot\left(T\right)+2.7008\cdot10^{-1} \tag{31}$$

- The convection losses $Q_{l.conv}$ are determined using eq 32, which shows the usual convection transfer expression:

$$Q_{l.conv} = h_{mix}\cdot A_{ob}\cdot\left(\overline{T}_s-\overline{T}_{env}\right) \tag{32}$$

where h_{mix} is the heat-transfer coefficient for mixed convection (kW/m^2·K). The mixed convection involved two kinds of mechanisms, natural convection (characterized by h_{nat} transfer coefficient) and forced convection (characterized by h_{for} transfer coefficient). The value of h_{mix} can be calculated using eq 33:

$$h_{mix} = \left(h_{nat}^{m} + h_{for}^{m} \right)^{1/m} \tag{33}$$

where the coefficient m is scalar which is fixed beforehand according to the receiver type; its value is between 3 and 4.[35] For an external receiver such as the one in this case study, the value of m is 3.2.[35] The coefficients h_{nat} and h_{for} are computed from the Nusselt number for natural convection and forced convection, respectively, as seen in eqs 34 and 35, where k_{air} is the thermal conductivity of air [kW/((m^2/m)·K)].

$$h_{nat} = \frac{Nu_{nat} \cdot k_{air}}{H_{req}} \tag{34}$$

$$h_{for} = \frac{Nu_{for} \cdot k_{air}}{D_{req}} \tag{35}$$

Each Nu number is computed using an empirical correlation, and it depends on the flow regime. In the case of natural convection, in addition to Reynolds and Prandtl numbers, two additional dimensionless numbers are required such as Grashof (Gr_{air}) and Rayleigh (Ra_{air}) numbers. These last dimensionless numbers are calculated using eqs 36 and 37:

$$Gr_{air} = \frac{g \cdot \beta_{air} \cdot \left(\overline{T}_s - \overline{T}_{env} \right) \cdot H_{req}^3}{\kappa_{air}^2} \tag{36}$$

$$Ra_{air} = Gr_{air} \cdot \mathrm{Pr}_{air} \tag{37}$$

where β_{air} is the volumetric expansion coefficient (K^{-1}), κ_{air} is the kinematic viscosity (m^2/s), and Pr_{air} is the Prandtl number of air, which is determined with an analogous expression than eq 23. In order to use, eqs 37 and 38 must be satisfied:[23]

$$\frac{D_{req}}{H_{req}} \geq \frac{35}{Gr_{air}^{0.25}} \tag{38}$$

Using the values of Pr_{air} and Ra_{air}, the Nusselt number for natural convection (Nu_{nat}), for turbulent flow, can be estimated using eq 39.[38] The Nusselt number for forced convection (Nu_{for}) is calculated using eq 40, where Re_{air} is the Reynolds number of air.

$$Nu_{nat} = \left[0.825 + \frac{0.387 \cdot Ra_{air}^{1/6}}{\left(1 + \left[\frac{0.492}{\mathrm{Pr}_{air}} \right]^{9/16} \right)^{8/27}} \right]^2 \quad (39)$$

$$Nu_{for} = 0.0455 \cdot \left(\mathrm{Re}_{air} \right)^{0.81} \quad (40)$$

The equations used to predict the heat-transfer coefficients are reported to provide a good estimation within the operating range according to the literature where the fitting was obtained.[38] By using the same model for different cases, the comparison is consistent so that the differences should not be ascribed to the equations used to estimate them.

IV.1.2.3. Pressure Drop

The pressure drop is a core point for the design of the equipment because a lower pressure drop usually means lower operating costs. The energy consumed to overcome pressure drop must be provided using pumps. The pressure drop ΔP_{tot} is estimated considering the tube pressure drop, and the pressure drop is given by the tower height, as seen in eq 41:

$$\Delta P_{tot} = \Delta P_{receiver} + \Delta P_{tower} = \Delta P_{tube} \cdot N_{bun\mathrm{Sec}} + \Delta P_{tower} \quad (41)$$

where $\Delta P_{receiver}$ is the receiver pressure drop (Pa), ΔP_{tube} is the pressure drop across one tube (Pa), $N_{bun\mathrm{Sec}}$ is the number of bundles per receiver section, and ΔP_{tower} is the pressure drop associated to the tower (Pa).

- ΔP_{tower} can be estimated using eq 42:

$$\Delta P_{tower} = \rho_{MS} \cdot g \cdot H_{tower} \quad (42)$$

- ΔP_{tube} is determined with eqs 43 and 44, considering different design variables, such as the fanning factor (f), the rugosity of tubes (in this work, it is considered

as stainless steel $\zeta = 0.2 \cdot 10^{-5} m$ [39]), H_{req} and d_{in}, or flow variables, such as Reynolds number of the molten salts (Re_{MS}) and v_{MS}. The curvature length of tubes (inlet and outlet connections) is not considered, in order to follow the same assumption presented for H_{req}.

$$\Delta P_{tube} = \rho_{MS} \cdot f \cdot \frac{H_{req}}{d_{in}} \cdot \frac{v_{MS}^2}{2} \tag{43}$$

$$\frac{1}{\sqrt{f}} = -2 \cdot \log\left(\frac{\zeta / d_{in}}{3.7} + \frac{2.51}{\mathrm{Re}_{MS} \cdot \sqrt{f}} \right) \tag{44}$$

The power consumption of the pumps (W_{pump}) can be determined employing eq 45, where V_{MS} is the volumetric flow of molten salts (eq 46) (m^3/s) and η_{pump} is the pump efficiency, which is assumed to be 0.8.

$$W_{pump} = \frac{\Delta P_{tot}}{\eta_{pump}} \cdot V_{MS} \tag{45}$$

$$V_{MS} = \frac{m_{MS}}{\rho_{MS}} \tag{46}$$

To evaluate the tradeoff between the operating costs, related to pumping the fluid, versus the global heat-transfer coefficient including the conduction across the pipe and the heat flux that a pipe can hold and the investment cost of the selection of the unit, we consider limited number of external diameters, 5 d_{ex}, from 4 to 10 thicknesses within the TEMA standard.[24]

IV.1.2.4. Objective Function

The objective function (*Z*) consists of three different items: (1) the annualized equipment capital cost; (2) the operating costs; and (3) the influence of more efficiency operation. The equipment capital cost was estimated considering the volume of the material [V_{st} (m^3)], which is calculated as shown in eq 47. The operating costs are related

to the pump energy consumption, which can be estimated using the pressure drop, as shown in eq 45. The influence of efficiency was taken into account considering a hypothetical production of the energy not captured by the unit. The part of the total energy not produced by the plant, Q_{loss}, should be obtained using nonrenewable sources, such as coal, which will generate CO_2 emissions: the more efficient the unit is, the lower the amount of emissions produced will be. Thus, a penalty to lower efficiencies can be introduced in the objective function using as variable Q_{loss}. Thus, the objective function is given by eq 48:

$$V_{st} = \frac{\pi}{4} \cdot \left(d_{ex}^2 - d_{in}^2 \right) \cdot H_{req} \cdot N_{tb} \cdot N_{bundle} \tag{47}$$

$$Z = \frac{\left(V_{st} \cdot \rho_{st} \cdot C_{st} \right)}{K_{rec} \cdot EL_{rec}} + W_{pump} \cdot \left(744 \frac{kWh}{kW \cdot month} \right) \cdot C_{elec} + Q_{loss} \cdot \left(744 \frac{kWh}{kW \cdot month} \right) \cdot EP_{CO_2} \cdot C_{CO_2} + C_{area} \cdot \Delta Area \tag{48}$$

where ρ_{st} is the density (kg/m^3) and C_{st} is the cost of the material of the tube ($/kg), EL_{rec} is the time considered for amortization purposes (year), K_{rec} is the number of months considered for amortization purposes (month/year), C_{elec} is the cost of electricity ($/kWh), EP_{CO_2} is the equivalent production of CO_2 if the energy was obtained from nonrenewable sources (kg CO_2/kWh), C_{CO_2} is the cost of CO_2 per kg ($/kg CO_2), C_{area} is the penalty value for nonused area [$/(m^2·month)], assumed to be 2000 $/(m^2·month), and $\Delta Area$ is the difference between the value of A_{ob} and $A_{req,\min}$ (m^2). The value of EL_{rec} considered was 30 years old, based on literature data.[35,40] The value of C_{elec} is estimated considering that the energy would be supplied by the CSP plants; thus, $C_{elec} = 0.16 \$/kWh$.[9] The values of EP_{CO_2} and C_{CO_2} are estimated using mean values of previous reports: in the case of EP_{CO_2}, the value is considered according to the estimation of United Nations, $EP_{CO_2} = 0.632\, kgCO_2/kWh$;[41] the value of C_{CO_2} is usually autoassigned by the companies themselves to consider the CO_2 footprint as a cost for its production, and a mean value could be $C_{CO_2} = 40 \$/kgCO_2$.[42] The values of Incoloy steel variables are

collected from different sources: the value of ρ_{st} is 7950 kg/m^3,[43,44] meanwhile, the value of C_{st} is 25 $/kg.[45]

The objective function for the second stage of the model is the same as eq 48 but with fixing design variables (i.e., the first term and the A_{ob} value inside the $\Delta Area$ term). This equation enables us to consider the fluctuation of production and weather and radiation variable for each month and also the corresponding amortization of the equipment.

IV.1.3. Solution Procedure

CSP facilities are sized at a design point.[8,9] However, the performance must be evaluated over a year. The solution procedure for the design of units operating under variable resources results in large nonlinear nonconvex mixed-integer nonlinear programming (MINLP) problems. Several works are presented in the literature to solve MINLP formulations applied to solar applications, such as energy supply superstructures.[46] However, in the case of unit design, nonlinearities involved in the estimation of heat-transfer coefficients, pressure drop, fanning factor, and so forth., including logarithms, ratios, power exponents, and fractions of the previous ones, present additional challenges. Therefore, in this work, we presented a two-stage approach to address the problem.[14] In the first stage, the equipment is designed for the scenario that presents the most demanding conditions; this first stage corresponds to a MINLP problem. Using the results of the design problem, in the second stage, a new nonlinear programming (NLP) problem is formulated to study one-year time horizon.

The design problem, an MINLP, consists of 111 continuous variables and 46 discrete variables involved in a total of 74 equations. The equations applied are the ones presented in Section 2. The upper bounds and lower bounds for the design variables are collected in Table S2. Since the design problem is an MINLP, different nonlinear solvers are used for a multi-start optimization procedure. Once the design is fixed, the model is reformulated to study the one-year performance using historic data. The thermal storage of the CSP plant mitigates short time variability in the operation, and therefore, monthly

discretization is assumed. Control of the operation is out of the scope of the work. In this case, the same equations of the first stage are applied, but a majority of design variables are fixed (such as diameters, areas, number of tubes, etc.). The variables related to heat transfer and flows (i.e., heat-transfer coefficients, Reynolds numbers, air mass flow, molten salt flow, etc.) are reformulated as monthly dependent variables: $h_{for} \rightarrow h_{for}(m)$; this reformulation implies an increase in the number of variables due to their dependence on the time period. The following list presents the variables that should be reformulated as monthly depended variables: Q_{req}, v_{MS}, m_{MS}, η_{ther}, $\bar{T}_s$, HF_{tube}, R_{conv}, h_{in}, Nu_{MS}, Re_{MS}, Q_{loss}, $Q_{l.refl}$, $Q_{l.rad}$, $Q_{l.conv}$, T_{env}, Gr, Ra, Nu_{nat}, h_{nat}, Nu_{for}, h_{for}, h_{mix}, ΔP_{tube}, f, ΔP_{tot}, W_{pump}, and Z. The NLP monthly performance problem presents a total of 511 constraints, which are divided into 24 inequalities and 487 equations, with a total of 487 variables involved if the plant operates 12 months.

IV.1.4. Cases of Study

In this work, three different locations are considered in order to study the effect of different weather and radiation conditions in the design and its effects in heat transfer. The locations selected are Almería (Spain), Arizona (USA), and Scotland (UK).

The three locations present different mean profiles of wind velocity (Figure S1, in Supporting Information) and also different ranges of values. Scotland has the highest values and a curved profile; Almería shows semi-oscillating values around 4.5 m/s, being the second higher value interval; finally, Arizona presents a constant mean value (2.8 m/s). The atmospheric temperature (Figure S2) follows the same profile in all locations, but there is a larger difference between the lowest and highest temperature in Arizona (around 20 K), followed by Almería (close to 15 K) and Scotland (around 12 K).

The profiles of radiation are also very different from one case to the other. In this work, direct normal irradiation, DNI, was used to characterize the radiation (Figure S3). First, it can be observed that there is a large difference between the radiation profile of Scotland and that of Arizona or Almería. Scotland's DNI follows a monotonic positive

tendency until April, and later, the trend becomes negative. Almería presents a profile that has larger values during summer and spring months and lower during autumn or winter, describing a curve with the minimum value in December and the highest in July. The case of Arizona also shows a similar profile, but the yearly variation is smaller.

Furthermore, two scenarios will be studied for each location: (a) SHF scale, which results in different mean productions, and (b) SMP, which involves different plant sizes. These scenarios shed light into the effect of production capacity and weather characteristics in the values of heat-transfer variables: comparing and presenting a range of variable values at different weather (SMP scenario) and variation of values due to larger production at the same location (SHF). The mean production in the SMP scenario will be calculated considering only the operating months: if a case does not operate for 12 months, the mean production will be determined with a lower number of months. This approach is applied in order to not overdesign the receiver.

IV.1.4.1. General Data and SHF Scenarios

The data related to weather and radiation conditions are the inputs that the model requires for the design of the receiver. In particular, the essential data for the present model are wind speed, atmospheric temperature, and DNI data, which are presented in Figures S1–S3 of the Supporting Information. These raw data need a previous processing to be employed on the model:

1) the values of Q_{req} must be determined for each month and scenario; and
2) the wind speed data must be rescaled according to the procedure of eqs 6 and 7 using Q_{req} values. The Q_{req} data were determined using eq 49:

$$Q_{req} = \frac{DNI \cdot A_{heli} \cdot (\eta_{heli}) \cdot d_{month}}{d_{month} \cdot h_{sun}} \tag{49}$$

where DNI is the mean direct normal irradiation of the month considered [kWh/(m^2·d)], A_{heli} is the area of heliostat field (m^2), η_{heli} is the efficiency of heliostat field, d_{month} is the

number of days of the month (d), and h_{sun} is the number of sun hours with enough irradiation (h). Some of these variables can be fixed according to the following points:

- η_{heli} was assumed to be 0.90.
- A_{heli} value must be the same in the SHF scenario, and the value chosen was 317,880 m^2, as previous works.[9]

The h_{sun} value was calculated comparing the hourly DNI data of a typical day, for each location and month,[47] with the minimum radiation threshold, which was considered 250 W/m^2;[48] the values of h_{sun} and d_{month} are collected from an institutional data base.[47] The values of Q_{req} for each location, for SHF scenarios, are plotted in Figure 2, and the wind speed data rescaled are collected in Supporting Information (see Figure S4). In Figure 2, it can be seen that each location shows a different energy availability profile and range of values. Furthermore, due to the constraint on the radiation threshold (250 W/m^2), the Scotland profile presents 5 months below the radiation threshold; thus, these months cannot be considered to operate the thermodynamic cycle.

The profile of Q_{req} is location dependent. In the case of Arizona, the fluctuation is small and around a mean value of 205 MW, presenting the highest values of the three locations. In the case of Scotland, the energy absorbed shows low fluctuation, but the mean value is 53 MW, presenting the lowest value of all locations. Oppositely, the case of Almería shows a profile with the largest fluctuation during the year, due to the weather of the region, presenting a range of values between 100 and almost 200 MW, with a mean value of around 150 MW. These three cases allow a comprehensive study for the effect of the radiation profile on the design and on the heat-transfer variables.

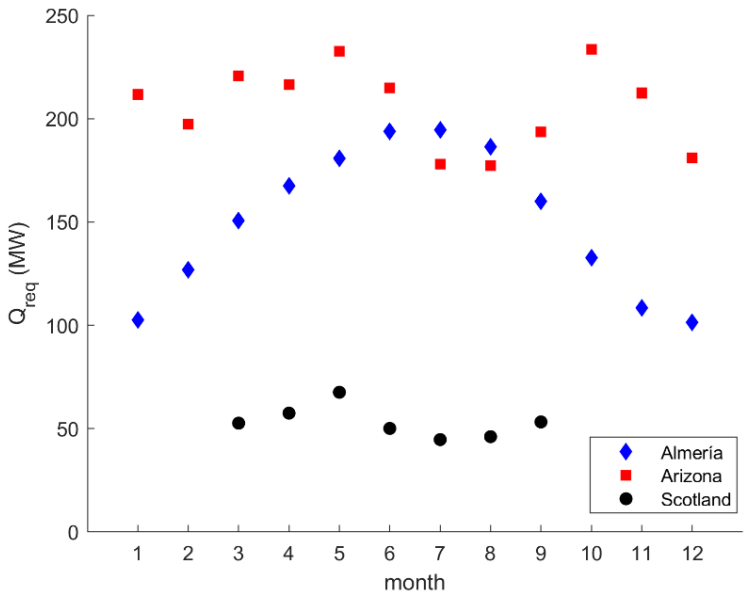

Figure 2. Q_{req} data for each location (SHF scenario).

IV.1.4.2. SMP Scenarios

To study the second scenario, where the facilities have the SMP capacity in MW at every location, the value of A_{heli} must be rescaled to provide the energy required. In this work, the rescaling of A_{heli} is performed using the mean annual production values of each location ($MV_{location}$); these values are calculated considering the operating months for each location. Later, the largest mean production value (MV_{LV}) between all locations is defined, and a correction factor for each location ($CF_{location}$) is calculated according to eq 50. The $MV_{location}$ and $CF_{location}$ results are collected on Table 1; the rescaled Q_{req} data are plotted on Figure 3, and the new wind speed data are represented on Figure S5.

$$CF_{location} = \frac{MV_{LV}}{MV_{location}} \tag{50}$$

Table 1. Correction Factors for the SMP Case

Location	Almería	Arizona	Scotland
$MV_{location}$ (MW)	150.46	205.83	53.12
$CF_{location}$	1.37	1.00	3.87

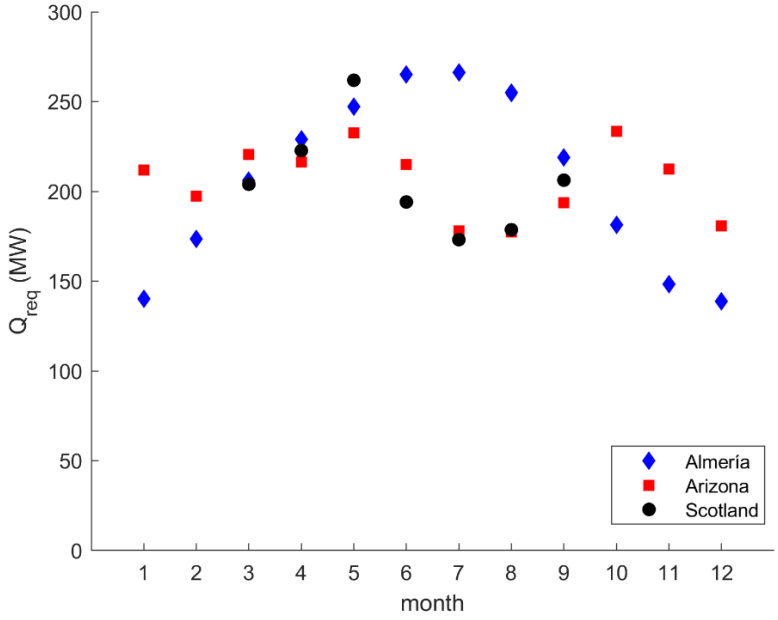

Figure 3. Q_{req} data rescaled for each location (SMP scenario).

In Figure 3, the data corresponding to Almería data are above the ones from Arizona, which is the opposite case with respect to the SHF scenario; this is due to the fact that Almería presents larger seasonal variability, with lower values during autumn and winter months, and it must be offset with higher values during summer and spring. Scotland's data are close to Arizona's data, with minor differences in spring-early summer months in order to offset the value of May.

IV.1.5. Results

In this section, the results obtained for the different locations are presented in two subsections. Section 5.1 compares different designs for the three locations and two plant sizes while in section 5.2, the performance of the designs under various scenarios are presented.

IV.1.5.1. Receivers Designs

The first step consists of the design of the optimal receiver according to the characteristics of the location. Inputs of the weather and radiation data are required (see Section 4). The model described in Section 2 is solved as an MINLP for each location. Following the design criteria of considering the most demanding operating condition, each location has a different design month, but this month will be the same for both scenarios, SMP and SHF. According to Figure 2, the design months considered for equipment design in the cases of Almería, Arizona, and Scotland were July, October, and May, respectively. In Table 2 the most important variables of the receiver design are presented for each location for both two scenarios: SHF and SMP.

Table 2. Receiver design for each scenario and location

Variable	Almería		Arizona		Scotland	
	SHF	SMP	SHF	SMP	SHF	SMP
H_{req} (m)	7.265	7.473	7.344	7.344	4.087	7.675
D_{req} (m)	5.429	7.219	6.446	6.446	4.087	7.675
A_{ob} (m^2)	194.629	266.240	233.609	233.609	82.435	290.694
A_{proj} (m^2)	123.905	169.494	148.72	148.72	52.45	185.062
H_{tower} (m)	132.269	150.544	142.217	142.217	99.851	149.439
d_{ex} (m)	0.022	0.032	0.032	0.032	0.022	0.025
d_{in} (m)	0.020	0.030	0.030	0.030	0.020	0.024
A_{flow} (m^2)	0.029	0.040	0.035	0.035	0.010	0.039
N_{tb}	88	56	50	50	30	88
N_{bundle}	8	12	12	12	14	10
$n_{tubeTOT}$	704	672	600	600	420	880
B_{tube} (m)	0.002	0.002	0.002	0.002	0.008	0.002
B_{bundle} (m)	0.002	0.002	0.002	0.002	0.010	0.002

As expected, higher values of Q_{req} result in the need for a larger unit. The total area can be increased by a larger number of tubes or longer and wider tubes. The solution is not straightforward. In the case of Arizona, both scenarios present the same values because the production rate is the same; thus, there is no difference in the receiver

design. Almería and Scotland cases present changes on the designs due to the need for rescaling the heliostat field.

In the case of Almería, the increased production capacity from SHF to SMP results in the use of larger tubes (slightly longer and 33% larger D_{req}) and 33% larger diameter of the pipes (d_{in} and d_{ex} increase) but in a lower amount of the total number of tubes ($n_{tubeTOT}$), one-third less per bundle. This fact can be explained comparing the increase in the value of A_{ob} against the value required for the SHF scenario (37% higher). Furthermore, the value of A_{flow} increases with respect to the SHF scenario because of the larger d_{in}, close to 38%. This can be justified based on eq 13, where the effect of increasing d_{in} is higher than decreasing N_{tb}. The values of B_{tube} and B_{bundle} show that the tubes have the same split in both scenarios, which indicates that the increase in the values of D_{req} and A_{proj} is related to the different distribution of tubes in a larger value of N_{bundle}, according to eq 12. The new larger value of H_{tower} is also related to the larger production capacity, as seen in eq 6.

The case of Scotland is similar to the one presented for Almeria. The SMP scenario requires a far larger unit compared to the one required under the SHF. The tubes employed in the SMP scenario have around double the length (H_{req}) and larger flow area A_{flow}, close to 4 times larger, due to the change in N_{tb}. These changes in the design of the tubes and the notable increase of the number of tubes, $n_{tubeTOT}$, result in an increase in the value of A_{ob} close to 3.5 times that obtained for the SHF scenario. The large difference in A_{ob} is directly related to the $CF_{location}$ value of Scotland (see Table 1) because Scotland is a region with low solar radiation and even a non-continuum production (see Figure 2); thus, the heliostat field expansion should be larger than Almería's case. In this case, B_{tube} and B_{bundle} show different values in each scenario, which was lower in the SHF case. This reduction can be related with D_{req} and $n_{tubeTOT}$ because the increase of D_{req} is slightly lower than that of the number of tubes, $n_{tubeTOT}$ (close to twice larger, vs, more than twice larger) and also with the increment in the tube diameter in the SMP case. Larger and more

tubes are needed as well as with a smaller separation between them. The larger value of H_{tower} in the SMP scenario has the same explanation than the one presented for Almería's case, the larger value of Q_{req}.

If the three SMP scenarios are compared, the general rule is that the total production does not only define the geometry of the receiver but also that it is not possible to establish a range of values for the variables, considering Q_{req} due to the number of trade-offs in terms of area needs and power consumption, which makes the mathematical formulation a powerful tool for the design of the receiver. However, changing the value of $HF_{\max}$ has a notable effect of design variables values; an example with the value $HF_{\max} = 465 kW / m^2$ is presented in Supporting Information Table S3. The reduction of $HF_{\max}$ implies larger units because the design is more conservative.

IV.1.5.2. Unit Performance

In this section, the most important results obtained after the study of the three locations' performance are presented. More information about convective heat-transfer coefficients is reported in the Supporting Information (Tables S4–S6).

Figure 4 presents the evolution of m_{MS} and h_{in} during a year. For all locations, it can be observed that the m_{MS} values follow the same tendency as the radiation in that particular place, but in the SMP case, the variation is larger than in the SHF case for Almería (Figure 4a) and Scotland (Figure 4c). This variation is closely related to the $CF_{location}$ value (Table 1). Furthermore, there are subtle differences between the scenarios of each location. These differences can be related to the value of A_{flow} and its discontinuous nature as a result of the standard diameter sizes. A larger change of A_{flow} results in a more notable alteration in the profile of m_{MS}. Even though the variable that determines the profile of m_{MS} is the solar radiation, these results show that the design may also have an effect on the operating variables. The comparison between m_{MS} and

h_{in} in Figure 4 shows that there is a direct relationship between their profiles, as expected. Close to the same, h_{in} values are obtained in SMP and SHF scenarios for each location. It can be due to the fact that the range of values of eq 21 is mainly determined by d_{in}, and the variation of Nu_{MS} describes the tendency of data.

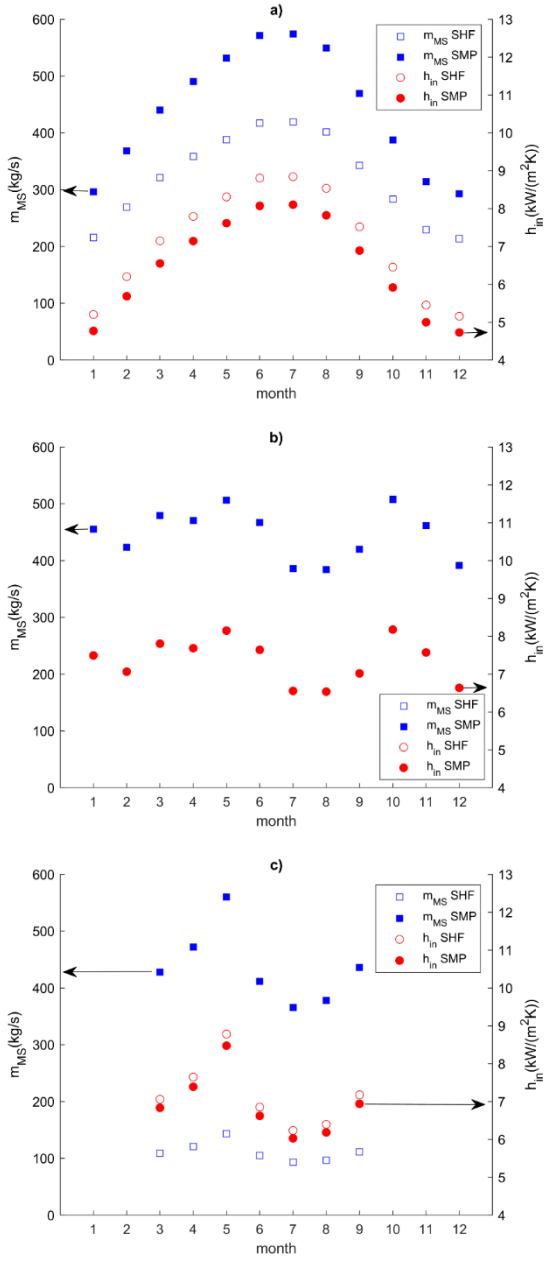

Figure 4. Fluctuation of salt flow and h_{in} during a year for each location and for both scenarios: (a) Almería; (b) Arizona; and (c) Scotland.

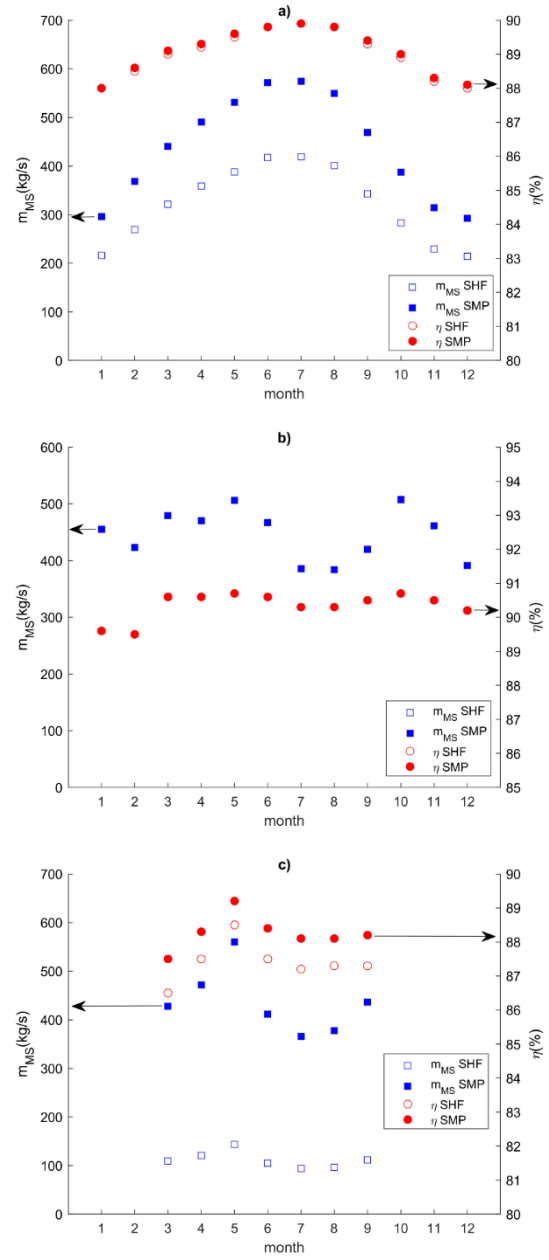

Figure 5. Fluctuation of salt flow and efficiency during a year for each location and both scenarios: (a) Almería; (b) Arizona; and (c) Scotland.

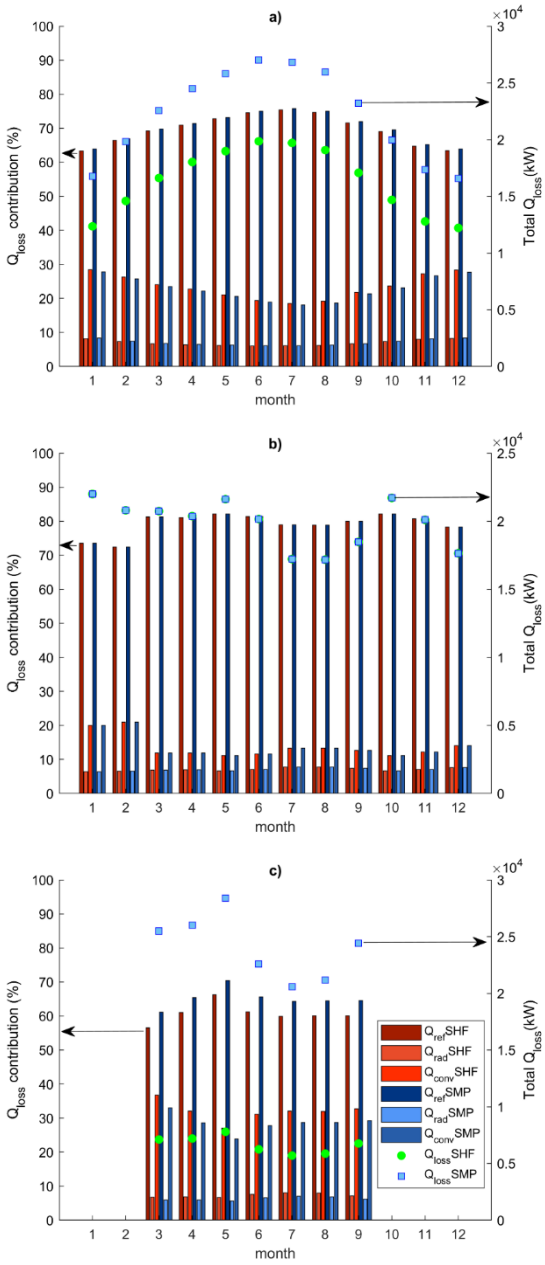

Figure 6. Contribution of each thermal loss mechanism during a year for each location and both scenarios: (a) Almería; (b) Arizona; and (c) Scotland.

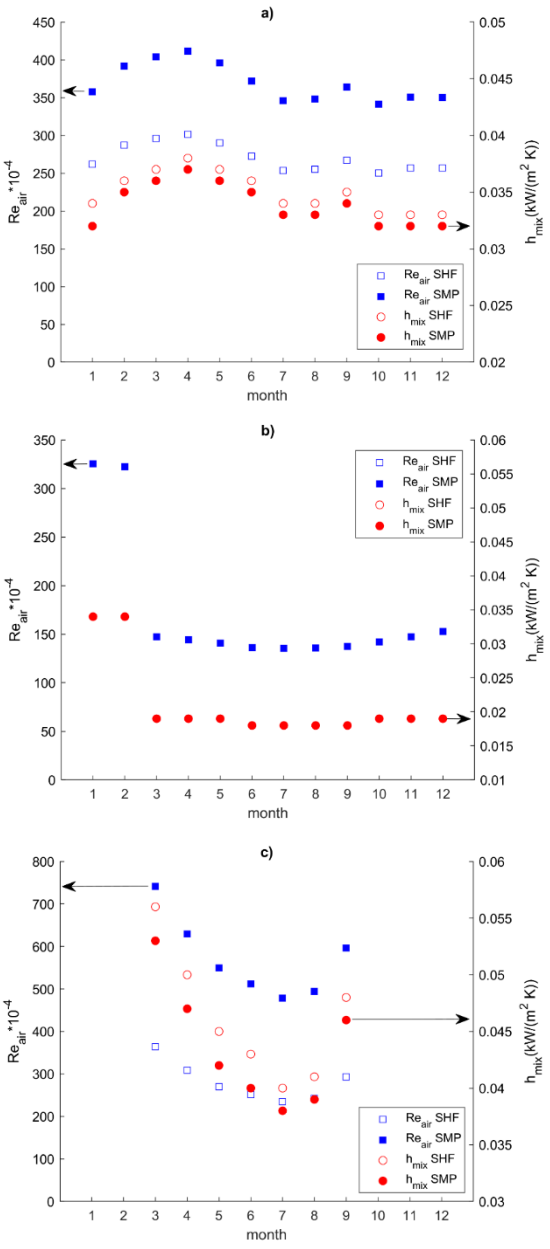

Figure 7. Fluctuation of $\mathrm{Re}_{air} \times 10^{-4}$ and h_{mix} during a year for each location and both scenarios: (a) Almería; (b) Arizona; and (c) Scotland.

The changes in η_{therm} with m_{MS} were also studied. They are presented in Figure 5. In all locations, the variation of η_{therm} between both scenarios is lower than or close to 1% and presents the same profile as m_{MS}. Furthermore, it can be noticed that the case of Arizona (Figure 5b) achieves the highest values of η_{therm}, considering SMP and SHF cases

of Almería (Figure 5a) and Scotland (Figure 5c). It means that the rescaling of Q_{req} does not affect so much η_{therm}, but the radiation profile is a key factor to achieve larger efficiencies. As a result, it can be said that the lower the fluctuation in radiation, the higher the η_{therm} is reached.

Evaluating the contributions of thermal losses (Figure 6), it can be observed that reflection losses represent the largest decrease in the efficiency, above half of the total losses [approx. Arizona—75% (Figure 6b), Almería—65% (Figure 6a), Scotland—60% (Figure 6c)]. As eq 27 is linearly depended on Q_{req}, the radiation represents around 10% or less of the losses in all cases. However, the larger the mean ambient temperature ($\overline{T}_{env}$), the larger the radiation losses in that location, which can explain the increase of the contribution of $Q_{l.rad}$ to the total Q_{loss}. This temperature could also affect $Q_{l.conv}$, but the effect of the wind (studied by Re_{air}) is more important, as seen in the values of h_{mix} in Figure 7. h_{mix} has a direct dependence with Re_{air}, and the values are mostly the same in both scenarios, SMP and SHF, for each location. The range of values and profile are determined by the wind speed (which affects Re_{air}). Note that the non-rescaled minimum velocities range from 2 to 6 m/s (Arizona location), while the maximum velocities range from 5 to 10 m/s (Scotland location), see Figure S1, which are twice the ones of the previous location. As wind speed is lower [Arizona scenario (Figure 7b)], h_{mix} presents values 30–50% lower than other locations, Almería (Figure 7a) and Scotland (Figure 7c), which shows the effect of the weather conditions (wind) on the convective heat transfer. Looking at Tables S5–S7, the contribution of h_{mix} (h_{nat} and h_{for}) can be compared. For all cases, the value of h_{nat} is close to 1×10^{-2}; meanwhile, h_{for} is higher (except to Arizona scenario because from March, both values are similar), so the value of h_{mix} is very close to h_{for}.

Another variable that is affected by m_{MS} is ΔP_{tube}, which is shown in Figure 8. First, weather conditions affect the ΔP_{tube} profile in all locations, as seen in Figure S6. However, the comparison of ΔP_{tube} between locations shows that there is no relationship with m_{MS} because the ΔP_{tube} increment is not proportional to the corresponding increase of m_{MS}.

These variations are related to the design of the receiver. In Figure 8, the pressure drop is presented versus Q_{req}. In Figure 8a, SHF scenarios show higher values of ΔP_{tube} than SMP ones and also a larger interval of values in the case of Scotland. However, the analysis of the results must consider the different receiver design (Table 2). This comparison is presented in Figure 8b. SMP scenarios show lower $\Delta P_{receiver}$ values than SHF scenarios for the same Q_{req}. This is due to the distribution of tubes: a larger n_{tubbun} and lower n_{bundle} results in lower $\Delta P_{receiver}$. The reduction of $\Delta P_{receiver}$ is an option to increase the viability of the equipment, due to the decrease of W_{pump}, but a trade-off with the heat transfer across the tube wall has to be achieved. A lower n_{bundle} implies that ΔT_{bundle} could be larger and also HF_{tube}; the tubes bundles must operate with a value HF_{tube} lower than $HF_{TA,\max}$.

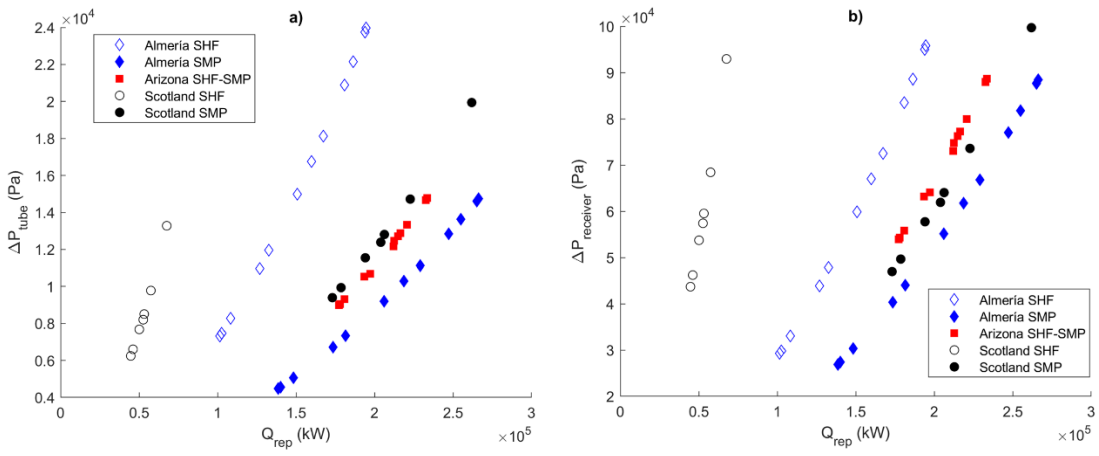

Figure 8. Fluctuation of pressure drop and Q_{req} during a year for each location and both scenarios: (a) tube pressure drop and (b) receiver pressure drop (considering bundles).

IV.1.6. Conclusions

This work develops a two-stage strategy for the design of central tubular solar receivers to simultaneously consider the number of trade-offs involved in the selection of size and tube layout. It allows evaluating the effect of the location of the facility on both the sizing of the units and on the operating variables. The location affects the design due to the effect of variables such as weather conditions, radiation profile, or even water availability. The optimal design and the performance are formulated as a two-step

procedure, where first, the equipment is designed applying a MINLP, and later, the study of the performance is approached as an NLP.

Three locations were considered: Almería (Spain), Arizona (USA), and Scotland (UK). Each of them has a different radiation profile, operation period, and weather so that the comparison between them presents useful information about design tendencies and heat-transfer behavior. Furthermore, two different scenarios were considered for each location: SHF (different mean production) and SMP (same mean production). The design results show larger power production and larger units. However, the particular sizing of the elements is location dependent. The increment of area is attributed to larger tubes, in general, but to a lower amount of tubes in the case of Almería. However, the total production does not define the geometry of the receiver.

The operating results provide useful information on how these receivers work. The study shows that the heat-transfer coefficient, h_{in}, follows the same profile than m_{MS} for each location and scenario, depending on the value of the inner diameter. The variation of η_{therm}, which depends on m_{MS}, is lower than 1% for all locations and scenarios; furthermore, higher radiation profile values and higher efficiencies are seen. The thermal losses correspond mainly to the reflection mechanism (65–75%) and second to the convection mechanism, being less important radiation losses due to the work temperature (close to 10%). Finally, the evolution of $\Delta P_{receiver}$ is related with the number of bundles and tube per bundle that the design has: larger bundles (more tubes) and lower $\Delta P_{receiver}$; however, it implies that the thermal stress of the tube could be larger. The variability of solar and wind velocities presents the opportunity to develop algorithms and solution procedures to include two-stage stochastic programming in the design of heat transfer.

IV.1.7. Nomenclature

d_{ex}: external tube diameter (m).

d_{in}: internal tube diameter (m).

M: set of external diameters options.

n_M : number of external diameters options.

J : set of internal diameters options.

n_J : number of internal diameters options.

m : m-element of M .

j : j-element of J .

$y_{de,m}$: binary variable of m-external diameter option.

$y_{\boldsymbol{di},j,m}$: binary variable of mj-external diameter option.

HD_{ratio} : Relation between the height and the diameter of the receiver (m).

H_{req} : Receiver height (m).

D_{req} : Receiver diameter (m).

H_{tower} : tower height (m).

Q_{req} : required heat to be absorbed by molten salts (kW).

v_{Ht} : wind speed value at tower height (m/s).

v_{meas} : wind speed (m/s).

H_{meas} : height where v_{meas} was measured (m).

ω : friction coefficient or Hellman exponent.

$A_{req,\min}$: minimum total area required (m^2).

$HF_{\max}$: maximum heat flow across the tube wall (kW/m^2).

A_{flow} : flow section required across a tube bundle (m^2).

n_{path} : number of splits for molten salt flow.

ρ_{MS} : density of molten salts (kg/m^3).

m_{MS} : total flow of molten salts (kg/s).

v_{MS} : velocity of molten salts inside tubes (m/s).

A_{ob} : designed area (m^2).

A_{proj} : projected area (m^2).

N_{bundle} : number of bundles.

B_{bundle} : separation between bundles (m).

B_{tube} : separation between tubes (m).

N_{tb} : number of tubes per bundle.

η_{ther} : thermal efficiency of the receiver.

Cp_{MS} : specific heat of molten salts [kJ/(kg·K)].

T_{out} : outlet temperature of molten salts (K).

T_{in} : inlet temperature of molten salts (K).

HF_{tube} : heat flow across the tubes wall (kW).

ΔT_{bundle} : temperature increment in each bundle (K).

$\overline{T}_s$: tube surface mean temperature (K).

$\overline{T}_{MS}$: molten salts mean temperature (K).

R_{cond} : heat resistance due to the conduction of tubes (K/kW).

R_{conv} : convection heat resistance of molten salts (K/kW).

k_{tube} : thermal conductivity of tubes [kW/((m^2/m)·K)].

h_{in} : convective heat transfer coefficient of molten salts [kW/(m^2·K)].

Nu_{MS} : Nusselt number of molten salts.

Pr_{MS} : Prandtl number of molten salts.

μ_{MS} : viscosity of the molten salts [kg/(m·s)].

k_{MS} : thermal conductivity of the molten salts [kW/((m^2/m)·K)].

Re_{MS} : Reynolds number of the molten salts.

Q_{loss} : energy lost by heat transfer mechanisms (kW).

$Q_{l.refl}$: heat losses due to reflection mechanism (kW).

$Q_{l.rad}$: heat losses due to radiation mechanism (kW).

$Q_{l.conv}$: heat losses due to convection mechanism (kW).

α_{eff} : receiver effective absorbance.

α : receiver absorbance.

σ_{SB} : Stefan-Boltzmann constant [kW/(m^2·K^4)].

ε_{eff} : receiver effective emissivity.

$\overline{T}_{env}$: mean atmospheric temperature (K).

ε : receiver emissivity.

h_{mix} : heat transfer coefficient for mixed convection (kW/m^2·K).

h_{nat} : heat transfer coefficient for natural convection (kW/m^2·K).

h_{for} : heat transfer coefficient for forced convection (kW/m^2·K).

m : Scalar of receiver type mix convection transfer.

k_{air} : thermal conductivity of air [kW/((m^2/m)·K)].

Nu_{nat} : Nusselt number for natural convection.

Nu_{for} : Nusselt number for forced convection.

Gr_{air} : Grashof number of air.

Ra_{air} : Rayleigh number of air.

β_{air} : volumetric expansion coefficient of air (K^{-1}).

κ_{air} : kinematic viscosity of air (m^2/s).

$\Pr_{air}$: Prandtl number of air.

ΔP_{tot} : total pressure drop (Pa).

ΔP_{tube} : pressure drop across one tube (Pa).

$N_{bun\mathrm{Sec}}$: number of bundles per receiver section.

ΔP_{tower} : pressure drop associated to the tower (Pa).

g : gravity acceleration (m/s^2).

f : fanning factor.

ζ : rugosity of tubes (m).

W_{pump} : power consumption of pumps (kW).

V_{MS} : volumetric flow of molten salts (m^3/s).

η_{pump} : pump efficiency.

V_{st} : volume of Incoloy steel (m^3).

Z : objective function ($/month).

ρ_{st} : density of the material of the tube (kg/m^3).

C_{st} : cost of the material of the tube ($/kg).

EL_{rec} : time assigned to amortization purpose (year).

K_{rec} : number of months considered for amortization purpose (month/year).

C_{elec} : cost of electricity ($/kWh).

EP_{CO_2} : equivalent production of CO_2 if the energy was obtained from non-renewable sources (kg CO_2/kWh).

C_{CO_2} : cost of CO_2 per kg ($/kg CO_2).

C_{area} : penalty value for non-used area ($/($m^2$·month)).

$\Delta Area$: difference between the value of A_{ob} and $A_{req,\min}$ (m^2).

$\Delta P_{receiver}$: total pressure drop through the receiver (Pa).

DNI : direct normal irradiation [kW/(m^2·h)].

A_{heli} : area of the heliostat field (m^2).

η_{heli} : efficiency of the heliostat field.

d_{month} : number of days of the month (d).

h_{sun} : number of sun hours with enough irradiation (h).

$MV_{location}$: mean annual production value of the location (MW).

MV_{LV} : largest mean annual production value (MW).

$CF_{location}$: correction factor of the location.

$n_{tubeTOT}$: total number of tubes.

IV.1.8. References

1. IDEA. Data and statistic. Available in: https://www.iea.org/statistics/?country=WORLD&year=2016&category=Energy%20supply&indicator=TPESbySource&mode=chart&dataTable=BALANCES (accessed June 11, 2020).
2. Vasques, T. L.; Moura, P.; de Almeida, A. A review on energy efficiency and demand response with focus on small and medium data centers. *Energy Effic.* **2019**, *12*, 1399–1428, DOI: 10.1007/s12053-018-9753-2
3. Eurostat. Statistics Explained. Renewable energy statistics. https://ec.europa.eu/eurostat/statistics-explained/index.php/Renewable_energy_statistics (accessed June 14, 2020).
4. UN, United Nations. Climate action. https://www.un.org/en/climatechange/ (accessed June 8, 2020).
5. Carlini, E. M.; Schroeder, R.; Birkebæk, J. M.; Massaro, F. EU transition in power sector: How RES affects the design and operations of transmission power systems. *Electr. Power Syst. Res.* **2019**, *169*, 74– 91, DOI: 10.1016/j.epsr.2018.12.020
6. He, Y.-L.; Qiu, Y.; Wang, K.; Yuan, F.; Wang, W.-Q.; Li, M.-J.; Guo, J.-Q. Perspective of concentrating solar power. *Energy* **2020**, *198*, 117373, DOI: 10.1016/j.energy.2020.117373.
7. Liu, M.; Steven Tay, N. H.; Bell, S.; Belusko, M.; Jacob, R.; Will, G.; Saman, W.; Bruno, F. Review on concentrating solar power plants and new developments in high temperature thermal energy storage technologies. *Renewable Sustainable Energy Rev.* **2016**, *53*, 1411– 1432, DOI: 10.1016/j.rser.2015.09.026.
8. Gonzalez Finat, A.; Liberali, R. *Concentrating Solar Power From Research to Implementation*; European Communities: Luxembourg, 2007; pp 1– 39.
9. Martín, L.; Martín, M. Optimal year-round operation of a concentrated solar energy plant in the south of Europe. *Appl. Therm. Eng.* **2013**, *59*, 627– 633, DOI: 10.1016/j.applthermaleng.2013.06.031.

10. García, S.; Martín, M. Analysis of the performance of Concentrated Solar Power facilities using different thermal fluids. *Chem. Eng. Res. Des.* **2020**, *168*, 46, DOI: 10.1016/j.cherd.2021.01.030. Rev. Submitted.
11. Fernández, A. G.; Gomez-Vidal, J.; Oró, E.; Kruizenga, A.; Solé, A.; Cabeza, L. F. Mainstreaming commercial CSP systems: A technology review. *Renew. Energy* **2019**, *140*, 152– 176, DOI: 10.1016/j.renene.2019.03.049.
12. Hayat, M. B.; Ali, D.; Monyake, K. C.; Alagha, L.; Ahmed, N. Solar energy—A look into power generation, challenges, and a solar-powered future. *Int. J. Energy Res.* **2019**, *43*, 1049– 1067, DOI: 10.1002/er.4252.
13. Zhang, H. L.; Baeyens, J.; Degrève, J.; Cacères, G. Concentrated solar power plants: Review and design methodology. *Renewable Sustainable Energy Rev.* **2013**, *22*, 466–481, DOI: 10.1016/j.rser.2013.01.032.
14. Luceño, J. A.; Martín, M. Two-step optimization procedure for the conceptual design of A-frame systems for solar power plants. *Energy* **2018**, *165*, 483– 500, DOI: 10.1016/j.energy.2018.09.177.
15. Luceño, J. A.; Martín, M. Optimal design of aging systems: A-frame coolers design under fouling. *Comput. Chem. Eng.* **2019**, *122*, 47– 58, DOI: 10.1016/j.compchemeng.2018.05.015.
16. Heyns, J. A. Performance characteristics of an air-cooled steam condenser incorporating a hybrid (dry/wet) dephlegmator. M.Sc. Thesis, University of Stellenbosch, Stellenbosch, South Africa, 2008.
17. Sharma, P.; Chandra, L.; Ghoshdastidar, P. S.; Shekhar, R. A novel approach for modelling fluid low and heat transfer in an Open Volumetric Air Receiver using ANSYS-FLUENT. *Sol. Energy* **2020**, *204*, 246– 255, DOI: 10.1016/j.solener.2020.04.031.
18. Barreto, G.; Canhoto, P.; Collares-Pereira, M. Parametric analysis and optimisation of porous volumetric solar receivers made of open-cell SiC ceramic foam. *Energy* **2020**, *200*, 117476, DOI: 10.1016/j.energy.2020.117476.
19. Navalho, J. E. P.; Pereira, J. C. F. A comprehensive and fully predictive discrete methodology for volumetric solar receivers: application to a functional parabolic dish solar collector system. *Appl. Energy* **2020**, *267*, 114781, DOI: 10.1016/j.apenergy.2020.114781.

20. Chen, S.; Li, W.; Yan, F. Thermal performance analysis of a porous solar cavity receiver. *Renew. Energy* **2020**, *156*, 558– 569, DOI: 10.1016/j.renene.2020.04.077.
21. Gimeno-Furio, A.; Hernandez, L.; Martinez-Cuenca, R.; Mondragón, R.; Vela, A.; Cabedo, L.; Barreneche, C.; Iacob, M. New coloured coatings to enhance silica sand absorbance for direct particle solar receiver applications. *Renew. Energy* **2020**, *152*, 1– 8, DOI: 10.1016/j.renene.2020.01.053
22. Behar, O.; Khellaf, A.; Mohammedi, K. A review of studies on central receiver solar thermal power plants. *Renewable Sustainable Energy Rev.* **2013**, *23*, 12– 39, DOI: 10.1016/j.rser.2013.02.017.
23. Pérez Gómez, E. Diseño térmico y análisis económico y medioambiental de una planta termosolar de 30 MW con tecnología de torre central, acumulación de calor mediante sales fundidas y operación ininterrumpida. B.Sc. Thesis, Universidad Carlos III de Madrid, 2013.
24. Jebamalai, J. S. M. Receiver Design Methodology for Solar Tower Power Plants. M.Sc. Thesis, KTH School of Industrial Engineering and Management, 2016.
25. Wei, M.; Fan, Y.; Luo, L.; Flamant, G. Fluid Flow distribution optimization for minimizing the peak temperature of a tubular solar receiver. *Energy* **2015**, *91*, 663–677, DOI: 10.1016/j.energy.2015.08.072.
26. Sánchez-González, A.; Rodríguez-Sánchez, M. R.; Santana, D. Aiming factor to flatten the flux distribution on cylindrical receivers. *Energy* **2018**, *153*, 113– 125, DOI: 10.1016/j.energy.2018.04.002.
27. Carrizosa, E.; Domínguez-Bravo, C.; Fernández-Cara, E.; Quero, M. Optimization of multiple receivers solar power tower systems. *Energy* **2015**, *90*, 2085– 2093, DOI: 10.1016/j.energy.2015.08.005.
28. Alonso-Montesinos, J.; Monterreal, R.; Fernández-Reche, J.; Ballestrín, J.; Carra, E.; Polo, J.; Barbero, J.; Batlles, F. J.; López, G.; Enrique, R.; Martínez-Durbán, M.; Marzo, A. Intra-hour energy potential forecasting in a central solar power plant receiver combining Meteosat images and atmospheric extinction. *Energy* **2019**, *188*, 116034, DOI: 10.1016/j.energy.2019.116034.
29. Wang, G.; Niu, S.; Yu, S.; Lin, J.; Chen, Z.; Hu, P. Parametric Study on Integrated Thermal and Mechanical Performance of Molten Salt Receiver for Solar Tower Plant. *Int. J. Thermophys.* **2020**, *41*, 23, DOI: 10.1007/s10765-020-2603-4.

30. Yu, Q.; Fu, P.; Yang, Y.; Qiao, J.; Wang, Z.; Zhang, Q. Modeling and parametric study of molten salt receiver of concentrating solar power tower plant. *Energy* **2020**, *200*, 117505, DOI: 10.1016/j.energy.2020.117505.
31. Peterseim, J. H.; White, S.; Hellwig, U. Novel solar tower structure to lower plant cost and construction risk. *AIP Conf. Proc.* **2016**, *1734*, 070025, DOI: 10.1063/1.4949172.
32. Wagner, M. J. Simulation and predictive performance modeling of utility-scale central receiver system power plants. M.Sc. Thesis, University of Wisconsin-Madison, 2008.
33. Mizutani, F. T.; Pessoa, F. L. P.; Queiroz, E. M.; Hauan, S.; Grossmann, I. E. Mathematical programming model for heat exchanger network synthesis including detailed heat exchanger designs. 1. Shell-and-tube heat exchanger design. *Ind. Eng. Chem. Res.* **2003**, *42*, 4009– 4018, DOI: 10.1021/ie020964u.
34. TEMA, Tubular Exchanger Manufacturers Association INC. *Standards of the Tube Exchanger Manufacturers Association*, 9th ed.; Gaddis, D., Ed.; Tubular Exchanger Manufacturers Association INC: New York, 2007; pp. 5.1-1– 5.2-3.
35. Drake, T.; Bruce, K.; Frank, B. *Baseload Nitrate Salt Central Receiver Power Plant Design (Final Report)*; Abengoa Solar LLC: Sandia National Lab: Colorado, 2014; pp 1– 52.
36. DWIA, Danish Wind Industry Association. Wind Energy Reference Manual. 2003. http://drømstørre.dk/wp-content/wind/miller/windpower%20web/en/stat/units.htm (accessed February 7, 2020).
37. Bañuelos-Ruedas, F.; Camacho, C. A.; Rios-Marcuello, S. Methodologies Used in the Extrapolation of Wind Speed Data at Different Heights and Its Impact in the Wind Energy Resource Assessment in a Region. *Wind Farm—Technical Regulation, Potential Estimation and Siting Assessment*; IntechOpen, 2010.
38. Churchill, S. W.; Chu, H. H. S. Correlating equations for laminar and turbulent free convection from a vertical plate. *Int. J. Heat Mass Tran.* **1975**, *18*, 1323– 1329, DOI: 10.1016/0017-9310(75)90243-4.
39. White, F. M. Viscous Flow in Ducts. *Fluid Mechanics*, 7th ed.; Mc Graw Hill: New York, 2011, pp 347– 453.
40. Zavoico, A. B. *Solar Power: Tower Design Basis Document*, Revision 0; Sandia National Lab: San Francisco, 2001; pp 35– 119.

41. UNEPFI, United Nations Environment Programme Finance Initiative. The GHG Indicator: UNEP Guidelines for Calculating Greenhouse Gas Emissions for Businesses and Non-Commercial Organisations. 2000. https://www.unepfi.org/fileadmin/documents/ghg_indicator_2000.pdf (accessed June 14, 2020).
42. CDP, Carbon Pricing Connect. October 2017. https://www.cdp.net/en/climate/carbon-pricing/carbon-pricing-connect (accessed July 17, 2020).
43. SPECIALMETALS. The story of the "INCOLOY® allows series," from 800, through 800H, 800HT®. 2004. https://www.specialmetals.com/assets/smc/documents/alloys/incoloy/incoloy-alloys-800h-800ht.pdf (accessed July 5, 2020).
44. High Temp Metals. Alloy 800/800AT/800H technical data. 2015. http://www.hightempmetals.com/techdata/hitempIncoloy800data.php (accessed July 5, 2020).
45. Aesterion Steels LLP. Incoloy 800 Tube, Tubing & Pipe. http://aesteironsteelpipes.com/uns-n08800-incoloy-800-tube-tubing-pipe-258.html#price (accessed 5 July 2020).
46. Palys, M. J.; Daoutidis, P. Using hydrogen and ammonia for renewable energy storage: A geographically comprehensive techno-economic study. *Comput. Chem. Eng.* **2020**, *136*, 106785, DOI: 10.1016/j.compchemeng.2020.106785.
47. PVGIS, Photovoltaic Geographical Information System. The European Commission's science and knowledge service, 2020. Available online. https://ec.europa.eu/jrc/en/pvgis (accessed 12 March 2020).
48. Martín, J. H. Diseño y análisis de una planta termosolar de torre central con configuraciones de único o doble receptor operando con sales fundidas. B.Sc. Thesis, Universidad Carlos III de Madrid, 2012.

IV.1.9. Supporting Information

IV.1.9.1. Supporting Information tables

Table S1. Friction coefficient values for different ground topographies[1]

Landscape type	Friction coefficient, ω
Lakes	
Ocean	0.10
Smooth hard ground	
Grasslands (gound level)	0.15
Tall crops, hedges and shrubs	0.20
Heavily forested land	0.25
Small town with some trees and shrubs	0.30
City areas with high rise buildings	0.40

Table S2. Upper bounds and lower bounds of variables

Variable	Unit	Lower bound	Upper bound
H_{req}	m	2	30
D_{req}	m	4	18
HD_{ratio}	-	1	2
A_{req}	m2	0	2700
A_{ob}	m2	0	2700
v_{MS}	m/s	1	4
d_{ex}	m	0.02	0.06
d_{in}	m	0.001	0.059
N_{tb}	-	1	100
N_{bundle}	-	1	50
B_{tube}	m	0.002	0.01
B_{bundle}	m	0.002	0.01
ΔP_{tube}	Pa	0	1.00E+06

Table S3. Design results with 465 kW/m^2 as $HF_{\max}$

Variable	Almería		Arizona		Scotland	
	SHF	**SMP**	**SHF**	**SMP**	**SHF**	**SMP**
H_{req} (m)	9.262	10.829	10.132	10.132	5.617	10.745
D_{req} (m)	9.158	10.829	10.047	10.047	5.617	10.745
A_{ob} (m^2)	418.557	578.680	502.385	502.385	155.684	569.761
A_{proj} (m^2)	266.462	368.399	319.828	319.828	99.111	362.721
H_{tower} (m)	132.269	150.544	142.217	142.217	99.851	149.439
d_{ex} (m)	0.025	0.032	0.025	0.025	0.025	0.025
d_{in} (m)	0.024	0.030	0.024	0.024	0.024	0.024
A_{flow} (m^2)	0.033	0.040	0.042	0.042	0.010	0.039
N_{tb}	75	56	96	96	23	88
N_{bundle}	14	18	12	12	28	14
$n_{tubeTOT}$	1050	1008	1152	1152	644	1232
B_{tube} (m)	0.002	0.002	0.002	0.002	0.002	0.002
B_{bundle} (m)	0.002	0.002	0.002	0.002	0.002	0.002

Table S4. Contribution of h_{nat} and h_{for} in h_{mix} for Almería's scenarios

SAME HELIOSTAT FIELD (SHF)			**SAME MEAN PRODUCTION (SMP)**		
h_{nat} **(kW/m^2 K)**	h_{for} **(kW/m^2 K)**	h_{mix} **(kW/m^2 K)**	h_{nat} **(kW/m^2 K)**	h_{for} **(kW/m^2 K)**	h_{mix} **(kW/m^2 K)**
1.00E-02	0.03	0.03	1.00E-02	0.03	0.03
1.00E-02	0.033	0.033	1.00E-02	0.032	0.032
1.00E-02	0.033	0.034	1.00E-02	0.033	0.033
1.00E-02	0.034	0.034	1.00E-02	0.034	0.034
1.00E-02	0.033	0.034	1.00E-02	0.033	0.033
1.00E-02	0.032	0.032	1.00E-02	0.032	0.032
1.00E-02	0.031	0.031	1.00E-02	0.030	0.030
1.00E-02	0.031	0.031	1.00E-02	0.030	0.031
1.00E-02	0.032	0.032	1.00E-02	0.031	0.032
1.00E-02	0.030	0.030	1.00E-02	0.029	0.030
1.00E-02	0.030	0.030	1.00E-02	0.030	0.030
1.00E-02	0.030	0.030	1.00E-02	0.029	0.030

Table S5. Contribution of h_{nat} and h_{for} in h_{mix} for Arizona's scenarios

SAME HELIOSTAT FIELD (SHF)			SAME MEAN PRODUCTION (SMP)		
h_{nat} (kW/m² K)	h_{for} (kW/m² K)	h_{mix} (kW/m² K)	h_{nat} (kW/m² K)	h_{for} (kW/m² K)	h_{mix} (kW/m² K)
1.10E-02	0.031	0.031	1.10E-02	0.031	0.031
1.10E-02	0.031	0.031	1.10E-02	0.031	0.031
1.00E-02	0.016	0.018	1.00E-02	0.016	0.018
1.00E-02	0.016	0.017	1.00E-02	0.016	0.017
1.00E-02	0.016	0.017	1.00E-02	0.016	0.017
1.00E-02	0.016	0.017	1.00E-02	0.016	0.017
1.00E-02	0.016	0.017	1.00E-02	0.016	0.017
1.00E-02	0.016	0.017	1.00E-02	0.016	0.017
1.00E-02	0.016	0.017	1.00E-02	0.016	0.017
1.00E-02	0.016	0.017	1.00E-02	0.016	0.017
1.00E-02	0.016	0.018	1.00E-02	0.016	0.018
1.10E-02	0.017	0.018	1.10E-02	0.017	0.018

Table S6. Contribution of h_{nat} and h_{for} in h_{mix} for Scotland's scenarios

SAME HELIOSTAT FIELD (SHF)			SAME MEAN PRODUCTION (SMP)		
h_{nat} (kW/m² K)	h_{for} (kW/m² K)	h_{mix} (kW/m² K)	h_{nat} (kW/m² K)	h_{for} (kW/m² K)	h_{mix} (kW/m² K)
-	-	-	-	-	-
1.10E-02	0.053	0.053	1.10E-02	0.050	0.050
1.10E-02	0.047	0.047	1.10E-02	0.044	0.044
1.10E-02	0.042	0.042	1.10E-02	0.040	0.040
1.00E-02	0.040	0.040	1.00E-02	0.038	0.038
1.00E-02	0.038	0.038	1.00E-02	0.036	0.036
1.00E-02	0.039	0.039	1.00E-02	0.037	0.037
1.00E-02	0.045	0.046	1.00E-02	0.043	0.043
-	-	-	-	-	-
-	-	-	-	-	-
-	-	-	-	-	-
-	-	-	-	-	-

IV.1.9.2. Supporting Information figures

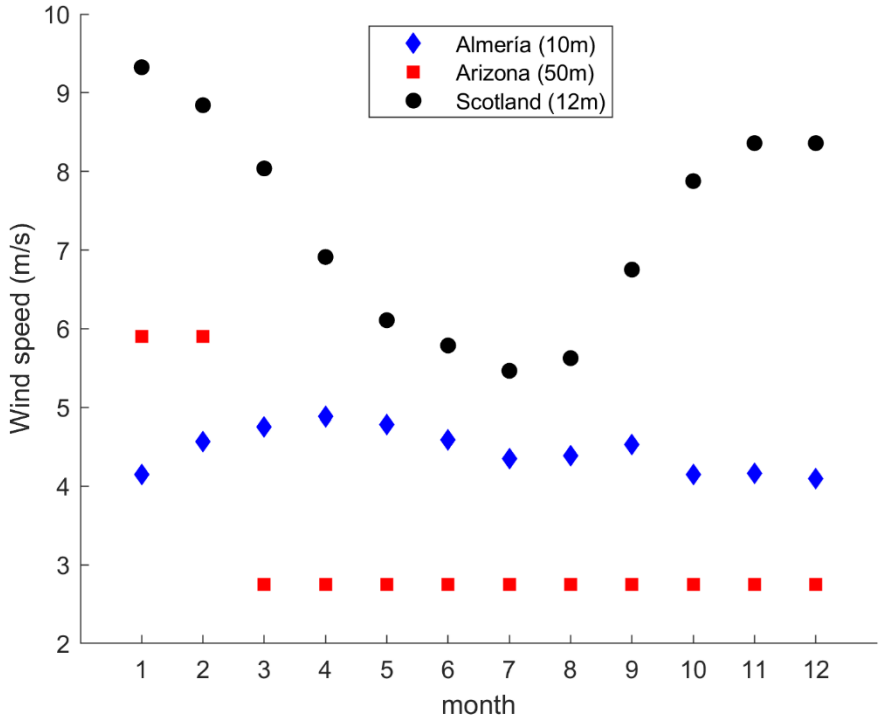

Figure S1: Wind speed data for each location (non-rescaled) [2-4]

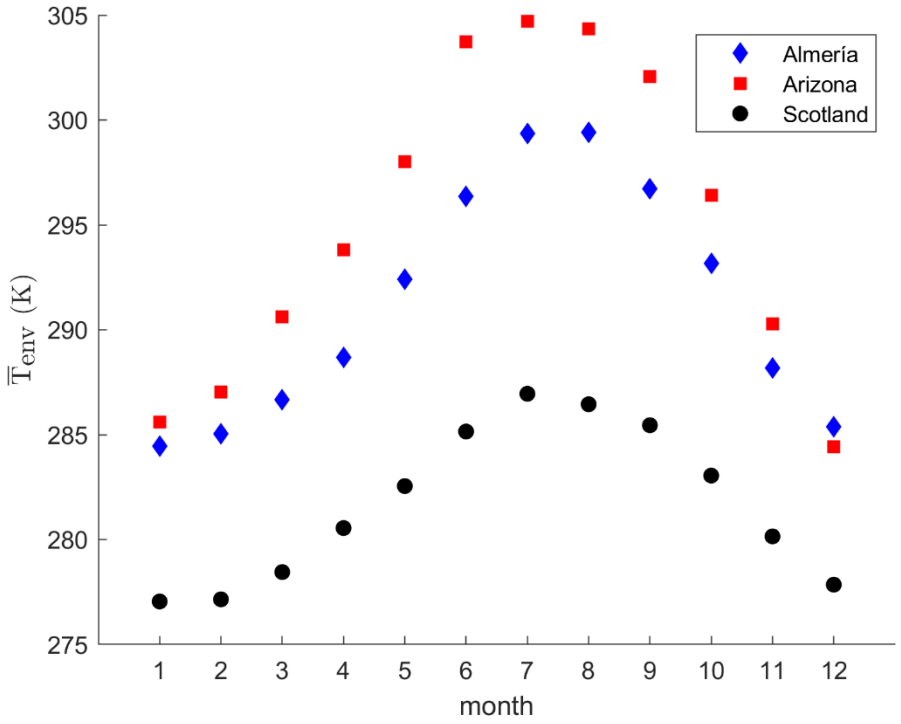

Figure S2: Temperature of environment for each location

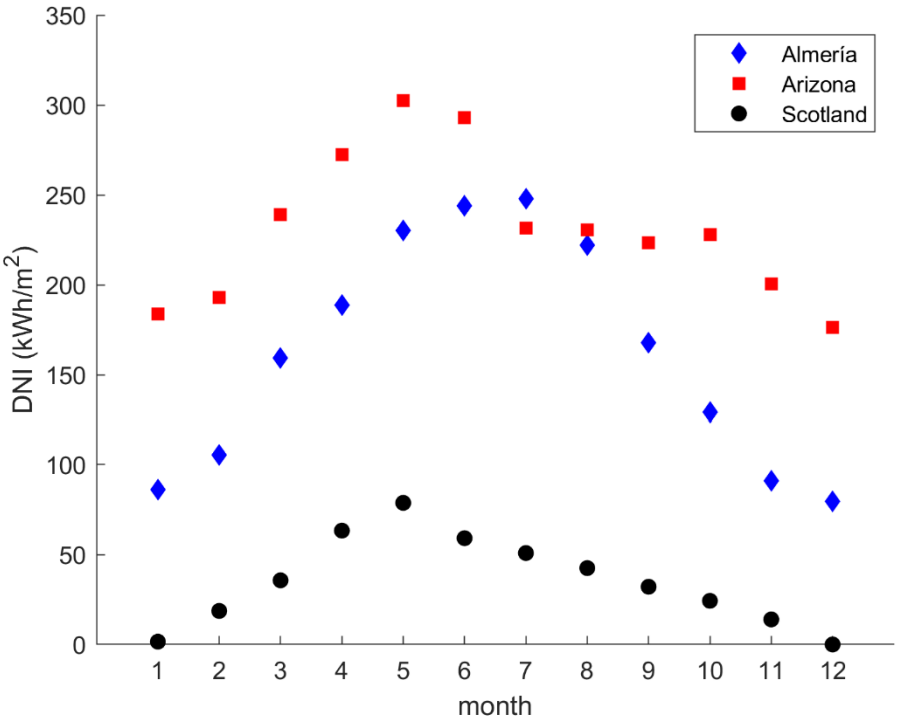

Figure S3: Direct Normal Irradiation (DNI) for each location

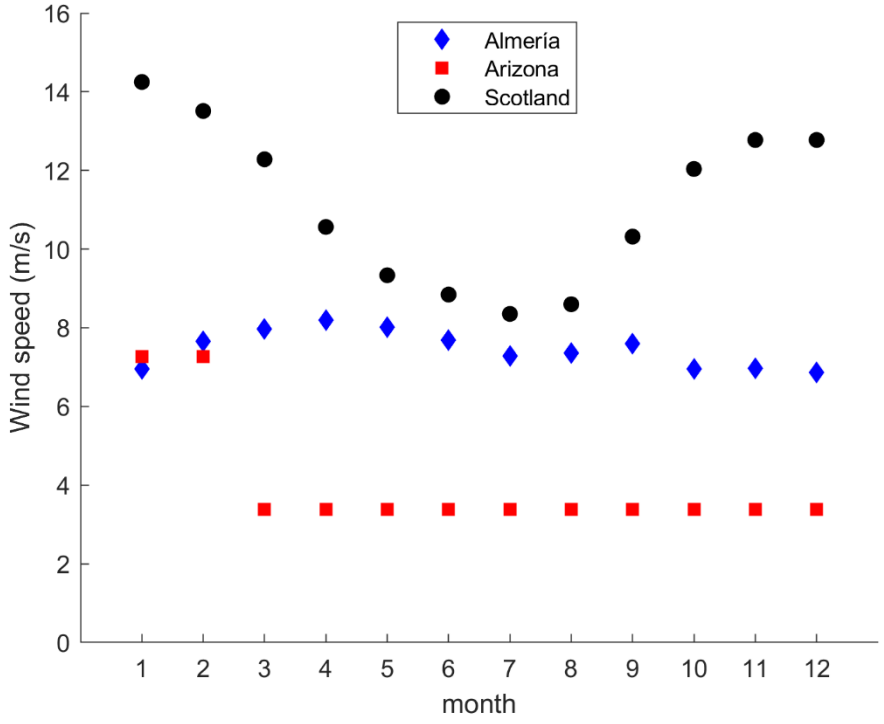

Figure S4: Rescaled wind speed data for SHF scenario.

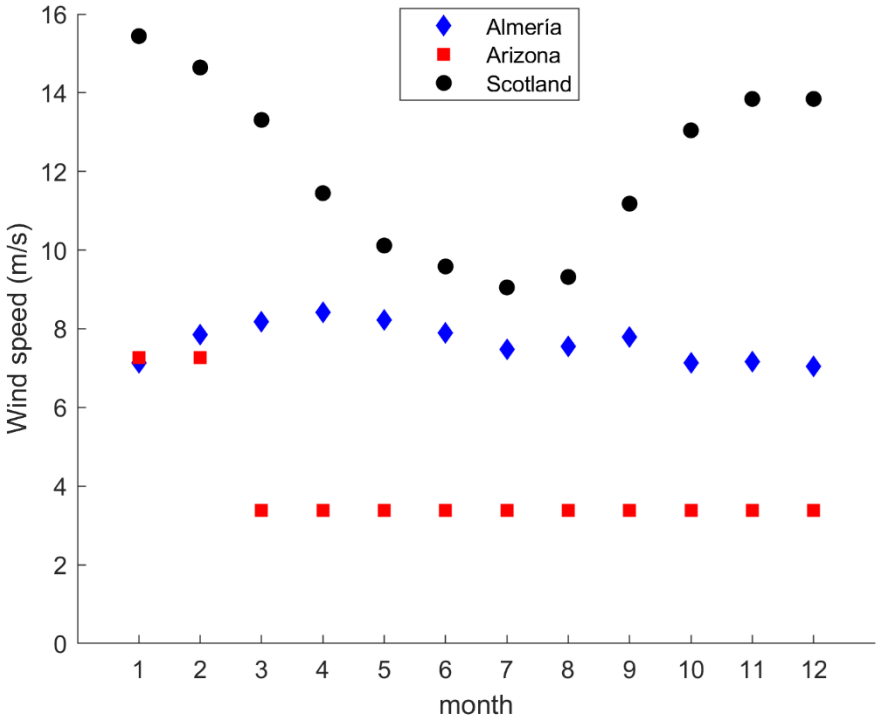

Figure S5: Wind speed rescaled data for SMP scenario.

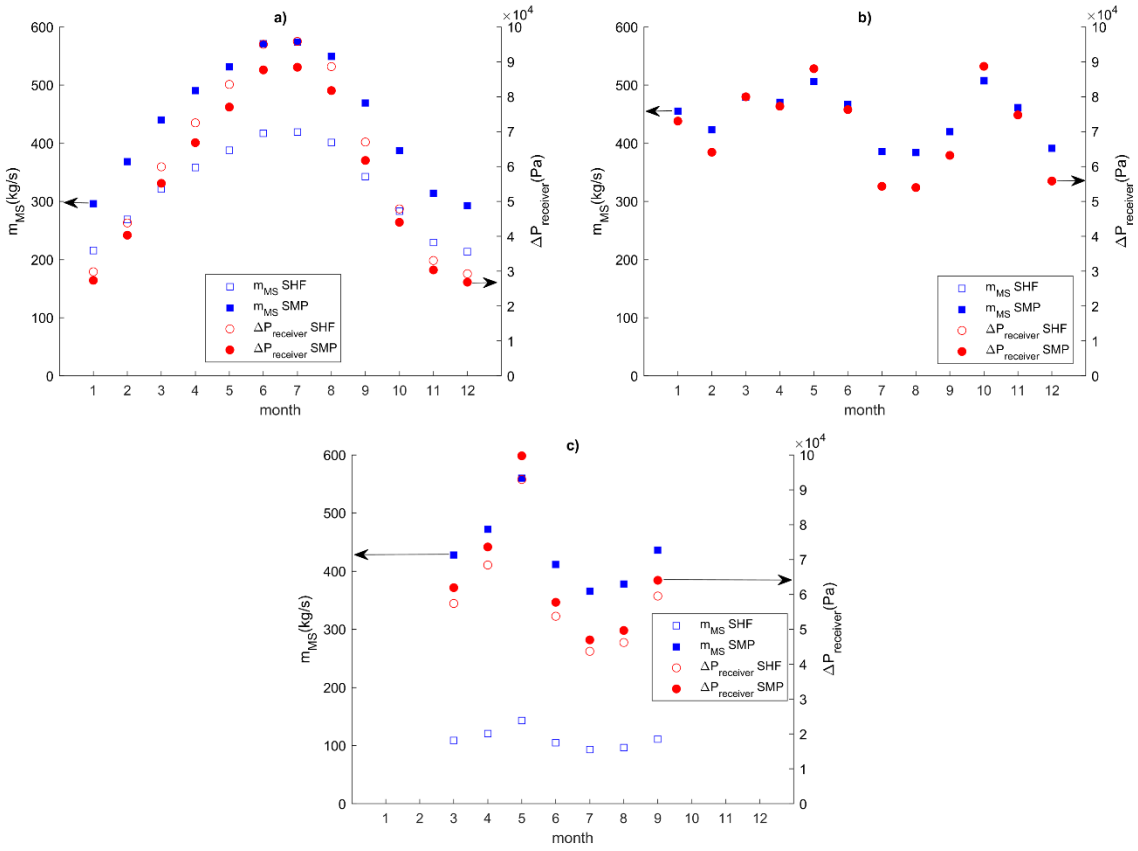

Figure S6: Fluctuation of pressure drop with mass flow for each location: a) Almería; b) Arizona; c) Scotland.

IV.1.9.3. References

1. Bañuelos-Ruedas, F.; Camacho, C.A.; Rios-Marcuello, S. Methodologies Used in the Extrapolation of Wind Speed Data at Different Heights and Its Impact in the Wind Energy Resource Assessment in a Region. In "Wind Farm – Technical Regulation, Potential Estimation and Siting Assessment". IntechOpen, 2010. https://doi.org/10.5772/20669.
2. Northern Arizona University. State of Arizona Wind resource maps. (Accessed 24 February 2020). Available at: https://in.nau.edu/clean-energy-research/wind-resource-maps/.
3. AEMET, Agencia Estatal de Meterología. DATOS AEMET - Open Data - / Viento. (Accessed 24 February 2020). Available at: https://datosclima.es/Aemethistorico/Vientostad.php.
4. Met Office. Western Scotland: climate. (Accessed 24 February 2020). Available at: https://www.metoffice.gov.uk/binaries/content/assets/metofficegovuk/pdf/weather/learn-about/uk-past-events/regional-climates/western-scotland_-climate---met-office.pdf

CAPíTVLO V

CONCLVSiONES GENERALES Y TRABAJOS FVTVROS

V. CONCLUSIONES GENERALES Y TRABAJOS FUTUROS

V.1. Conclusiones Parciales

En este Capítulo se presentan las conclusiones alcanzadas a lo largo de los trabajos enmarcados en la Tesis. El Capítulo se encuentra estructurado siguiendo la distinción según el sistema estudiado: Estudios relativos a la tecnología de enfriamiento seco A-frame; y Estudio del Colector Central.

V.1.1. Estudios relativos a la tecnología de enfriamiento seco A-frame

La importancia de los sistemas de enfriamiento A-frame en las plantas de potencia por concentración solar (CSP) recae en la alta dependencia de agua de los sistemas de refrigeración convencionales de este tipo de instalaciones. Generalmente la incidencia de radiación solar, que es el parámetro que define la capacidad de producción de la planta, es mayor en regiones con una disponibilidad limitada de agua, lo cual implica un mayor coste de los sistemas de refrigeración húmeda tradicionales (ej. torre de enfriamiento). El uso de sistemas de enfriamiento por aire (en esta Tesis, considerando la arquitectura A-frame) permite evitar el consumo de agua asociable al sistema de refrigeración, pero presenta un nuevo consumo de energía derivado del uso de ventiladores de aire. Buscando reducir este consumo de energía, se llevaron a cabo los siguientes estudios.

El primer trabajo sobre la tecnología A-frame se centró en la definición de un modelo detallado para su diseño, el cual incluyó las variables de diseño más importantes

en este tipo de equipos de refrigeración de aire. Algunas de dichas variables fueron el ángulo de apertura, el número de tubos por fila y la separación entre tubos, su distribución en diferentes filas de tubos y bancos de tubos, o las variables características de los tubos (ej. diámetros, longitud) y de las posibles superficies extendidas de transferencia de energía (aletas). El modelo fue aplicado en el caso de una planta CSP, y se presentó una metodología de optimización en dos etapas para el diseño conceptual del equipo y una estimación de la operación mensual. La primera etapa consistía en un problema MINLP, el cual era resuelto considerando el mes de máxima carga de refrigeración, que permitía obtener el diseño del equipo; dicho problema fue resuelto aplicando un algoritmo Branch and Bound desarrollado a medida para el problema. La segunda etapa de la metodología cubría la operación mensual del equipo, y fue formulada como un problema MINLP multi-periodo; con este nuevo MINLP se obtuvo información acerca del consumo de potencia por cada ventilador del equipo, cuántos se encontraban en operación o parados, y el flujo de aire que circulaba por cada ventilador. Este estudio de optimización permitió reducir el consumo de potencia reportado por trabajos previos en un 20% (representado un total de 0.7% de la energía producida por la planta CSP), lo cual implica una notable cantidad de energía. Además, la metodología puso de manifiesto que la evaluación multi-periodo del diseño mejora el rendimiento del equipo (ej. se redujo el flujo mensual de aire gracias al aumento del gradiente de temperatura), y se mostró que la operación está estrechamente relacionada con el perfil de radiación de la localización de la planta (ej. mayores consumos durante los meses de veranos debidos al aumento de producción). Sin embargo, los resultados revelaron que el efecto combinado de la localización, la disponibilidad de agua y las condiciones climáticas afectan de manera considerable a la selección entre una torre de enfriamiento y un sistema A-frame, siendo más competitiva la primera opción excepto en escenarios desérticos o con una muy limitada disponibilidad de agua.

El segundo trabajo profundizó en el estudio del diseño de equipos de transferencia de energía considerando el efecto del ensuciamiento durante la operación del mismo. El ensuciamiento es un fenómeno que reduce progresivamente el rendimiento del equipo debido a la acumulación de partículas sólidas en las superficies de transferencia de energía. El modelo desarrollado en el trabajo previo fue extendido considerando un

modelo para evaluar el efecto de la deposición de partículas en la superficie de transferencia de calor (es decir, en la superficie externa de los tubos), debido a la aparición de una nueva resistencia térmica, y en el incremento de la pérdida de carga a través del banco de tubos. El problema fue dividido en dos etapas, las cuales fueron: 1) diseño óptimo del equipo aplicando el modelo ya desarrollado, y considerando el mes con las condiciones más exigente de operación y ensuciamiento; y 2) evaluación del tiempo de operación antes de realizar un número determinado de limpiezas del equipo. La primera etapa fue formulada como un problema MINLP para obtener el diseño del sistema A-frame para unas condiciones concretas de ensuciamiento (4 escenarios considerados) y el mes de mayor demanda de refrigeración. En esta primera etapa, el coeficiente global de transferencia de energía (U) se calculó para el último año de operación, con el objetivo de considerar las condiciones más exigentes de ensuciamiento. En la segunda etapa, el coeficiente U fue recalculado para cada mes, y posteriormente se formuló un conjunto de problemas MINLP multi-periodo para cubrir todas las ventanas de tiempo. Se incluyó una estimación del coste de la limpieza del equipo basándose en la potencia no producida debido a la parada del equipo. Los resultados mostraron el diseño óptimo conceptual, de acuerdo con los datos de ensuciamiento aplicados, la planificación de limpiezas óptima, y los valores de las variables de operación como son el uso de ventiladores, flujos de aire, etc. El consumo de potencia fue reducido en términos generales, pero se observó que el consumo se veía incrementado durante la operación hasta el momento de la siguiente limpieza, momento en el cual se reducía de nuevo.

V.1.2. Estudio del Colector Central

El colector solar es uno de los equipos más característicos de las plantas CSP, y es el lugar donde el fluido de transferencia de calor absorbe la energía suficiente para producir vapor de agua en etapas posteriores. En la presente Tesis se estudió la arquitectura del colector central

En el estudio del colector central se desarrolló una metodología de dos etapas para el diseño de este tipo de equipos, y para la evaluación del coeficiente de transferencia de energía. En la primera etapa, el diseño del equipo fue obtenido aplicando una formulación

MINLP del problema. Las variables geométricas del diseño fueron presentadas considerando como opciones los valores estándar en mercado, y su diferente distribución. Además, el efecto de la localización de la planta y de las condiciones climáticas en el diseño fueron evaluadas mediante el estudio de tres localizaciones diferentes (Arizona, Escocia, y Almería). La segunda etapa, que cubre la operación y la evaluación de la transferencia de energía, fue desarrollada aplicando una formulación NLP con las variables de diseño fijadas. Como en la etapa de diseño, el conjunto de localizaciones consideradas permitió estudiar la fluctuación y diferencias en los perfiles de las variables de operación y el comportamiento de la transferencia de energía.

Tres localizaciones (Arizona, Escocia, y Almería) fueron consideradas debido a las diferencias en sus perfiles de radiación, sus condiciones climáticas (ej. velocidad del viento), y en sus periodos de operación, ya que es posible que algunas localizaciones tengan que operar dentro de una ventana de tiempo menor. Además, para poder realizar una comparación más profunda, se consideraron dos escenarios diferentes para cada localización: 1) misma producción media durante el periodo de operación; y 2) mismo tamaño del campo de heliostatos, lo que implica una producción diferente debido a las diferencias en el perfil de radiación.

Los resultados de los diseños mostraron que mayores valores de producción requerían unidades más grandes, en todas las localizaciones. Sin embargo, aunque el dimensionamiento del equipo se veía afectado por la localización estudiada, se identificó que la localización no era el único parámetro de decisión final, ya que el dimensionamiento del área puede relacionarse con el uso de tubos más largos, pero también con la variación en el número de tubos en vez de en su tamaño. Este hecho puede deberse a que probablemente alguna restricción específica no fue considerada durante la formulación del modelo (ej. patrones de distribución estándar comerciales). Los resultados de la operación concluyeron que mayores valores de radiación permitían obtener valores de eficiencia del equipo más altos. Las pérdidas totales de calor se relacionaban principalmente con fenómenos de reflexión (65-75%), seguido de la aportación de las pérdidas por convección; las pérdidas por radiación representaban la menor parte de las pérdidas, debido principalmente a las temperaturas de trabajo consideradas.

V.2. Conclusiones Finales

1. Se estudió el diseño óptimo de los sistemas de refrigeración seca A-frame mediante un modelado matemático del equipo. Se formuló un problema de optimización MINLP, que incluyó las variables más características de este tipo de equipos (como son el ángulo de apertura, la caracterización y distribución de los tubos, o la distribución de los sistemas de ventiladores), y fue resuelto mediante la aplicación de una metodología Branch and Bound diseñada a medida. Las variables fueron acotadas utilizando valores comunes de otros diseños.
2. La operación de los equipos A-frame fue evaluada mediante un problema MINLP multi-periodo, mostrando el comportamiento de este tipo de equipos durante un año de operación típico. Optimizando previamente el diseño del equipo para una localización concreta, se consiguió reducir hasta en un 20% el consumo de energía del equipo (aproximadamente un 4% de la producción de la instalación). Además, se determinó que no todos los ventiladores deberían funcionar simultáneamente, sino que dependiendo de la época del año la operación variaría (funcionando a plena capacidad durante verano).
3. El efecto de los fenómenos de pérdida de eficiencia en el diseño de los equipos fue también estudiado para el caso de los enfriadores A-frame, considerando dos cinéticas de ensuciamiento diferentes (lineal y sigmoidea). Se formuló un problema MINLP empleando el modelo matemático presentado en trabajos previos, pero incluyendo el efecto del ensuciamiento en las variables pertinentes (ej. coeficiente global de transferencia de energía, o pérdida de carga). Los resultados obtenidos mostraron la necesidad de aumentar y redistribuir el área de transferencia del equipo para poder suplir la pérdida de eficiencia.
4. La variación del periodo de operación de los equipos A-frame debido al ensuciamiento fue evaluada, teniendo en cuenta las posibles etapas de limpieza del equipo y su coste derivado, formulando un conjunto de problemas MINLP multi-periodo. El aumento del tiempo máximo de operación del equipo influía de manera notable en el área total de éste, a la vez que presentaba un menor número

de limpiezas. Después de optimizar varios escenarios de operación, se llevó a la conclusión de una venta de 8 años de operación era la idónea para el caso de estudio, permitiendo mantener el consumo energético del equipo en torno al 4% de la producción de la instalación.

5. El diseño de los colectores centrales fue llevado a cabo proponiendo un modelo MINLP para los colectores centrales tubulares, en el cual la inclusión de variables enteras permite distribuir de manera más eficiente los tubos del colector y permite considerar opciones comerciales estándar como límites de las variables. Además, se estudió el efecto del clima de la localización de la planta en el diseño del equipo, y el efecto de diferentes escenarios de producción, considerando tres localizaciones diferentes (Almería, Arizona, y Escocia). Los diseños obtenidos mostraron que mayores capacidades de producción implicaban unidades más grandes, en las cuales se podía compensar el incremento de área o con un mayor número de tubos o un mayor diámetro de tubo.
6. La operación del colector central fue estudiada para diferentes perfiles de radiación, condiciones climáticas, y capacidades de producción aplicando una formulación NLP, en la cual el diseño del equipo se encontraba fijado. El comportamiento de las variables de transferencia de energía mostró que el perfil de radiación de la localización definía la eficiencia del equipo, a la vez que los perfiles de velocidades de aire afectaban de manera significativa a la transferencia de calor por convección. Además, se identificó que podían existir otras posibles dependencias con las variables de diseño para reducir la pérdida de carga en el interior de los tubos, a la vez que se controlase la tensión térmica de éstos.

V.3. Trabajos Futuros

A la vista de los resultados obtenidos a lo largo de la presente Tesis, se proponen las siguientes líneas de actuación para trabajos futuros:

1. Estudio simultáneo de la operación y los procesos de mantenimiento de los equipos de transferencia de calor:

   Las plantas CSP dependen especialmente de las condiciones climáticas de la localización donde se emplazan y de la disponibilidad de recursos, como el agua. Por ejemplo, en un escenario de clima semidesértico, los enfriadores de aire son una opción de refrigeración muy atractiva, pero su diseño y operación se ven afectados por fenómenos de ensuciamientos y la variabilidad de las condiciones externas. Estas condiciones externas afectan a otros sistemas de la instalación como pueden ser el colector central o el campo de heliostatos. En esta línea de actuación, un trabajo futuro sería la formulación de estudios acerca del funcionamiento óptimo de la instalación completa, a la vez que se considera la programación de limpiezas durante un largo horizonte temporal en el coste global de diseño y operación, continuando con el desarrollo de metodologías que ya se ha realizado en trabajos derivados de la Tesis [DOI: 10.1016/j.compchemeng.2021.107312].

2. Estudio de la operación de los equipos considerando fenómenos estocásticos:

   La variabilidad e incertidumbre asociada a los fenómenos climatológicos que pueden tener lugar en las localizaciones más interesantes para plantas CSP representa un punto de importancia vital para su futura operación. La predicción o preparación realista y no sobreestimada de estos sucesos, y su posible efecto en la producción de la instalación, permitiría obtener instalaciones mucho más fiables de cada a su operación a lo largo de la vida útil de los equipos. Este tipo de fenómenos podrían definirse mediante procesos estocásticos integrados en los modelos ya desarrollados, permitiendo obtener ahorros significativos en los costes

de operación gracias a la planificación de una política correcta de mantenimiento. Un punto de partida para esta línea de investigación puede verse desarrollado en los trabajos derivados de la Tesis [DOI: 10.1016/j.energy.2020.118861].

3. Desarrollo de modelos y procedimientos de resolución simultánea de diseño y operación de equipos de transferencia de calor:

   Los actuales marcos de optimización utilizados presentan la necesidad de formular dos problemas para abordar con éxito el diseño riguroso del equipo, y poder posteriormente evaluar su operación. Alcanzar la capacidad de estudiar simultáneamente ambos aspectos reduciría el tamaño de los modelos, aún con un posible incremento de la dificultad de resolución.

CAPíTVLO Vi

LiSTADO DE CONTRiBVCiONES

ARTÍCULOS EN REVISTAS INTERNACIONALES:

Luceño, J.A.; de la Fuente, E.; Martín, M. Optimal Design of Solar Receivers in CSP Plants: Effects of Facility Location. *Ind. Eng. Chem. Res.* **2021**, *XXX*, XXX-XXX (ASAP), DOI: 10.1021/acs.iecr.0c05383.

Lozano-Santamaria, F.; Luceño, J.A.; Martín, M.; Macchietto, S. Optimal operation and cleaning scheduling of air coolers in concentrated solar plants. *Comput. Chem. Eng.* **2021**, *150*, 107312, DOI: 10.1016/j.compchemeng.2021.107312.

Lozano-Santamaria, F.; Luceño, J.A.; Martín, M.; Macchietto, S. Optimal Design of Solar Receivers in CSP Plants: Effects of Facility Location. *Energy* **2020**, *213*, 118861, DOI: 10.1016/j.energy.2020.118861.

Luceño, J.A.; Martín, M. Optimal design of aging systems: A-frame coolers design under fouling. *Comput. Chem. Eng.* **2019**, *122*, 47-58, DOI 10.1016/j.compchemeng.2018.05.015.

Luceño, J.A.; Martín, M. Two-step optimization procedure for the conceptual design of A-frame systems for solar power plants. *Energy* **2018**, *165*, 483-500, DOI 10.1016/j.energy.2018.09.177.

CAPÍTULOS DE LIBRO:

Luceño, J.A.; Martín, M. **Chapter 9. Solar thermal energy**. In *Sustainable Design for Renewable Processes*. Martín, M.; Ed. Elsevier Science: 2021. ISBN 9780128243251.

Martín, M.; Luceño, J.A. **(679g) Optimal Design of Aging Systems: A-Frame Coolers Design Under Fouling**. In *2018 AIChE Annual Meeting proceedings*. Elsevier: Amsterdam; 2018. ISBN 978-0-8169-1108-0.

Luceño, J.A.; Martín, M. **Optimal design and operation of A-frame systems for solar power plants**. In *27th European Symposium on Computer Aided Process Engineering*. Elsevier: Amsterdam, 2017. ISBN: 9780444640802.

COMUNICACIONES EN CONFERENCIAS Y CONGRESOS:

Santamaria, F.L.; Luceño, J.A.; Martín, M.; Macchietto, S. *Optimal cleaning schedule of air coolers in concentrated solar power plants*. **ChemEngDayUK 2021**. April 8th 2021. Conference program: https://www.bradford.ac.uk/ei/chemical-engineering/chemengdayuk2021/conference-information/.

Martín, M.; Luceño, J.A. *(679g) Optimal Design of Aging Systems: A-Frame Coolers Design Under Fouling*. **2018 AIChE Annual Meeting**. 2018. Conference program: https://www.aiche.org/conferences/aiche-annual-meeting/2018.

Martín, M.; Luceño, J.A. *Optimal design and operation of A-frame systems for solar power plants*. **27th European Symposium on Computer Aided Process Engineering**. October 1st-5th 2017. Conference proceedings: https://www.elsevier.com/books/27th-european-symposium-on-computer-aided-process-engineering/espuna/978-0-444-63965-3.

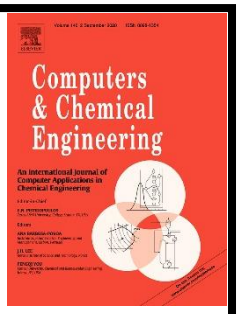

Optimal operation and cleaning scheduling of air coolers in concentrated solar plants

Lozano Santamaría, F.; **Luceño, J.A.**; Martín, M.; and Macchietto, S.

Computers and Chemical Engineering, **2020**, *XX*, XXX-XXX

DOI: 10.1016/j.compchemeng.2021.107312

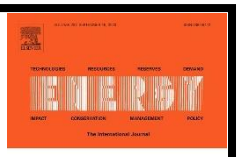

Stochastic modelling of sandstorms affecting the optimal operation and cleaning scheduling of air coolers in concentrated solar power plants

Lozano Santamaría, F.; **Luceño, J.A.**; Martín, M.; and Macchietto, S.

Energy, **2020**, *213*, 118861

DOI: 10.1016/j.energy.2020.118861

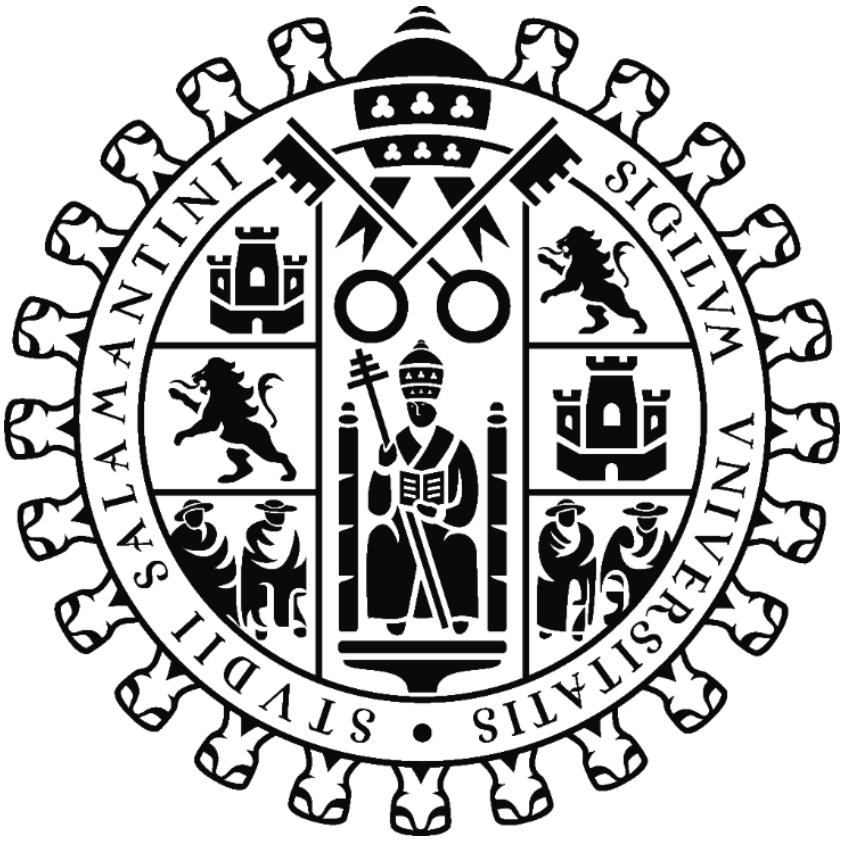
SALAMANTINI
SIGILLVM
VNIVERSITATIS
STVDII